Interaction of extreme ocean waves with offshore structures

Daniel Anthony Guy Walker

Magdalen College

A thesis submitted in partial fulfillment of the requirements for the degree of Doctor of Philosophy at the University of Oxford

Trinity Term 2006

Department of Engineering Science
University of Oxford
Parks Road
Oxford OX1 3PJ

Interaction of extreme ocean waves with offshore structures

A thesis submitted in partial fulfillment of the requirements for the degree of Doctor of Philosophy at the University of Oxford

Daniel Anthony Guy Walker

Magdalen College

Trinity Term 2006

Abstract

With most of the world's untouched oil and gas resources offshore and the possibility that hurricanes are becoming more frequent and more intense, the risks associated with offshore oil and gas production are increasing. Therefore, there is an urgent need to improve current understanding of extreme ocean waves and their interaction with structures.

This thesis is concerned with the modelling of extreme ocean waves and their diffraction by offshore structures, with the ultimate aim of proposing improved tools for guiding airgap design. The feasibility of using linear and second order diffraction solutions with a suitable incident wave field to predict extreme green water levels beneath multi-column structures is investigated. Such tools, when fully validated, could replace the need to carry out model tests during preliminary design.

When contemplating airgap design it is crucially important that consideration is given to the largest waves in a sea state, the so-called freak or rogue waves. This thesis studies the nature of one specific freak wave for which field data is available, namely the Draupner New Year wave. Unique features of this wave are identified, distinguishing it from a typical large wave, and an estimate of the probability of occurrence of the wave is given. Furthermore, a design wave, called NewWave, is proposed as a good model for large ocean waves and is validated against field and experimental data.

The diffraction of regular waves and NewWaves by a number of structural configurations is studied. In order to assess the validity of using diffraction solutions for the purposes of airgap design, comparisons are made with measured wave data from a programme of wave tank experiments. Wave data for a real platform configuration are examined to highlight the key issues complicating the validation of diffraction based design tools for real structures. The ability of diffraction theory to reproduce real wave measurements is discussed. The phenomenon of near-trapping is also investigated, allowing guidelines for airgap design to be established.

Acknowledgements

It is a pleasure to thank the following people who have contributed to my work and life as a graduate student at Oxford.

First and foremost, I would like to gratefully acknowledge the outstanding supervision of Prof. Rodney Eatock Taylor and Prof. Paul Taylor. Their combined experience, enthusiasm and insight have provided me with unparalleled supervision. Rodney introduced me to offshore engineering as an undergraduate and nurtured my development from the beginning. I thank him for his support and the confidence he has shown in me over the past four years. Paul's steadfast encouragement and continuous feed of ideas will always be appreciated. Our frequent impromptu discussions, particularly at the beginning of this project, provided the impetus for a lot of the work presented in this thesis. I would also like to thank Dr. Jun Zang for her patience and support.

I would like to acknowledge the financial support of the Engineering and Physical Sciences Research Council, Shell International Exploration and Production, and the Royal Academy of Engineering.

This project has benefited greatly from a collaboration with Shell, who have advised on offshore structures of interest and provided experimental data. I would particularly like to thank Dr. George Forristall, who helped initiate this project, and Mr. Christopher Shaw and Dr. Kevin Ewans, who were a pleasure to work with during my time at Shell. I would also like to thank Dr. Peter Tromans of Ocean Wave Engineering for providing the crest elevation statistics presented in this thesis, and Dr. Sverre Haver of Statoil for providing the field data studied.

During this DPhil I have been fortunate to spent two months at the University of Western Australia, Perth, working with Dr. Mark Cassidy. I would like to thank Mark and Dr. Byron Byrne (at Oxford) for their help setting up this visit.

Within the Ocean Engineering Group at Oxford I would like to thank Ben Western, Wei Bai, Chris Smith and Ning Dezhi, with whom I have shared offices, for providing a well-balanced working day. Thanks also to Cliff Ohl and Tim Stallard for their help during the early stages of my work. During 2005 two European placement students visited, namely Niels Eernink and Baptiste Meunier, who provided frequent and welcome relief from work.

I would like to thank the many friends I have made outside of my work, for enriching my life immeasurably simply by being such interesting and diverse people. From Magdalen alone I thank Arjun Goyal, Christoph Erben, Adam Zimbler, Ben van Duren, Ian Phillips, Pete Rudebeck, Ben Allgrove, Heather Daniell, Sarah Levine-Gronningsater, Amin Benaissa, Joris Hemelaar and Julia Paolitto, to mention only a few. I also thank my friends and colleagues on the committees I have served as a graduate. Our experiences will always be remembered. As a graduate I have been fortunate to cross paths again with a friend from my undergraduate years, Sarah Bond, who was appointed lecturer at Keble with me in 2005. We have enjoyed countless SCR meals together! Special thanks must be reserved for Helen Sarsfield, for being my best friend at Oxford for the past seven years.

I am forever indebted to my parents, Sylvia and Gary, for their dependable support throughout my life. Finally, and most importantly of all, I thank Bec, for everything.

Contents

Chapter 1

Introduction

1.1 Background

In the context of rising energy demand, it is widely accepted that fossil fuels will remain a growth industry. Most of the world's untouched (non-OPEC) oil and gas resources are offshore and therefore energy companies must develop more offshore oil and gas infrastructure, most of which will be subject to extreme ocean waves. With hurricanes becoming more frequent and perhaps more intense, the risks associated with offshore oil and gas exploration and production are increasing.

For these reasons, the ability to design offshore structures to withstand extreme wave impacts is becoming increasingly important for oil and gas production, resulting in a renewed enthusiasm from the energy industry to invest in new offshore technologies and support an improved understanding of ocean waves. Extreme waves have been sinking ships and damaging oil and gas production facilities for decades, with the subsequent loss of many human lives. However, at present the offshore industry is not able to predict accurately the effects of large ocean waves impacting structures and, as a result, the occurrence of such waves can cause considerable damage to oil and gas facilities. Although large ocean waves may not always threaten the overall integrity of an offshore structure, vertical water projection can damage equipment and lead to long periods of expensive production downtime, which in turn has detrimental consequences for the world's energy economy.

The offshore industry is particularly interested in the prediction of the maximum height to which significant volumes of water are projected above mean sea level. For steel space frame structures, the structure itself has comparatively little effect on the large ocean waves that pass through it. Hence the determination of an adequate airgap for such structures requires two factors to be taken into consideration: (i) at what elevation is the local mean water

level on which the waves ride and (ii) how tall are the crests of the largest waves? When the dimensions of the free surface piercing structure are larger, for example in the case of a gravity based platform, diffraction effects must also be included in any analysis leading to airgap prediction. It is this latter case that is studied in this project.

This project models extreme ocean waves and their diffraction by offshore structures, with the ultimate aim of proposing improved tools for guiding airgap (height of the lower deck above mean sea level) design.

At present most platform designs incorporating large diameter columns are model tested in wave tanks with little prior idea as to the effect the wave-structure interaction will have on extreme water levels. Linear diffraction solutions, which are based on small amplitude wave theory, and incident monochromatic wave fields are commonly used by the offshore industry prior to model testing to obtain an estimate of the extreme free surface magnifications in the vicinity of a structure. However, the ability of linear diffraction to accurately predict the magnitude and location of the most extreme free surface magnifications is in doubt and a monochromatic wave field is of course not a good representation of the ocean surface. Therefore, from the offshore industry's standpoint, the emphasis of current research should endeavour to develop improved models for real ocean waves, address the effectiveness of linear diffraction theory at predicting extreme water levels around structures, and study the significance of nonlinear diffraction effects.

Scaled model tests are very expensive to carry out, so if they can be avoided by developing alternative computational design tools then design costs can be greatly reduced. Furthermore, model tests are time consuming and consequently prolong the design process. At a later stage in the design process (post model testing) it is often necessary to make modifications to a platform design and because of the excessive cost and time delay associated with further model testing, the modified desigu is often installed without investigating the effects the modifications will have on extreme water levels. Computational design tools would enable the effects of any structural modifications to be assessed cheaply and quickly prior to installation. However, the offshore industry will not replace model testing by a new set of design tools until they are confident that these tools are reproducing what occurs in reality. This work seeks to propose such reliable design tools and makes progress towards instilling confidence in these tools.

Figure 1.1 shows Shell's Brent B platform in the North Sea in storm conditions. This photograph serves as an excellent illustration of the studied problem. In order to predict accurately the required airgap for multicolumn gravity based structures such as the Brent B platform,

there are two problems to tackle: (i) obtain a realistic model for large ocean waves and (ii) model how large ocean waves interact with a structure. Therefore this project considers both the generation of very large amplitude waves in the absence of the structure (so called freak or rogue waves) and the free surface magnification effects resulting from the interaction of waves with the structure.

Figure 1.1: Shell's Brent B platform in the North Sea in storm conditions.

A study into the physics and statistics of freak waves has been undertaken in which a design wave is examined. This design wave, which accurately models the irregular shape and random background of large ocean waves, is used to successfully capture the spatial characteristics of a measured freak wave and is validated further using storm data from the North Sea and experimental data. This project uses the extreme design wave as the incident wave field in the wave-structure diffraction analysis, unlike most previous research which considers only monochromatic wave fields.

The wave-structure interaction is modelled using linear and second order diffraction solutions. The important features of a nonlinear diffraction solution can be investigated by extending linear diffraction theory to a second order approximation using a Stokes expansion procedure. A quadratic boundary element method is used in this study to solve the three-dimensional water wave diffraction problem. The majority of previous work in this area has concentrated on the prediction of hydrodynamic forces on structures rather than water elevations, and so this work begins to address that imbalance.

The current use of linear diffraction theory to guide airgap design is commonly acknowledged to be inadequate although no detailed study has been carried out to comprehensively demonstrate this. Therefore, the comparative utility of linear and second order diffraction solutions at predicting green water (continuous water) levels needs to be addressed. In addition, studying second order diffraction theory enables nonlinear wave phenomena, such as second order near-trapping of waves between columns, to be examined. Near-trapped modes are quasi-resonant type responses which are excited at critical frequencies, and are discussed in detail in the literature review. Robust fully nonlinear codes are not currently available to perform the above-mentioned tasks.

In order to assess the validity of using diffraction solutions in the design of offshore structures comparisons are made with data from a programme of wave tank experiments, which were carried out by Shell at the Canadian Hydraulics Centre (Ottawa, Canada) for a specific four-column gravity based structure. The structure tested consists of a multilevel deck supported above the ocean surface by a concrete gravity substructure resting on the sea bed. The concrete substructure is composed of a caisson with four large diameter columns mounted on top. The principal objective of the tests was to determine the airgap required for the lower deck to avoid green-water impact under extreme storm conditions.

Comparisons are made between the measured surface magnifications in the vicinity of the model structure (provided by Shell) and those predicted here by linear and second order diffraction theories. Through comparing experimental data with diffraction solutions the ultimate aim is to address the following key question: if you do not carry out model tests, then can you rely upon linear and second order diffraction solutions to accurately guide airgap design? Progress towards a definitive answer to this question has been achieved.

The results from the diffraction analyses carried out in this study are incorporated into the surface response statistics (SRS) method of Tromans and Vanderschuren (1995). The SRS method is used to compute extreme surface elevation statistics around a four-column gravity based structure, and comparisons are made with measured wave data. Combining the use of diffraction theory with the SRS method could provide an invaluable tool for offshore structure design.

This project provides an improved understanding of extreme ocean waves and suggests improved design tools for modelling the effects of these waves on offshore structures. The conclusions drawn from this work and the research initiated from these conclusions will help the energy industry to develop offshore fields in hostile oceans more quickly and more safely.

With the emergence of offshore wind farms and wave power as viable renewable energy sources and a growing interest internationally in floating islands for use as airports and industrial plants, the findings of this project are of use beyond the oil and gas industry. Indeed, the design wave and diffraction solutions implemented in this study are also used to examine wave interaction effects with large arrays of columns, which could potentially be used for the supporting structure of a floating island.

This project has been undertaken with the support of technical staff from Shell Exploration and Production, Rijswijk, Netherlands, who have guided the choice of platform configuration of practical interest and supplied the experimental data.

1.2 Literature review

The aim of this section is to provide a critical review and analysis of the literature relevant to the problem outlined in Section 1.1. An evaluation of what has been achieved by previous researchers will place the current research into context. Extreme ocean waves, ocean wave modelling and water wave diffraction are discussed, introducing the theoretical framework and methodological focus of the work undertaken in this project.

1.2.1 Extreme ocean waves

As the world ponders the lessons from the Asian tsunami which occurred on December 26th 2004, the growing issue of freak waves is being heavily debated. Unlike tsunami, freak waves are not triggered by earthquakes or landslides and do not cause the same cataclysmic destruction. Freak waves pose a danger to ships and offshore structures that are unlucky enough to be in the path of a larger and steeper wave than they are engineered for.

Extreme ocean waves capable of sinking large ships are rare but recent studies have shown that they are much less rare than previously believed. Over the last two decades more than 200 super-carriers (cargo ships over 200m long) have been lost at sea (*Freak waves spotted from space*, BBC News Online, 22 July 2004); for further information on some of these incidents see, for example, Faulkner and Buckley (1997). Eyewitness reports suggest that many were sunk by high and violent walls of water that rise up suddenly, even in moderately calm waters. For many years tales of such waves were regarded as fantasy, but regular ship losses and damage to offshore structures provide mounting evidence that freak waves exist. Also, there are many examples of recorded waves that exceed the height and steepness predictions derived from existing models. Therefore an improved understanding of how, why and when these waves occur has become a research priority in recent years.

It is not adequately understood how freak waves are formed, although they are reported more frequently in certain regions, for instance in the Gulf Stream, the Nantucket Shoals and around Cape Horn. Refraction around shoals and islands, and interactions between waves, sea currents and the wind, possibly offer the best explanations. What is clear though is that conventional wave theory is insufficient to explain the regularity of these extreme wave events.

Following a number of incidents of wave induced damage on ships off the eastern South African coast during the nineteen-fifties, sixties and early seventies, the subject of freak waves began to attract attention; see for example Mallory (1975). At this time, the World Meteorological Organisation adopted the following definition of a freak wave: A freak wave is a wave of considerable height ahead of which there is a deep trough. A number of eye witness observations by experienced seamen support the occurrence of an accompanying deep trough.

As discussed by Kharif and Pelinovsky (2003), the term 'extreme wave' is usually associated with the tail of some statistical distribution of wave heights (e.g. the Rayleigh distribution) whereas the term 'freak wave' is used to describe large waves occurring more often than would be expected from the background probability distribution. That said, whether these waves should be called freak waves, rogue waves or extreme storm waves remains a subject of discussion between scientists in the field, who have different views on their generating mechanisms. The most widely accepted criterion for freak waves today is perhaps one which is based on wave height: a freak wave has a height of at least 2-2.2 times the significant wave height (Kharif and Pelinovsky 2003).

Kharif and Pelinovsky (2003) carried out a review of the possible physical mechanisms leading to the generation of freak waves. They considered a number of linear models, including: dispersion enhancement of transient wave groups; geometrical focusing in basins of variable depth; and wave-current interaction. The influence of nonlinear Benjamin-Feir instability on the generation of freak waves was also discussed. Kharif and Pelinovsky demonstrated that freak waves can occur in both deep and shallow waters.

Are freak waves extremely rare realisations of a typical, slightly non-Gaussian population or are they typical realisations of a strongly non-Gaussian population? This question was posed by Haver and Andersen (2000), who commented that if freak waves are found to be realisations of a very non-Gaussian surface process, then the emphasis of research in this area should be on the physical mechanisms governing these events. This will include a search for mechanisms which, over limited time and space, can transform a slightly non-Gaussian surface field into a very non-Gaussian field possibly incorporating extreme waves. However, at present the existence of a separate freak wave population is not proven. Indeed, Robin

and Olagnon (1991) carried out a thorough analysis of wave data from the Frigg field in the North Sea in which almost two million individual waves were analysed, and found that the observed extremes (wave heights and crest heights) were well within the heights expected.

In an effort to prove the phenomenon or lay the rumours to rest, a consortium of 11 organisations from six European Union countries founded the MaxWave project (European Commission project number EVK:3-2000-00544) in December 2000. As part of the project, the European Space Agency (ESA) tasked two of its Earth-scanning satellites to monitor the oceans with their radars. The radars sent back 'imagettes', which are pictures showing the shape of the sea surface in a rectangle measuring 10km by 5km. The imagettes were taken every 200km and 30,000 imagettes were produced by the two satellites during a three-week period in 2001.

The MaxWave project, lead by Wolfgang Rosenthal of the GKSS Research Centre in Geesthacht, Germany, represented the first concerted attempt to detect the occurrence of freak waves globally. Prompted by a report published on the MaxWave findings in 2004, Rosenthal told the British Broadcasting Corporation that, "Two large ships sink every week on average, but the cause is never studied to the same detail as an air crash. It simply gets put down to 'bad weather'."

It was reported in The Engineer (25 February - 10 March 2005) that a growing number of researchers and naval architects are beginning to claim that many of the ships lost to 'bad weather' have probably been hit by a single extreme wave. Some researchers claim that such a wave was to blame for the infamous sinking of the Derbyshire bulk carrier (see for example Faulkner and Buckley 1997), a new ship, off Japan's coast in 1980 with the loss of 44 lives. Despite such incidents, requests to engineer ships to withstand freak waves have gone unheard with the classification societies considering freak waves to be sufficiently rare so that ships do not need to be engineered to survive them. However, the MaxWave survey revealed 10 extreme waves during the surveyed period, all of which had heights in excess of 25m (The Engineer, 25 February - 10 March 2005), and since the satellites used by the MaxWave survey could only sample the ocean surface rather than continuously monitor it, the real number of extreme waves during the surveyed period is likely to be much higher.

In addition to MaxWave, the existence of freak waves is also strongly supported by numerous field measurements. Concentrating on the Danish sector of the North Sea, Sand et al. (1990) identified a number of large waves with heights approximately twice that of the significant wave height which, according to the criteria defined above, classifies them as freak waves. As noted by Sand et al., even if the largest of 2000-3000 waves are considered then these

realisations are still well outside what would be expected within a second order framework. These measurements were recorded in a water depth of 40m, and hence the wave profiles under extreme conditions are significantly affected by the sea bottom. Sand et al. also referred to large wave occurrences in deeper water, one of particular interest being a case from the Ekofisk field in the Norwegian sector of the North Sea, where local structural damage was reported at heights in excess of 20m above still water level. The significant wave height in the region at this time is not known although a value of 10-12m is probably reasonable, therefore suggesting a wave height of approximately twice the significant wave height.

Perhaps one of the most closely examined recorded freak waves is the New Year wave, which occurred at the Draupner platform in the Norwegian sector of the North Sea on 1st January 1995. The water depth in this region is approximately 70m. In a sea-state with a significant wave height of approximately 12m, this freak wave, which has a peak elevation of 18.5m (crest height) above still water level, was unambiguously recorded using a downward looking laser device. During severe winter storms in the North Sea wave crests of 6-7m are commonplace, and so the reliable measurement of an 18.5m crest (contributing to an overall wave height of 26m) seems particularly extreme relative to the background waves. Indeed, Hagen (2002) analysed the data recorded at Draupner and concluded that the event is a rare occurrence in a relatively common storm. Inspection of the surface elevation time history shows that the depth of the trough preceding the New Year wave was only 6.5m, and so there was no obvious indication of the approaching extreme wave. Haver and Andersen (2000) undertook a review of freak wave occurrences with reference to the New Year wave and reported that the wave caused minor damage to equipment on the deck. Possible factors leading to the generation of this wave could be: (1) energy focusing as the wave system is travelling in space (Stansberg 2000); or (2) surface disturbances causing third and fourth order correction processes to become very significant for a short time and over a limited spatial area. However, the underlying physics leading to the generation of such a wave is not yet resolved and so these are simply hypotheses.

As well as sinking ships, freak waves have been causing significant damage to offshore oil and gas production facilities for decades and the offshore industry, in contrast to the shipping industry, has responded by building stronger platforms in an effort to withstand abnormal conditions. One well publicised incident was the Ocean Ranger disaster in Newfoundland in 1982, where a freak wave is thought to have flooded and capsized the rig (Kjeldsen 1997), killing all 84 people on board. More recently, the past two years (2004 and 2005) have seen some of the most severe hurricanes on record, with extensive damage to offshore oil and

gas infrastructure in the Gulf of Mexico. Following Hurricane Ivan (a Category 5 storm) in September 2004, it emerged that the storm generated a wave with a height greater than 27m (recorded by sensors on the ocean floor), which is thought to be the tallest wave measured to date. Such a wave height indicates that the intensity of Ivan exceeds that of the 100-year return period storm upon which some design criteria are based. The majority of the damage to offshore infrastructure caused by this storm was due to waves inundating the deck structure (Offshore, February 2005). In one instance, wave inundation damage to a platform's deck at an elevation of approximately 20m above still sea level was observed. Water inundation of a deck dramatically increases the horizontal load and overturning moment on the structure, resulting in the potential failure of primary structural members and collapse. Therefore it seems likely that an inadequate deck height for this storm was the principal factor causing such extensive damage to a number of platforms, which is prompting a review of the current deck height design criteria.

1.2.2 NewWave theory

In regions such as the North Sea and the Gulf of Mexico, the design of offshore structures is principally concerned with the environmental loads and peak surface elevations generated by extreme storms. As noted by Tromans et al. (1991), for the design of offshore structures a random sea state is conventionally modelled using a deterministic, monochromatic, periodic wave theory. The wave height and period used by this theory are assumed to correspond to some extreme environmental condition; for example, the highest wave arising on average in a three hour interval in a sea state corresponding to the most extreme storm expected in a one hundred year interval. An alternative to this design approach involves determining the structural response within a given time interval via a computationally demanding time domain simulation (Tromans et al. 1991). Such a simulation would include the random, spectral and directional properties of the extreme storm. A number of accurate computational programs exist within industry for implementing such time domain simulations and the results produced by these programs are much improved from those generated using deterministic calculations, based on the monochromatic wave approach. The periodic wave used in deterministic calculations tends to overestimate wave kinematics and hence the fluid load (Tromans et al. 1991).

In an effort to avoid lengthy random time domain simulations while retaining the associated accuracy, a convenient 'design-wave' can be utilised. For a linear random model of the ocean surface, the average shape of a large crest in both time and space is found to be a scaled autocorrelation function, as is shown mathematically by Lindgren (1970) and Boccotti (1983).

This idea was transferred to offshore engineering practice by Tromans et al. (1991), where it is now known as NewWave.

NewWave models the irregular shape and random background of large ocean waves as a set of independent sinusoidal components of random amplitude. A linear NewWave involves the superposition of these components with an extreme crest being generated when many of the components composing the spectrum come into phase. Tromans et al. (1991) provided a full derivation of this theory and demonstrated its use in the prediction of extreme loads on single columns.

Jonathan and Taylor (1997) compared the predictions of the NewWave model with surface elevation measurements recorded offshore in the North Sea. Large nonlinear crests from these measured time series were linearised and compared against the NewWave profile. Excellent agreement was found and so it was concluded that NewWave is able to accurately reproduce offshore measurements of large crests.

1.2.3 Nonlinear water wave effects

Real waves in nature are nonlinear. Although most waves in a random sea are small and approximately obey a linear model, for airgap design one is concerned with the largest waves occurring in a random sea state, which are very high and steep, and hence a linear description of such waves is inadequate.

A more complete solution beyond linear theory can be reached through means of a perturbation procedure whereby successive approximations are developed. Such a methodology was adopted by Stokes (1847) and a more recent contribution to the description of Stokes waves is that of Fenton (1990), who presents Stokes' wave theory retaining all terms up to fifth order. Stokes' mathematical description of a water wave provides a convenient method for assessing nonlinear wave contributions. An alternative approach is to use full second order wave theory to study the second order contributions to a wave record in detail. A derivation of second order wave theory for finite water depth and directionally spread seas was undertaken by Dean and Sharma (1981) and more recently by Dalzell (1999). The basic approach to the problem was originally outlined by Longuet-Higgins (1962) for the deep water problem. The most significant difference between the work carried out by Dalzell and the earlier work of Dean and Sharma and Longuet-Higgins is Dalzell's use of symbolic computations to cope with the many hyperbolic functions that arise immediately in finite depth problems. The extension of an exact analytical approach beyond second order has proven to be problematical (Tromans and Taylor 1998).

As noted by Forristall (1999), one of the most obvious manifestations of nonlinearity in the ocean is the apparent asymmetry between crests and troughs; crests become taller and sharper whereas troughs become less deep and more rounded. In an effort to obtain a sufficiently accurate description of this crest sharpening for engineering design, Forristall (1999) carried out an analysis of wave crest distributions and found that much of the theoretical nonlinearity can be captured by second order calculations. Comparisons between second order simulations of wave crests and field measurements of high wave crests showed excellent agreement in both deep and shallow water. Forristall also reported that three dimensional simulations that account for directional spreading of waves produce crests that are approximately 2% lower than the two dimensional simulations in deep water. Shallow water causes the simulated waves to become more nonlinear and hence the crests are higher. Forristall was reluctant to draw any definite conclusions from the analysis undertaken as the accuracy of the measured data used was not certain.

The measured height of wave crests is influenced by both the type of sensor used and the location of the sensor on a platform (Forristall 1999). In an effort to investigate these two factors, the Wave Crest Sensor Intercomparison Study (WACSIS) was conducted at the Meet-post Noordwijk measurement platform in the North Sea during the winter of 1997/98 (van Unen et al. 1998). In this study, waves were continuously recorded using a number of wave measurement devices and video recordings of the waves were made during daylight hours. The measurements recorded in this study provide a useful source of reliable data for testing water wave theories.

Using wave elevation data from the WACSIS measurement programme, Taylor and Williams (2004) implemented a data-driven analysis technique to assess whether second order wave theory can reproduce important nonlinear features in field data. Assuming that the dominant nonlinear correction is second order, Taylor and Williams showed that the average shapes of maxima in the underlying linear wave components matched the NewWave profile. On the basis that NewWave is a good model for the linear contribution to large crests and troughs, the magnitude of the second order contribution required to estimate crest elevation statistics was derived from the WACSIS data for several storms. The results computed were in good agreement with the second order random wave simulations of Prevosto and Forristall (2002).

1.2.4 Linear water wave diffraction

The analysis of wave-body interaction is a three-dimensional, fully nonlinear problem, which has not been exactly solved, even for regular waves. However, if certain assumptions and simplifications are accepted, low order analytical models can be developed. If the typical

dimension associated with a body (e.g. column diameter) is sufficiently large compared with the wavelength and surface wave amplitude, then separation effects due to viscosity can be neglected and diffraction effects dominate. In any case, the effects of viscosity are expected to have much less influence on surface elevations than on wave forces. In addition, diffraction theory assumes that the flow is incompressible and irrotational, and that surface tension effects can be neglected. Together, these assumptions imply that a scalar velocity potential can describe the flow, satisfying Laplace's equation within the fluid domain.

Through a perturbation expansion, this potential can be expressed as a sum of linear and nonlinear components using a perturbation parameter, which is small. As in Stokes theory for waves alone, the potential can then be solved at each order successively using the lower order solutions to generate the boundary conditions necessary to solve for the higher order components.

Solutions to the linear diffraction problem have been successfully implemented and are generally accepted in the offshore industry. Havelock (1940) began work in this area by developing an analytical solution for the diffraction of incident regular waves from a single cylinder in water of infinite depth. McCamy and Fuchs (1954) extended this result to finite water depth. An overview of this early work is given by Mei (1989).

1.2.5 Nonlinear water wave diffraction

The limitation of linear diffraction theory is that it is based on small amplitude wave theory and the associated assumption of linearity. The important features of a nonlinear diffraction solution can be investigated by extending linear diffraction theory to a second order approximation using a perturbation expansion procedure. Second order diffraction theory is complicated by the inhomogeneous free surface boundary condition that must be addressed at second order. A solution is sought through an integration of quadratic products of the first order velocity potential and its derivatives over the entire free surface. A number of numerical techniques have been proposed to solve the second order diffraction problem, one of which is a quadratic boundary element method (Eatock Taylor and Chau 1992). A quadratic boundary element method uses quadratic panels to discretise the body surface and free surface, which achieves a high degree of accuracy (e.g. well converged results) using fewer elements than a linear panel method.

Through a consideration of forces only, Lighthill (1979) first noted that in regular waves the second order problem can be treated in the same way as the first order problem but with the addition of an apparent fluctuating pressure distribution on the free surface at a frequency

double that of the first order wave. Lighthill used this double frequency pressure distribution, which is derived from the first order solution, to obtain a solution for the second order force on a body.

Molin (1979) considered the explicit evaluation of the second order velocity potential by drawing an analogy with forced mechanical oscillation. Molin separated the velocity potential into two components: (1) a forced 'locked wave' component which satisfies the inhomogeneous free surface condition; and (2) a 'free wave' component which satisfies the homogeneous free surface condition. Based upon this decomposition, Kriebel (1990) developed a second order solution for the diffraction of a monochromatic wave by a bottom-mounted circular cylinder. Kriebel used this solution to compute the free surface elevation around a single cylinder to second order and found that the maximum second order run-up on the cylinder in cases of steep waves ($\kappa A \geq 0.25$, where κ and A are the wavenumber and wave amplitude respectively), exceeded that predicted by linear diffraction theory by more than 50%. Subsequently, Kriebel (1992) conducted a series of laboratory experiments measuring the runup around a vertical bottom-mounted circular cylinder subject to monochromatic nonlinear waves. These experiments confirmed that the second order component of free surface elevation contributes a significant proportion of the total runup. For very steep waves in deep water ($\kappa A \geq 0.25$ and $\kappa h \geq 1.5$, where h is the water depth) the maximum runup measured was found to exceed the linear theory prediction by 60 to 80%, where for the same test cases, the second order theory prediction was exceeded by only 20 to 40%. Using the same locked- and free-wave decomposition, Eatock Taylor and Huang (1997) presented a solution for the second order velocity potential, generalised for an axi-symmetric body in monochromatic waves. Eatock Taylor and Huang also found that the maximum free surface elevation predicted by second order theory greatly exceeded that given by linear theory.

Kim and Yue (1989) studied the diffraction of regular waves by a vertical axisymmetric body and obtained the double frequency diffraction potential. Kim and Yue validated their method by extensive convergence testing and comparisons with semi-analytic results for the second order forces and moments on a uniform vertical circular cylinder. Complete second order forces, moments, surface pressures and runup on a vertical cylinder are presented by Kim and Yue. To generalise the second order theory to irregular waves described by a continuous spectrum, Kim and Yue (1990) went on to consider the general second order wave-body interactions caused by bichromatic incident waves and solved the resulting sum and difference frequency problems. The quadratic transfer functions for the sum and difference frequency wave excitation and body response were compared with those computed using

existing approximation methods for a number of simple geometries. Kim and Yue noted that the contributions from the second order potential, which are typically neglected in design, can dominate the total load in many cases.

Eatock Taylor and Fonquernie (2001) applied second order diffraction analysis to the case where the incident waves form a focused wave group (known in the offshore industry as NewWave). Eatock Taylor and Fonquernie first analysed unidirectional focused waves at second order in the absence of a diffracting body, and then combined this theory with a semi-analytical solution for second order diffraction by a vertical circular cylinder. Results were obtained for the resulting scattered wave field and the horizontal force on the cylinder. For the cases examined, which were effectively in deep water waves, it was found that the second order effects in a focused wave have a much more significant influence on the local scattered wave elevation than on the force.

The second order diffraction of a directionally spread focused wave group by a bottom-mounted circular cylinder was studied by Buldakov et al. (2004). Buldakov et al. obtained numerical solutions for JONSWAP amplitude spectra for an incoming wave group with different types of directional spreading. The results were compared with corresponding results for a unidirectional wave group of the same amplitude spectrum. It was concluded that the directionally spread case was qualitatively similar to that of the unidirectional case with slightly smaller surface elevation and force amplitudes. The amplitude reduction becomes larger for larger spreading angles.

Malenica and Molin (1995) used eigen-function expansions and an integral equation technique to develop expressions for the third order velocity potential for the specific case of regular waves incident upon a vertical bottom-mounted circular cylinder. Malenica and Molin only considered the velocity potential components relevant to the calculation of third order forces and did not develop any expressions for the third order diffracted free surface elevation. The third order results generated by Malenica and Molin were compared with experimental data (Moe 1993). The third order force measurements showed significant scatter, causing comparison with the theoretical values to be inconclusive. With regard to the validation of their theory, Malenica and Molin expressed regret over the lack of reliable experimental data and the possibility that physical experiments were insufficiently reliable for the measurement of third order forces. Since then, however, considerable progress in this area has been made. Most notably, Huseby and Grue (2000) investigated the first seven harmonic components of the horizontal force on a vertical cylinder experimentally. Huseby and Grue compared their measurements with perturbation and fully nonlinear wave models and found excellent

agreement for small and moderate wave amplitudes.

The development of fully nonlinear diffraction codes is currently being pursued by a number of individuals but, to the author's knowledge, a validated code for an arbitrary 3D body is not yet available. Both finite element (FE) and boundary element (BE) methods have been developed to solve the fully nonlinear wave-body interaction problem. In a study comparing the FE and BE approaches, Wu and Eatock Taylor (1995) showed that the FE approach had significant advantages: although the FE method requires the whole flow domain to be decretised and the BE method requires only the boundary, the computational resources required to handle the fully populated BE matrices are found to be substantially larger. This observation initiated a series of investigations based on FE models (see for example Greaves et al. (1997) and Wu et al. (1998)). During the course of this work, a feasibility study of a coupled FE-BE approach was also conducted by Wu and Eatock Taylor (2003) in 2D. Eatock Taylor et al. (2005) extended this coupled approach to 3D and investigated the nonlinear interaction of steep transient waves with flared structures. Eatock Taylor et al. argued that the motivation for a coupled approach was based on a consideration of the relative strengths and weaknesses of the FE and BE methods when implemented separately; a FE model is suitable away from a body, where the domain is regular, and a BE discretisation is suitable near a body, where the moving mesh is complex. Eatock Taylor et al. describe the FE and BE models that have been developed for the coupled analysis; the two approaches were developed and verified independently, prior to incorporation in the coupling algorithms. Eatock Taylor et al. presented results for a number of test cases, including nonlinear wave diffraction by a fixed vertical circular cylinder in a long rectangular wave tank. Despite the successes of the work discussed here, the application of robust fully nonlinear codes to assist in the design of offshore structures seems likely to be some time away.

The state of the art in wave diffraction analysis for offshore engineering applications is the computer program WAMIT, which uses the panel method for analysing hydrodynamic wave-body interactions to second order. Today WAMIT has the capability of complete second order analysis (including sum and difference frequency components) in monochromatic, bichromatic and bidirectional waves. Since the first release of the linear program in 1987 at the Massachusetts Institute of Technology, it has gained widespread recognition in the offshore field for its ability to analyse complex structures with a high degree of accuracy and efficiency. Today WAMIT is managed by WAMIT Inc, which was founded by Prof. J. Nicholas Newman and Dr. Chang-Ho Lee in 1999, and is licensed to more than 80 industrial and research organisations worldwide. The theoretical basis for WAMIT is described in detail

by Lee and Newman (2004) and in many other publications cited on the WAMIT Inc website (www.wamit.com).

1.2.6 Water wave diffraction from arrays of bodies

For the case of waves incident upon an array of bodies, the effect of a given body on the incident wave is to produce a scattered wave which will, in turn, be scattered by all adjacent bodies. Hence the computation of the velocity potential must account for the diffraction of the incident wave field by each body and the multiple scattering from all other bodies. A description of all the possible interactions that can take place is typically provided by associating with each body a general potential describing waves radiating away from that body. This potential, together with the incident potential, describes the total wave field. Early work on this type of problem was associated with studies of pile arrays and twin-hull vessels, and was usually limited to the evaluation of forces (see, for example, Kagemoto and Yue 1986).

One possible solution to this hydrodynamic interaction problem is via the calculation of diffraction by the entire array of bodies acting as a single unit. A number of numerical methods are available for this calculation and are discussed by Mei (1978). The drawback to this approach is that the computations become difficult to perform for large arrays of bodies.

Studying the two dimensional scattering of acoustic radiation by an array of circular cylinders, Twersky (1952) developed an iterative method which incorporated multiple reflections between the cylinders. Twersky's iterative method for multiple scattering used an addition theorem to express the waves around each cylinder in terms of the waves around all other cylinders. However, as the number of bodies in an array increases the number of interacting wave components grows rapidly and the calculation becomes unmanageable (Linton and Evans 1990b).

A third possible solution comes from a direct matrix method, and was originally proposed by Spring and Monkmeyer (1974). By approximating the scattered waves emanating from each body as a plane wave at the other bodies, Simon (1982) produced a direct matrix solution for a uniformly spaced linear array of axisymmetric bodies. This simplification is only valid for large spacing and is known as either the plane-wave or wide-spacing approximation. McIver and Evans (1984) extended this approach to study wave loading on arrays of fixed vertical circular cylinders. McIver and Evans included a correction term in this plane-wave approximation and obtained improved results over Simon at smaller cylinder separations (compared to wavelength).

Combining the multiple scattering technique and the direct matrix method discussed above, Kagemoto and Yue (1986) developed an exact algebraic method for calculating the wave hydrodynamics for an array of bodies. The wave field around each body was represented as a series of waves of undetermined amplitude. A transformation was then applied to express the influence of the wave system at one body in terms of the influence at the other bodies. The system was then solved simultaneously for the unknown amplitude coefficients. Comparing with results generated using a three-dimensional hybrid-element diffraction method, this approach was found to give reasonable agreement for several two and four cylinder arrays (truncated and bottom-mounted) for all first order quantities.

Eatock Taylor and Sincock (1989) applied a hybrid boundary element technique to provide a linear diffraction analysis for Tension Leg Platform (TLP) and semisubmersible structures in regular waves. This hybrid technique coupled a finite element discretisation of the inner flow field near the structure with either a boundary element or eigenseries representation of the outer far field behaviour. The velocity potential was then solved for the nodes of the inner finite element domain and along fictitious boundaries throughout the fluid. Based on the assumption of linearity, Eatock Taylor and Sincock found that the local wave heights can be increased by a factor of up to two as a result of hydrodynamic interactions between columns.

Considering arrays of vertical bottom mounted circular cylinders exclusively, the scattering of water waves by arrays cylinders was solved exactly by Linton and Evans (1990b). Linton and Evans significantly improved the direct matrix method proposed by Spring and Monkmeyer (1974) by developing a greatly simplified expression for the first order velocity potential in the local vicinity of a cylinder, which leads to comparatively simple formulae for force and free surface elevation. Linton and Evans presented force and free surface elevation data for regular waves incident upon a group of four cylinders situated at the vertices of a square. Comparisons were made with the approximate method of McIver and Evans (1984), and the result developed by Linton and Evans was found to be more efficient for large arrays of cylinders.

Maniar and Newman (1997) used Linton and Evans' (1990) method and a high-order three-dimensional spline-Galerkin panel method, described by Lee et al. (1996), to study the loads on linear arrays of bottom-mounted circular cylinders aligned along an axis. Maniar and Newman found that when the number of cylinders is large but finite, near-resonant modes occur between adjacent cylinders at critical wavenumbers and this results in unusually large loads on each cylinder in an array. These modes are associated with the existence of homogeneous solutions for the diffraction of waves by an infinite array of bodies, which

correspond to the occurrence of trapped waves in a channel. For an array which is large but finite, there are no homogeneous solutions although the responses in the vicinity of these wavenumbers are nearly resonant and are commonly referred to as near-trapping. The results presented by Maniar and Newman suggest that the peak load magnitude on each cylinder increases in proportion to the total number of cylinders in an array. For an array of 100 cylinders the maximum load which is experienced by any cylinder in the array is 35 times the load on a single isolated cylinder for the same incident wavenumber. Maniar and Newman commented that the occurrence of these high loads at critical wavenumbers could have serious practical consequences for very large periodic structures subject to wave loading.

Studying a submerged horizontal cylinder in an open channel, Ursell (1951) was the first to identify trapped modes in first order wave theory. For small cylinder radii and infinite depth, Ursell proved that although some energy generally radiates to infinity, energy at discrete frequencies below a certain cutoff was trapped near the cylinder and did not radiate.

Longuet-Higgins (1967) also worked on the phenomenon of trapping. Prompted by the observation of regular large amplitude oscillations in the vicinity of an island, Longuet-Higgins demonstrated the trapping of wave energy around islands. Using first order inviscid shallow water wave theory to study the flow around a submerged circular sill, Longuet-Higgins proved the existence of certain eigenfrequencies at which the rate of decay was extremely slow.

More recently, the existence of trapped waves has been established by Linton and Evans (1992), Evans et al. (1994), Evans and Porter (1998) and other references cited therein. Motivated by the work of Maniar and Newman (1997), Evans and Porter (1997) used the interaction theory of Linton and Evans (1990b) to show how large peaks in the forces on circular arrays of four, five and six cylinders develop as the gaps between the cylinders are reduced. The largest forces were found to arise when the near-trapped mode corresponds to a standing wave motion, in agreement with the largest forces in linear arrays. Kagemoto et al. (2002) experimentally analysed this trapped mode phenomena for linear arrays of cylinders. For incident regular waves at the predicted near-trapped mode frequencies, the magnification effects observed were substantially lower than predicted by theory. Kagemoto et al. postulated that the observed discrepancy was likely to be due to dissipative effects taking place at the boundary layers around the cylinder walls.

As discussed by Walker and Eatock Taylor (2005), in addition to dissipation effects, two further departures from the ideal conditions discussed so far would be expected to mitigate the considerable magnification effects predicted for large arrays of cylinders. These are: (1) disorder in the array geometry (i.e. varying cylinder spacings and/or diameters), and

(2) departure from the assumption of monochromatic incident waves. The implications of disorder have been considered by Duclos and Clément (2004), who showed that a small level of disorder (less than 0.5% of the cylinder spacing for the array they considered) is sufficient to substantially reduce the large forces associated with near-trapped modes. The second mitigating effect, the fact that real ocean waves are not regular, was investigated by Walker and Eatock Taylor and some of the results from that study are presented in this thesis.

The second order water wave diffraction of an incident monochromatic wave field by an array of vertical bottom-mounted circular cylinders was solved using a semi-analytical approach by Malenica et al. (1999). This was a continuation of similar approaches that were initiated independently by Huang and Eatock Taylor (1996) and Malenica (1997). The method proposed obtains the second order potential by combining eigenfunction expansions with an integral representation. Unlike the indirect approach for second order forces (Lighthill 1979 and Molin 1979), this approach gives complete second order information about local flow characteristics (pressure, velocities, wave elevation etc.) and thus provides a basis for solving the third order problem. The influence of wave incidence, cylinder radius and cylinder configuration on the total diffracted wave field was examined. As in the first order case considered by Linton and Evans (1990b) and Maniar and Newman (1997), the importance of interaction effects when calculating the local and global quantities was again highlighted. The results presented by Malenica et al. suggest that the phenomenon of near-trapping in cylinder arrays also occurs at second order. In particular, near-trapping was found to occur when the double frequency associated with the second order wave coincides with the linear near-trapping frequency.

Ghalayini and Williams (1991) presented an exact second order solution for predicting second order (sum and difference frequency) hydrodynamic forces on an array of bottom mounted, surface piercing vertical cylinders of arbitrary cross section in water of arbitrary uniform depth in the presence of monochromatic waves. Ghalayini and Williams provided an efficient numerical technique to treat the free surface integral appearing in the second order force formulation. Moubayed and Williams (1995) extended the method of Ghalayini and Williams (1991) to compute the second order hydrodynamic forces due to the action of bichromatic waves. Moubayed and Williams generated results for an array of four cylinders, which illustrate the importance of interaction effects at both the sum and difference frequencies on the second order forces. For the sum frequency problem, the loading component due to the second order potential represents the dominant term at that order. For the difference frequency problem, however, the quadratic term (derived from the first order potential) and the second

order incident wave contributions were found to be dominant.

1.3 Project objectives

Based on the project background described in Section 1.1 and the current state of research outlined in the literature review in Section 1.2, the objectives of this DPhil project are to:

1. Study the physics and statistics of extreme wave occurrences on the open sea. Examine the harmonic structure of these waves and endeavour to identify features that distinguish a freak wave from a 'typical' large wave occurrence. Investigate the probability of occurrence of freak waves.

2. Implement the linear 'design wave' called NewWave and verify it against field data and experimental data. Attempt to capture the spatial characteristics of a freak wave occurrence by incorporating nonlinear corrections into the NewWave model.

3. Through consultation with Shell Exploration and Production, select an offshore structure configuration of practical interest (referred to as Structure A below) for which surface elevation model test data is available. Wave interaction with this structure is considered in this thesis.

4. Implement linear water wave diffraction theory to study the linear interaction of monochromatic waves and NewWaves with multi-column structures. Verify the results against published data.

5. Study the linear near-trapping of waves by linear arrays of cylinders and Structure A. Explore whether the large magnification effects associated with near-trapping exist for incident NewWaves.

6. Thoroughly investigate the linear interaction of waves with Structure A and identify the most extreme linear surface magnification effects in the vicinity of the structure. Examine the effect of a subsurface caisson on the linear diffracted wave field and the effect of directional spreading. Compare the diffraction predictions with experimental data and assess the validity of using a linear diffraction solution in the design of offshore structures. Establish how much of what is observed in reality can be captured by linear diffraction theory.

7. Implement second order water wave diffraction theory to study the second order interaction of monochromatic waves and NewWaves with multi-column structures. Verify the results against published data.

8. Investigate the existence of second order near-trapped modes for a general four-column array and for Structure A. Examine the surface response resulting from the second order diffraction of an incident NewWave by Structure A. The computational burden associated with the second order calculation will prevent larger cylinder arrays from being considered. Carry out extensive convergence testing to ensure that accurate results are obtained.

9. Thoroughly investigate the second order interaction of waves with Structure A and identify the most extreme second order surface magnification effects in the vicinity of the structure. Compare the magnitudes of the linear and second order contributions to the overall surface response and comment on the significance of the second order terms. Compare the effect of a subsurface caisson on the second order diffracted wave field with the effect on the linear field. Compare the diffraction predictions with experimental data and assess the validity of using a second order diffraction solution in the design of offshore structures - establish how much of what is observed in reality can be captured by second order diffraction theory.

10. Incorporate the results from the diffraction analyses for Structure A into the surface response statistics (SRS) method of Tromans and Vanderschuren (1995). Compute extreme surface elevation statistics around the structure.

11. Provide to Shell Exploration and Production extreme surface elevation predictions for Structure A.

12. Produce guidelines for the offshore industry describing the accuracy of linear and second order diffraction solutions at predicting extreme green water levels beneath multi-column structures.

13. Assess the feasibility of using diffraction solutions in the design of offshore structures. Identify further work needed to continue the development of diffraction solutions for use in airgap design.

1.4 Synopsis

Each of the project objectives, referred to below with the numbers given above, are addressed in the following chapters:

1. Exact second order wave theory for use in assessing the magnitude and character of the second order contributions to large waves is outlined in Chapter 2. In Chapter 5

the physics and statistics of one specific extreme wave for which field data is available, namely the Draupner New Year wave, is studied. Unique features of the Draupner New Year wave are identified, distinguishing it from a typical large wave, and an estimate of the probability of occurrence of the wave is given.

2. A mathematical description of the NewWave model in given Chapter 2 and comparisons are made with field data and experimental data in Chapters 5 and 8 respectively. Stokes fifth order wave theory is defined in Chapter 2 and is used in Chapters 5 and 8 to correct a linear NewWave profile to fifth order. Comparisons are made between fifth order NewWave profiles and measured large crests.

3. A description of the considered offshore structure is given in Chapter 4. A review of the model test facility, experimental procedure undertaken and the measured surface elevation data available are also included in Chapter 4.

4. The linear diffraction problem is defined in Chapter 2 and a linear analytical solution for the diffraction of plane progressive waves by an array of bottom-mounted circular cylinders is given in Chapter 3. All necessary formulae for the computation of first order force and free surface elevation are derived. Verification of the linear solution and extension of the solution to the diffraction of NewWaves are presented in Chapter 6.

5. The phenomenon of linear near-trapping is studied for both linear arrays of cylinders and Structure A in Chapter 6. The linear diffraction of incident NewWaves is also considered in Chapter 6, with a particular emphasis on force and free surface magnification effects.

6. The magnitudes and locations of the largest linear surface magnifications in the vicinity of Structure A are identified for regular waves incident at a number of angles in Chapter 6. The maximum possible free surface elevations resulting from the linear diffraction of a NewWave by Structure A are also presented in Chapter 6. The effect of caisson height on the linear free surface magnification in the vicinity of Structure A is studied in Chapter 6. The effect of a caisson on near-trapping is also examined. The effect of directional spreading on the linear diffracted wave field around Structure A is investigated for incident regular waves and NewWaves in Chapter 6. Comparisons between measured surface elevations in the vicinity of Structure A (from model tests) and linear diffraction results are made for incident regular waves in Chapter 8, and conclusions on the ability of linear diffraction theory to reproduce real wave measurements are discussed.

7. The second order diffraction problem is defined in Chapter 2, and the analytical formulation and numerical implementation of the problem are described in detail in Chapter 3. The second order diffraction code implemented in this study is also discussed in Chapter 3. A description of the meshing scheme used in the second order solution procedure is given in Chapter 7. Verification of the second order results for incident monochromatic and bichromatic waves, and a discussion on the second order diffraction of NewWaves are presented in Chapter 7.

8. The phenomenon of near-trapping at second order is investigated for Structure A and for an array of four cylinders arranged at the vertices of a square in Chapter 7. The second order diffraction of an incident NewWave by Structure A is also studied in Chapter 7. A discussion of the convergence testing carried out in achieving reliable second order results is given in Chapter 7.

9. The second order diffracted wave field around Structure A is examined for incident regular waves in Chapter 7. The surface response resulting from the second order diffraction of a NewWave by Structure A is also presented in Chapter 7. The relative significance of the linear and second order contributions is discussed. The effect of caisson height on the second order free surface in the vicinity of Structure A is studied in Chapter 7, and comparisons are made with corresponding linear results. Comparisons between measured surface elevations in the vicinity of Structure A (from model tests) and second order diffraction results are made for incident regular waves in Chapter 8, and conclusions on the ability of second order diffraction theory to reproduce real wave measurements are drawn.

10. Extreme surface elevation statistics around Structure A (computed using the SRS method) are given in Chapter 8, together with comparisons with measured wave data.

11. The diffraction results presented in Chapters 6 and 7 for Structure A, and the comparisons with measured wave data in Chapter 8, are provided to Shell Exploration and Production.

12. The ability of linear and second order diffraction solutions to predict extreme green water levels beneath multi-column structures is discussed in Chapter 8, alongside comparisons between the diffraction solutions and measured wave data. The key issues complicating the validation of diffraction based design tools for real structures are outlined. A review of the most significant conclusions from this project and the implications for the offshore industry is given in Chapter 9.

13. The feasibility of using diffraction solutions in the design of offshore structures is discussed in Chapter 9. The likelihood of diffraction solutions replacing model testing during preliminary design is commented on. Chapter 9 also outlines some suggested areas of future work.

Chapter 2

Water wave theories

2.1 Introduction

This chapter introduces some of the mathematical concepts used in Chapters 5 and 8 for the analysis of experimental and field wave data. Water wave diffraction theory is also outlined, which is proposed as a design tool for predicting green water levels around offshore structures.

As discussed in the background (Section 1.1) and literature review (Section 1.2), monochromatic waves cannot be used for the accurate simulation of extreme storm waves, so a more realistic representation of ocean waves is required. To this end a mathematical description of the design wave called NewWave is presented in this chapter.

For airgap design one must consider the largest waves occurring in a sea state and in order to model the true magnitude and character of these waves it is necessary to examine in detail the nonlinear contributions. Therefore an extension of linear wave theory to Stokes' (1847) second order wave theory is developed in this chapter, using a perturbation expansion procedure. The linear water wave diffraction problem is then defined and is extended to a second order approximation, again using a perturbation expansion procedure.

Based on the work of Fenton (1990), Stokes fifth-order wave theory is also defined and finally, exact second order wave theory is outlined using the results derived by Dalzell (1999).

2.2 NewWave theory

In the literature review a convenient design wave called NewWave was introduced. In this section a mathematical description of NewWave is given and later, in Chapters 5 and 8, it is demonstrated that a linear NewWave shows good agreement with the average linear profile of a large wave crest.

For a linear random model of the ocean surface, the average shape of a large crest in both time and space is found to be a scaled autocorrelation function (Lindgren 1970 and Boccotti 1983). A linear NewWave is a scaled autocorrelation function based on the underlying wave energy spectrum, which is given by:

$$\rho(\tau) = \frac{1}{\sigma^2} \int_0^\infty S(\omega) \cos(\omega\tau)\, \mathrm{d}\omega \tag{2.1}$$

where ω is the linear angular frequency, $S(\omega)$ is the wave spectrum and σ is the standard deviation of the wave record. The shape of NewWave, as described by Equation 2.1, can be discretised by a sum of a finite number (N) of sinusoidal wave components. For completeness, the definition is now extended to include spatial dependencies, but limiting this to unidirectional seas. The discretised NewWave can be written as:

$$\eta(X,\tau) = \frac{\alpha}{\sigma^2} \sum_{n=1}^{N} S(\omega_n)\Delta\omega \cos(\kappa_n X - \omega_n \tau) \tag{2.2}$$

where $X = x - x_0$, the distance relative to the point of occurrence of the large crest; $\tau = t - t_0$, the time relative to the time of occurrence of the large crest; α is the linear crest amplitude and κ_n is the wavenumber of the n^{th} wave component. The angular frequency and wavenumber components are related by the linear dispersion equation (e.g. $w_n^2 = \kappa_n g$ for deep water, where g is gravity). The wave spectra considered in this study are defined in the results chapters.

2.3 Stokes water wave theory

The mathematical derivation presented in this section is based on the procedure outlined by Dean and Dalrymple (1991).

For the purposes of this section a Cartesian coordinate system (x, y, z) is defined with x measured in the direction of wave propagation, z measured upwards from the still water level and y orthogonal to x and z. It is assumed that the waves are two dimensional in the $x - z$ plane, that they are progressive in the positive x direction and that they propagate over a smooth horizontal bed in water of constant undisturbed depth h. The waves have a wavelength λ and a wave period T. The perturbation approach is outlined in this section for periodic waves, although it should be noted that it also holds for non-periodic waves (e.g. NewWave).

The sign convention used in this chapter defines the velocity components u, v and w, in the positive x, y and z directions respectively, as:

$$u = \frac{\partial \phi}{\partial x};\ v = \frac{\partial \phi}{\partial y};\ w = \frac{\partial \phi}{\partial z} \tag{2.3}$$

where ϕ is a velocity potential. For the boundary value problem under consideration, both linear and nonlinear boundary conditions are applied to a linear governing differential equation. The linear governing equation and linear boundary conditions are:

- Governing differential equation

$$\nabla^2 \phi = \frac{\partial^2 \phi}{\partial x^2} + \frac{\partial^2 \phi}{\partial z^2} = 0. \tag{2.4}$$

- Bottom boundary condition

$$\frac{\partial \phi}{\partial z} = 0 \quad \text{on } z = -h. \tag{2.5}$$

- Lateral boundary condition

$$\phi(x, z, t) = \phi(x + \lambda, z, t). \tag{2.6}$$

- Periodicity boundary condition

$$\phi(x, z, t) = \phi(x, z, t + T). \tag{2.7}$$

The nonlinear boundary conditions are:

- Dynamic free surface boundary condition (DFSBC)

$$\frac{p}{\rho} + \frac{1}{2}\left[\left(\frac{\partial \phi}{\partial x}\right)^2 + \left(\frac{\partial \phi}{\partial z}\right)^2\right] + \frac{\partial \phi}{\partial t} + gz = C_B(t) \quad \text{on } z = \eta(x, t) \tag{2.8}$$

  where p is a constant (usually taken as gauge pressure), ρ is water density, g is gravity and C_B is the Bernoulli constant.

- Kinematic free surface boundary condition (KFSBC)

$$\frac{\partial \phi}{\partial z} = \frac{\partial \eta}{\partial t} + \frac{\partial \phi}{\partial x}\frac{\partial \eta}{\partial x} \quad \text{on } z = \eta(x, t). \tag{2.9}$$

It is convenient to express the governing equation and related boundary conditions in nondimensional form. This is achieved through the introduction of the following dimensionless variables:

$X = \kappa x$; $Z = \kappa z$; $\Pi = \frac{\eta}{A}$; $\Phi = \frac{\kappa\phi}{A\sqrt{g\kappa}}$; $T = t\sqrt{g\kappa}$; $Q = \frac{\kappa}{g}C_B(t)$; $\omega = \frac{s}{\sqrt{g\kappa}}$; $P = \frac{\kappa p}{\rho g}$.

Here A, s, and κ are wave amplitude, wave angular frequency and wavenumber respectively.

Therefore the governing Equation 2.4 becomes:

$$\frac{\partial^2\Phi}{\partial X^2} + \frac{\partial^2\Phi}{\partial Z^2} = 0. \tag{2.10}$$

The bottom, lateral and periodicity boundary conditions remain unchanged in nondimensional form (although the bottom condition is now of course applied at $Z = -\kappa h$). However, the free surface boundary conditions are modified; the DFSBC becomes:

$$P + \frac{(\kappa A)^2}{2}\left[\left(\frac{\partial\Phi}{\partial X}\right)^2 + \left(\frac{\partial\Phi}{\partial Z}\right)^2\right] + (\kappa A)\frac{\partial\Phi}{\partial T} + Z = Q(t) \quad \text{on } Z = \kappa A\Pi \tag{2.11}$$

where P is taken as zero on the free surface, and the KFSBC becomes:

$$\frac{\partial\Phi}{\partial Z} = \frac{\partial\Pi}{\partial T} + (\kappa A)\frac{\partial\Phi}{\partial X}\frac{\partial\Pi}{\partial X} \quad \text{on } Z = \kappa A\Pi. \tag{2.12}$$

For linear wave theory these surface boundary conditions are expanded about $Z = 0$, the still water level, and then products of small quantities, such as $(\partial\Phi/\partial X)^2$, are neglected.

For the present second order development, a perturbation assumption is introduced whereby the variables describing the flow will be incorporated into a power series in terms of a perturbation parameter, which is assumed to be small. The various series will converge as the number of terms considered increases. In point of fact, convergence towards a complete solution does not occur for very steep waves, unless a different perturbation parameter to that chosen by Stokes is used. The original expansion procedure, however, has many advantages when applied to moderate order approximations, and so is considered exclusively here.

In the perturbation approach of Stokes, the small (i.e. less than unity) perturbation parameter is taken to be κA, which will be defined here as ϵ. The linear solution will be independent of ϵ, the second order solution will depend on ϵ, the third order solution will depend on ϵ^2, and so on. All quantities are thus decomposed into power series in ϵ:

$$\Pi = \Pi_1 + \epsilon\Pi_2 + \epsilon^2\Pi_3 + \cdots \tag{2.13}$$

$$\Phi = \Phi_1 + \epsilon\Phi_2 + \epsilon^2\Phi_3 + \cdots \tag{2.14}$$

$$Q(T) = \epsilon Q_1(T) + \epsilon^2 Q_2(T) + \epsilon^3 Q_3(T) + \cdots \tag{2.15}$$

$$\omega = \omega_1 + \epsilon\omega_2 + \epsilon^2\omega_3 + \cdots \tag{2.16}$$

Each subscripted variable above is taken as having the same order of magnitude and hence each additional term in the series represents a quantity smaller than the preceding one by a factor of order ϵ. By substituting these series into the governing equations given earlier, it becomes possible to obtain progressively higher order solutions, each expressed in terms of preceding ones. This procedure is reasonably straightforward except for dealing with the free surface boundary conditions, which contain nonlinear terms and are applied at the unknown free surface $Z = \kappa A\Pi$ rather than $Z = 0$. This potential difficulty is dealt with by expanding the free surface boundary conditions about $Z = 0$ in terms of $\epsilon\Pi$, and retaining the higher order terms up to ϵ^3 (Equation 2.17) and ϵ^2 (Equation 2.18). Using the Taylor series, Equations 2.11 and 2.12 on $Z = 0$ become respectively:

$$\left\{\frac{1}{2}\epsilon^2\left[\left(\frac{\partial\Phi}{\partial X}\right)^2 + \left(\frac{\partial\Phi}{\partial Z}\right)^2\right] + \epsilon\frac{\partial\Phi}{\partial T} + Z\right\}$$
$$+ \epsilon\Pi\frac{\partial}{\partial Z}\left\{\frac{1}{2}\epsilon^2\left[\left(\frac{\partial\Phi}{\partial X}\right)^2 + \left(\frac{\partial\Phi}{\partial Z}\right)^2\right] + \epsilon\frac{\partial\Phi}{\partial T} + Z\right\} + \frac{\epsilon^3\Pi^2}{2}\frac{\partial^3\Phi}{\partial Z^2\partial T} = Q(T) \tag{2.17}$$

and

$$\left(\frac{\partial\Phi}{\partial Z} - \frac{\partial\Pi}{\partial T} - \epsilon\frac{\partial\Phi}{\partial X}\frac{\partial\Pi}{\partial X}\right) + \epsilon\Pi\frac{\partial}{\partial Z}\left(\frac{\partial\Phi}{\partial Z} - \epsilon\frac{\partial\Phi}{\partial X}\frac{\partial\Pi}{\partial X}\right) + \frac{\epsilon^2\Pi^2}{2}\frac{\partial^3\Phi}{\partial Z^3} = 0. \tag{2.18}$$

The fact that Π and $Q(T)$ are not functions of elevation has been accounted for in the above expressions.

Now, substituting the perturbation expansions (Equations 2.13 to 2.16) into the linear governing equation and linear boundary conditions (Equation 2.10 and Equations 2.5 to 2.7) and retaining only terms of the first order in ϵ (the others being much smaller) yields:

$$\nabla^2\Phi_1 + \epsilon\nabla^2\Phi_2 = 0. \tag{2.19}$$

$$\frac{\partial\Phi_1}{\partial Z} + \epsilon\frac{\partial\Phi_2}{\partial Z} = 0 \quad \text{on } Z = -\kappa h. \tag{2.20}$$

$$\Phi_1(X, Z, T) + \epsilon\Phi_2(X, Z, T) = \Phi_1(X + 2\pi, Z, T) + \epsilon\Phi_2(X + 2\pi, Z, T). \tag{2.21}$$

$$\Phi_1(X,Z,T) + \epsilon\Phi_2(X,Z,T) = \Phi_1(X,Z,T+T_p) + \epsilon\Phi_2(X,Z,T+T_p). \tag{2.22}$$

where T_p is the dimensionless wave period, $2\pi/\omega$. At the free surface, the DFSBC and KFSBC (both on $Z = 0$) are given respectively by:

$$\frac{\epsilon}{2}\left[\left(\frac{\partial\Phi_1}{\partial X}\right)^2 + \left(\frac{\partial\Phi_1}{\partial Z}\right)^2\right] + \frac{\partial\Phi_1}{\partial T} + \epsilon\frac{\partial\Phi_2}{\partial T} + \Pi_1 + \epsilon\Pi_2 + \epsilon\Pi_1\frac{\partial^2\Phi_1}{\partial Z\partial T} = Q_1(T) + \epsilon Q_2(T) \tag{2.23}$$

and

$$\frac{\partial\Phi_1}{\partial Z} + \epsilon\frac{\partial\Phi_2}{\partial Z} - \frac{\partial\Pi_1}{\partial T} - \epsilon\frac{\partial\Pi_2}{\partial T} - \epsilon\frac{\partial\Phi_1}{\partial X}\frac{\partial\Pi_1}{\partial X} + \epsilon\Pi_1\frac{\partial^2\Phi_1}{\partial Z^2} = 0. \tag{2.24}$$

The nonlinear boundary value problem outlined at the beginning of this section can now be reformulated into an infinite set of linear equations of ascending orders. These linear equations are obtained by equating the coefficients of like powers of ϵ; this procedure is now used to separate the equations by order.

2.3.1 First order perturbation equations

By gathering together all terms that do not depend on ϵ, the linear equations are obtained:

- From 2.19

$$\nabla^2\Phi_1 = 0. \tag{2.25}$$

- From 2.20

$$\frac{\partial\Phi_1}{\partial Z} = 0 \quad \text{on } Z = -\kappa h. \tag{2.26}$$

- From 2.17

$$\frac{\partial\Phi_1}{\partial T} = -\Pi_1 + Q_1(T) \quad \text{on } Z = 0. \tag{2.27}$$

- From 2.18

$$\frac{\partial\Pi_1}{\partial T} = \frac{\partial\Phi_1}{\partial Z} \quad \text{on } Z = 0. \tag{2.28}$$

- From 2.21

$$\Phi_1(X,Z,T) = \Phi_1(X+2\pi,Z,T). \tag{2.29}$$

- From 2.22

$$\Phi_1(X,Z,T) = \Phi_1(X,Z,T+T_p). \tag{2.30}$$

These equations agree with those easily derived using small amplitude wave theory. Solving these equations yields the following results (in nondimensional form):

$$\Phi_1 = \frac{\cosh(\kappa h + Z)}{\omega \cosh \kappa h} \sin(X - \omega T). \tag{2.31}$$

$$\Pi_1 = \cos(X - \omega T). \tag{2.32}$$

$$\omega_1^2 = \tanh \kappa h. \tag{2.33}$$

$$Q_1(T) = 0. \tag{2.34}$$

2.3.2 Second order perturbation equations

Similarly, gathering together all terms of order ϵ, the second order equations are obtained:

- From 2.19

$$\nabla^2 \Phi_2 = 0. \tag{2.35}$$

- From 2.20

$$\frac{\partial \Phi_2}{\partial Z} = 0 \quad \text{on } Z = -\kappa h. \tag{2.36}$$

- From 2.17

$$\Pi_2 + \frac{\partial \Phi_2}{\partial T} - Q_2(T) = -\frac{1}{2}\left[\left(\frac{\partial \Phi_1}{\partial X}\right)^2 + \left(\frac{\partial \Phi_1}{\partial Z}\right)^2\right] - \Pi_1 \frac{\partial^2 \Phi_1}{\partial Z \partial T}$$
$$= 0 \quad \text{on } Z = 0. \tag{2.37}$$

- From 2.18

$$\frac{\partial \Phi_2}{\partial Z} - \frac{\partial \Pi_2}{\partial T} = \frac{\partial \Phi_1}{\partial X}\frac{\partial \Pi_1}{\partial X} - \Pi_1 \frac{\partial^2 \Phi_1}{\partial Z^2} \quad \text{on } Z = 0. \tag{2.38}$$

- From 2.21

$$\Phi_2(X, Z, T) = \Phi_2(X + 2\pi, Z, T). \tag{2.39}$$

- From 2.22

$$\Phi_2(X, Z, T) = \Phi_2(X, Z, T + T_p). \tag{2.40}$$

Note that these equations are linear in the variables of interest, Φ_2 and Π_2. Note also that the free surface boundary conditions, Equations 2.37 and 2.38, have inhomogeneous terms that depend on the first order solution and since the first order solution is known, the terms on the right-hand side of Equations 2.37 and 2.38 are also known.

The second order solution is most conveniently sought using the combined free surface boundary condition, which is obtained by eliminating Π_2 between Equations 2.37 and 2.38:

$$-\frac{\partial^2\Phi_2}{\partial T^2}-\frac{\partial\Phi_2}{\partial Z}+\frac{\partial Q_2(T)}{\partial T}=-\frac{\partial\Phi_1}{\partial X}\frac{\partial\Pi_1}{\partial X}+\frac{\partial\Pi_1}{\partial T}\frac{\partial^2\Phi_1}{\partial Z\partial T}+\Pi_1\frac{\partial}{\partial Z}\left(\frac{\partial^2\Phi_1}{\partial T^2}+\frac{\partial\Phi_1}{\partial Z}\right)$$
$$+\frac{1}{2}\frac{\partial}{\partial T}\left[\left(\frac{\partial\Phi_1}{\partial X}\right)^2+\left(\frac{\partial\Phi_1}{\partial Z}\right)^2\right]\quad\text{on } Z=0. \tag{2.41}$$

Substituting Φ_1 and Π_1 from 2.31 and 2.32 and using trigonometric identities, the right-hand side of Equation 2.41, which for convenience is called D here, can be expressed simply as:

$$D=\frac{3\omega_1}{\sinh 2\kappa h}\sin 2(X-\omega T). \tag{2.42}$$

To proceed further a trial solution for $\Phi_2(X,Z,T)$ is needed. A suitable trial solution is:

$$\Phi_2(X,Z,T)=A_2\cosh 2(\kappa h+Z)\sin 2(X-\omega T) \tag{2.43}$$

which satisfies Laplace's equation and the bottom boundary condition.

It is clear from Equation 2.41 that $\partial Q_2(T)/\partial T = 0$, as this term does not depend on $\sin 2(X-\omega T)$ and all the other terms do. Therefore $Q_2(t)$ = constant, Q_2 say. Substituting Equation 2.43 into Equation 2.41 gives A_2 as:

$$A_2=\frac{3}{8}\frac{\omega}{\sinh^4\kappa h}, \tag{2.44}$$

and hence:

$$\Phi_2(X,Z,T)=\frac{3}{8}\frac{\omega\cosh 2(\kappa h+Z)}{\sinh^4\kappa h}\sin 2(X-\omega T) \tag{2.45}$$

To determine the corresponding free surface elevation, $\Pi_2(X,T)$, the second order DFSBC, Equation 2.37, is used. Subsituting for Φ_1, Π_1 and Φ_2 using Equations 2.31, 2.32 and 2.45 yields the following result (in dimensional form):

$$\eta_2(x,t)=\frac{3H_1^2s^2\cosh 2\kappa h}{16g\sinh^4\kappa h}\cos 2(\kappa x-st)+Q_2+\frac{H_1^2s^2}{8g}\left[1+\cos 2(\kappa x-st)\right]$$
$$-\frac{H_1^2s^2}{16g\sinh^2\kappa h}\left[\cosh 2\kappa h+\cos 2(\kappa x-st)\right] \tag{2.46}$$

where H_1 is the first order wave height ($H_1 = 2A$). There are two options available to establish where the $z = 0$ datum should be chosen:

1. Specify the Bernoulli constant to be zero and separate η into mean (η_m) and fluctuating (η_f) terms:

$$\eta_2 = \eta_m + \eta_f. \tag{2.47}$$

Then from Equation 2.46 these two components are found to be given by:

$$\eta_m = -\frac{H_1^2 s^2}{16g\sinh^2\kappa h} = -\frac{H_1^2\kappa}{8\sinh 2\kappa h} \tag{2.48}$$

and

$$\eta_f = \frac{\kappa H_1^2}{16}\frac{\cosh\kappa h}{\sinh^3\kappa h}(2+\cosh 2\kappa h)\cos 2(\kappa x - st). \tag{2.49}$$

2. Specify h as the mean water level depth - i.e. η has a zero mean ($\eta_m = 0$). The Bernoulli constant is then:

$$Q = \frac{H_1^2 s^2}{16\sinh^2\kappa h} \tag{2.50}$$

and the fluctuating part of η_2 is again given by Equation 2.49.

The velocity potential and water surface displacement, to second order and in dimensional form, are thus:

$$\begin{aligned}\phi &= \epsilon\phi_1 + \epsilon^2\phi_2 \\ &= \frac{H_1 g}{2s}\frac{\cosh\kappa(h+z)}{\cosh\kappa h}\sin(\kappa x - st) + \frac{3}{32}H_1^2 s\frac{\cosh 2\kappa(h+z)}{\sinh^4\kappa h}\sin 2(\kappa x - st)\end{aligned} \tag{2.51}$$

and

$$\begin{aligned}\eta &= \epsilon\eta_1 + \epsilon^2\eta_2 \\ &= \frac{H_1}{2}\cos(\kappa x - st) + \frac{H_1^2\kappa}{16}\frac{\cosh\kappa h}{\sinh^3\kappa h}(2+\cosh 2\kappa h)\cos 2(\kappa x - st).\end{aligned} \tag{2.52}$$

The dispersion equation relating s to κ remains the same as that for linear theory:

$$s^2 = g\kappa\tanh\kappa h. \tag{2.53}$$

It is noted that there is a correction to the dispersion equation at third order.

2.3.3 Convergence

A measure of the validity of the Stokes expansion procedure is whether or not the series for ϕ converges. This can be checked for second order theory by verifying that the ratio of the second order amplitude to the first order amplitude (on $z = 0$) is less than unity:

$$R = \frac{\epsilon\phi_2}{\phi_1} = \frac{3}{8}\frac{\kappa A \cosh 2\kappa h}{\cosh\kappa h \sinh^3\kappa h} \ll 1. \tag{2.54}$$

In deep water, defined as $\kappa h > \pi$, the asymptotic forms of the hyperbolic functions can be substituted to reduce the ratio R to:

$$R = 3\, e^{-2\kappa h}\kappa A \ll 1. \tag{2.55}$$

Thus R is very small in deep water, particularly since κA has been assumed small previously. In shallow water, defined as $\kappa h < \pi/10$, the hyperbolic functions can again be replaced by the asymptotic values:

$$R = \frac{3}{8}\frac{\kappa A}{\kappa^3 h^3} = \frac{3}{64\pi^2}\left(\frac{\lambda^2 H_1}{h^3}\right) \ll 1. \tag{2.56}$$

The term in parentheses in Equation 2.56 is called the Ursell number, which, for second order Stokes theory to be valid, must have a magnitude obeying:

$$\frac{\lambda^2 H_1}{h^3} \ll \frac{64\pi^2}{3}. \tag{2.57}$$

The relative depth κh clearly becomes an important parameter in shallow water. Equation 2.56 can be written as $H_1/h \ll (16/3)(\kappa h)^2$, where κh is small, and hence places a severe restriction on wave height in shallow water.

It is noted that, for the deep water problem, it would perhaps be more appropriate to examine the ratio η_2/η_1, since it is known that $\phi_2 \to 0$ as $h \to \infty$.

2.4 Diffraction theory

This section introduces the theory of linear and second order water wave diffraction. A linear analytical diffraction solution and a numerical solution procedure for the linear and second order problems are described in Chapter 3.

The linear diffraction problem, which is based on small amplitude wave theory and the associated assumption of linearity, is first defined. The extension of linear diffraction theory to a second order approximation using a Stokes expansion procedure is then outlined, which will allow the important features of the nonlinear diffraction problem to be investigated in later chapters.

Together with the Sommerfeld radiation condition (discussed further below), the linear diffraction problem is defined by the following set of equations:

- Governing differential equation

$$\nabla^2\Phi = 0. \tag{2.58}$$

- Free surface boundary condition

$$\Pi = -\frac{\partial\Phi}{\partial T} \quad \text{on } Z = 0. \tag{2.59}$$

- Free surface boundary condition

$$\frac{\partial^2\Phi}{\partial T^2} + \frac{\partial\Phi}{\partial Z} = 0 \quad \text{on } Z = 0. \tag{2.60}$$

- Bottom boundary condition

$$\frac{\partial\Phi}{\partial Z} = 0 \quad \text{on } Z = -\kappa h. \tag{2.61}$$

- Body surface boundary condition

$$\frac{\partial\Phi}{\partial n} = 0 \quad \text{on the surface of the body.} \tag{2.62}$$

Here n denotes distance in a direction normal to the body surface and the nondimensional variables Φ, Π, T and Z are defined in Section 2.3. Equations 2.59 and 2.60 are derived from the linearised kinematic and dynamic free surface boundary conditions. Note that Equation 2.62 is true for a fixed body; if the body were moving then the right hand side would equal the component of velocity of the body resolved normal to the surface.

As for nonlinear wave theory described in Section 2.3, the nonlinearities of the diffraction problem again arise only in the two free surface boundary conditions. The nonlinear diffraction problem is thus defined in an analogous manner to the linear problem except that the complete nonlinear free surface boundary conditions now apply in place of Equations 2.59 and 2.60. Hence Φ_2 must satisfy Laplace's equation within the fluid domain and the boundary conditions defined by Equations 2.61 and 2.62, as well as the two free surface conditions, Equations 2.11 and 2.12, extended to three dimensions:

$$(\kappa A)\frac{\partial\Phi}{\partial T} + \frac{(\kappa A)^2}{2}\left[\left(\frac{\partial\Phi}{\partial X}\right)^2 + \left(\frac{\partial\Phi}{\partial Y}\right)^2 + \left(\frac{\partial\Phi}{\partial Z}\right)^2\right] + Z = Q(T) \quad \text{on } Z = \kappa A\Pi \tag{2.63}$$

and

$$\frac{\partial \Pi}{\partial T} + (\kappa A)\frac{\partial \Phi}{\partial X}\frac{\partial \Pi}{\partial X} + (\kappa A)\frac{\partial \Phi}{\partial Y}\frac{\partial \Pi}{\partial Y} - \frac{\partial \Phi}{\partial Z} = 0 \quad \text{on } Z = \kappa A \Pi \tag{2.64}$$

where P in the DFSBC is taken to be zero on the free surface and Y is a further dimensionless variable (in addition to those defined in Section 2.3) equal to κy. Finally a suitable radiation condition is needed. To introduce this condition the velocity potential must first be expressed as the sum of 'incident wave' and 'scattered wave' potentials, Φ_i and Φ_s respectively:

$$\Phi = \Phi_i + \Phi_s. \tag{2.65}$$

The radiation condition then requires that at large distances from the structure Φ_s corresponds to an outgoing wave. In dimensional form this condition can be formally written as:

$$\lim_{r \to \infty} \left[r^{1/2} \left(\frac{\partial \phi_s}{\partial r} - i\kappa \phi_s \right) \right] \tag{2.66}$$

where r is the radial ordinate.

As worked through earlier, the expansion method expresses Φ as a power series in the perturbation parameter ϵ (Equation 2.14). Following an analogous approach to before, Equation 2.14 is substituted into the governing equations, and a Taylor series expansion about $Z = 0$ is used to express the free surface conditions directly at $Z = 0$. Terms with like powers of ϵ are then gathered together to provide the governing equations for each successive approximation; terms of order ϵ define the second order problem expressing Φ_2 in terms of the first order quantities. The governing equations are:

- Governing differential equation

$$\nabla^2 \Phi = \frac{\partial^2 \Phi_2}{\partial X^2} + \frac{\partial^2 \Phi_2}{\partial Y^2} + \frac{\partial^2 \Phi_2}{\partial Z^2} = 0. \tag{2.67}$$

- Free surface boundary condition

$$\Pi_2 + \frac{\partial \Phi_2}{\partial T} = -(\kappa A) \left[\Pi_1 \frac{\partial^2 \Phi_1}{\partial Z \partial T} + \frac{1}{2} (\nabla \Phi_1)^2 \right] \quad \text{on } Z = 0. \tag{2.68}$$

- Free surface boundary condition

$$\frac{\partial^2 \Phi_2}{\partial T^2} + \frac{\partial \Phi_2}{\partial Z} = -(\kappa A)\Pi_1 \frac{\partial}{\partial Z} \left[\frac{\partial^2 \Phi_1}{\partial T^2} + \frac{\partial \Phi_1}{\partial Z} \right] - (\kappa A) \frac{\partial}{\partial T} (\nabla \Phi_1)^2 \quad \text{on } Z = 0. \tag{2.69}$$

- Bottom boundary condition

$$\frac{\partial \Phi_2}{\partial Z} = 0 \quad \text{on } Z = -\kappa h. \tag{2.70}$$

- Body surface boundary condition

$$\frac{\partial \Phi_2}{\partial n} = 0 \quad \text{on the surface of the body.} \tag{2.71}$$

The above equations for Φ_2 are identical to those defining the first order potential Φ_1, with the exception that Equations 2.68 and 2.69 have non-zero right hand sides.

Considering Φ_2 as the sum of 'incident wave' and 'scattered wave' potentials:

$$\Phi_2 = \Phi_2^{(i)} + \Phi_2^{(s)}, \tag{2.72}$$

$\Phi_2^{(i)}$ is known and is given by analytical expressions (Section 2.3) and so Equation 2.72 can be substituted into Equations 2.67 to 2.71 to define the problem in terms of $\Phi_2^{(s)}$.

In this section it has been shown that the second order diffraction problem can be readily formulated using a perturbation approach. For the present study, the second order diffraction problem is solved using the boundary element method, which is discussed in detail in Chapter 3.

2.4.1 Diffracted wave fields

To introduce the components of surface elevation discussed throughout this thesis, the linear and second order free surface elevations in the vicinity of a diffracting body for incident monochromatic waves are defined in this section using the results derived by Kim and Yue (1989). Similar results for incident bichromatic waves are given by Kim and Yue (1990).

The linear free surface elevation is given by:

$$\eta_1(t) = \Re\left[A\,\phi_1\,\mathrm{e}^{-i\omega t}\right] \tag{2.73}$$

where A is the linear wave amplitude, ϕ_1 is the first order potential and ω is the linear angular frequency. This expression is derived in Section 3.2 Chapter 3. The first order potential is composed of incident and scattered wave components, for which well-established numerical and analytical solutions are available; a linear analytical solution for wave diffraction by a fixed array of cylinders is given in Chapter 3.

When second order effects are included in the diffraction problem there are interactions at the sum and difference of the component frequencies of the incident waves. Therefore second order effects occur at frequencies away from that of the ambient wave energy.

For the diffraction of monochromatic incident waves the free surface elevation at second order can be expressed in the following form:

$$\eta_2(t) = \left[-\frac{1}{2g} (\nabla\phi_1)^2 + \frac{1}{g^2} \frac{\partial\phi_1}{\partial t} \frac{\partial^2\phi_1}{\partial t \partial z} - \frac{1}{g} \frac{\partial\phi_2}{\partial t} \right]_{z=0}. \tag{2.74}$$

The second order surface elevation defined by 2.74 can be decomposed into a time-independent (difference) term, $\eta_q^{(2-)}$, and a double-frequency (sum) term of amplitude $\eta^{(2+)}$, which in turn can be written as a sum of contributions from the first order ($\eta_q^{(2+)}$) and second order ($\eta_p^{(2+)}$) potentials:

$$\eta_2(t) = \Re\left[\left(\eta_q^{(2+)} + \eta_p^{(2+)} \right) \mathrm{e}^{-2i\omega t} \right] + \eta_q^{(2-)}. \tag{2.75}$$

$\eta_q^{(2-)}$, $\eta_q^{(2+)}$ and $\eta_p^{(2+)}$ are referred to as quadratic difference, quadratic sum and potential sum contributions respectively in this thesis. Note that for incident monochromatic waves the second order response does not incorporate a potential difference contribution, $\eta_p^{(2-)}$.

From Equation 2.74 and assuming Cartesian coordinates with the (x, y)-plane in the quiescent free surface and z positive upward, the double frequency and time-independent terms in Equation 2.75 can be expressed as:

$$\eta_q^{(2+)} = \left[-\frac{1}{4g} (\nabla\phi_1)^2 - \frac{\omega^2}{2g^2} \phi_1 \frac{\partial\phi_1}{\partial z} \right]_{z=0} \tag{2.76}$$

$$\eta_p^{(2+)} = \eta_2^{(i)} + \eta_2^{(s)} = \frac{2i\omega}{g} \left[\phi_2^{(i)} + \phi_2^{(s)} \right]_{z=0} \tag{2.77}$$

$$\eta_q^{(2-)} = \left[-\frac{1}{4g} |\nabla\phi_1|^2 + \frac{\omega^2}{2g^2} \phi_1 \frac{\partial\phi_1{}^*}{\partial z} \right]_{z=0} \tag{2.78}$$

where the superscripts 'i' and 's' denote incident and scattered potentials respectively and '*' denotes a complex conjugate. The second order potential, defined as the solution to an integral equation (see Chapter 3), is given in general form by Chau and Eatock Taylor (1992).

2.5 Fifth order water wave theory

Stokes wave theory is now presented to fifth order using the results derived by Fenton (1990). Fifth order wave theory is used in Chapters 5 and 8 to approximate the nonlinear contributions (up to fifth order) to a linear NewWave profile.

As outlined above, Stokes assumed that any variation can be represented by Fourier series and that the coefficients in these series can be written as perturbation expansions in terms of a parameter that increases with wave amplitude. Substitution of the perturbation expansions into the governing equations defining the water wave problem and manipulation of the series yields the solution.

The free surface elevation expanded to fifth order, $\eta^{(5)}(x,t)$, measured from the mean water level, is given by:

$$\kappa\eta^{(5)} = \sum_{n=1}^{5} \epsilon^n \sum_{m=1}^{n} B_{nm} \cos m\kappa(x - ct) + \cdots \tag{2.79}$$

where, as before, $\epsilon = \kappa A$. Note the different notation used here for surface elevation, with the superscript '(5)' indicating the sum of all orders up to five. The coefficients B_{nm} can be expressed in terms of hyperbolic functions of κh as:

$$B_{11} = 1 \tag{2.80}$$

$$B_{22} = \frac{\coth \kappa h\,(1 + 2C)}{2(1 - C)} \tag{2.81}$$

$$B_{31} = -\frac{3(1 + 3C + 3C^2 + 2C^3)}{8(1 - C)^3} \tag{2.82}$$

$$B_{33} = -B_{31} \tag{2.83}$$

$$B_{42} = \frac{\coth \kappa h\,(6 - 26C - 182C^2 - 204C^3 - 25C^4 + 26C^5)}{6(3 + 2C)(1 - C)^4} \tag{2.84}$$

$$B_{44} = \frac{\coth \kappa h\,(24 + 92C + 122C^2 + 66C^3 + 67C^4 + 34C^5)}{24(3 + 2C)(1 - C)^4} \tag{2.85}$$

$$B_{51} = -(B_{53} + B_{55}) \tag{2.86}$$

$$B_{53} = \frac{9(132 + 17C - 2216C^2 - 5897C^3 - 6292C^4 - 2687C^5 + 194C^6 + 467C^7 + 82C^8)}{128(3 + 2C)(4 + C)(1 - C)^6} \tag{2.87}$$

$$B_{55} = \frac{5(300 + 1579C + 3176C^2 + 2949C^3 + 1188C^4 + 675C^5 + 1326C^6 + 827C^7 + 130C^8)}{384(3 + 2C)(4 + C)(1 - C)^6} \tag{2.88}$$

where $C = \operatorname{sech} 2\kappa h$.

Now, dividing through by κ, Equation 2.79 can be expressed as:

$$\begin{aligned}\eta = {} & AB_{11}\cos\theta + \kappa A^2 B_{22}\cos 2\theta + \kappa^2 A^3 B_{31}\cos\theta + \kappa^2 A^3 B_{33}\cos 3\theta \\ & + \kappa^3 A^4 B_{42}\cos 2\theta + \kappa^3 A^4 B_{44}\cos 4\theta + \kappa^4 A^5 B_{51}\cos\theta \\ & + \kappa^4 A^5 B_{53}\cos 3\theta + \kappa^4 A^5 B_{55}\cos 5\theta\end{aligned} \tag{2.89}$$

where $\theta = \kappa(x - ct)$. As will become clear in Chapter 5, it is useful to reformulate Equation 2.89 into the following form (where each term has dimensions of length):

$$\begin{aligned}\eta = {} & (B_{11})D_{11} + (\kappa h B_{22})\frac{D_{22}}{h} + (\kappa^2 h^2 B_{31})\frac{D_{31}}{h^2} + (\kappa^2 h^2 B_{33})\frac{D_{33}}{h^2} \\ & + (\kappa^3 h^3 B_{42})\frac{D_{42}}{h^3} + (\kappa^3 h^3 B_{44})\frac{D_{44}}{h^3} + (\kappa^4 h^4 B_{51})\frac{D_{51}}{h^4} \\ & + (\kappa^4 h^4 B_{53})\frac{D_{53}}{h^4} + (\kappa^4 h^4 B_{55})\frac{D_{55}}{h^4}\end{aligned} \tag{2.90}$$

where the newly introduced D variables describe the temporal and spatial dependencies and are defined in terms of the linear wave record ($\eta_L = A\cos\theta$) and its Hilbert transform ($\eta_{LH} = A\sin\theta$), which introduces a ninety degrees phase shift into the record:

$$D_{11} = A\cos\theta = \eta_L \tag{2.91}$$

$$D_{22} = A^2\cos 2\theta = \eta_L^2 - \eta_{LH}^2 \tag{2.92}$$

$$D_{31} = A^3\cos\theta = (\eta_L^2 + \eta_{LH}^2)\eta_L \tag{2.93}$$

$$D_{33} = A^3\cos 3\theta = (\eta_L^2 - 3\eta_{LH}^2)\eta_L \tag{2.94}$$

$$D_{42} = A^4\cos 2\theta = (\eta_L^2 + \eta_{LH}^2)(\eta_L^2 - \eta_{LH}^2) \tag{2.95}$$

$$D_{44} = A^4 \cos 4\theta = (\eta_L^2 - \eta_{LH}^2)^2 - (2\eta_L \eta_{LH})^2 \tag{2.96}$$

$$D_{51} = A^5 \cos \theta = (\eta_L^2 + \eta_{LH}^2)^2 \eta_L \tag{2.97}$$

$$D_{53} = A^5 \cos 3\theta = (\eta_L^2 + \eta_{LH}^2)(\eta_L(\eta_L^2 - 3\eta_{LH}^2)) \tag{2.98}$$

$$D_{55} = A^5 \cos 5\theta = \left((\eta_L^2 - \eta_{LH}^2)^2 - (2\eta_L \eta_{LH})^2\right) \eta_L - 4\eta_{LH}^2 \eta_L (\eta_L^2 - \eta_{LH}^2) \tag{2.99}$$

Equation 2.90 can be simplified by replacing each bracketed term with a single coefficient, S_{nm}:

$$\begin{aligned} \eta =& S_{11} D_{11} + S_{22} \frac{D_{22}}{h} + S_{31} \frac{D_{31}}{h^2} + S_{33} \frac{D_{33}}{h^2} + S_{42} \frac{D_{42}}{h^3} \\ &+ S_{44} \frac{D_{44}}{h^3} + S_{51} \frac{D_{51}}{h^4} + S_{53} \frac{D_{53}}{h^4} + S_{55} \frac{D_{55}}{h^4}. \end{aligned} \tag{2.100}$$

The reformulated Stokes coefficients, S_{nm}, are plotted against κh in Figure 2.1. It is noted that the sum harmonic coefficients (S_{22}, S_{33}, S_{44} and S_{55}) all exhibit a plateau close to $\kappa h \sim 1.5$. This is a very convenient result and is referred to later in this thesis.

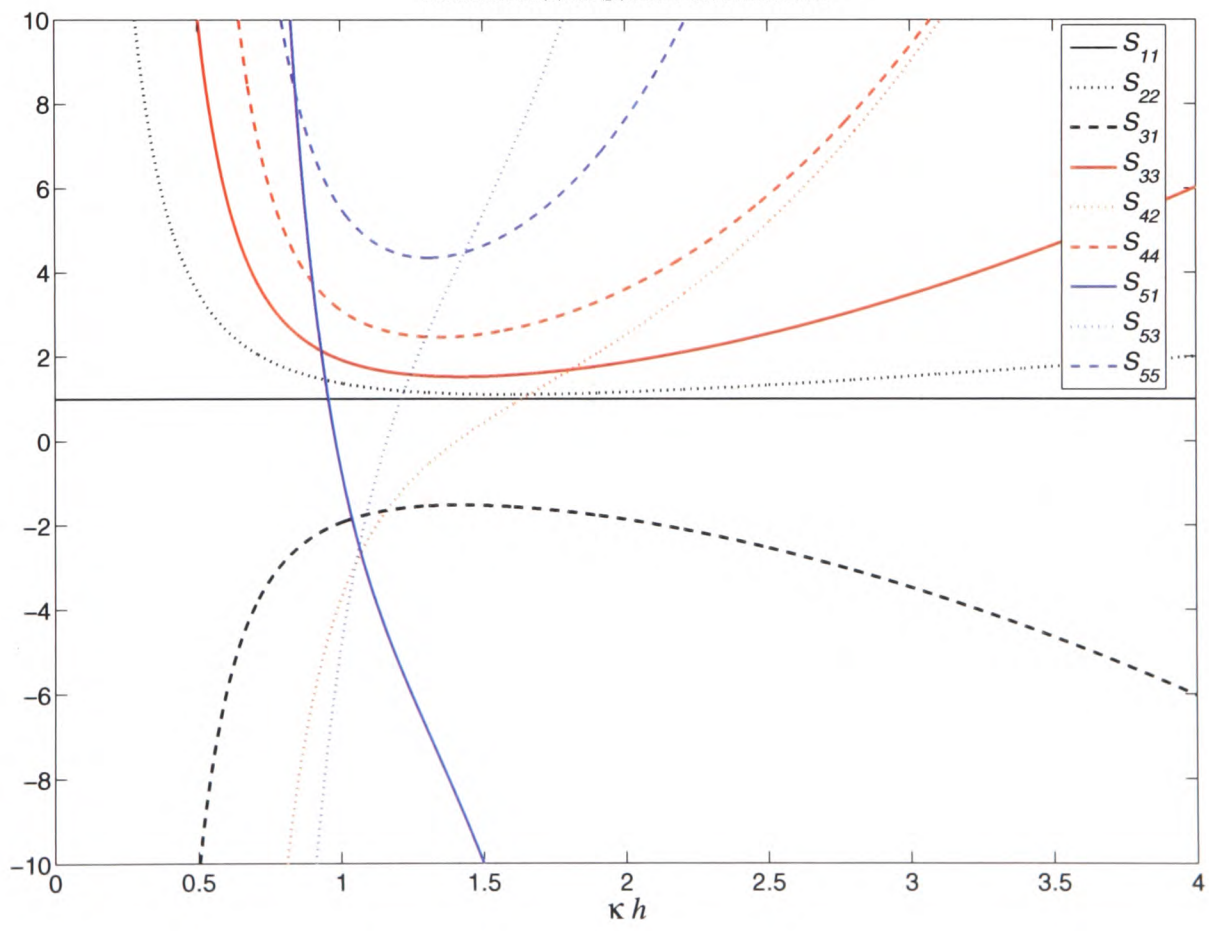

Figure 2.1: Reformulated Stokes coefficients, S_{nm}, plotted against κh.

2.6 EXACT SECOND ORDER WATER WAVE THEORY

Exact second order wave theory is now discussed for use in assessing the magnitude and character of the second order contributions to wave data. In this section the final results are quoted without any proof; a more detailed derivation is given by Dalzell (1999).

To obtain the second order wave-wave interaction coefficients, it suffices to consider the problem of two superimposed monochromatic wave trains. The two waves are assumed to be propagating in directions μ_j (for $j = 1, 2$), in a horizontal $x - y$ plane, where μ_j is measured positive in the counterclockwise direction looking down. The wavenumber components in the x and y directions in the horizontal plane are given by $|\kappa_j| \cos \mu_j$ and $|\kappa_j| \sin \mu_j$ respectively. It is convenient to define phase functions, ψ_j (for $j = 1, 2$), for the two waves where ψ_j is given by:

$$\psi_j = \kappa_j \vec{X} - \omega_j t + \zeta_j \tag{2.101}$$

where $\vec{X}$ is a position vector in the $x-y$ plane, t denotes time and ζ_j is an arbitrary constant phase. The angular frequency ω_j and wavenumber κ_j for each wave are related by the dispersion relation for finite depth:

$$\omega_j^2 = g|\kappa_j| \tanh(|\kappa_j|h). \tag{2.102}$$

The final expression for the second order wave elevation for the superposition of two waves is found to be:

$$\begin{aligned}
\eta = & \sum_{j=1}^{2} A_j \cos \psi_j \\
& + \sum_{j=1}^{2} \frac{A_j^2 |\kappa_j|}{4 \tanh(|\kappa_j|h)} \left[2 + \frac{3}{\sinh^2(|\kappa_j|h)} \right] \cos(2\psi_j) \\
& - \sum_{j=1}^{2} \frac{A_j^2 |\kappa_j|}{2 \sinh(2|\kappa_j|h)} + A_1 A_2 B_p(\kappa_1, \kappa_2) \cos(\psi_1 + \psi_2) \\
& + A_1 A_2 B_m(\kappa_1, \kappa_2) \cos(\psi_1 - \psi_2)
\end{aligned} \tag{2.103}$$

where A_j (for $j = 1, 2$) are the amplitudes of the two first order waves and the coefficients B_p and B_m are defined by:

$$B_p(\kappa_1,\kappa_2) = \frac{(\omega_1^2+\omega_2^2)}{2g} - \frac{\omega_1\omega_2}{2g}\left[1 - \frac{\cos(\mu_1-\mu_2)}{\tanh(|\kappa_1|h)\tanh(|\kappa_2|h)}\right] \times \left[\frac{(\omega_1+\omega_2)^2 + g|\kappa_1+\kappa_2|\tanh(|\kappa_1+\kappa_2|d)}{D_p(\kappa_1,\kappa_2)}\right] + \frac{(\omega_1+\omega_2)}{2gD_p(\kappa_1,\kappa_2)}\left[\frac{\omega_1^3}{\sinh^2(|\kappa_1|h)} + \frac{\omega_2^3}{\sinh^2(|\kappa_2|h)}\right] \tag{2.104}$$

and

$$B_m(\kappa_1,\kappa_2) = \frac{(\omega_1^2+\omega_2^2)}{2g} + \frac{\omega_1\omega_2}{2g}\left[1 + \frac{\cos(\mu_1-\mu_2)}{\tanh(|\kappa_1|h)\tanh(|\kappa_2|h)}\right] \times \left[\frac{(\omega_1-\omega_2)^2 + g|\kappa_1-\kappa_2|\tanh(|\kappa_1-\kappa_2|h)}{D_m(\kappa_1,\kappa_2)}\right] + \frac{(\omega_1-\omega_2)}{2gD_m(\kappa_1,\kappa_2)}\left[\frac{\omega_1^3}{\sinh^2(|\kappa_1|h)} - \frac{\omega_2^3}{\sinh^2(|\kappa_2|h)}\right] \tag{2.105}$$

where the functions D_p and D_m are given by:

$$D_p(\kappa_1,\kappa_2) = (\omega_1+\omega_2)^2 - g|\kappa_1+\kappa_2|\tanh(|\kappa_1+\kappa_2|h)) \tag{2.106}$$

and

$$D_m(\kappa_1,\kappa_2) = (\omega_1-\omega_2)^2 - g|\kappa_1-\kappa_2|\tanh(|\kappa_1-\kappa_2|h))\,. \tag{2.107}$$

The terms in Equation 2.103 can be numbered 1 to 5 consecutively and a description of each term is given below:

- Term 1: Linear wave contribution.
- Term 2: Wave self interaction component of the second order sum contribution.
- Term 3: Wave self interaction component of the second order difference contribution.
- Term 4: Wave-wave interaction component of the second order sum contribution.
- Term 5: Wave-wave interaction component of the second order difference contribution.

Chapter 3

Water wave diffraction solutions

3.1 Introduction

This chapter introduces an analytical solution to the linear water wave diffraction problem defined in Chapter 2. A numerical solution procedure for the linear and second order diffraction problems, based on the boundary element method, is also outlined. These diffraction solutions are used in Chapters 6 to 8 to investigate the interaction of water waves with fixed arrays of cylinders and a gravity based structure.

Firstly in this chapter, under the assumption of linear water wave theory, the diffraction of plane progressive waves incident upon an array of bottom mounted circular cylinders is solved using the method outlined by Linton and Evans (1990b). All necessary formulae for the computation of first order force and free surface elevation are presented. Because of the relative simplicity of this solution, it will be used in preference to a numerical solution to study the linear diffraction of waves by arrays of bottom mounted cylinders.

In order to study wave diffraction by a gravity based structure consisting of a subsurface caisson and four columns, a numerical diffraction solution will be used (at first and second order). A numerical solution procedure is described in this chapter, firstly for a general two-dimensional problem and then for the three-dimensional water wave diffraction problem. This solution will also be used to study the second order diffraction of waves by arrays of bottom mounted cylinders.

Finally, a numerical diffraction code called DIFFRACT, which uses the boundary element method to solve the linear and second order water-wave diffraction problems, is discussed.

3.2 Linear analytical diffraction solution

The analytical solution procedure proposed by Linton and Evans (1990b) for linear wave diffraction by an array of bottom mounted cylinders is presented in this section.

3.2.1 Formulation of the interaction analysis

Under the assumption of linear water wave theory there exists a velocity potential $\Phi(x, y, z, t)$, where x and y are coordinates lying on the mean free-surface, z is the vertical coordinate (positive upwards) and t is time. Here an array of N cylinders is considered and each cylinder extends vertically throughout the fluid domain between the free surface ($z = 0$) and the bottom ($z = -h$).

Assuming that all motion is time harmonic with angular frequency ω, the velocity potential can be written as:

$$\Phi(x, y, z, t) = \Re\left[\phi(x, y) f(z) e^{-i\omega t}\right] \tag{3.1}$$

where:

$$f(z) = -\frac{igA}{\omega}\frac{\cosh \kappa(z + h)}{\cosh \kappa h}, \tag{3.2}$$

A is the incident wave amplitude and g is gravitational acceleration. Note that the Φ defined here is different to the dimensionless Φ defined in Chapter 2. The frequency ω and wavenumber κ are related by the dispersion relation for finite water depth:

$$\kappa \tanh \kappa h = \frac{\omega^2}{g}. \tag{3.3}$$

The effect of a cylinder in the path of an incident wave is to produce a scattered wave that will in turn be scattered by adjacent cylinders. This repeated scattering continues throughout the array of cylinders and a suitable description of all the possible interactions can be provided by associating with each cylinder a general potential that describes waves radiating from that cylinder. The two dimensional function ϕ can thus be defined as the sum of an incident potential, ϕ_I, and a scattered potential, ϕ_S.

To simplify the notation used by Linton and Evans (1990), attention is restricted to an array of N identical cylinders, each of radius a. The parameters relating to the relative positions and sizes of the cylinders are shown in Figure 3.1.

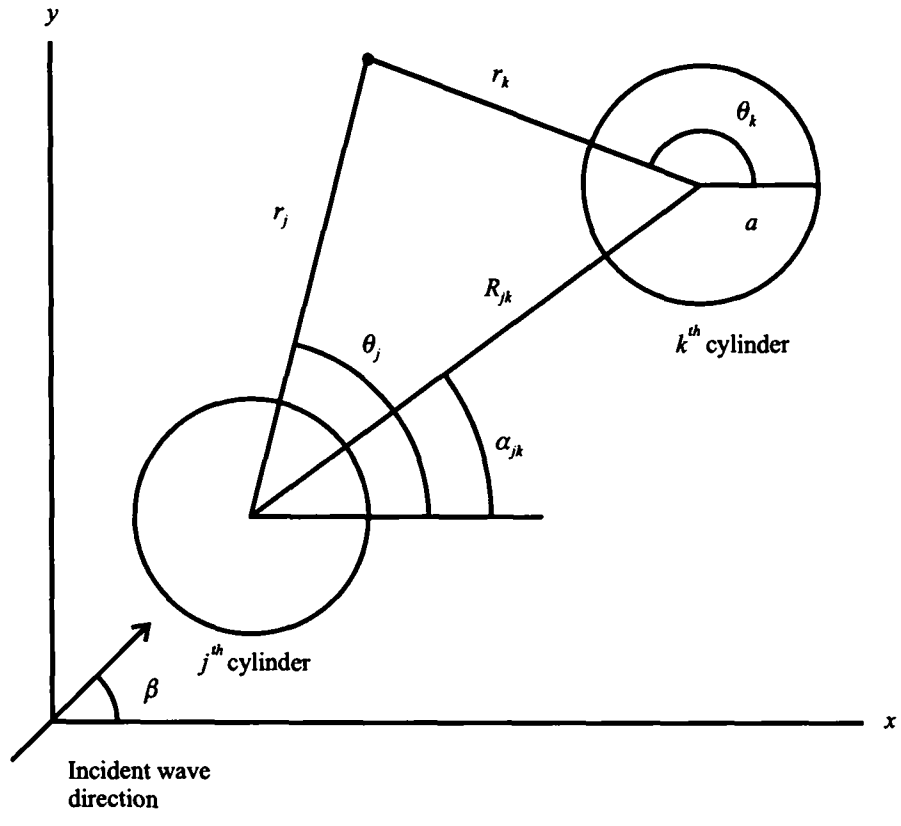

Figure 3.1: Plan view of two cylinders showing the parameters relating to the relative positions and sizes of the cylinders.

$N+1$ coordinate systems are used: one set of global polar coordinates (r, θ) centred at the origin, and N sets of local polar coordinates (r_j, θ_j) centred at (x_j, y_j) for $j = 1, 2, ..., N$. These coordinate systems are defined by:

$$x + iy = re^{i\theta} \tag{3.4}$$

and

$$(x - x_j) + i(y - y_j) = r_j\, e^{i\theta_j}. \tag{3.5}$$

The velocity potential of an incident plane wave propagating at an angle β to the x-axis can be expressed as:

$$\phi_I = e^{i\kappa(x\cos\beta + y\sin\beta)}. \tag{3.6}$$

By introducing a phase factor, I_j, associated with the j^{th} cylinder, 3.6 can be written in terms of the local coordinates associated with the j^{th} cylinder as:

$$\phi_I = I_j \, \mathrm{e}^{i\kappa r_j \cos(\theta_j - \beta)} \tag{3.7}$$

where

$$I_j = \mathrm{e}^{i\kappa(x_j \cos\beta + y_j \sin\beta)} \tag{3.8}$$

The incident velocity potential is now expressed as a sum of Bessel functions using the relation (Abramowitz and Stegun 1996):

$$\mathrm{e}^{i\kappa r\cos\theta} = \sum_{n=-\infty}^{\infty} (i)^n J_n(\kappa r)\, \mathrm{e}^{in\theta} = \sum_{n=-\infty}^{\infty} J_n(\kappa r)\, \mathrm{e}^{in(\theta+\pi/2)}, \tag{3.9}$$

which leads to:

$$\phi_I = I_j \sum_{n=-\infty}^{\infty} J_n(\kappa r_j)\, \mathrm{e}^{in(\theta_j - \beta + \pi/2)}. \tag{3.10}$$

The general form of the scattered potential associated with the j^{th} cylinder is expressed in the corresponding form:

$$\phi_S^j = \sum_{n=-\infty}^{\infty} A_n^j Z_n H_n(\kappa r_j)\, \mathrm{e}^{in\theta_j} \tag{3.11}$$

for a set of complex numbers, A_n^j (defined later). Here $H_n = J_n + iY_n$ denotes the Hankel function of the first kind, and the factor Z_n^j is given by:

$$Z_n \; (= Z_{-n}) = \frac{J_n'(\kappa a)}{H_n'(\kappa a)}\,. \tag{3.12}$$

Z_n is introduced here purely for convenience when satisfying the boundary condition of zero radial velocity on each cylinder later.

This expression for ϕ_S^j is justified by recalling that ϕ_S^j must satisfy Laplace's equation in the fluid domain and by asserting that the scattered wave system must consist of outgoing waves from the cylinder. Note also that each term in 3.11 is singular at the cylinder axis.

The total scattering potential of the array is simply the sum of 3.11 over all cylinders in the array and hence the total overall potential is given by:

$$\phi = \phi_I + \sum_{j=1}^{N} \phi_S^j$$
$$= I_j \sum_{n=-\infty}^{\infty} J_n(\kappa r_j)\, \mathrm{e}^{in(\theta_j - \beta + \pi/2)} + \sum_{j=1}^{N} \sum_{n=-\infty}^{\infty} A_n^j Z_n H_n(\kappa r_j)\, \mathrm{e}^{in\theta_j}. \qquad (3.13)$$

This expression can be written in terms of the local coordinates of the k^{th} cylinder (r_k, θ_k) using Graf's addition theorem for Bessel functions (Abramowitz and Stegun 1996). For our purposes here, this theorem can be written most usefully as:

$$H_n(\kappa r_j)\, \mathrm{e}^{in\theta_j} = \sum_{m=-\infty}^{\infty} J_m(\kappa r_k)\, H_{n+m}(\kappa R_{jk})\, \mathrm{e}^{im(\pi - \theta_k)} \mathrm{e}^{i(n+m)\alpha_{jk}} \qquad (3.14)$$

where $R_{jk} = \sqrt{(x_k - x_j)^2 + (y_k - y_j)^2}$ and α_{jk} is the angle defined positive anticlockwise from the positive x-axis to the line joining the centres of cylinders j and k (Figure 3.1).

Therefore:

$$\phi(r_k, \theta_k) = \sum_{n=-\infty}^{\infty} \left[I_k J_n(\kappa r_k)\, \mathrm{e}^{in(\theta_k - \beta + \pi/2)} + A_n^k Z_n H_n(\kappa r_k)\, \mathrm{e}^{in\theta_k} \right]$$
$$+ \sum_{j=1, \neq k}^{N} \sum_{n=-\infty}^{\infty} \sum_{m=-\infty}^{\infty} \left[A_n^j Z_n J_m(\kappa r_k) H_{n+m}(\kappa R_{jk})\, \mathrm{e}^{im(\pi - \theta_k)} \mathrm{e}^{i(n+m)\alpha_{jk}} \right]. \qquad (3.15)$$

The first term in this expression represents the velocity potential of the incident plane wave plus the scattered potential due to the k^{th} cylinder. The second term comes from Graf's addition theorem and represents the sum of the scattered potentials due to all cylinders other than the k^{th} cylinder, written in terms of the local polar coordinates centred at the axis of the k^{th} cylinder. As noted by Linton and Evans (1990b), by using the addition theorem in order to write functions of (r_j, θ_j) in terms of (r_k, θ_k), one must assume that $r_k < R_{jk}$. Therefore 3.15 is valid if $r_k < R_{jk}$ for all j, and so is an expansion valid close to cylinder k only.

In the derivation of Linton and Evans (1990b) the unknown coefficients A_n^j are determined by imposing the boundary condition of zero radial velocity on each cylinder; Linton and Evans differentiate 3.15 with respect to r_k and set the result equal to zero on $r_k = a$. To simplify the analysis an alternative approach suggested by Maniar and Newman (1997) is followed here. This approach (which ultimately leads to the same result as that produced using the

method of Linton and Evans) involves anticipating that the most general 'local' solution near the k^{th} cylinder can be expressed in the form:

$$\phi(r_k, \theta_k) = \sum_{n=-\infty}^{\infty} A_n^k \left[Z_n H_n(\kappa r_k) - J_n(\kappa r_k) \right] \mathrm{e}^{in\theta_k}. \tag{3.16}$$

This formula can be justified on the basis that:

1. $\frac{\partial \phi}{\partial r_k} = 0$ on $r_k = a$
2. The two terms are solutions to Laplace's equation
3. The Hankel function H_n specifies outgoing waves.

Equation 3.16 provides a simple formula for the velocity potential close to any cylinder ($r_k < R_{jk}$), hence simplifying the computation of force and free surface elevation.

Now, on each cylinder Equations 3.15 and 3.16 must be equal and so equating the Fourier coefficients with the same harmonic in θ_k provides the following linear system of equations:

$$A_m^k + \sum_{j=1, \neq k}^{N} \sum_{n=-\infty}^{\infty} A_n^j Z_n \, \mathrm{e}^{i(n-m)\alpha_{jk}} H_{n-m}(\kappa R_{jk}) = -I_k \, \mathrm{e}^{im(\pi/2-\beta)} \tag{3.17}$$

for $k = 1, \ldots, N$ and $m = -\infty, \ldots, \infty$.

Finally, in order to evaluate the constants A_n^j the infinite system 3.17 is truncated to an $N(2M+1)$ system of equations in $N(2M+1)$ unknowns:

$$A_m^k + \sum_{j=1, \neq k}^{N} \sum_{n=-M}^{M} A_n^j Z_n \, \mathrm{e}^{i(n-m)\alpha_{jk}} H_{n-m}(\kappa R_{jk}) = -I_k \, \mathrm{e}^{im(\pi/2-\beta)} \tag{3.18}$$

for $k = 1, \ldots, N$, $m = -M, \ldots, M$.

Increasing M will improve accuracy but at the expense of increasing computation time. It is suggested by Linton and Evans (1990b) that for all cases except where the cylinders are very close together, taking $M = 6$ produces results accurate to four significant figures. For all cases considered in this thesis $M = 6$ is used.

3.2.2 Wave elevation

An expression for wave elevation is now derived. By invoking the assumption of linearity in Bernoulli's equation and defining the time varying free surface as $z = \eta$, the dynamic

condition on linearised pressure gives:

$$\frac{\partial \Phi}{\partial t} + g\eta = 0 \tag{3.19}$$

on $z = 0$. Rearranging for η, substituting 3.1 and 3.2, and simplification leads to:

$$\eta = \Re\left[A\phi\, \mathrm{e}^{-i\omega t}\right], \tag{3.20}$$

which is also given in Equation 2.73 (see Section 2.4.1, Chapter 2).

For the evaluation of free surface amplitudes near to a particular cylinder (i.e. $r_k < R_{jk}$), ϕ can be given by Equation 3.16. For $r_k > 2d$ Equation 3.13 must be used, although it is worth noting that when using 3.13 far from the reference origin, ϕ_I should not be expressed as a sum of Bessel functions as many terms would be required in the resulting sum and hence increase the computation time.

3.2.3 Force

An expression for the force on the j^{th} cylinder is obtained by integrating the pressure, p, over the surface of the cylinder. The horizontal force in the x-direction is:

$$F_x = -\int_{-h}^{0}\int_{0}^{2\pi} p\, \cos\theta\, a \mathrm{d}\theta \mathrm{d}z. \tag{3.21}$$

By linearising Bernoulli's equation the following expression for pressure is obtained:

$$p = -\rho\left(\frac{\partial \Phi}{\partial t} + gz\right), \tag{3.22}$$

where ρ is the fluid density. This leads to:

$$F_x = \rho\int_{-h}^{0}\int_{0}^{2\pi} \frac{\partial \Phi}{\partial t}\, \cos\theta\, a \mathrm{d}\theta \mathrm{d}z. \tag{3.23}$$

Substituting 3.1 and 3.2 into 3.23 gives:

$$F_x = \Re\left[-i\omega\rho\int_{-h}^{0}\int_{0}^{2\pi} \phi\left(-i\frac{Ag}{\omega}\frac{\cosh\kappa(z+h)}{\cosh\kappa h}\right)\cos\theta\, a \mathrm{d}\theta \mathrm{d}z\, \mathrm{e}^{-i\omega t}\right]. \tag{3.24}$$

A similar expression for the force in the y-direction can be derived. The x and y linear forces can be expressed as $\Re[X^j e^{-i\omega t}]$, where X^j is a time independent factor given by:

$$X^j = -\frac{\rho g A a}{\kappa} \tanh \kappa h \int_0^{2\pi} \phi \left\{ \begin{array}{c} \cos\theta_j \\ \sin\theta_j \end{array} \right\} \mathrm{d}\theta_j. \tag{3.25}$$

Here the upper element of the bracketed pair refers to the force in the x-direction and the lower element to the force in the y-direction.

Using Wronskian relations for Bessel functions, Equation 3.16 can be manipulated to obtain an expression for the velocity potential on the surface of the k^{th} cylinder:

$$\phi(a, \theta_k) = -\frac{2i}{\pi \kappa a} \sum_{n=-\infty}^{\infty} \frac{A_n^k}{H_n'(\kappa a)} \mathrm{e}^{in\theta_k}. \tag{3.26}$$

Substituting 3.26 into 3.25 and carrying out the integration gives:

$$X^j = -\left\{ \begin{array}{c} i \\ 1 \end{array} \right\} \frac{2\rho g A \tanh \kappa h}{\kappa^2 H_1'(\kappa a_j)} \left(A_{-1}^j \left\{ \begin{array}{c} - \\ + \end{array} \right\} A_1^j \right), \tag{3.27}$$

which can be expressed in the form:

$$|X^j| = \frac{1}{2}|F| \left| A_{-1}^j \left\{ \begin{array}{c} - \\ + \end{array} \right\} A_1^j \right| \tag{3.28}$$

where F is the time independent factor in the linear force on an isolated cylinder in the direction of motion and is given by:

$$F = \frac{4\rho g A \tanh \kappa h}{\kappa^2 H_1'(\kappa a)}. \tag{3.29}$$

3.3 Numerical diffraction solution

In the present study, a numerical solution procedure will be used to solve the second order diffraction problem. Furthermore, because of the necessity to model wave interaction with a subsurface caisson (supporting four columns), a numerical solution for the first order problem will also be used (in addition to the linear analytical solution).

In this section the analytical formulation and numerical implementation for a general two dimensional problem are first outlined. This is then extended to the particular case of three-dimensional water wave diffraction. It is hoped that the theory developed for the general two dimensional problem will serve as a useful introduction to the more complex three dimensional problem; the formulation being simpler to follow because of the smaller number of variables

used. The work presented in this section is largely based on a review of boundary element methods given by Eatock Taylor (1982), and on the work of Becker (1992).

3.3.1 Analytical formulation for a two dimensional problem

For consistency with the water wave problem studied in this thesis, a solution to the two dimensional Laplace's equation is sought. To solve this differential equation both the complementary function and the particular integral must be found. The 'fundamental solution' can be looked upon as a form of complementary function that satisfies the differential equation and the actual unique solution is arrived at through application of the physical boundary conditions.

For illustrative purposes, consider an arbitrary two dimensional physical domain S, surrounded by a boundary Γ (Figure 3.2), in which a solution is sought. Within this solution domain assume that there is some interior point $\boldsymbol{p}$ (often referred to as the 'source' point) with coordinates (X, Y) and some other point $\boldsymbol{Q}$ on the boundary (often referred to as the 'field' point) with coordinates (x, y). Note that uppercase letters for coordinates indicate a fixed point and lowercase letters indicate a variable point.

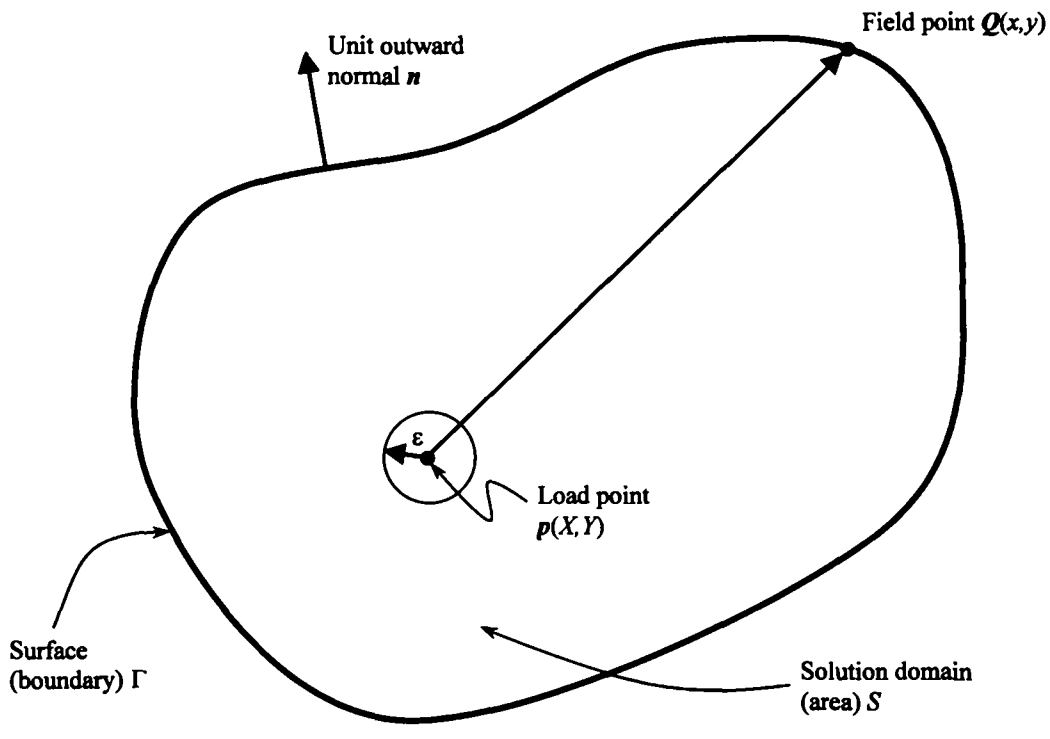

Figure 3.2: A two dimensional physical domain.

The fundamental solution to Laplace's equation, which is based on a two-dimensional solution of a concentrated potential or source at the point $\boldsymbol{p}$, can be shown to be:

$$\lambda(\boldsymbol{p}, \boldsymbol{Q}) = \frac{1}{2\pi} \ln\left(\frac{1}{r(\boldsymbol{p}, \boldsymbol{Q})}\right) \tag{3.30}$$

where $r(\boldsymbol{p},\boldsymbol{Q})$ is the distance between $\boldsymbol{p}$ and $\boldsymbol{Q}$, given by:

$$r(\boldsymbol{p}, \boldsymbol{Q}) = |\boldsymbol{p} - \boldsymbol{Q}| = \sqrt{(X - x)^2 + (Y - y)^2}. \tag{3.31}$$

The constant factor $(1/2\pi)$ is associated with the strength of the potential at point $\boldsymbol{p}$ although this can be considered arbitrary for present purposes. Note that the fundamental solution is singular; it becomes infinite as $\boldsymbol{p}$ and $\boldsymbol{Q}$ approach each other.

The essence of the boundary element formulation is to reduce the dimensionality of the studied problem by one. For the two dimensional case here, area variables are transformed to boundary variables on a line. This is achieved most conveniently using Green's second identity. This assumes the existence of two variables ϕ and λ, which both have continuous first and second derivatives: ϕ is the unknown potential that we seek and λ is the known fundamental solution to Laplace's equation. Applying Green's second identity to these two functions provides the following transformation from an area integral $\mathrm{d}S$ to a line integral $\mathrm{d}\Gamma$:

$$\int_S (\phi\nabla^2\lambda - \lambda\nabla^2\phi)\,\mathrm{d}S = \int_\Gamma \left(\phi\frac{\partial\lambda}{\partial n} - \lambda\frac{\partial\phi}{\partial n}\right)\mathrm{d}\Gamma \tag{3.32}$$

where n is the unit outward normal. An analogous equation can be used to reduce a volume integral to an area integral in a three dimensional problem. The potential ϕ satisfies Laplace's equation everywhere in the solution domain, whereas the fundamental solution λ satisfies $\nabla^2\lambda = 0$ everywhere except at the point $\boldsymbol{p}$ where it is singular. This singularity is overcome by surrounding the point $\boldsymbol{p}$ with a very small circle of radius ϵ (see Figure 3.2) and examining the solution in the limit as $\epsilon \to 0$. Accounting for this small circle, the area and boundary become $(S - S_\epsilon)$ and $(\Gamma + \Gamma_\epsilon)$ respectively, and Equation 3.32 becomes:

$$\int_{S-S_\epsilon} (\phi\nabla^2\lambda - \lambda\nabla^2\phi)\,\mathrm{d}S = \int_{\Gamma+\Gamma_\epsilon} \left(\phi\frac{\partial\lambda}{\partial n} - \lambda\frac{\partial\phi}{\partial n}\right)\mathrm{d}\Gamma. \tag{3.33}$$

Everywhere within the area $(S - S_\epsilon)$, $\nabla^2\phi = 0$ and $\nabla^2\lambda = 0$, which makes the left hand side of Equation 3.33 equal to zero. By splitting the surface integral over $(\Gamma + \Gamma_\epsilon)$ into two surface integrals the following expression is obtained:

$$0 = \int_\Gamma \left(\phi\frac{\partial\lambda}{\partial n} - \lambda\frac{\partial\phi}{\partial n}\right)\mathrm{d}\Gamma + \int_{\Gamma_\epsilon} \left(\phi\frac{\partial\lambda}{\partial n} - \lambda\frac{\partial\phi}{\partial n}\right)\mathrm{d}\Gamma. \tag{3.34}$$

A convenient way of evaluating the integral along the boundary Γ_ϵ in the above equation is to introduce an angle α measured anticlockwise from the x-axis at point $\boldsymbol{p}$ and substitute $\mathrm{d}\Gamma = \epsilon \mathrm{d}\alpha$. In addition, the following substitution is also used:

$$\frac{\partial \lambda}{\partial n} = \frac{\partial \lambda}{\partial r}\frac{\partial r}{\partial n} = \frac{1}{2\pi r}. \tag{3.35}$$

Now, imposing the limit $\epsilon \rightarrow 0$, the second integral in Equation 3.34 becomes:

$$\int_{\Gamma_\epsilon} \left(\phi \frac{\partial \lambda}{\partial n} - \lambda \frac{\partial \phi}{\partial n} \right) \mathrm{d}\Gamma = \frac{1}{2\pi} \int_0^{2\pi} \left[\phi \left(\frac{1}{\epsilon} \right) - \ln \left(\frac{1}{\epsilon} \right) \frac{\partial \phi}{\partial n} \right] \epsilon \, \mathrm{d}\alpha = \phi. \tag{3.36}$$

Substituting this result into Equation 3.34 and rearranging gives the following:

$$\phi(\boldsymbol{p}) + \int_\Gamma K_1(\boldsymbol{p}, \boldsymbol{Q}) \phi(\boldsymbol{Q}) \, \mathrm{d}\Gamma(\boldsymbol{Q}) = \int_\Gamma K_2(\boldsymbol{p}, \boldsymbol{Q}) \frac{\partial \phi(\boldsymbol{Q})}{\partial n} \, \mathrm{d}\Gamma(\boldsymbol{Q}) \tag{3.37}$$

where K_1 and K_2 are called the kernels and are defined as:

$$K_1(\boldsymbol{p}, \boldsymbol{Q}) = \frac{\partial \lambda(\boldsymbol{p}, \boldsymbol{Q})}{\partial n} \tag{3.38}$$

$$K_2(\boldsymbol{p}, \boldsymbol{Q}) = \lambda(\boldsymbol{p}, \boldsymbol{Q}) = \frac{1}{2\pi} \ln \left(\frac{1}{r(\boldsymbol{p}, \boldsymbol{Q})} \right). \tag{3.39}$$

Equation 3.37 is called the boundary integral equation (BIE) and it forms the starting point for the numerical solution procedure.

To make the BIE a truly 'boundary only' equation, the interior load point $\boldsymbol{p}$ must be moved to the boundary (where it will be referred to as point $\boldsymbol{P}$). This results in the equation:

$$C(\boldsymbol{P})\phi(\boldsymbol{P}) + \int_\Gamma K_1(\boldsymbol{P}, \boldsymbol{Q}) \phi(\boldsymbol{Q}) \, \mathrm{d}\Gamma(\boldsymbol{Q}) = \int_\Gamma K_2(\boldsymbol{P}, \boldsymbol{Q}) \frac{\partial \phi(\boldsymbol{Q})}{\partial n} \, \mathrm{d}\Gamma(\boldsymbol{Q}) \tag{3.40}$$

where the function $C(\boldsymbol{P})$ can be calculated by surrounding the boundary point $\boldsymbol{P}$ with a small circular arc of radius ϵ and then taking each term in Equation 3.40 in the limit as $\epsilon \rightarrow 0$. However, it is found that the term $C(\boldsymbol{P})$ does not have to be calculated explicitly; it can be obtained indirectly using physical considerations only.

The physical significance of the BIE is now discussed. The BIE is an integral equation that relates the boundary variables of the problem being solved (here ϕ and $\frac{\partial \phi}{\partial n}$) to a fundamental

solution that is applicable to any domain of any shape (here the kernels K_1 and K_2). The fundamental solution, which yields the kernels, simply computes the 'influence' of a concentrated potential at a given point $\boldsymbol{p}$ on any other point $\boldsymbol{Q}$, except when $\boldsymbol{p}$ coincides with $\boldsymbol{Q}$ where the solution is singular.

3.3.2 Numerical implementation for a two dimensional problem

The numerical evaluation of the BIE is now discussed. If the closed boundary of a domain can be described by an equation then an analytical solution to the BIE may be possible, although working through the solution is likely to be very tedious. To enable any arbitrary geometry to be considered it is necessary to perform the integration in the BIE numerically. The boundary integrals must be divided into small segments called boundary elements, which could potentially be straight lines, quadratic curves or cubic splines.

The numerical implementation of potential problems can be divided into five stages for convenience:

1. Division of the boundary into elements.
2. Numerical integration of the kernels.
3. Application of the boundary conditions.
4. Solution of the algebraic equations.
5. Calculation of the internal variables.

These stages are described in detail in Appendix A and a brief overview of the numerical procedure is given below.

Similar to the elements used in a finite element analysis, the elements making up the boundary of the studied domain are defined by a number of nodal points, the number depending on the type of elements used. Each nodal point has two variables associated with it: ϕ and $\frac{\partial \phi}{\partial n}$. Therefore, if there are N nodal points on the boundary then there will be $2N$ variables. For a problem to have a unique solution each nodal point must have either ϕ or $\frac{\partial \phi}{\partial n}$ prescribed on it. Hence there will be N unknowns and so N equations are needed to solve the problem. These N equations are generated by successively placing a specified potential or potential gradient at each node in turn and using the fundamental solution to calculate the potential or potential gradient at all the other nodes.

3.3.3 Analytical formulation for a three dimensional diffraction problem

The two dimensional formulation presented thus far is now extended to three dimensions. Of particular interest to this study, the three dimensional water wave diffraction problem is discussed. This problem can be tackled in a slightly different way by using a fundamental solution which satisfies some, but not all, of the boundary conditions.

The points $\boldsymbol{p}$ and $\boldsymbol{Q}$, and the distances r and ϵ, are as defined earlier, although now of course the problem incorporates a third dimension; i.e. points $\boldsymbol{p}$ and $\boldsymbol{Q}$ have coordinates (X, Y, Z) and (x, y, z) respectively etc.

As described in Section 2.4 Chapter 2, the solution to the diffraction problem is dependent upon obtaining the 'incident wave' and 'scattered wave' velocity potentials, ϕ_I and ϕ_S, which satisfy the free surface, sea bottom and radiation boundary conditions, together with some condition on the submerged surface of the body. By defining the problem in terms of integral equations, numerical solutions to the diffraction problem can be obtained for arbitrary three dimensional bodies.

The development of the integral equations for the unknown potentials follows a standard technique described, for example, by Brebbia (1980). The starting point is Green's second identity, defined earlier in Equation 3.32, but now in a form to enable transformation from a volume integral $\mathrm{d}V$ to an area integral $\mathrm{d}S$:

$$\int_V (\phi \nabla^2 \lambda - \lambda \nabla^2 \phi)\, \mathrm{d}V = \int_S \left(\phi \frac{\partial \lambda}{\partial n} - \lambda \frac{\partial \phi}{\partial n} \right) \mathrm{d}S. \tag{3.41}$$

Here S is to be taken as the surface formed by the submerged surface of the body S_B, the sea bottom, the free surface and a cylinder surface S_C at infinity. The function ϕ is the unknown potential at point $\boldsymbol{p}$, and hence satisfies:

- Laplace's equation everywhere in the volume V;
- The free surface boundary condition;
- The sea bottom boundary condition;
- The radiation boundary condition.

The function λ can be any function and for the three dimensional formulation it is convenient to define λ as:

$$\lambda = G(\boldsymbol{p};\boldsymbol{Q}) = \frac{1}{r} + H(\boldsymbol{p};\boldsymbol{Q}) \tag{3.42}$$

where:

$$r = r(\boldsymbol{p};\boldsymbol{Q}) = |\boldsymbol{p}-\boldsymbol{Q}| = \sqrt{(X-x)^2+(Y-y)^2+(Z-z)^2} \tag{3.43}$$

and G is the Green's function. It is assumed that H is a regular harmonic function everywhere in the volume V (i.e. it satisfies Laplace's equation in V). The function G, however, is not a harmonic function if the field point $\boldsymbol{Q}$ lies within V. Hence Equation 3.41 can be written as:

$$\int_V \phi(\boldsymbol{Q})\nabla^2\left(\frac{1}{r}\right)\mathrm{d}V = \int_S \left[\phi(\boldsymbol{Q})\frac{\partial G(\boldsymbol{p};\boldsymbol{Q})}{\partial n_Q} - G(\boldsymbol{p};\boldsymbol{Q})\frac{\partial \phi(\boldsymbol{Q})}{\partial n_Q}\right]\mathrm{d}S_Q \tag{3.44}$$

where $\boldsymbol{Q}$ has been used in the right hand side as the integration variable and n_Q is the normal at $\boldsymbol{Q}$. Furthermore, if it is assumed that the Green's function satisfies the free surface, sea bottom and radiation boundary conditions, then the integral over the closed surface S can be replaced by an integral over the submerged surface of the body S_B. This is the key difference between this problem and the two dimensional problem in Section 3.3.1. Therefore Equation 3.44 becomes:

$$\begin{aligned}\int_{S_B}\left[\phi(\boldsymbol{Q})\frac{\partial G(\boldsymbol{p};\boldsymbol{Q})}{\partial n_Q} - G(\boldsymbol{p};\boldsymbol{Q})\frac{\partial \phi(\boldsymbol{Q})}{\partial n_Q}\right]\mathrm{d}S_Q &= \lim_{\epsilon\to 0}\int_V \phi(\boldsymbol{Q})\nabla^2\left(\frac{1}{r+\epsilon}\right)\mathrm{d}V \\ &= \phi(\boldsymbol{p})\lim_{\epsilon\to 0}\int_V \frac{-2\epsilon}{r(r+\epsilon)^3}\,\mathrm{d}V. \end{aligned} \tag{3.45}$$

When considering the right hand side of Equation 3.45 it is convenient to distinguish three cases, these being:

1. If $\boldsymbol{p}$ lies wholly inside V, then a small sphere of radius r_0 can be circumscribed around $\boldsymbol{p}$ and the integral becomes:

$$\lim_{\epsilon\to 0}\int_0^{r_0}\frac{-2\epsilon}{r(r+\epsilon)^3}4\pi r^2\,\mathrm{d}r = -4\pi. \tag{3.46}$$

2. If $\boldsymbol{p}$ lies on the surface S_B (but not on the free surface) and the surface S_B is smooth, a small hemisphere of radius r_0 can be circumscribed about $\boldsymbol{p}$ and the integral becomes:

$$\lim_{\epsilon \to 0} \int_0^{r_0} \frac{-2\epsilon}{r(r+\epsilon)^3} 2\pi r^2 \, \mathrm{d}r = -2\pi. \tag{3.47}$$

3. If $\boldsymbol{p}$ lies wholly outside V, then the integral is zero since the integrand is only non-zero in the vicinity of $r = 0$:

$$\lim_{\epsilon \to 0} \int_r^{\infty} \frac{-2\epsilon}{r(r+\epsilon)^3} 4\pi r^2 \, \mathrm{d}r = 0. \tag{3.48}$$

Therefore Equation 3.45 becomes:

$$\int_{S_B} \left[\phi(\boldsymbol{Q}) \frac{\partial G(\boldsymbol{p}; \boldsymbol{Q})}{\partial n_Q} - G(\boldsymbol{p}; \boldsymbol{Q}) \frac{\partial \phi(\boldsymbol{Q})}{\partial n_Q} \right] \mathrm{d}S_Q$$

$$= \begin{cases} -4\pi\phi(\boldsymbol{p}) & \text{for } \boldsymbol{p} \text{ inside } V \\ -2\pi\phi(\boldsymbol{p}) & \text{for } \boldsymbol{p} \text{ on } S_B \\ 0 & \text{for } \boldsymbol{p} \text{ outside } V. \end{cases} \tag{3.49}$$

Note that if $\boldsymbol{p}$ lies on the surface S_B and the free surface, then the constant 2π in the second part of Equation 3.49 is reduced to π. Also, if $\boldsymbol{p}$ lies at a discontinuity of S_B, then the constant becomes the solid angle enclosed by V.

Various forms of integral equation can be derived from 3.49 - e.g. the second part of 3.49 yields the integral equation:

$$2\pi\phi(\boldsymbol{p}) + \int_{S_B} \phi(\boldsymbol{Q}) \frac{\partial G(\boldsymbol{p}; \boldsymbol{Q})}{\partial n_Q} \, \mathrm{d}S_Q = \int_{S_B} G(\boldsymbol{p}, \boldsymbol{Q}) \frac{\partial \phi(\boldsymbol{Q})}{\partial n_Q} \, \mathrm{d}S_Q \tag{3.50}$$

for a point $\boldsymbol{p}$ on the surface S_B. The right hand side of Equation 3.50 is specified by the boundary condition on S_B and so Equation 3.50 can be used to find the unknown potential function ϕ. To solve this integral equation the unknown potentials are defined in terms of a discrete set of values at the nodal points, and the integral equations are approximated by linear matrix equations in an exactly analogous manner to that described for the two dimensional problem (see Appendix A). The value of ϕ at any point within the fluid volume V can then be obtained from the first part of 3.49.

The integral equation 3.50 holds for the first order potential $\phi^{(1)}$, which satisfies the conventional homogeneous linear free surface boundary condition. The condition on the second order potential $\phi^{(2)}$ is, however, of the form:

$$\frac{\partial \phi^{(2)}}{\partial z} - \frac{\Omega^2}{g}\phi^{(2)} = f(x,y) \tag{3.51}$$

where $f(x,y)$ can be expressed in terms of $\phi^{(1)}$ and Ω is the second order sum frequency. The implication of Equation 3.51 is that the classical integral equation 3.50 is modified for the second order potential to include a free surface integral over S_F (Eatock Taylor and Chau 1992):

$$2\pi\phi^{(2)}(\boldsymbol{p}) + \int_{S_B} \phi^{(2)}(\boldsymbol{Q}) \frac{\partial G(\boldsymbol{p};\boldsymbol{Q})}{\partial n_Q} \,\mathrm{d}S_Q - \int_{S_F} G(\boldsymbol{p},\boldsymbol{Q}) f(\boldsymbol{p},\boldsymbol{Q}) \mathrm{d}S_Q = \int_{S_B} G(\boldsymbol{p},\boldsymbol{Q}) \frac{\partial \phi^{(2)}(\boldsymbol{Q})}{\partial n_Q} \,\mathrm{d}S_Q \tag{3.52}$$

where S_F is the free surface outside the body.

The equations given in this section presuppose knowledge of the form of the Green's function. In three dimensions $G(\boldsymbol{p};\boldsymbol{Q})$ is required to satisfy:

$$\nabla^2 G = \delta(\boldsymbol{p} - \boldsymbol{Q}) \tag{3.53}$$

where δ is the Dirac delta function, together with the free surface, sea bottom and radiation boundary conditions. $G(\boldsymbol{p};\boldsymbol{Q})$ must be expressible as a simple source $1/r$ plus a regular harmonic function (as defined in Equation 3.42). The resulting function has been expressed in various forms by John (1950), Wehausen and Laitone (1960) and others.

3.3.4 Discretisation of the integral equations for a three dimensional diffraction problem

The discretisation of the integral Equation 3.50 is now briefly discussed for the studied three dimensional problem. The surface S_B can be characterised by n_j nodes; at the i^{th} node (x_i, y_i, z_i) the potential can be designated ϕ_i and the normal velocity is defined as $\partial\phi_i/\partial n = v_i$. Equation 3.50 can be approximated by nodal collocation yielding:

$$\phi_j + \frac{1}{2\pi}\int_{S_B} \frac{\partial G_j}{\partial n_Q} \sum_{i=1}^{n_j} N_i \phi_i \,\mathrm{d}S_Q = \frac{1}{2\pi}\int_{S_B} G_j \sum_{i=1}^{n_j} N_i v_i \,\mathrm{d}S_Q \tag{3.54}$$

where N_i are the shape functions for interpolating the values of ϕ_i and v_i between the nodes. A similar expression incorporating a free surface integral over S_F can be written for Equation 3.52.

In Equation 3.54 the integration variable corresponds to the point $\boldsymbol{Q}(x, y, z)$ and:

$$G_j = G(\boldsymbol{p}_j; \boldsymbol{Q}) = G(X_j, Y_j, Z_j; x, y, z). \tag{3.55}$$

Equation 3.54 can be written in matrix form as:

$$([I] + [A])[\phi] = [B][v] \tag{3.56}$$

where I is the identity matrix and the matrices A and B are clearly defined from Equation 3.54. This equation is exactly analogous to Equation A.23 defined in Appendix A for the two dimensional problem.

3.4 Numerical diffraction code: DIFFRACT

DIFFRACT is a numerical diffraction code developed at the Department of Engineering Science, University of Oxford, which utilises the boundary element method to solve the three-dimensional water-wave diffraction problem to second order. Both the first and second order velocity potentials can be computed for monochromatic, bi-chromatic, uni-directional and bi-directional waves incident upon fixed and floating bodies of arbitrary shape. This study uses the DIFFRACT code to model wave interaction with fixed arrays of bottom mounted cylinders (at second order) and a fixed gravity based structure (at first and second order), for incident monochromatic waves and focused wave groups.

The calculation procedure for a fixed body is separated into four distinct parts:

1. Computation of the first order velocity potential.
2. Evaluation of this potential at each node on the discretised free surface.
3. Evaluation of the boundary integral equation over the quiescent free surface.
4. Approximation of the second order velocity potential.

A detailed description of the numerical formulations used by DIFFRACT is given by Chau (1989) and Chau and Eatock Taylor (1992).

The main features of DIFFRACT are as follows:

- Quadratic boundary elements are used, which allow DIFFRACT to employ relatively

coarse meshes (compared with meshes used in constant panel methods) and hence reduce computation time.

- One and two plane symmetry is used to reduce computation time for symmetric structures.

- Meshes for the body surface and free surface are generated using a mesh generator.

- Calculations can be performed for deep water and finite water depth.

- Single or multiple arbitrary shaped fixed or freely floating bodies can be considered in the fluid domain.

- First and second order hydrodynamic wave forces and moments acting on a body can be calculated.

- First and second order free surface elevations on and around a body can be calculated.

- By appropriate post-processing, the results from DIFFRACT can be used to consider incident irregular waves and focused wave groups.

Prior to this present study, DIFFRACT has been extensively used to investigate wave diffraction by a single cylinder. Through comparisons with linear analytical solutions, semi-analytical second order solutions and published data, both force and free surface elevation results have been rigorously verified for a single cylinder. DIFFRACT has been further verified in a study carried out by Zang et al. (2003), which considered the hydrodynamics of ship shaped floating bodies. Zang et al. found the first and second order forces and wave elevations generated by DIFFRACT to agree remarkably well with experimental data recorded in a wave basin for a unidirectional focused wave group incident upon a ship shaped body. Furthermore, DIFFRACT has been used in a study of wave diffraction by tension leg platforms (Eatock Taylor and Huang 1996).

Each of the above mentioned tests serve to confirm the accuracy of the algorithms and numerical code implemented by DIFFRACT.

Chapter 4

Wave diffraction experiments

4.1 Introduction

Prior to the present study, a programme of physical hydraulic model tests was carried out to assist in determining the optimal deck elevation for an offshore structure proposed in the Sea of Okhotsk near Sakhalin Island, Russia. The principal objective of the tests was to determine the deck elevation required to avoid green water impact under extreme storm conditions.

The physical model tests were conducted at the Canadian Hydraulics Centre (CHC) in Ottawa, Canada. The platform tested, called LUNA, consists of a multilevel deck structure supported above the ocean surface by a concrete gravity substructure (CGS) resting on the sea bed. The LUNA model included a replica of the CGS and a deck structure that could be fixed at different elevations. The model was fitted with instrumentation for measuring water surface elevations at various locations under the deck.

One of the aims of the present study is to assess the effectiveness of linear and second order diffraction theories in guiding airgap design. Therefore, the measured wave field around the model will be compared to diffraction theory predictions to help assess how much of what occurs in reality is captured by the solutions.

This chapter provides a description of the test facility and the experimental procedure undertaken. The wave data available for analysis are also discussed. Analysis of the results from these experiments and comparisons with the diffraction solutions are given in Chapter 8.

4.2 The LUNA platform

LUNA's concrete substructure is made up from a rectangular box-shaped caisson supporting four large diameter concrete columns. Photographs of the LUNA model in the wave basin prior to testing are shown in Figure 4.1. The grey box-shaped base is the caisson, supporting

the large diameter concrete columns (black with yellow bands near the top). The comparatively slender steel columns supporting the deck are white with coloured bands. The small diameter black cylinders, projecting up from one of the concrete columns, are conductors used for transporting hydrocarbons to the deck for processing, and serve no structural purpose.

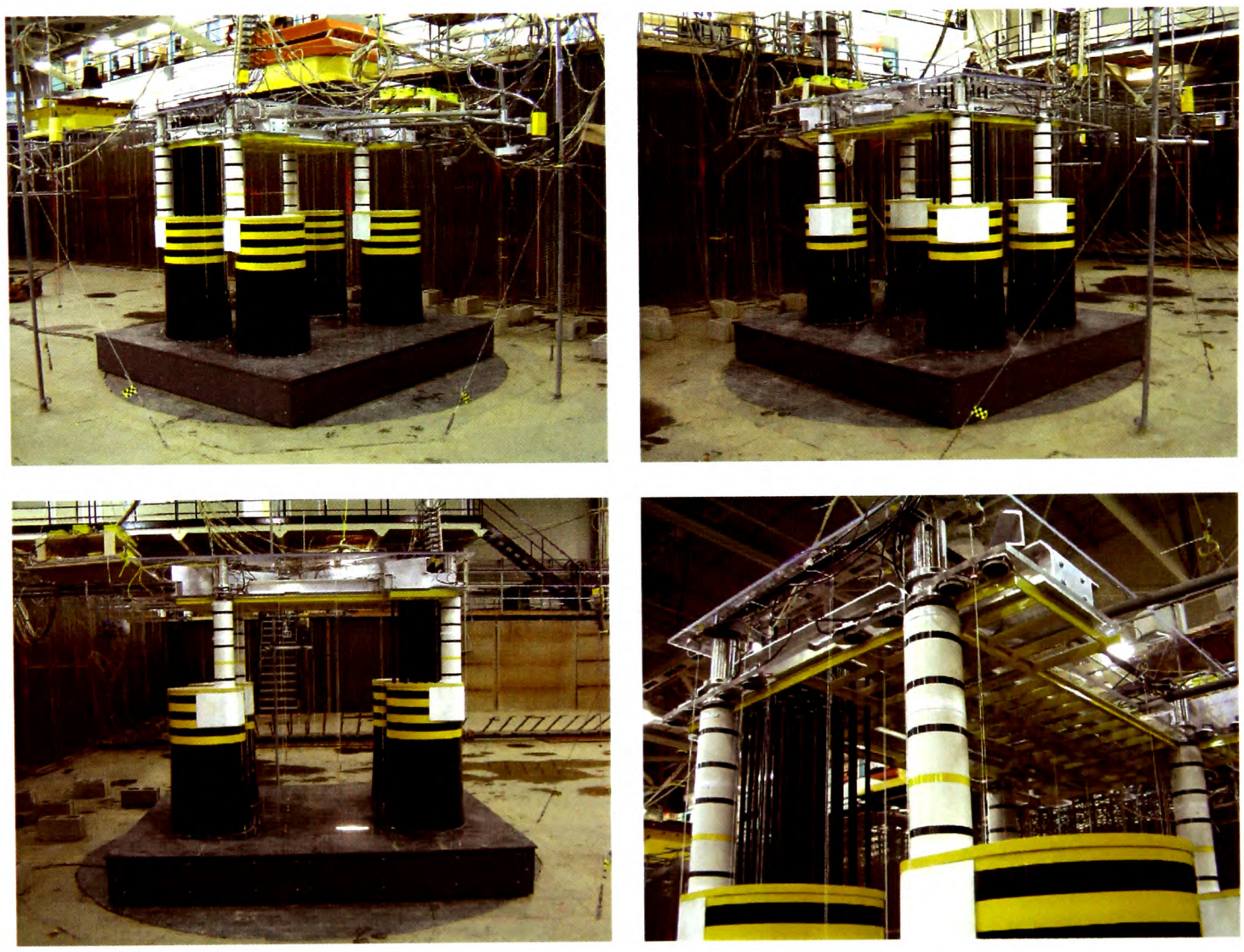

Figure 4.1: Photographs of the LUNA model.

The design still water level for all LUNA model tests was 53.13m. The structural parameters for the platform are as follows:

Caisson:

Height = 15m

Length (forward to aft) = 121.03m

Width (port to starboard) = 108.48m

Concrete columns:

Columns terminate 45.2m above the top of the caisson (i.e. 60.2 above the seabed and 7.07m above design still water level)

Diameter varies from 26m at the bottom to 23.9m at mid-height and above

Centre-to-centre spacing = 68.1m and 40.5m

Steel columns:

Diameter = 6m

Centre-to-centre spacing = 68.1m and 40.5m

Only wave interaction with the concrete substructure is considered in this thesis; the steel columns and deck structure are not included in the diffraction analysis. A diagram of the substructure showing the above dimensions, the mean water level and the direction of wave propagation, is given in Figure 4.2.

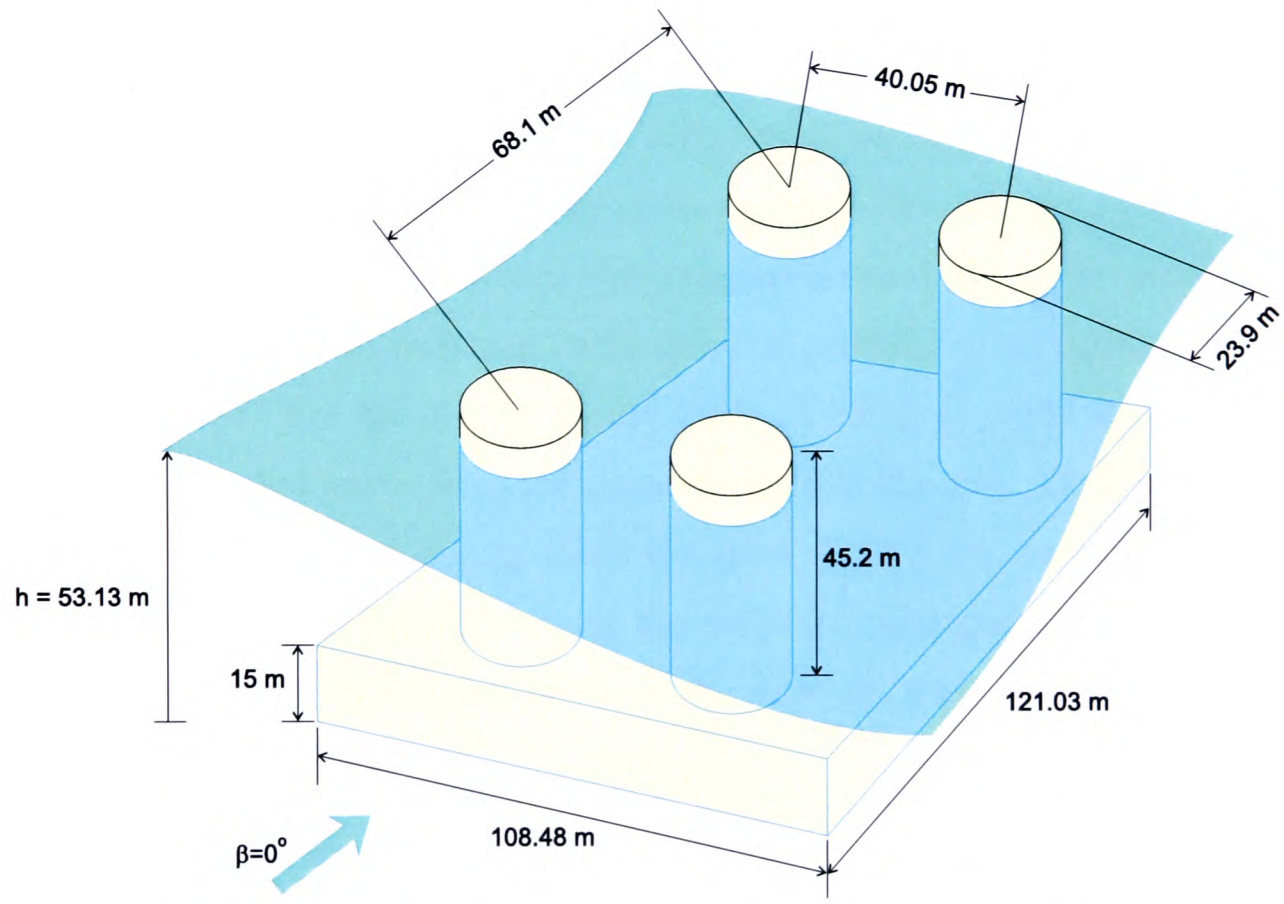

Figure 4.2: LUNA substructure showing the mean water level and the direction of wave propagation.

Because of the necessity to model wave interaction with a subsurface caisson in addition to an array of columns, a numerical diffraction solution at first order, as well as second order, is used in this study. The variation of the diameter of the concrete columns between the top of the caisson and 15.5m below mean sea level is thought to have a small effect on the diffracted wave field and so is not accounted for in subsequent analysis.

4.3 Test facility

The model tests were carried out in the CHC's Multidirectional Wave Basin (MWB). The MWB is a 3m deep rectangular basin with a width of 30m and a length of 20m. Note that the full 3m depth of the basin is not used in these tests (a discussion on scaling is given in Section 4.4).

The MWB is equipped with a multidirectional wave generator installed along one of the sides of 30m length. Wave verification studies carried out by the CHC have shown the wave generation system installed to be highly accurate and repeatable.

The accurate simulation of realistic wave conditions depends not only on the ability to generate the desired waves, but also on the ability to effectively absorb wave energy around the perimeter of the basin. The MWB has wave absorbers installed along the three sides not occupied by the wave machine. The absorber opposite the wave generator has reflection coefficients of approximately 2-6% over a wide range of water depths, wave heights and wave frequencies. Removable guide walls can be installed to partially or completely cover the side absorbers as required. For the LUNA model tests, 11.5m long guide walls were installed along both sides to guide waves from the generator to the test site. These solid guide walls help to control the loss of wave energy along the sides of the basin due to diffraction effects and so help to enhance the homogeneity of the sea state produced at the test site. Guide walls extending along the full length of the basin were not used because they would have exacerbated cross-mode oscillations.

4.4 Scaling

The model tests have been conducted using a geometric scale of 1:45. Froude scaling has been used to convert quantities measured in the model tests to full scale values. The scaling relationships are derived from similitude of the Froude number (Fr), which represents the relative balance between gravitational and inertial forces. Since wave motion and wave-structure interactions are governed by a balance between the gravitational and inertial forces acting on water particles, similitude of the Froude number between model tests and full scale, together with geometric similitude, ensures that the model tests provide a realistic simulation of these processes. The full scale value for a particular quantity is obtained by multiplying the value measured in the model test by an appropriate scale factor (λ). Scale factors for selected quantities used in this study are listed in Table 4.1. In this thesis all measured quantities are expressed as full scale values.

Quantity	Scale factor (λ)	Typical value at full scale	Corresponding value in model test
Froude number	$\lambda_{Fr} = \frac{\lambda_v}{(\lambda_g \lambda_l)^{1/2}} = 1.0$	1.0	1.0
Length	$\lambda_l = 45.0$	100 m	2.22 m
Wave height	$\lambda_H = \lambda_l = 45.0$	9.9 m	0.22 m
Water depth	$\lambda_h = \lambda_l = 45.0$	53.13 m	1.18 m
Time	$\lambda_t = \sqrt{\lambda_l} = 6.71$	180 mins	26.83 mins
Wave period	$\lambda_T = \lambda_t = 6.71$	12.7 s	1.89 s

Table 4.1: Scale factors for selected quantities. λ_v = velocity scale factor. λ_g = gravitational acceleration scale factor (=1).

Finding a fluid for the model tests with a suitably scaled surface tension was not possible (Cornett et al. 2002). The ideal scale law for surface tension (σ) is:

$$\lambda_\sigma = 1.025\lambda_l^2. \tag{4.1}$$

By substituting $\lambda_l = 45$ into this equation one finds that the model tests should have been conducted in a fluid that has a surface tension approximately 2076 times smaller than that of sea water. However, the fluid used in these model tests was fresh water and so the surface tension scale factor was approximately 1 (i.e. the surface tension in the model tests was approximately 2076 times too large). This means that the physical processes that are sensitive to surface tension were not simulated correctly. Surface tension is an important parameter affecting the formation and character of spray (which is also affected by wind, salinity and current) and even the runup against physical structures. Consequently, certain aspects of the fluid-structure interaction may not have been modelled accurately in these model tests. For example, the large surface tension will cause the spray droplets in the model tests to be oversized and will reduce the level of aeration in the model flows. Therefore, it is reasonable to expect the wave-structure interactions in the model tests to feature more green water and less white water than those at full scale. It was for this reason that a large experimental scale was chosen for these tests, to minimise scale effects resulting from improper scaling of surface tension (and fluid viscosity). Unfortunately, it is not possible to establish the precise nature or magnitude of these potential inaccuracies although it is thought that the deviations from reality are sufficiently small for useful comparisons with the diffraction solutions to be made.

4.5 Instrumentation and data acquisition

Vertical motion of the free surface was measured using capacitance-wire wave probes, which operate by sensing the change in capacitance that occurs as a portion of the insulated wire becomes wetted. The signal is directly proportional to the length of wire that is wetted, regardless of whether the wetting is continuous (e.g. caused by green water) or intermittent (e.g. caused by white water). Each wave probe has an accuracy of ± 1 mm at model scale, which is equivalent to ± 45 mm at full scale.

Fourteen wave probes were used to measure wave conditions during the undisturbed tests. Wave probes 1-5 were arranged in a linear array away from the test site for measuring wave reflections from the main absorbers opposite the wave machine; these five probes remained in place during the model tests. Wave probe 10 was located at the centre of the test site and probes 6-9 and 11-14 were arranged in a 2.2m (100m at full scale) radius circle around probe 10 (see Figure 4.3 (a)).

Twenty six wave probes were deployed during the model tests to measure wave conditions in the local vicinity of the model. The probe layout for the model tests is shown in Figure 4.3 (b). Note that probe 11 is at the centre of the test site and probes 2, 3, 6, and 26 measured waves overtopping the concrete columns, which are not of direct interest in this study.

Measurements of the three-dimensional structure of the waves were obtained using a pair of two-axis electromagnetic current meters. The readings from these instruments were analysed to resolve the multi-directional properties of the sea states created at the test site.

Two different data acquisition systems were used to convert the analogue voltage signals from the wave probes into digital form. A low-speed system was used during the undisturbed tests, sampling the data at 25 Hz and a high-speed system was used for the model tests that sampled the data at 149 Hz.

4.6 Data available

Undisturbed wave tests were carried out to measure and verify the wave conditions generated at the test site without the model in place. The LUNA model was installed at the test site following the undisturbed tests. Tests were carried out for four deck elevations: 22m, 23.5m, 25m and 38m above lowest astronomical tide. The 38m deck elevation is sufficiently high for waves not to come into contact with the deck and, because of the large amount of white water-deck interaction occurring at the lower deck levels, only tests with this elevation are

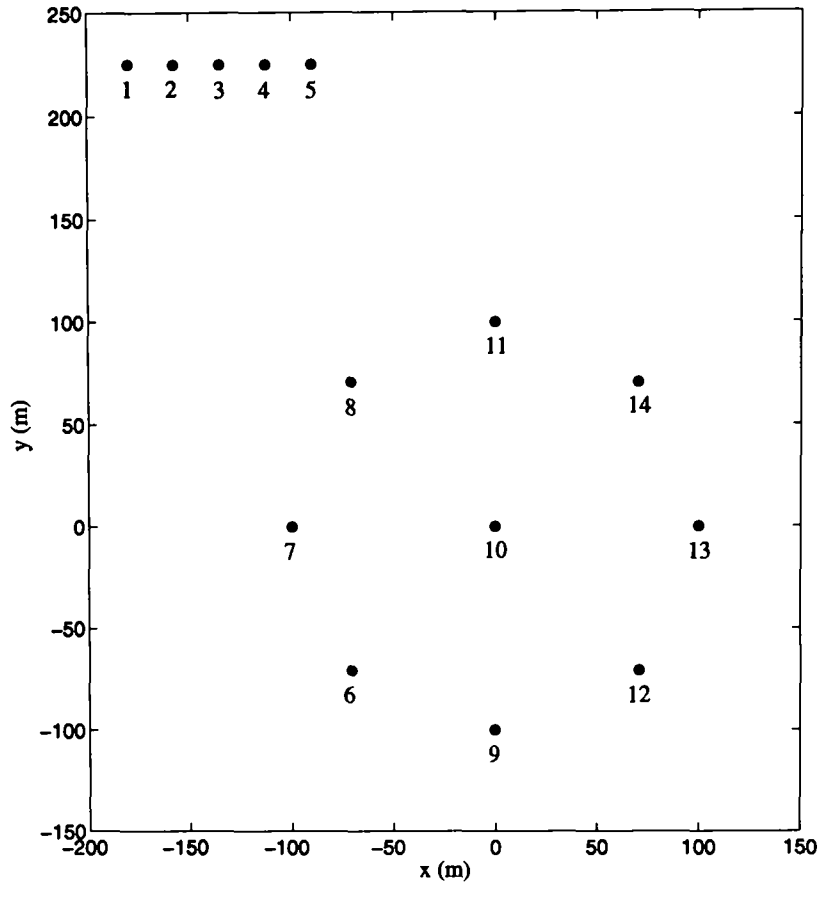

(a) Undisturbed wave probe locations

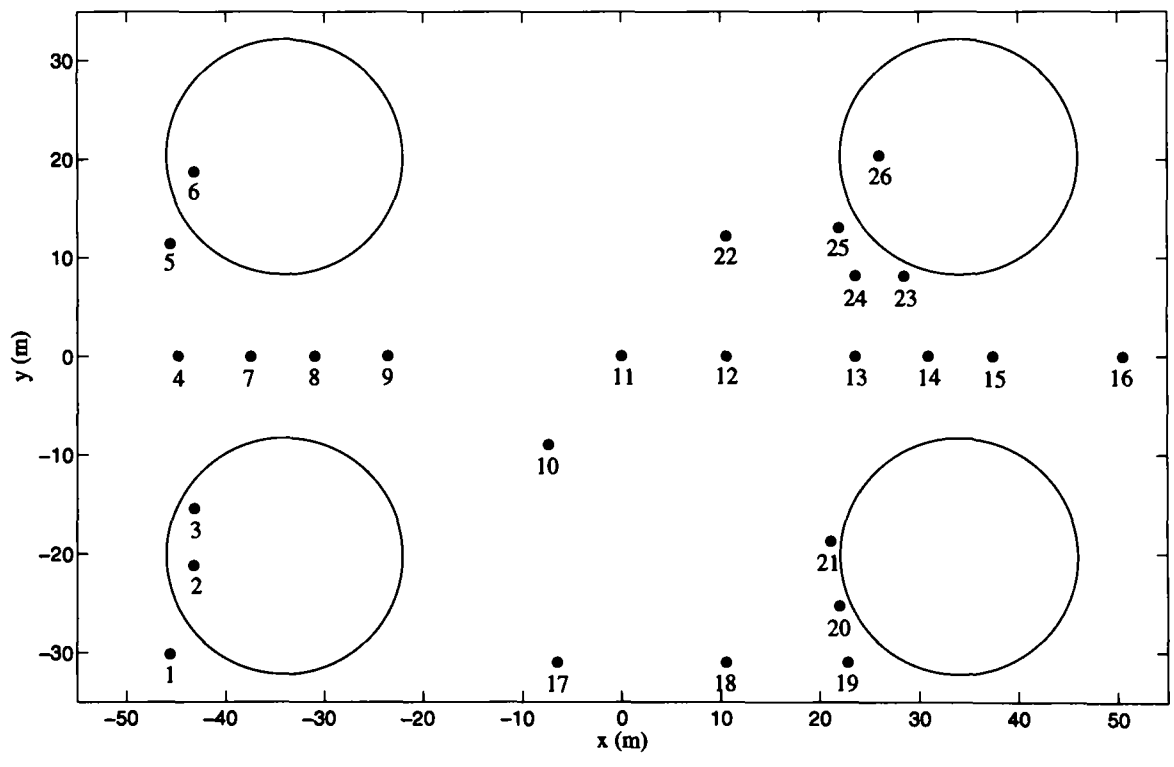

(b) Model test wave probe locations

Figure 4.3: Wave probe locations for the wave tank tests. The large circles on plot (b) show the LUNA concrete columns. Incident waves propagate from left to right. Full scale dimensions are given.

considered in this study.

A range of wave conditions were carried out for both the undisturbed and model tests: regular waves, unidirectional irregular waves and multidirectional irregular waves. All irregular waves were synthesised to match a JONSWAP spectrum (Hasselmann et al. 1973) with a peak enhancement factor (γ) of 2. The irregular tests were conducted for extreme wave conditions associated with a return period of 100 years and data were recorded for three hours at full scale (26.83 minutes at model scale).

The multidirectional waves were generated using a directional spectral density function, given by:

$$S(f,\theta) = S(f) \times D(\theta) \tag{4.2}$$

where $S(f)$ is a direction-independent frequency spectrum (the JONSWAP spectrum for these tests) and $D(\theta)$ is a frequency-independent directional spreading function. A cosine power form was used for $D(\theta)$ in these tests, which is defined by:

$$D(\theta) = \frac{\Gamma(s+1)}{\sqrt{\pi}\Gamma(s+0.5)} \cos^{2s}(\theta - \theta_M) \quad \text{for } |\theta - \theta_M| < \pi/2, \tag{4.3}$$

where Γ is the gamma function, θ_M is the mean wave direction and s is the spreading index. A spreading index of $s = 7$ was used for the multidirectional tests, producing a wave field in which the wave directions have a standard deviation of 15 degrees and the maximum wave angles are within 45 degrees of the mean direction. For the unidirectional tests the waves travel along the x-axis (i.e. zero incident wave angle) and $\theta_M = 0$ for the multidirectional tests.

The repeatability of the wave conditions has been assessed by: (1) comparing wave statistics computed for multiple runs of the same control signal; (2) computing the cross-correlation of the free surface elevation time histories from multiple runs; (3) comparing the heights and periods of individual waves in the measured wave trains from multiple runs. The results from these analyses indicated that the sea states created at the test site were highly repeatable. Therefore, data are available for the incident undiffracted waves at the test site during the undisturbed tests, and for the same waves as they interact with the model during the model tests.

Eight tests are considered in this thesis; four with the model absent (undisturbed) and four

with the LUNA model in place with the deck at an elevation of 38m. The target met-ocean conditions for these tests are given in Table 4.2. The data set numbering used in this table will be referred to in later analysis.

Data set	Wave conditions	H, H_s (m)	T, T_p (s)
Undisturbed			
1	Regular	10	12.7
2	Regular	14	12.7
3	2D Irregular	9.9	14.3
4	3D Irregular	9.9	14.3
Model tests			
5	Regular	10	12.7
6	Regular	14	12.7
7	2D Irregular	9.9	14.3
8	3D Irregular	9.9	14.3

Table 4.2: Met-ocean conditions for the regular, unidirectional (2D) irregular and multidirectional (3D) irregular wave data studied. $s = 7$ was used for the multidirectional tests.

Chapter 5

Freak wave occurrences

5.1 Introduction

When contemplating airgap design it is crucially important that consideration is given to the extreme tail end of the wave height distribution, the so-called freak or rogue wave occurrences. The proven existence of such events and our inability to understand them are an indication of the amount of work left to do. This chapter studies the nature of one specific freak wave occurrence for which field data are available, namely the Draupner New Year wave. Mathematical tools are developed that will be further implemented in Chapter 8 when studying the LUNA model test data.

Ocean surface waves are both random in time and nonlinear. For a linear random model of the sea surface, the average shape of a large crest is found to be the scaled auto-correlation function, as is shown mathematically by Lindgren (1970) and Boccotti (1983). Using field data from the North Sea, the applicability of this simple result is discussed in this chapter. Stokes-type corrections up to fifth order are incorporated in an approximate but robust manner, valid at least locally in space and time. Exact second order wave theory is used to check the accuracy of the approximate Stokes treatment and to clarify the magnitude and character of the second order contributions. A giant wave, called the New Year wave, recorded at the Draupner platform in the North Sea at 15:20 on 1st January 1995, is examined. In a sea-state with a significant wave height of approximately 12m, this freak wave, which has a peak elevation of 18.5m above still water level, was unambiguously recorded. The local asymmetries of this wave are removed using the Stokes model, allowing the probability of occurrence of this remarkable event to be estimated, based on the standard Rayleigh distribution for linear crest amplitude. It is concluded in this chapter that new physics, not incorporated in standard approaches to offshore engineering design, may have played an important role in the generation of this freak wave.

The results and discussion in this chapter are drawn from Walker et al. (2005).

5.2 Background

The Draupner platform is situated in the Norwegian sector of the North Sea in water of 70m depth. Two twenty minute surface elevation time series from the Draupner platform are considered in this study, each having an average wave period, T_Z, of 12.5 seconds, corresponding to an average frequency, f_Z, of 0.08Hz. Therefore each time series contains approximately 100 waves. The first time series, recorded from 15:20 on the 1st January 1995, contains the New Year wave, and the second was recorded one hour later from 16:20. Hereafter these two wave records will be referred to as Draupner 1520 and 1620 data sets. The data were measured using a downward looking laser device. The significant wave heights for the 1520 and 1620 data sets are 11.92m and 12.04m respectively and the sampling rate for both is 2.1Hz. Previous analyses of freak waves with reference to the New Year wave has been undertaken by Haver and Andersen (2000) and Provosto and Bouffandeau (2002).

The time series plots for the two Draupner wave records are shown in Figure 5.1. The data analysed display obvious nonlinear behaviour; the shapes of the crests are consistently sharper and larger than their trough equivalents. The 'design wave' called NewWave is shown to be an acceptable local model for the linear contribution to large waves in these data sets. Waves in nature are, however, nonlinear, and so higher order effects are assessed here both through the introduction of simple Stokes-type corrections and the implementation of exact second order wave theory (Dean and Sharma (1981), Dalzell (1999)). Furthermore, spectral analysis is used to identify unique features of the New Year wave which distinguish it from a typical large wave.

5.3 Crest-trough comparison

Average large crest and trough profiles for the two studied data sets, computed using the largest 50% of crests and troughs, are shown in Figure 5.2. These profiles are obtained by extracting the local time history around each large crest and trough, resetting the time series so that peak crest elevation and peak trough depression occur at zero time, and then averaging across all the time series. The average trough profiles have been shown inverted for comparison with the crest profiles. As one would expect, the results presented show that the crests are higher and spikier, and the troughs are less deep and more rounded. The New Year wave is omitted from this averaging process because it is so extreme compared to all other waves in either record.

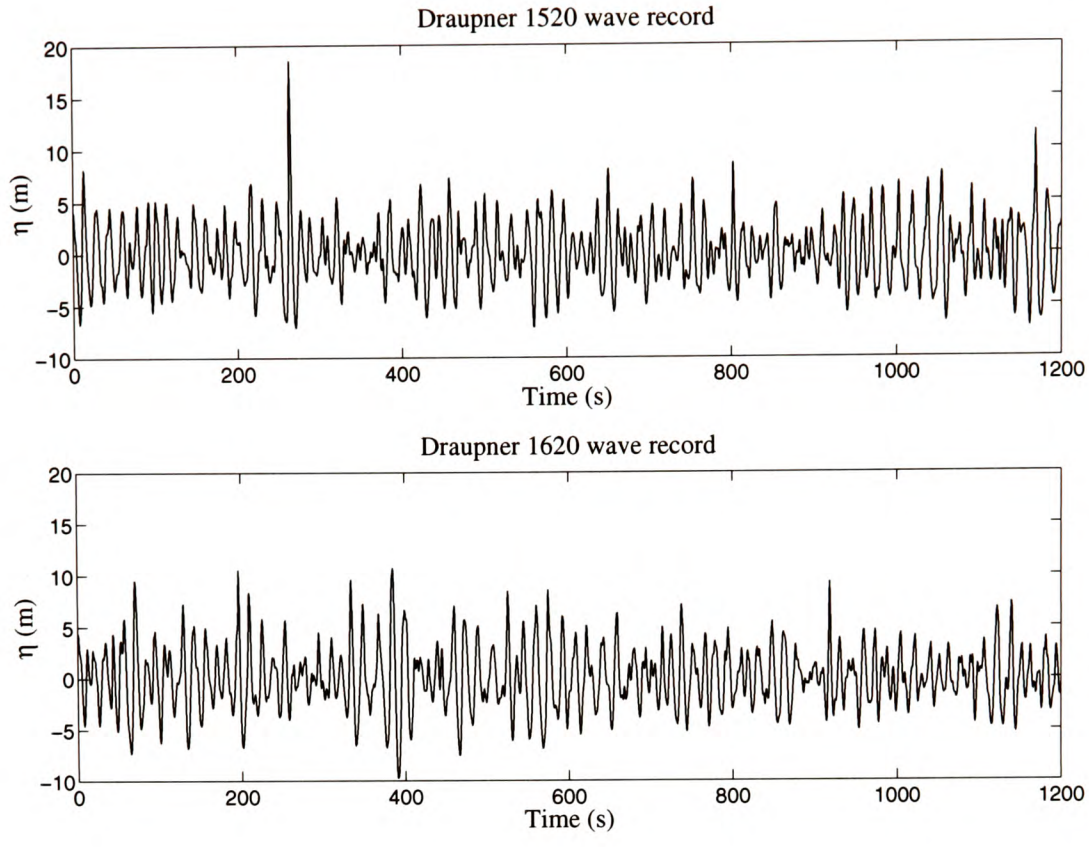

Figure 5.1: Time series plots for the Draupner 1520 and 1620 wave records.

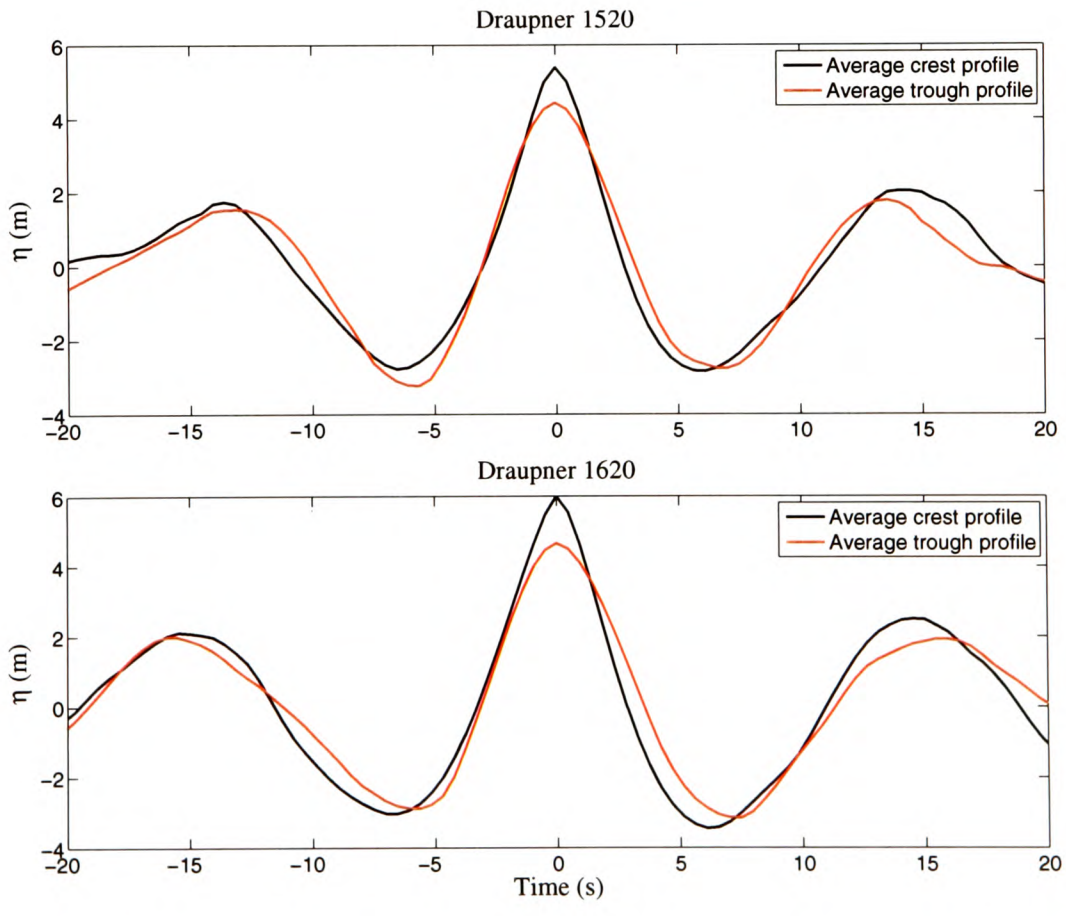

Figure 5.2: Average large crest and trough profiles for the Draupner 1520 and 1620 wave records.

Qualitatively, the apparent asymmetry between crests and troughs for free surface waves is the most obvious manifestation of nonlinearity in the ocean, and this effect has been observed unambiguously in the data studied here. The magnitude of this effect can be illustrated by sorting peak crest elevations and peak trough depressions into ascending order and then plotting the n^{th} largest crest against the n^{th} largest trough. Such plots for the two Draupner wave records are shown in Figure 5.3, where a dashed 1:1 line has been included to help illustrate the asymmetry of the waves. It is worth emphasising that there is no particular temporal relationship between the n^{th} largest crest and the n^{th} largest trough.

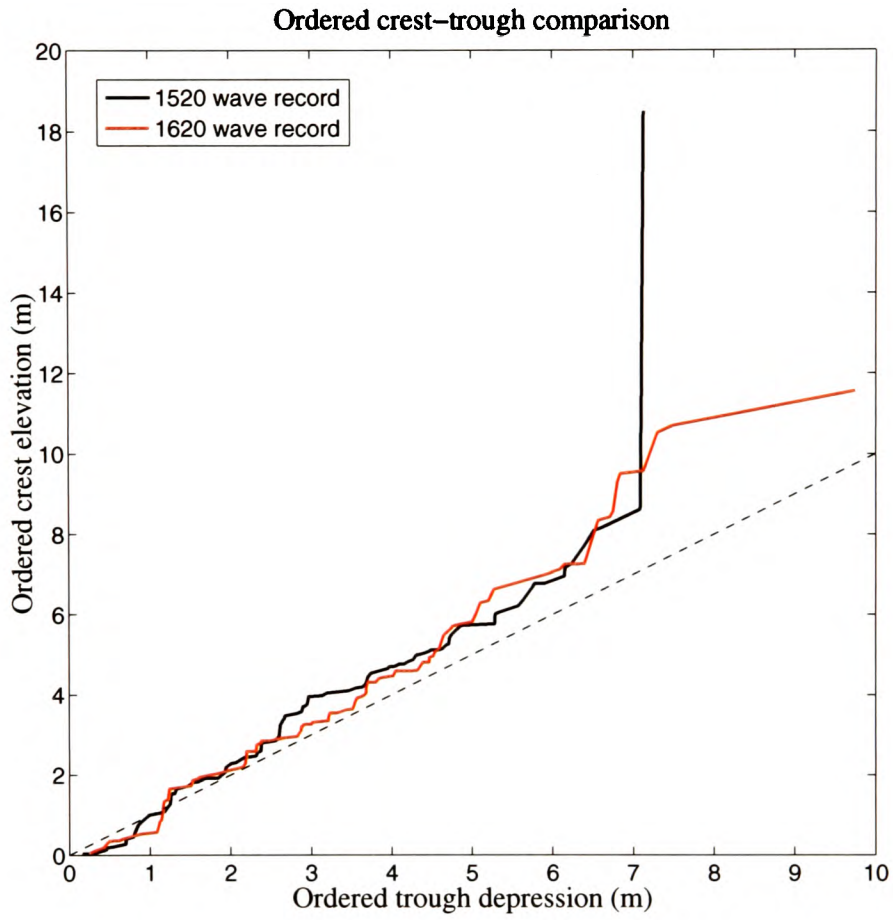

Figure 5.3: Ordered crest elevation plotted against ordered trough depression for the Draupner 1520 and 1620 wave records. A 1:1 line is shown (dashed line).

Both data sets produce largely predictable results, with crest-trough asymmetry increasing as the size of the crests and troughs increase. It is perhaps curious to note that for very small crests and troughs (with an elevation or depression $<\sim$ 1m) the size of the trough depression is actually greater than the corresponding crest elevation on average. Uncertainty in the true location of the mean sea level could perhaps be the cause of this. Indeed, when handling time series containing a relatively small number of waves, averaging should take place over an integer number of periods when removing any tidal contribution, otherwise small errors can be introduced.

A major drawback to presenting such results for the Draupner data is that there are comparatively few instances of large waves within the data. Hence towards the top end of such ordered data sets there is considerable sample variability.

5.4 NewWave comparison

In regions such as the North Sea and the Gulf of Mexico the design of offshore structures is concerned with the environmental loads and peak surface elevations generated by extreme storms. As an alternative to running many hours of random time domain simulation, a convenient 'design-wave' based on the average shape of an extreme crest in a linear random Gaussian process can be used (Lindgren (1970) and Boccotti (1983)). In offshore engineering this 'design-wave' has become known as NewWave. As outlined in Chapter 2 Section 2.2, the linear NewWave is proportional to the autocorrelation function, which is the Fourier transform of the power spectrum (Equation 2.1).

NewWave models the broad-banded character of large ocean waves as a set of independent freely propagating sinusoidal components of different amplitude. A linear NewWave involves the superposition of these components with an extreme crest being generated when all the components come into phase. The NewWave profile is now compared with the average linear large crest profile for the two Draupner data sets.

From a consideration of a Stokes water wave expansion, it can be easily shown that the odd harmonics (which will be dominated by the linear contribution) can be readily extracted from a time series using the expression:

$$\eta_{odd} = \frac{\eta_C - \eta_T}{2} \tag{5.1}$$

where η_C is the average large crest profile (crest elevation taken as positive) and η_T is the average large trough profile (trough depression taken as negative). To obtain η_C and η_T the largest 50% of crests and troughs have been averaged, again with the New Year wave omitted.

Figure 5.4 compares the scaled η_{odd} profile (which is approximately the average linear profile) with the NewWave profile computed using Equation 2.2 (Chapter 2 Section 2.2) for the two Draupner wave records. The New Year wave has been excluded for this comparison since one cannot expect its second order components to be removed using Equation 5.1.

The agreement is good in the local vicinity of the extreme peaks although some variability develops away from $t = 0$. One discrepancy is that the central peaks of the η_{odd} profiles

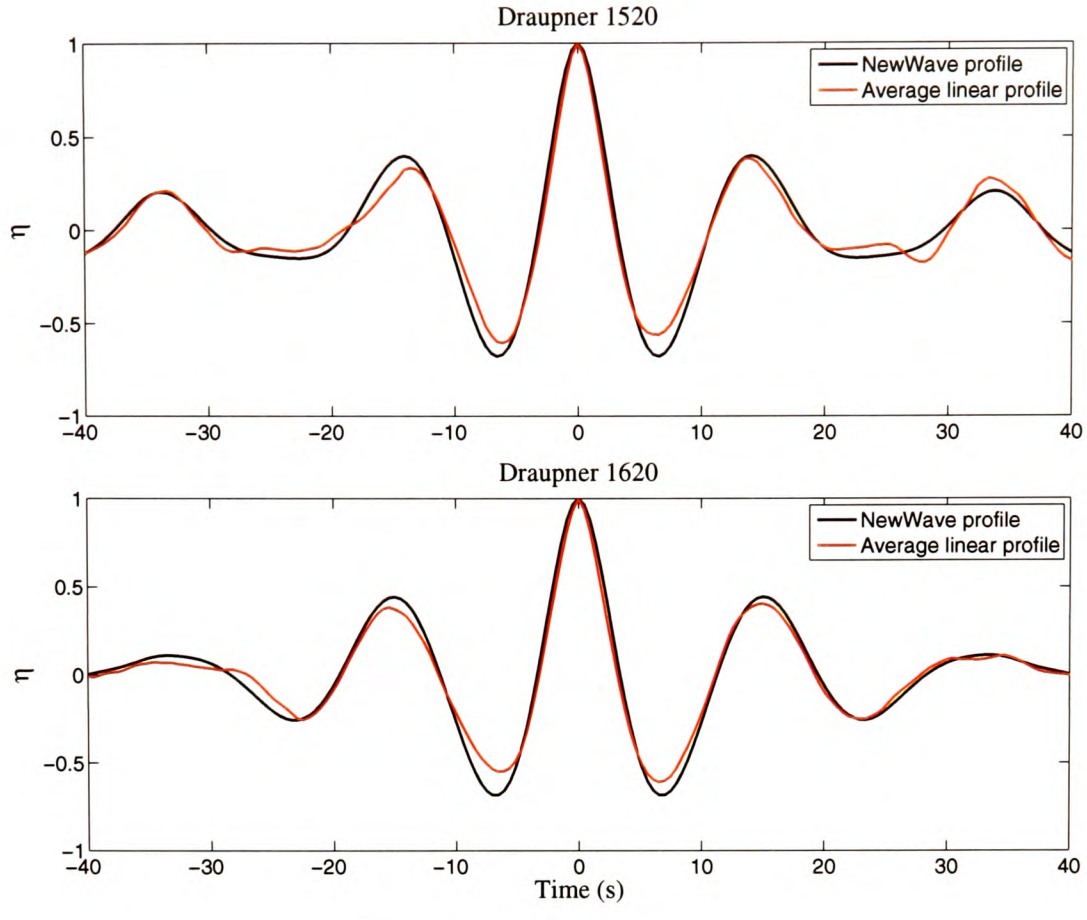

Figure 5.4: Comparison of the average linear large crest profile with the linear NewWave profile for the Draupner 1520 and 1620 wave records. The crest amplitudes have been normalised such that the peak crest elevations equal 1.

are slightly narrower for both the 1520 and 1620 data sets. This is likely to be caused by the third order harmonic contribution retained in η_{odd}. The large differences found between the data averages and NewWave far away from $t = 0$ for both data sets can be attributed to statistical variability, as there are a comparatively small number of large waves in each record.

NewWave has been extensively verified for field data in both deep and shallow water (Jonathan and Taylor (1997), Taylor and Williams (2004)), so it is reasonable to conclude that NewWave is a valid model for the underlying linear data and that the discrepancies observed are the result of statistical variability and/or a large third harmonic contribution. Later in this chapter the NewWave profile is modified to incorporate nonlinear corrections up to fifth order and a comparison is made with the New Year wave profile.

5.5 Second and third order corrections

Attention is now turned to the nonlinear contributions to a wave record not considered thus far. Stokes-type corrections are presented as a means of approximating the second and third order contributions to a wave record. An alternative approach would be to use the exact second order interaction kernel of Dean and Sharma (1981) and Dalzell (1999), and this will

also be discussed later. Here a technique is outlined that enables the second and third order sum contributions to a wave record to be temporally decomposed.

The first three terms of a Stokes regular wave expansion can be written as:

$$\eta(t) = A\cos\phi(t) + \frac{S_{22}}{h}A^2\cos 2\phi(t) + \frac{S_{33}}{h^2}A^3\cos 3\phi(t) \tag{5.2}$$

where A is the linear wave amplitude, h is the water depth and $\phi(t)$ is the phase. The coefficients S_{22} and S_{33} are related to the standard Stokes coefficients defined by Fenton (1990) by $S_{22}/h = \kappa B_{22}$ and $S_{33}/h^2 = \kappa^2 B_{33}$ (Chapter 2 Section 2.5). Stokes expansions are usually written as products of the non-dimensional coefficients with powers of the wavenumber κ, not the undisturbed water depth h. However, since the intention here is to make use of Stokes theory for irregular wave trains, h is known (here taken as 70m) and κ would have to be approximated along with B_{22}. The standard Stokes coefficients and the modified versions used here are defined in Chapter 2 Section 2.5 up to fifth order.

An approximation for the second order sum contribution for an irregular wave will be derived first. For this purpose it is convenient to use a Hilbert transform, which introduces a ninety degrees phase shift into a signal. Thus the Hilbert transform of the linear record $\eta_L(t) = A(t)\cos\phi(t)$ is given by:

$$\eta_{LH}(t) = A(t)\sin\phi(t) \tag{5.3}$$

where the amplitude, A, is now assumed to be slowly varying in time. The double frequency contribution can be approximated in terms of the linear record and its Hilbert transform in the form:

$$\eta_2 = A^2\cos 2\phi = \left(\eta_L^2 - \eta_{LH}^2\right). \tag{5.4}$$

Similarly, the third order sum contribution is approximated as:

$$\eta_3 = A^3\cos 3\phi = \eta_L\left(\eta_L^2 - 3\eta_{LH}^2\right). \tag{5.5}$$

Note that Equations 5.4 and 5.5 are identical to the expressions given for D_{22} and D_{33} in Chapter 2 Section 2.5. The magnitudes of the second and third order sum contributions are now sought. A number of techniques could potentially be employed to find the coefficients

S_{22}/h and S_{33}/h^2 for use with Equations 5.4 and 5.5. The approach followed here involves estimating the linear contribution by accounting only for the second order corrections, and then performing a search to find the value of S_{22}/h that sets the skewness of the linearised time series to zero. From Equations 5.2 and 5.4 and neglecting the third order contribution (assuming this to be much smaller than the second order contribution), the linear time series can be approximated as:

$$\eta_L(t) \approx \eta(t) - \frac{S_{22}}{h}\left(\eta_L(t)^2 - \eta_{LH}(t)^2\right). \tag{5.6}$$

In order to proceed further it is necessary to make the assumption that the linear record and its Hilbert transform, η_L and η_{LH} in brackets on the right-hand side of Equation 5.6, are approximately equal to the entire measured record and its corresponding Hilbert transform (η and η_H) respectively. This is a reasonable assumption provided the terms in the Stokes expansion are ordered as $|\eta_L| >> |\eta_2| >> |\eta_3|$. Then:

$$\eta_L(t) \approx \eta(t) - \frac{S_{22}}{h}\left(\eta(t)^2 - \eta_H(t)^2\right). \tag{5.7}$$

To obtain η in these expressions the raw data must be high-pass filtered at some suitable cut-off frequency (found through a spectral decomposition of the signal) so as to remove any second order difference (set-down) contribution.

For our purposes here, skewness is most simply defined by the following summation over all data points:

$$\text{Skewness} = \frac{1}{N\sigma^3}\sum_{i=1}^{N}\eta_{Li}^3 \tag{5.8}$$

where σ is the standard deviation of the linear record.

The linear record defined by Equation 5.7 can be easily computed and the coefficient S_{22}/h that results in zero skewness can be found. Because of the variability associated with the New Year wave together with its highly nonlinear structure, it seems sensible to exclude the New Year wave when computing the coefficient S_{22} for the 1520 data. For comparison, S_{22} is computed for the 1520 data both including and excluding the New Year wave. The results yielded from the above analysis for the two Draupner data sets are given in Table 5.1.

Data set	S_{22} for zero skewness
Draupner 1620	1.022
Draupner 1520 (including freak wave)	1.351
Draupner 1520 (excluding freak wave)	0.959

Table 5.1: Table of second order coefficient values for the Draupner 1520 and 1620 wave records. Values are given to three decimal places.

Excluding the New Year wave, the two data sets have a comparable S_{22} coefficient for zero skewness (~ 1.0). The effect of including the freak wave in the 1520 data increases the size of the second order sum coefficient, S_{22}, by 41% (from 0.959 to 1.351). Surface elevation histograms have been plotted for the high-pass filtered 1520 and 1620 data (η) and the linearised data (η_L), which has been defined using Equation 5.7 together with the S_{22} values computed for zero skewness. Figure 5.5 shows both the histograms of the surface elevation records and their reflections about the origin to help illustrate the degree of skewness present in the data. The plots have been smoothed using a 29-point average to help reveal the underlying shapes. For the 1620 record all data points were considered, whereas for the 1520 record data points within a 45 second interval centred at the New Year wave were excluded. Upon linearising the data the histograms and their reflections are found to overlie almost exactly. If all of the 1520 data points are considered and a S_{22} value of 1.351 is used, the resulting surface elevation histogram and its reflection for the linearised data still show considerable mismatch. In the context of a short record of approximately 100 waves, the New Year wave is indeed extraordinary!

For comparison with Figure 5.3, Figure 5.6 shows a plot of ordered crest elevation against ordered trough depression for the linearised Draupner wave records, again computed using Equation 5.7 and the S_{22} values found for zero skewness. With the exception of the largest values in each ordered data set, the plots now show comparatively little asymmetry, deviating only slightly from the 1:1 line for all crest and trough sizes.

The reasoning behind the re-definition of the Stokes expansion coefficients outlined in Chapter 2 Section 2.5 is now explained. When approximating the nonlinear components in a measured wave record, the choice of the wavenumber κ is ambiguous. Some possibilities are: (1) Use a wavenumber value based on the peak frequency (i.e. the frequency of the most energetic waves); (2) Use a wavenumber value based on the mean zero-crossing frequency; (3) Use a local time-varying wavenumber value based on an instantaneous effective frequency at each point in the record. Here an alternative approach is used whereby a single κh (wavenumber-depth product) value is sought through a comparison of the S_{22}/h value computed for zero

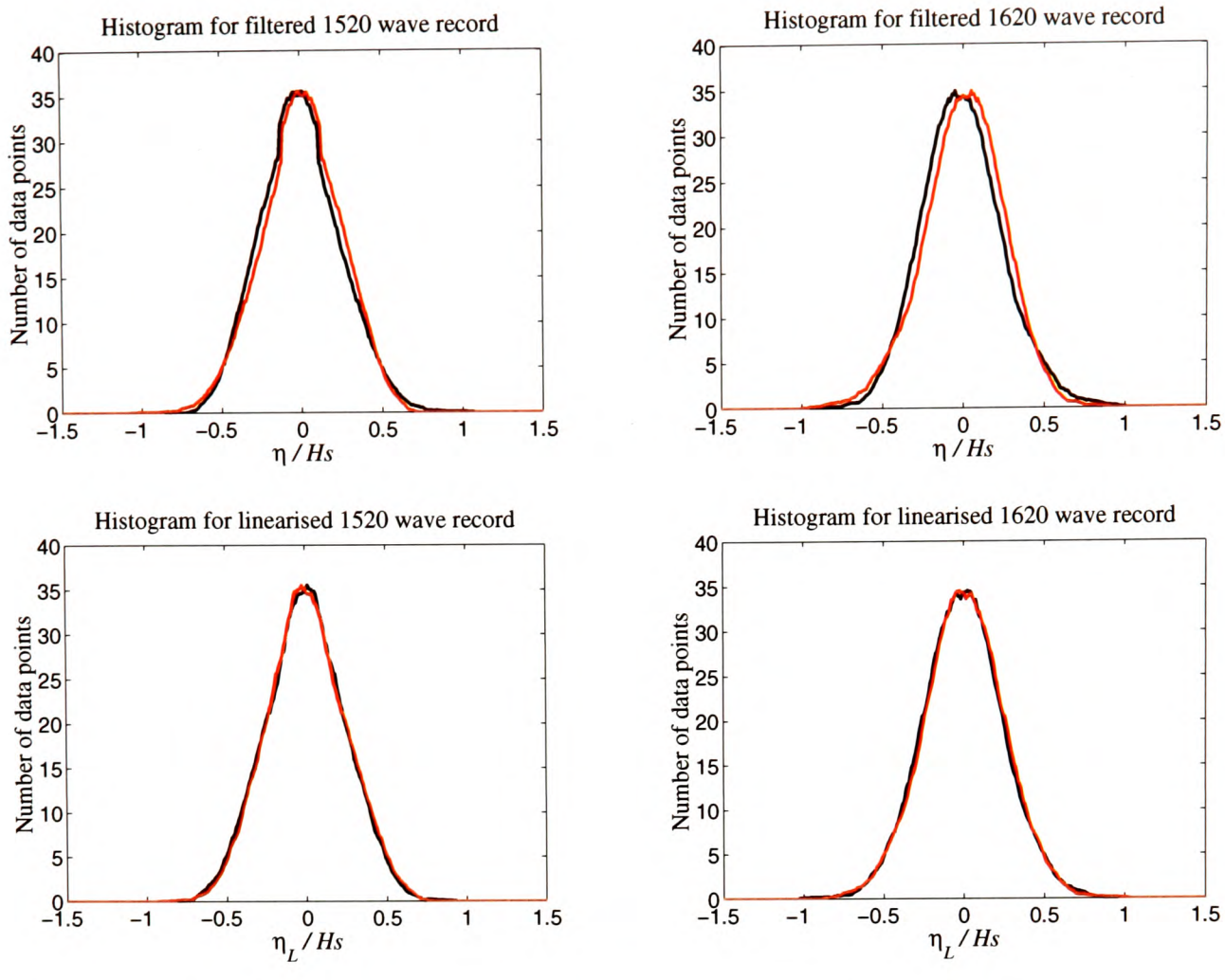

Figure 5.5: Surface elevation histograms (black lines) with their reflections about the origin superimposed on top (red lines) for the high-pass filtered data (η) and the linearised data (η_L). Surface elevation has been normalised by dividing through by the significant wave height, Hs. All data points have been considered except those within a 45 second interval around the New Year wave in the 1520 data.

skewness with the appropriate Stokes second order coefficient, as defined in Chapter 2. The computed value of κh can then be used to estimate the third order Stokes coefficient, S_{33}/h^2 (and higher order coefficients if required).

Upon estimating the S_{22}/h coefficients for zero skewness, it was found that a suitable κh value for use in the computation of the third order Stokes coefficient is 1.6. To help illustrate the reasoning for this decision, Figure 5.7 plots the variation of the theoretical Stokes coefficients, S_{22} and S_{33}, with κh, and also shows two horizontal lines corresponding to the values of S_{22} found for zero skewness (the horizontal line drawn for the 1520 data is for the case where the New Year wave has been excluded). From this figure it is clear that, for this particular water depth (70m), both the second and third order coefficients, S_{22} and S_{33}, are relatively insensitive to the exact κh value used in the calculation. A κh value of 1.6 corresponds to the minimum of the S_{22} curve and a wave period of 13.8 seconds; which is sufficiently close to the average wave period, T_Z, of 12.5 seconds for such a wavenumber to be deemed reasonable.

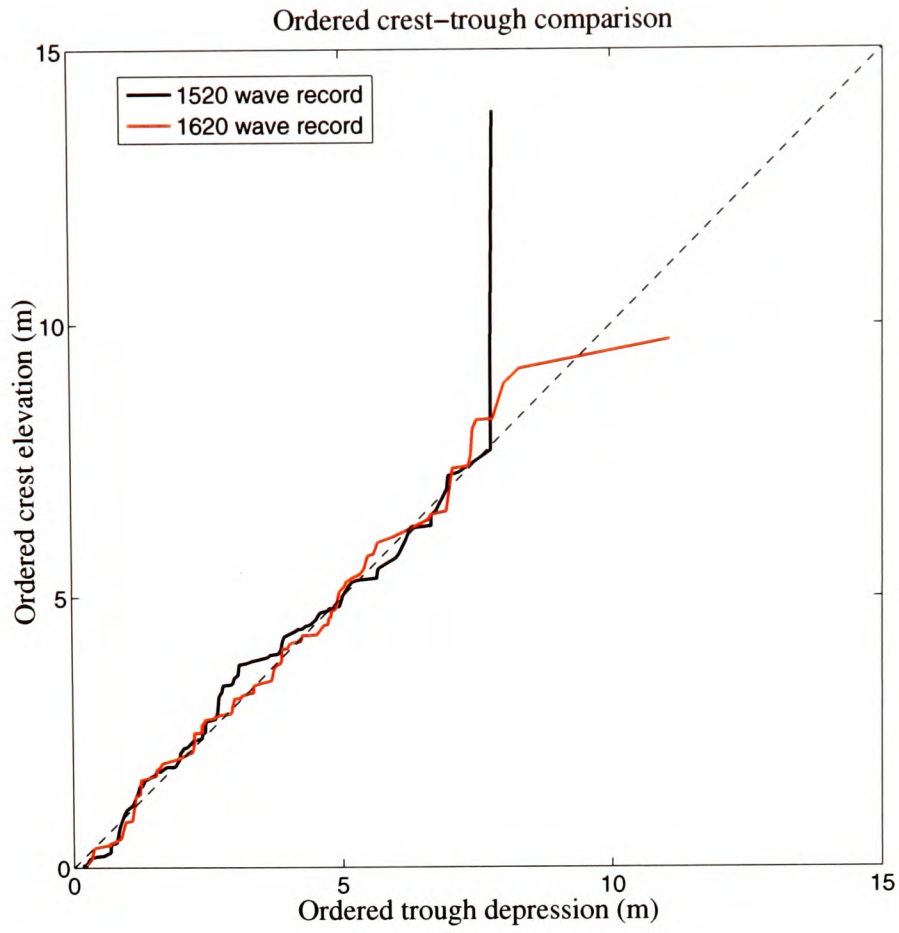

Figure 5.6: Ordered crest elevation plotted against ordered trough depression for the linearised Draupner 1520 and 1620 wave records. A 1:1 line is shown (dashed line).

The choice of a suitable wavenumber will be considered further later when discussing exact second order wave theory.

Using a κh value of 1.6, the second and third order sum coefficients, S_{22} and S_{33}, are found to be 1.10 and 1.57 respectively (using Equations 2.81 and 2.83, Section 2.5 Chapter 2). Hence the first three terms in the Stokes wave expansion for the Draupner data can be approximated as:

$$\eta(t) = A\cos\phi(t) + \frac{1.10}{70}A^2\cos 2\phi(t) + \frac{1.57}{70^2}A^3\cos 3\phi(t). \tag{5.9}$$

The slight discrepancy between the values of S_{22} found for zero skewness ($S_{22} \sim 1.0$) and the value computed using $\kappa h = 1.6$ ($S_{22} = 1.10$) can be attributed to the relatively small effect of directional spreading on the magnitude of second order sum contributions (Forristall 1999). This effect will be considered further in Chapter 8 Section 8.2.8 for the experimental data.

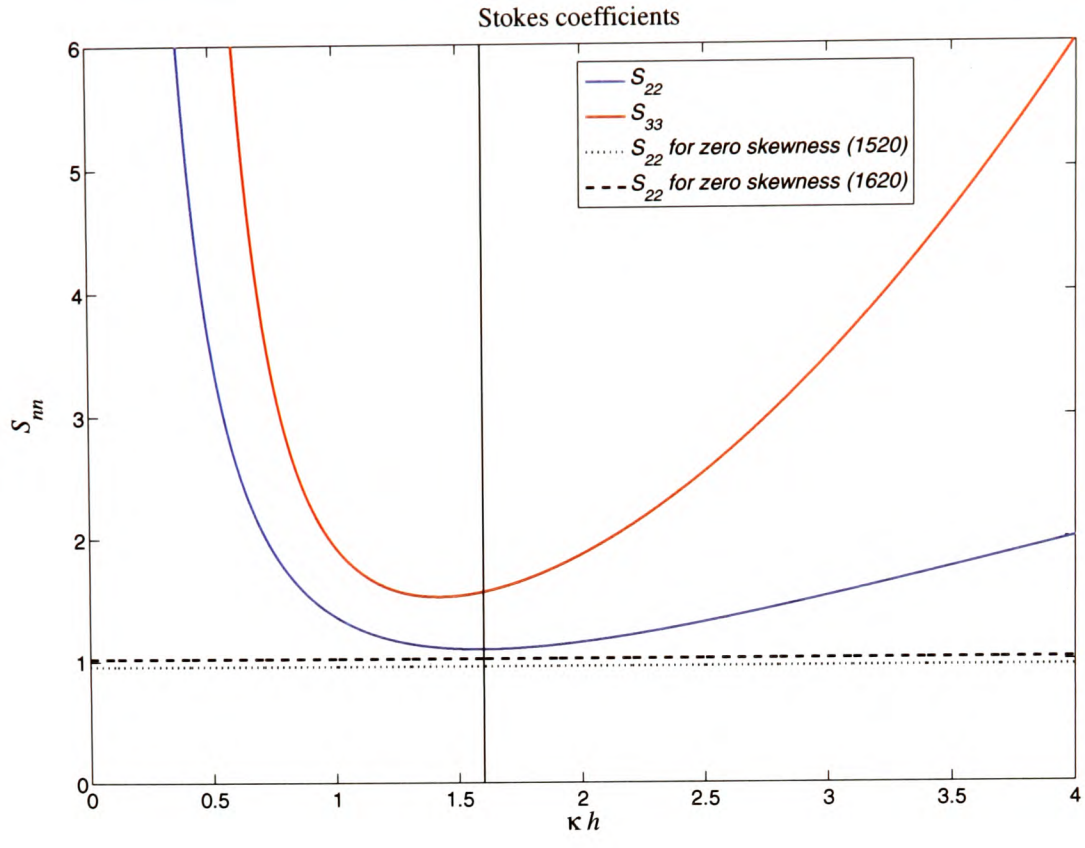

Figure 5.7: Stokes second and third order sum coefficients, S_{22} and S_{33}, plotted against κh. Horizontal lines are shown corresponding to the S_{22} values computed for zero skewness. A vertical line is drawn at $\kappa h = 1.6$.

5.6 Fifth order NewWave

When the linear NewWave profile is compared against the New Year wave profile, considerable mismatch is found. The NewWave model is now modified to include nonlinear corrections up to fifth order using the theory outlined in Chapter 2 Section 2.5; modified versions of the Stokes coefficients defined by Fenton (1990) are used and suitable expressions for the temporal contributions for all nonlinear terms up to fifth order have been derived using the linear wave record and its Hilbert transform. For the estimation of the Stokes coefficients $\kappa h = 1.6$ has again been used. Figure 5.8 plots the fifth order NewWave profile together with its first, second and third order contributions (fourth and fifth order contributions have been excluded as they are too small to clearly illustrate graphically). Figure 5.8 also shows a comparison between the fifth order NewWave and the New Year wave. A linear NewWave amplitude of 14.7m is used as this corresponds to an amplitude of 18.5m in the fifth order corrected NewWave profile, matching the amplitude of the measured New Year wave. This comparison does not incorporate any representation of the second order difference contribution, which is discussed in Sections 5.8, 5.9 and 5.10.

The effects of including nonlinear contributions are largely as one would expect; the crests become narrowed and raised, while the troughs are broadened and raised. Predictably, the

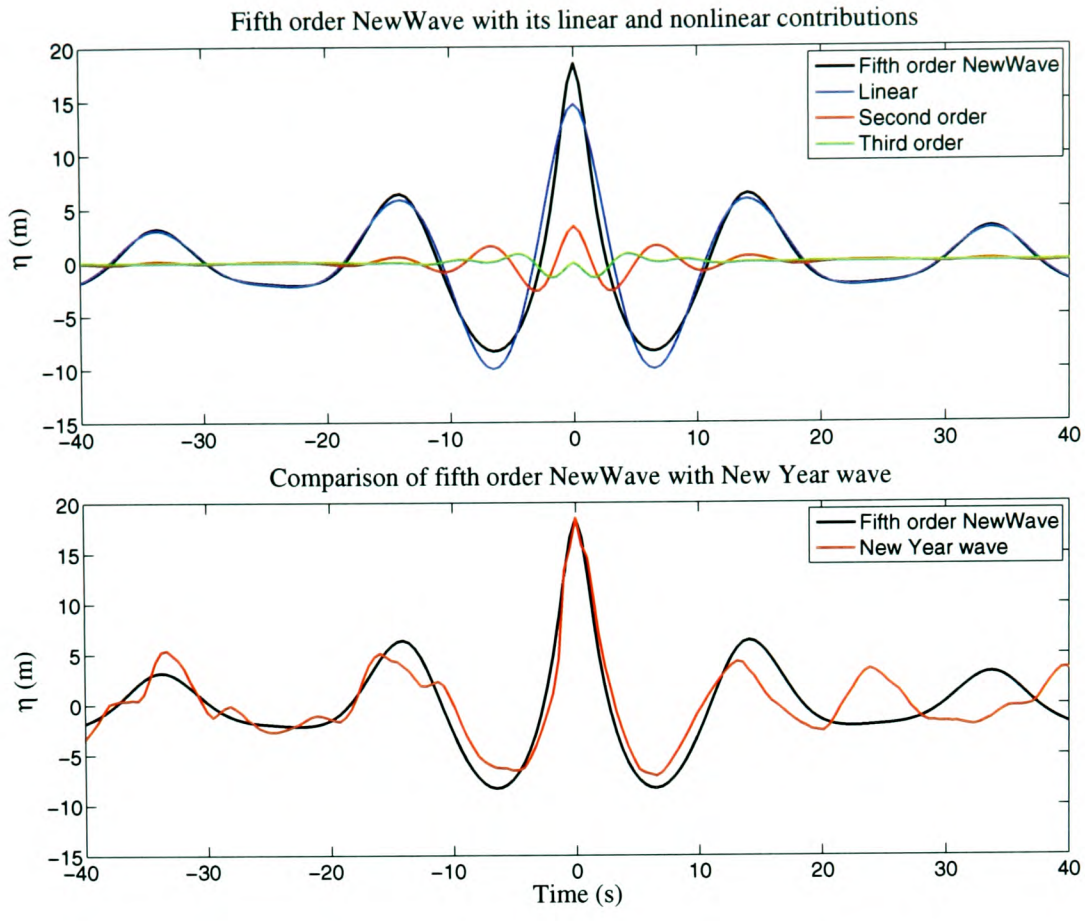

Figure 5.8: A comparison of the fifth order NewWave profile with its constituent contributions (first, second and third order only) and the New Year wave.

size of the nonlinear contributions decreases rapidly as the order increases. Beyond second order, the effects of non-linearity are most pronounced close to the apex of a crest; the crest is sharpened further. Quantitatively, by including nonlinear corrections up to fifth order, the peak crest of the NewWave profile has been raised by 26% (from 14.7m to 18.5m) whereas the deepest troughs have been raised by 17% (from 10.0m to 8.3m). The agreement between the fifth order NewWave profile and the New Year wave profile close to the peak is surprisingly good, with the broad banded nature of the freak wave being captured quite well. The troughs either side of the peak crest are still predicted to be too deep; the actual trough depths are 6.5m and 7.1m. Hence the New Year wave is slightly broader banded, having shallower troughs and lower crests adjacent to the main peak.

Assuming the standard Rayleigh distribution for linear crest amplitude and taking the linear crest amplitude to be 14.7m, it is found that the New Year wave is approximately a 1 in 2×10^5 wave for this particular sea state (with a significant wave height of $\sim$ 12m).

5.7 Spectral decomposition

Spectral analysis will now be used to assist in decomposing a wave record into its constituent components. The Draupner 1520 data set will be considered here.

It is obviously difficult to identify the frequency range over which the linear and higher order contributions are significant. Hence it is useful to decompose the data in the time domain into its constituent components and then Fourier transform each component individually to obtain estimates for the isolated spectral contributions. Spectra for the estimated second order difference, second order sum and third order sum contributions are now examined.

Approximations for the temporal contributions to the second and third order sum terms are defined in Equations 5.4 and 5.5. An approximation for the second order difference contribution can be obtained using the ideas of multiple-scales analysis (Bender and Orszag 1978) to specifically define $A(t)$ to be a slowly varying function of time with a time scale comparable to the second order difference contribution, and $\phi(t)$ to be a fast phase variation. As for the second and third order sum contributions, the slowly varying envelope function $A(t)$ can be expressed in terms of the linear record and its Hilbert transform as:

$$A(t) = \sqrt{\eta_L(t)^2 + \eta_{LH}(t)^2}. \tag{5.10}$$

The spectrum of the wave envelope defined by Equation 5.10 can be used to estimate the frequency range of the second order difference contribution.

The overall wave spectrum and estimated spectra for the second order difference, second order sum and third order sum contributions are shown in Figure 5.9. In order to remove some of the statistical variability in the data, smoothed spectra have been produced using a 15-point running average. This averaging process causes a slight broadening of the spectra. The aim here is to separate the various contributions in the frequency domain and to find the range of frequencies over which each contribution is present. Therefore, true power values are not of interest and so the vertical scale for each spectrum has been normalised such that the maximum peak of each is unity.

As is shown in Figure 5.9, the approach outlined clearly identifies the range of frequencies over which each contribution is present and hence has been a success. In addition, the spectral decomposition undertaken helps to partly justify the narrow-banded Stokes-type treatment adopted in this study since the second order difference, second order sum and third order sum contributions are reasonably well separated in frequency.

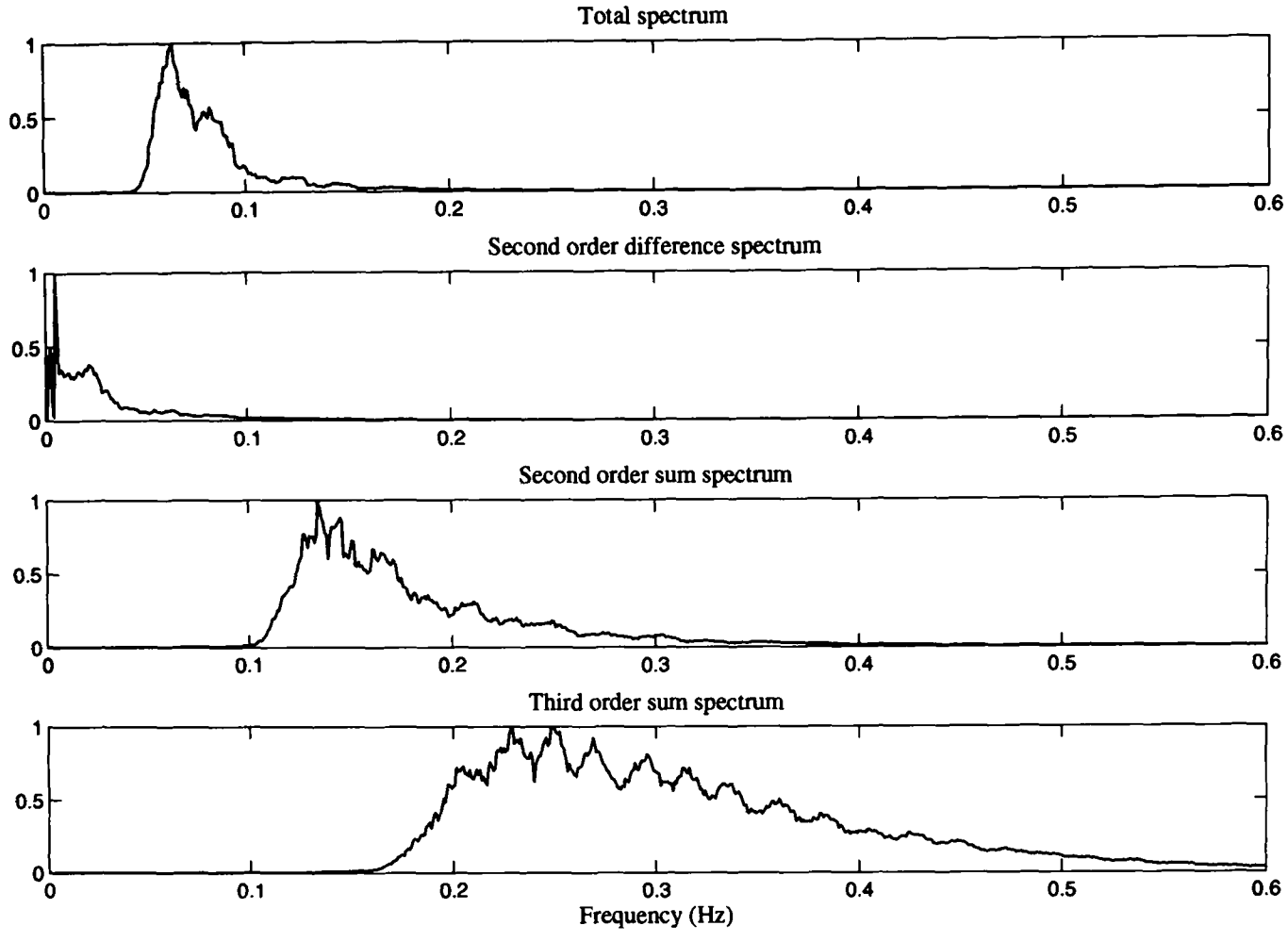

Figure 5.9: Smoothed power spectra for the Draupner 1520 wave record.

5.8 Second order difference contribution

The second order difference contribution is now investigated for the largest waves in the two Draupner wave records. From a spectral decomposition of the data (as shown above for the 1520 data), it is found that the second order difference contribution can be extracted by low-pass filtering the data at 0.04Hz (for both the 1520 and 1620 data) - i.e. set all frequency components above this cut-off value to zero. This cut-off frequency has been chosen so as to maximise the second order difference contribution and minimise the linear contribution that is passed through the filter. Time series plots for the largest waves in the Draupner 1520 and 1620 data sets together with their computed second order difference contributions for three different filtering frequencies are shown in Figure 5.10.

For the largest wave in the 1620 data, the second order difference contribution is found to have a negative value (i.e. there is a set-down in the second order difference contribution) and this set-down remains for progressively lower filtering frequencies. This is what one would expect for a large free wave on the open sea and is observed for all large waves (largest 10%) analysed in the two Draupner data sets, with the exception of the New Year wave. The second order

difference contribution to the New Year wave exhibits a substantial set-up (i.e. has a positive value), which is entirely unexpected. One might conclude that some linear contribution must have passed through the filter causing the apparent set-up. However, this hypothesis is soon dispelled through low-pass filtering at progressively lower frequencies, where one still finds the set-up present. No explanation of this anomalous behaviour can be offered at this time.

It is worth noting that the peak second order difference contribution to a wave will not necessarily coincide exactly with the occurrence of the wave peak, and this is illustrated in Figure 5.10 for the largest wave in the 1620 data. The reason for this is that the peak second order difference contribution will occur at the instance of the maximum in the envelope signal, $A(t)$, rather than the maximum of the higher frequency signals constrained by the envelope.

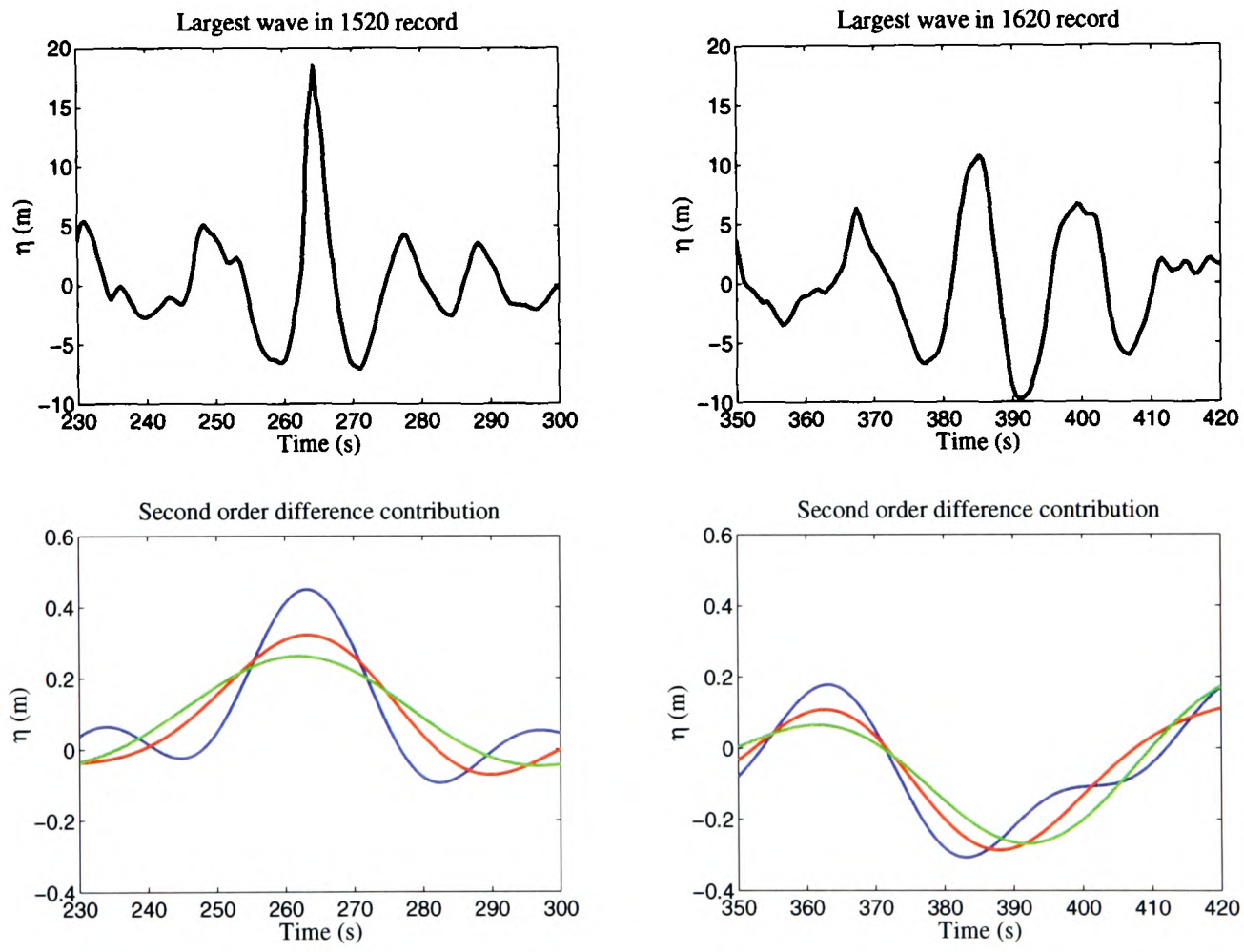

Figure 5.10: Time series plots for the largest waves in the Draupner 1520 and 1620 wave records together with their second order difference contributions (positioned beneath) for three different filtering frequencies; 0.04Hz (blue line), 0.03Hz (red line) and 0.02Hz (green line).

5.9 Second order difference model

As a first approximation to the second order difference contribution the following equation can be used (Dean and Dalrymple 1991):

$$\eta_{2-} = -\frac{A^2\kappa}{2\sinh 2\kappa h}. \tag{5.11}$$

This equation represents the wave self-interaction component of the total second order difference contribution (see Equation 2.103 Chapter 2 Section 2.6). The envelope function in this approximation can be defined using Equation 5.10 so long as the mean square value of this function is removed. Hence an approximation for the second order difference contribution is given by:

$$\eta_{2-} = -\frac{\kappa}{2\sinh 2\kappa h}\left(A^2 - \overline{A^2}\right). \tag{5.12}$$

Figure 5.11 compares the low-pass filtered second order difference contribution (using a cut-off frequency of 0.04Hz) to the Draupner 1520 data with the approximation defined by Equation 5.12. In Figure 5.11 the vertical scale of the approximation is arbitrarily set to allow the set-down predicted for the New Year wave to have the same magnitude as the actual set-up found in the data.

This very crude long wave approximation has managed to capture the position of most of the long bound wave set-ups and set-downs in the filtered profile. Note the alignment of the deepest set-down at $\sim$ 1170 seconds, corresponding to the time of occurrence of the second largest wave in the 1520 record. However, close to the New Year wave at $\sim$ 265 seconds there is a complete mismatch. As is clear from the figure, no suitable scaling factor can be found to allow all the peak values to be reproduced exactly.

5.10 Exact second order wave theory

Exact second order wave theory, as outlined by Dean and Sharma (1981) and more recently by Dalzell (1999), is now used to help assess the magnitude and character of the second order difference contribution further. In addition, to help validate the approximation procedure for nonlinear contributions implemented in this study, comparisons are made between the second order sum contribution computed using exact second order wave theory and that approximated in terms of the linear record and its Hilbert transform.

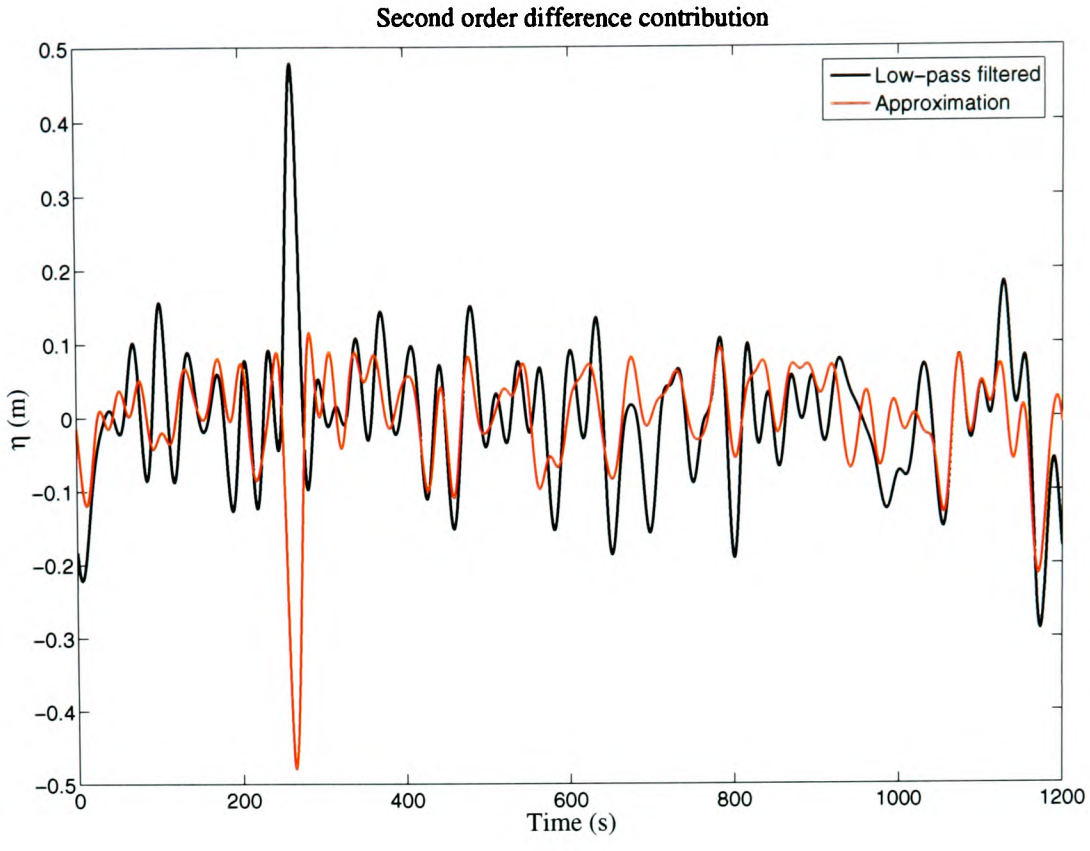

Figure 5.11: Approximation for the second order difference contribution to the Draupner 1520 wave record.

The second order equations given by Dalzell (1999) for two linear wave components are defined in Chapter 2 Section 2.6. From measured spectra, second order contributions based on NewWave profiles for both the Draupner 1520 and 1620 data sets have been computed using Equation 2.2 and Equations 2.103 to 2.107. Equations 2.103 to 2.107 are defined for two linear wave components and so a simulation of a NewWave surface profile defined by N linear components involves the summation of N second order Stokes waves (i.e. summing over j from 1 to N in terms 1 to 3 in Equation 2.103) together with the summation of the $O(N^2)$ wave-wave interaction components (terms 4 and 5 in Equation 2.103) for all possible pairs of different linear wave components.

As before, the largest waves in the Draupner 1520 and 1620 data sets are considered here. The linear amplitude of each wave is taken to be the linear NewWave amplitude required to produce a fifth order NewWave amplitude equal to the total wave amplitude (as is illustrated in Figure 5.8 for the New Year wave). Assuming unidirectional wave motion, Figure 5.12 shows the second order sum and difference contributions to each wave calculated using exact second order wave theory. These second order contributions are compared with an approximation for the second order sum contribution (Equation 5.4 together with the coefficient S_{22}/h computed using $k = 1.6/h$) and the low-pass filtered second order difference contribution (obtained using a cut-off frequency of 0.04Hz). Table 5.2 summarises these comparisons.

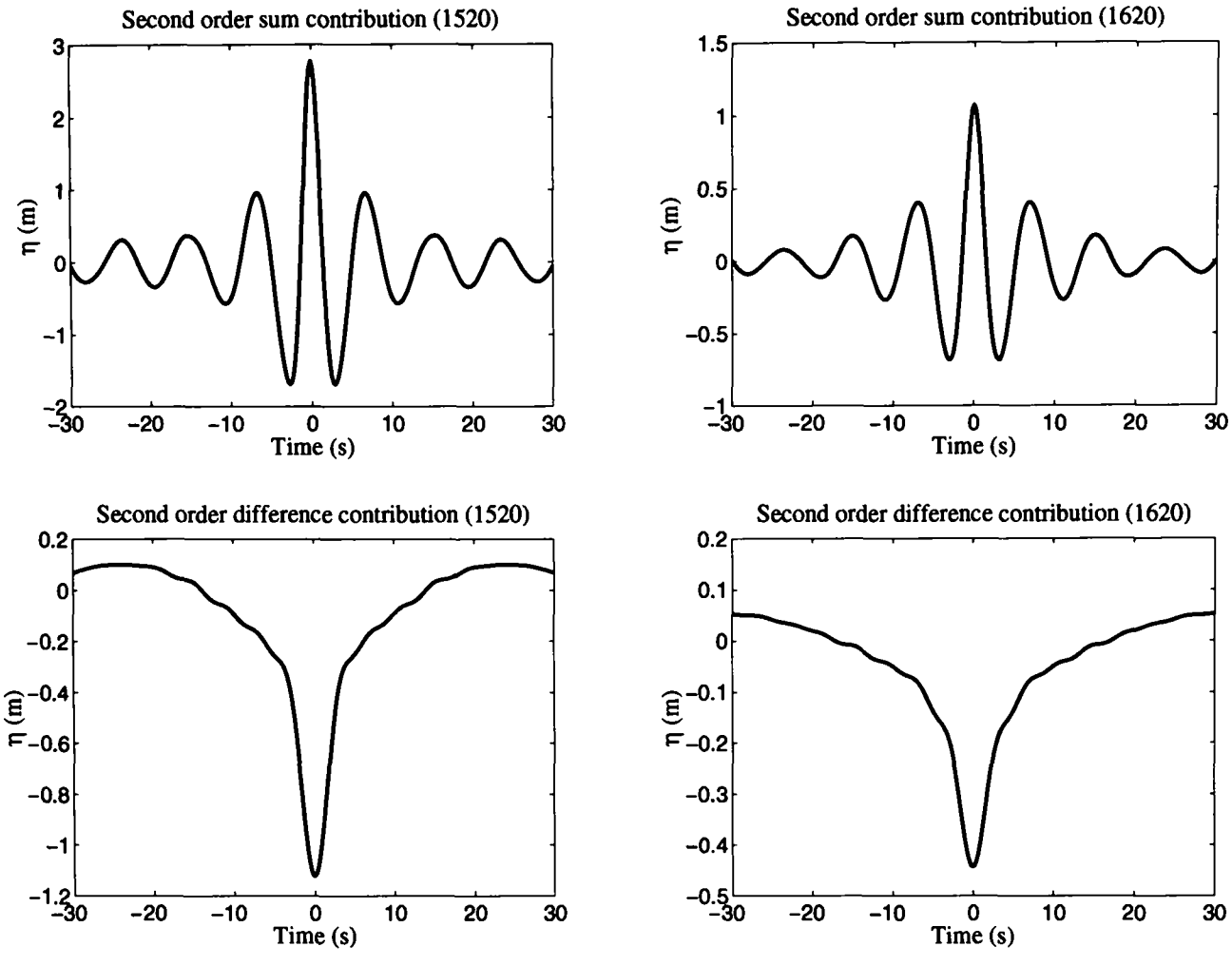

Figure 5.12: Second order sum and difference contributions for the largest waves in the Draupner 1520 and 1620 wave records calculated using exact second order wave theory.

Wave	η_{2A+}	η_{2T+}	η_{2F-}	η_{2T-}
Largest wave in 1520 record	+2.82	+2.77	+0.48	-1.12
Largest wave in 1620 record	+1.13	+1.07	-0.34	-0.44

Table 5.2: Table comparing second order contributions for the largest waves in the Draupner 1520 and 1620 wave records. η_{2A+} is the second order sum approximation; η_{2F-} is the filtered second order difference contribution; η_{2T+} and η_{2T-} are the second order sum and difference contributions respectively calculated using exact second order wave theory. Values given are in metres (m).

For both data sets the second order sum approximation, η_{2A+}, agrees very well with the value computed using full second order wave theory, η_{2T+}; to one decimal place the values agree exactly. Using the values in Table 5.2 the second order sum coefficients, S_{22}, computed using exact second order wave theory are found to be 0.90 and 0.87 for the Draupner 1520 and 1620 data sets respectively. These values are close to those computed earlier for zero skewness ($S_{22} \approx 1$). This comparison helps to validate the approximation procedure adopted in this study, namely to express all nonlinear contributions in terms of the linear wave record

and its Hilbert transform. The agreement here also confirms that it was reasonable to define $\kappa h = 1.6$ for the calculation of the Stokes coefficients.

The second order difference contribution to the largest wave in the 1620 data defined by exact second order wave theory, η_{2T-}, is relatively close to the low-pass filtered value, η_{2F-}, observed in the data. The discrepancy can perhaps be attributed to directional spreading of the linear wave components, which is known to reduce the magnitude of the second order difference set-down beneath an energetic group (Forristall 1999). In stark contrast, for the New Year wave, a set-down of -1.12m is predicted by second order wave theory although the data exhibits a set-up in the apparent second order difference contribution of +0.48m. An observed set-up in wave measurements around a large structure could be attributed to nonlinear wave diffraction, but since the Draupner platform is a steel space-frame structure this explanation is unlikely to be valid here. Whilst a broadening of the spectral peak during a sufficiently steep focus event is well known to occur due to third order Benjamin-Feir wave-wave interactions (Yuen and Lake (1982), Peregrine (1983), Baldock et al. (1996)), filtering of the low frequency wave components in the measured wave record with progressively lower cut-off frequencies (0.04, 0.03, 0.02Hz) shows that this set-up is a robust feature remaining at very low frequencies. To the author's knowledge, this study is the first to identify such anomalous behaviour in this extraordinary wave.

5.11 Conclusions

Field data from the North Sea has been used to explore the shapes of large ocean surface waves. NewWave has been proposed as a good model for the linear contribution to large waves. Stokes-type corrections have been used to approximate the nonlinear bound harmonics present, and a technique has been developed that enables the magnitude of the second and higher order contributions to a wave record to be estimated.

Unique features of the Draupner New Year wave have been identified, distinguishing it from a typical large wave. A fifth order NewWave profile reproduces the New Year wave reasonably well close to the peak, although is still too narrow banded. By linearising the New Year wave profile, its probability of occurrence is estimated to be 1 in 2×10^5 waves - an unlikely but obviously not impossible event in a record containing approximately 100 waves!

As one would expect for a large wave in the open sea, exact second order wave theory predicts a large set-down in the second order difference contribution to the New Year wave. The field data exhibits an anomalous set-up for the New Year wave, whereas all the other large waves

show a local set-down. Unexplained behaviour such as this prompts the suggestion that new physics, not incorporated in standard approaches to offshore engineering design, is likely to have played an important role in the generation of this freak wave. The suggestion of such new physics has initiated plentiful debate and research internationally, although further work pursuing this unknown physics lies beyond the scope of this project brief.

Chapter 6

Linear diffraction results

6.1 Introduction

This chapter presents linear diffraction results generated using the analytical solution of Linton and Evans (1990b) and the numerical diffraction code DIFFRACT. Both the analytical and numerical solutions have been extensively verified against published data and some of the comparisons made are presented in this chapter.

The effect of the LUNA caisson on the linear diffracted wave field around the structure is studied using DIFFRACT. The diffraction of incident regular waves by arrays of bottom mounted cylinders is then considered. The phenomenon of near-trapping (Section 1.2.6 Chapter 1) is studied for both linear arrays of cylinders and the LUNA four-cylinder array. The effect of the LUNA caisson on near-trapping is also examined.

Analytical linear diffraction theory is extended for application to incident NewWaves. The diffraction of an incident NewWave by an array of bottom mounted cylinders is considered, with a particular emphasis on force and free surface magnification effects. Through the generalization of linear NewWave diffraction theory, a simplified expression is used to calculate the maximum free surface elevation at any point in the vicinity of a diffracting body for a given incident NewWave.

Finally, the effect of directionally spreading an incident wave field on the resulting diffracted wave field in the vicinity of the LUNA structure is considered.

Only linear diffraction results are presented in this chapter. Further linear results for the LUNA structure are presented in Chapter 8, where comparisons are made with the experimental data. Second order diffraction results are presented in Chapter 7.

6.2 SOLUTION VERIFICATION

Many comparisons with published data have been made to confirm the accuracy of the computer code implementing the analytical diffraction solution, two of which are presented in this section. As discussed in Chapter 3, the DIFFRACT code has been extensively implemented at first order for a single cylinder. However, in order to address the objectives of the current study, DIFFRACT has been applied to four cylinder arrays and hence it is important to compare the results generated against published data and/or a validated analytical solution. One comparison between the DIFFRACT solution and the analytical solution is presented.

Firstly, force results generated using the analytical solution are compared with results published by Linton and Evans (1990a). The particular case considered is an array of four bottom mounted cylinders arranged at the vertices of a square of side length R (=$2d$). The various parameters for the test case are $a/d = 0.5$ and $\beta = \pi/4$, where a is the cylinder radius and β is the incident wave angle (shown in Figure 3.1 Chapter 3). The cylinders are numbered clockwise from 1 to 4 and are positioned at $(-d, d)$, (d, d), $(d, -d)$ and $(-d, -d)$ respectively, so that the forces in the direction of wave advance on cylinders 1 and 3 are identical. Figure 6.1 shows the non-dimensional force in the direction of wave advance, X, plotted against κa. The force has been non-dimensionalised by dividing through by F, defined in Chapter 3 Section 3.2.3, Equation 3.29. The force responses show good agreement with a correction published by Linton and Evans (1990a) to their original paper (Linton and Evans 1990b); the plots in the original paper were inaccurate due to an insufficient number of data points being used to represent them. Note how interaction effects between the cylinders can be extremely important in determining the amplitude of the first order force. These effects are examined in this Chapter.

A further test of the analytical solution is now performed that examines the free surface elevation in the local vicinity of a square four-cylinder array, away from the surface of the cylinders. A comparison is made with results produced by Ohl et al. (2001a) for the test parameters: $a = 0.203$m, $R = 0.812$m ($R/a = 4$), $\kappa = 2.58\text{m}^{-1}$ ($\kappa a = \pi/6$), $\beta = 0$. The free surface elevation has been non-dimensionalised by dividing by the linear wave amplitude, A. A contour plot and three-dimensional surface plot for the surface elevation in the vicinity of the cylinder array are given in Figure 6.2. These plots show excellent agreement with the wave field presented by Ohl et al., which was also generated using analytical linear diffraction theory. The cylinders are excluded from the surface plot in Figure 6.2 to help provide an improved view of the linear wave field around the array.

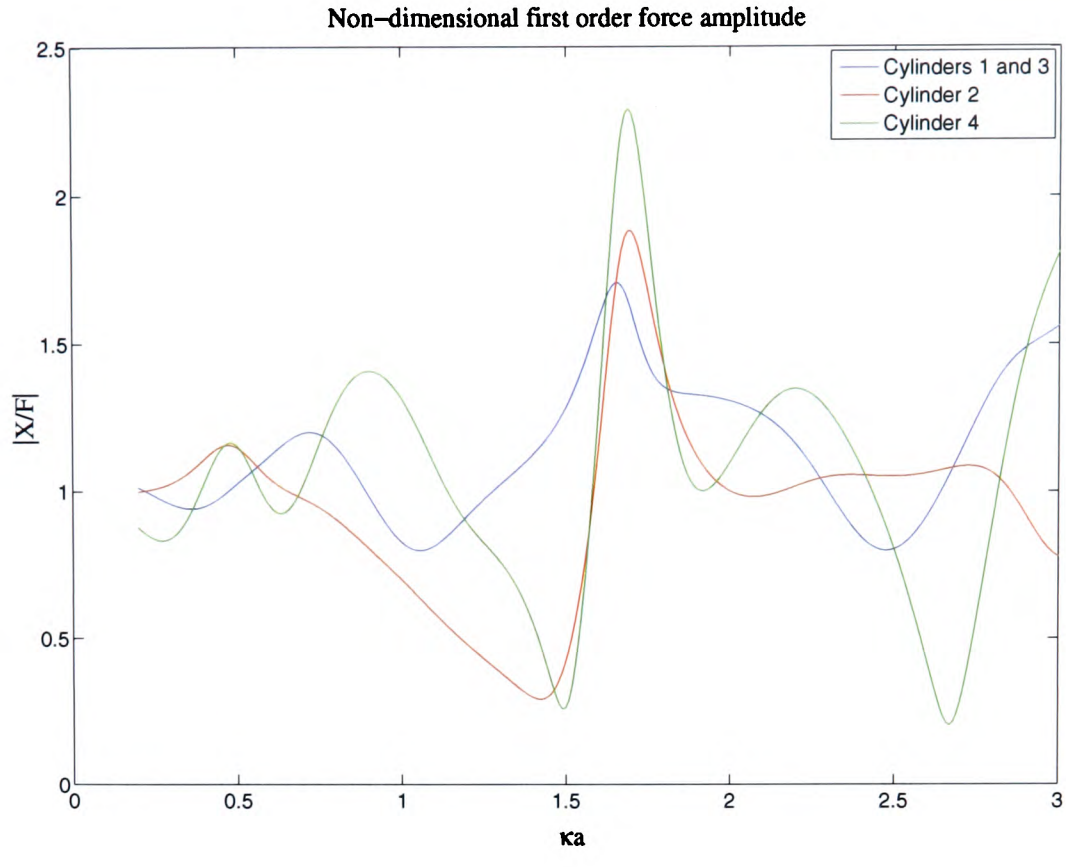

Figure 6.1: Non-dimensional amplitude of the first order force in the direction of wave advance for a group of four cylinders arranged at the vertices of a square. $a/d = 0.5$; $R/d = 2$; $\beta = \pi/4$.

A comparison between the analytical and numerical diffraction solutions is now presented. For this purpose, the free surface runup around a square four-cylinder array is computed. The cylinder configuration and wave field considered correspond to that used by Malenica et al. (1999) in their study of second order near-trapping, which is examined further in Chapter 7. The parameters for the test are: $R/a = 4$, $\kappa a = 0.468$, $\beta = \pi/4$. Figure 6.3 shows the magnitude of the non-dimensional runup around each cylinder generated using both the analytical and numerical solutions plotted against θ, where θ is measured positive anticlockwise from the positive x-direction. The cylinders are now numbered clockwise from 1 to 4 and are positioned at (d, d), $(d, -d)$, $(-d, -d)$ and $(-d, d)$ respectively, which corresponds to the quadrant numbering used by DIFFRACT. The analytical and numerical results show very close agreement, confirming the accuracy of the numerical solution procedure at first order. The meshing scheme used to produce the numerical results is described in Section 7.2 Chapter 7.

For each comparison presented in this section excellent agreement has been found. Many further comparisons have been made with published data and between the analytical and numerical solutions and similarly close agreement is found. It is thus reasonable to assume that the codes implementing the analytical and numerical solutions are generating an accurate representation of the linear diffracted wave field for a given cylinder array.

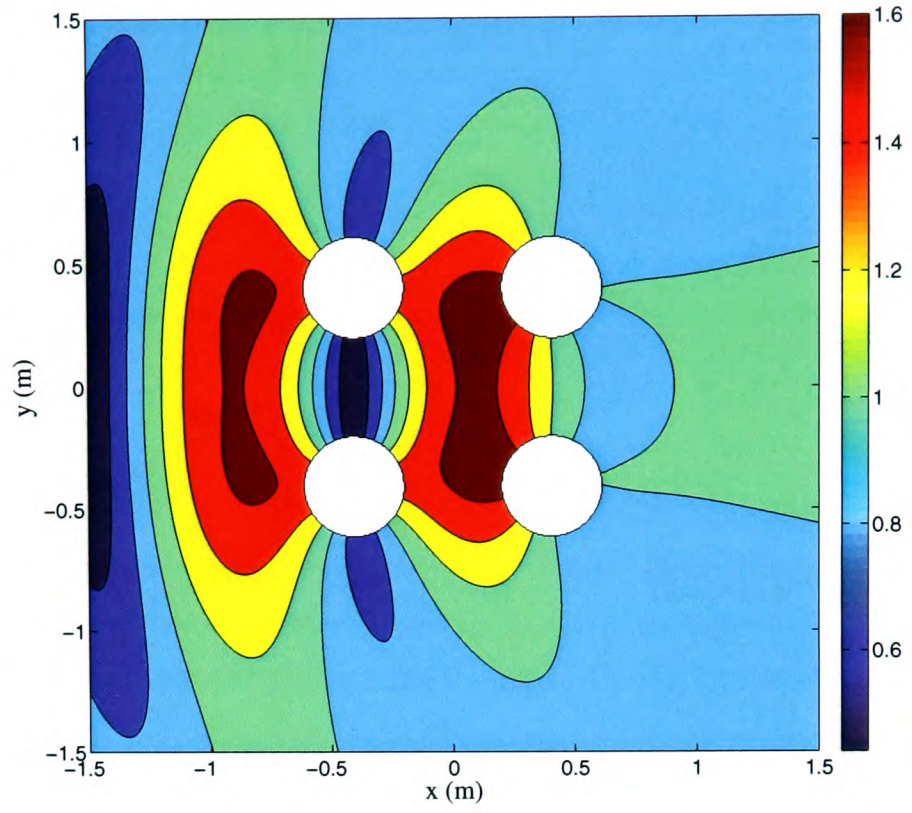

(a) Contour plot

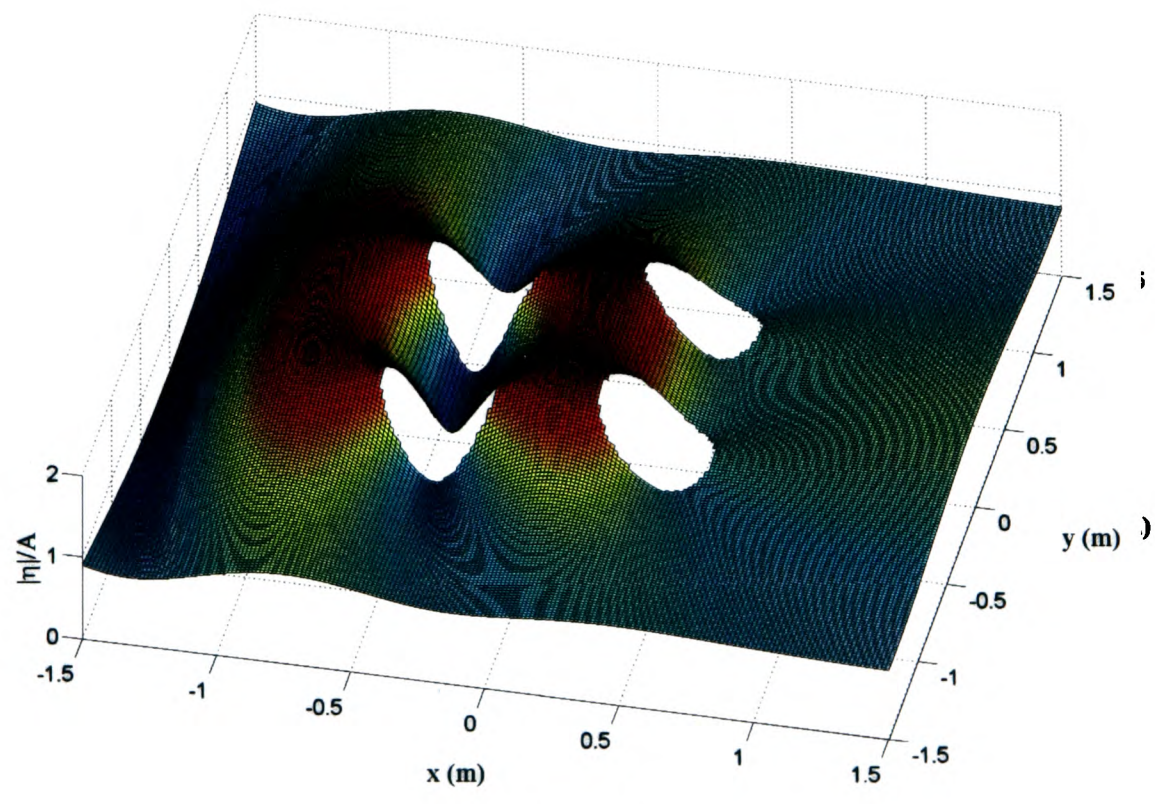

(b) Surface plot

Figure 6.2: Non-dimensional linear surface elevation around an array of four cylinders. $a = 0.203\text{m}$; $R = 0.812\text{m}$; $\kappa = 2.58\text{m}^{-1}$; $\beta = 0$.

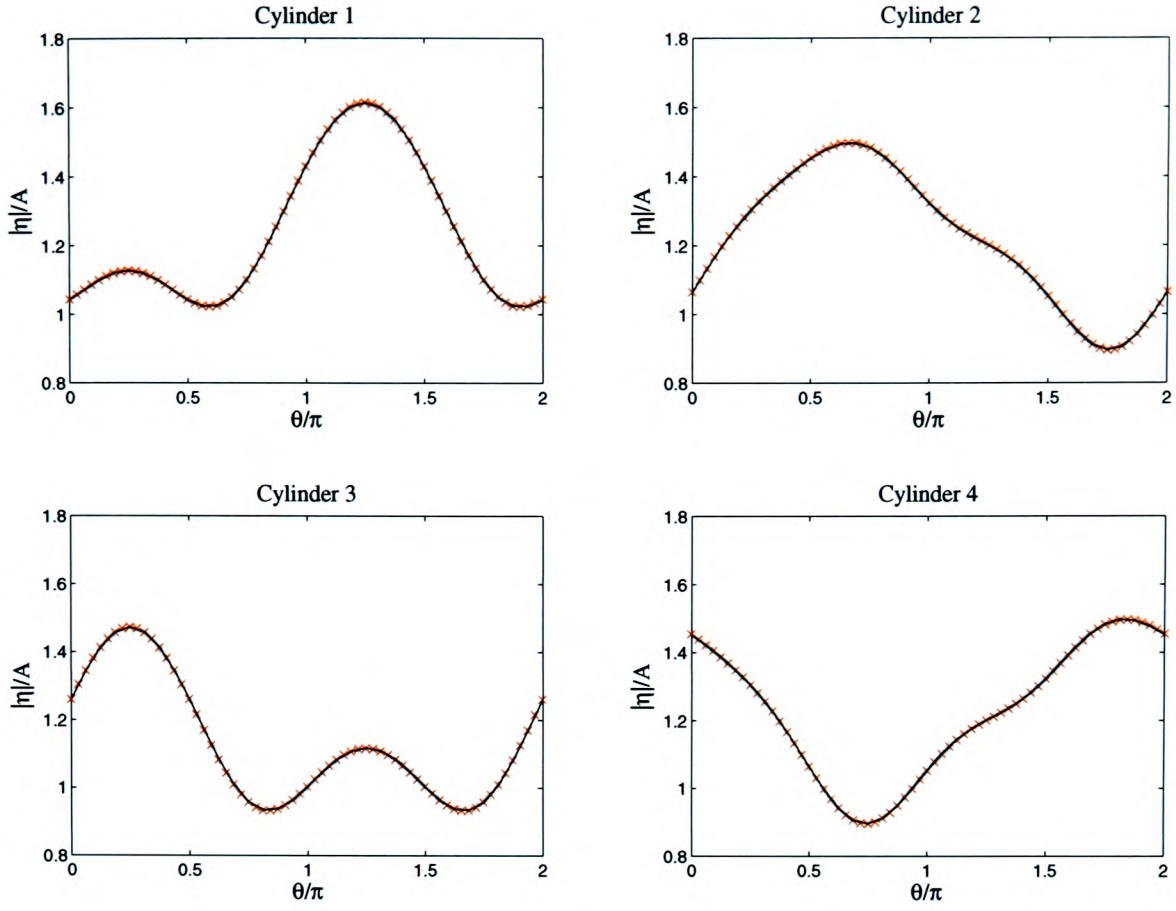

Figure 6.3: Non-dimensional first order runup around an array of four cylinders. $R/a = 4$; $\kappa a = 0.468$; $\beta = \pi/4$. Black solid line: analytical solution. Red crosses: numerical solution.

Together with the model test data, which are discussed in Chapter 8, the linear diffraction solutions are now used to investigate in detail the linear diffraction effects around structures supported by arrays of columns, with a particular emphasis on the LUNA platform geometry.

6.3 Effect of caisson

The effect of caisson height, h_c, on the linear free surface magnification in the vicinity of the LUNA structure (described in Chapter 4) is now examined. Unfortunately no model tests were performed for waves incident upon the caisson or cylinders alone. Therefore, DIFFRACT must be used to study the effect of the caisson on the overall linear diffracted wave field. The reader will recall that the analytical diffraction solution is only applicable to wave interaction with bottom mounted vertical cylinders and hence cannot be used here.

The effect of the caisson is likely to depend on the frequency of the incident waves. Three regular wave frequencies, chosen from the wave conditions specified for the irregular wave model test, will be considered in this section, namely:

- f=0.01Hz - this corresponds to a long incident wave (wavelength = 2.2km) that has a frequency comparable to the second order difference term.

- f=0.07Hz - this corresponds to the peak period for the 100-year sea state (wavelength = 270m).

- f=0.2Hz - this corresponds to a short incident wave (wavelength = 39m) that has a frequency comparable to the higher order harmonics (second order and above).

Wave-structure interaction in the absence of the caisson (i.e. h_c=0) is analysed, together with the whole structure (caisson with four cylinders mounted on top) for five caisson heights (h_c= 5, 10, 15, 20 and 25m). For each case the linear magnification along the x-axis is computed at 5m increments for -60m< x <60m (which almost extends along the full x-length of the caisson, 121.03m). The effect of the caisson beyond this x-range is not of interest for airgap design.

The same size elements are used in the meshing of the structure for each caisson height and tests have been carried out to ensure that converged results have been obtained. A comprehensive discussion of meshing and convergence is given in Chapter 7.

Figure 6.4 shows plots of linear surface magnification along the x-axis for incident frequencies 0.01Hz and 0.07Hz and each considered caisson height. For short incident waves (f=0.2Hz) the caisson height is found to have no distinguishable effect on the linear surface magnification along the x-axis.

From Figure 6.4 the caisson height is found to have a very small effect on the diffracted wave field for long incident waves (f=0.01Hz). In contrast however, caisson height has an appreciable effect on the diffracted wave field for incident regular waves at f=0.07Hz. The following changes are associated with an increase in caisson height for this frequency: (i) For $x >\sim -35$m the linear magnification is increased; (ii) For $x <\sim -35$m the linear magnification is reduced; (iii) The peak surface magnification is increased and shifted downstream.

The large surface enhancements caused by the caisson at f=0.07Hz could possibly be accompanied by a strong reflection upstream which, because of the phasing, causes destructive interference, hence explaining effect (ii) above. For h_c=15m, which is the actual height of the LUNA caisson, the caisson increases the peak linear surface magnification of incident regular waves at f=0.07Hz by 18.9% (from 1.32 to 1.57).

The effect of caisson height on the second order diffraction solution will be investigated in Section 7.4.4 Chapter 7.

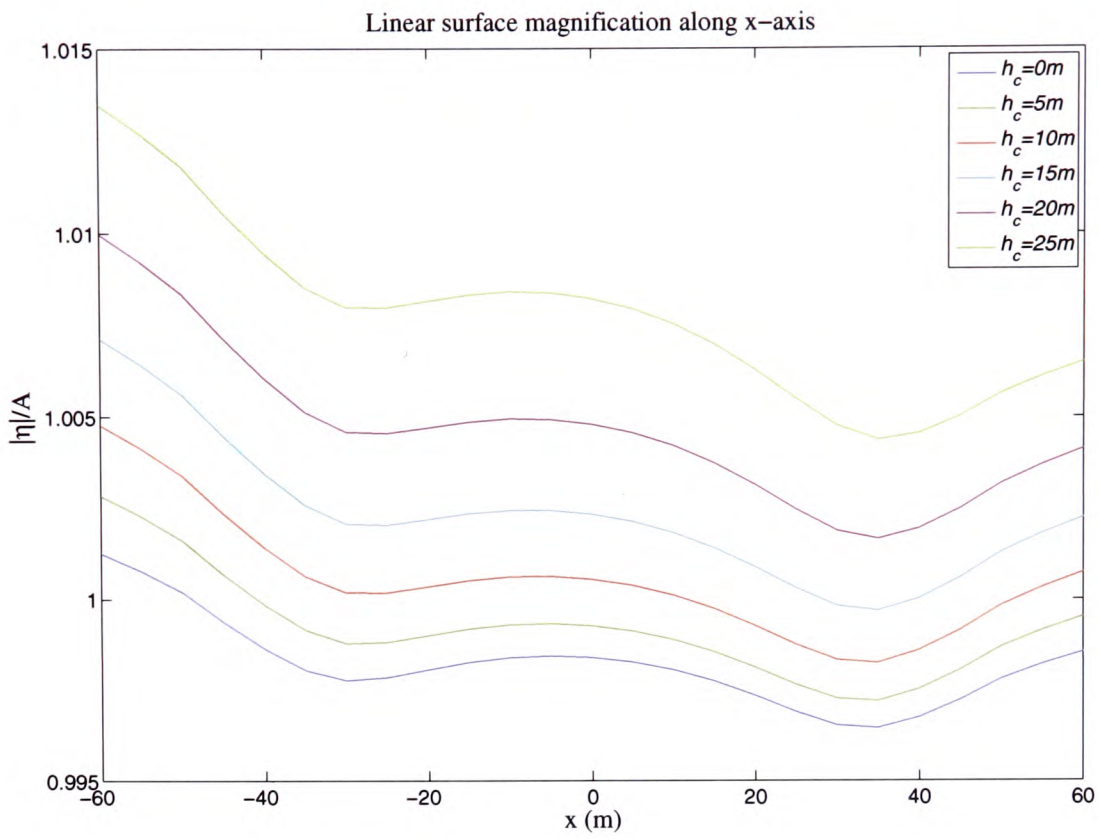

(a) f=0.01Hz

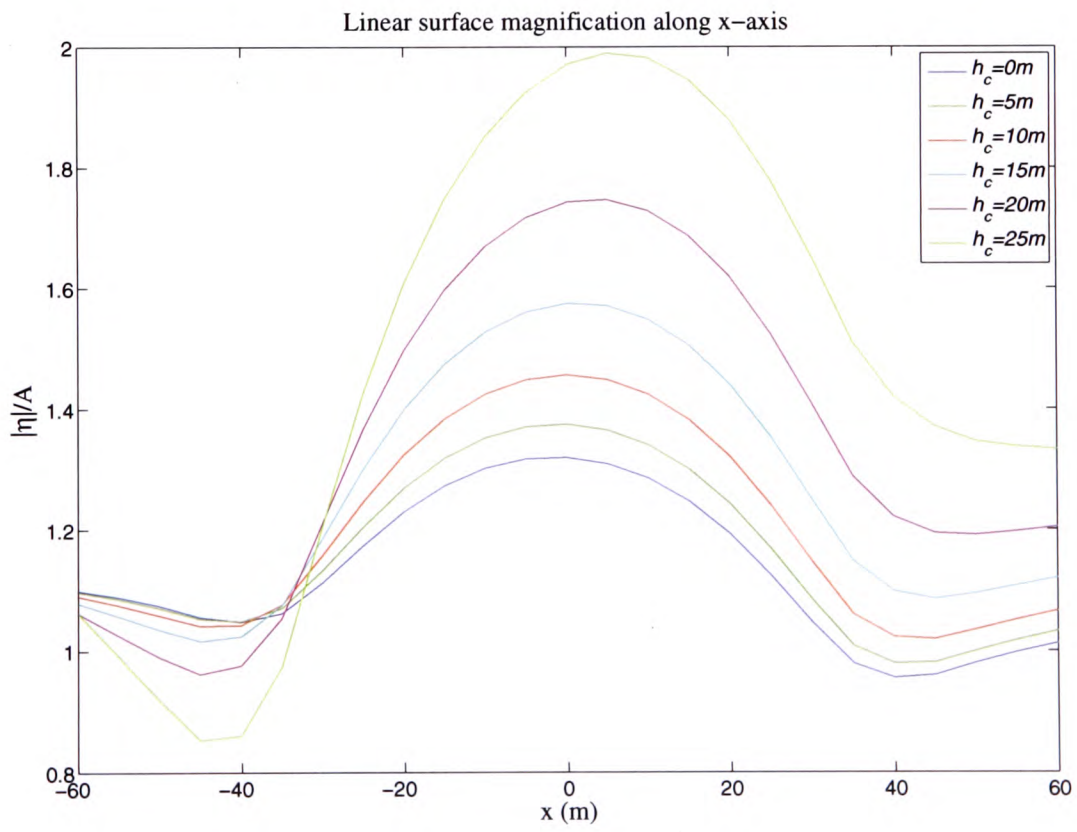

(b) f=0.07Hz

Figure 6.4: Effect of caisson height (h_c) on the linear surface magnification along the x-axis.

6.4 INCIDENT REGULAR WAVES: NEAR-TRAPPED MODES

Trapped modes and the associated phenomenon of near-trapped modes were described in Section 1.2.6 Chapter 1. Near-trapping for finite arrays of cylinders is explored in this section. Although the emphasis of this study is on the prediction of surface elevations, force results are also presented to help illustrate the characteristics of near-trapping.

To introduce and motivate an investigation into near-trapped modes for arrays of four cylinders arranged at the vertices of a square or rectangle, which is the geometrical configuration of particular interest to this project, linear arrays of cylinders aligned along an axis for which near-trapped modes have been studied in detail are first considered.

6.4.1 LINEAR ARRAYS

The interaction of regular waves with linear arrays of bottom mounted cylinders is investigated in this section using the analytical diffraction solution. The cylinders are equally spaced along the x-axis with their axes centred at $x = x_j$ $(j = 1, 2, \cdots, \mathrm{N})$ and $x_{j+1} - x_j = 2d$.

Regular waves incident upon multiple cylinder arrays can produce some remarkable hydrodynamic interference effects. At critical frequencies, the waves scattered by the cylinders constructively interfere causing large magnifications in force and free surface elevation. These critical frequencies are commonly termed near-trapped mode frequencies for reasons explained below.

Maniar and Newman (1997) studied the forces on linear arrays of bottom mounted cylinders aligned along an axis. Using a high order three dimensional spline-Galerkin panel method, Maniar and Newman found that when the number of cylinders is large but finite, near-resonant modes occur between adjacent cylinders when they are at a critical spacing relative to the incident frequency. This results in large forces on each cylinder in an array, compared to the force on an isolated cylinder. These modes are associated with the existence of trapped waves around a cylinder in a channel. The existence of such trapped waves has been established by Linton and Evans (1992), Evans, Levitin, and Vassiliev (1994), Evans and Porter (1998) and other references cited therein.

As an introduction to near-trapped modes, some results first published by Maniar and Newman (1997) will be reproduced. Figure 6.5 shows the magnitude of the horizontal wave force acting on the middle cylinder of an array of nine in head waves (i.e. $\beta = 0$) over a range of frequencies for two geometrical configurations, $a/d = 1/4$ and $a/d = 1/2$. The wave force on a single isolated cylinder of the same radius has been included for comparison. The forces are

normalised on the basis of unit wave amplitude, density, depth, cylinder radius and gravity. It is worth emphasising that the plots show the force on one cylinder, not the total force on the cylinder array that would be expected to increase with array size.

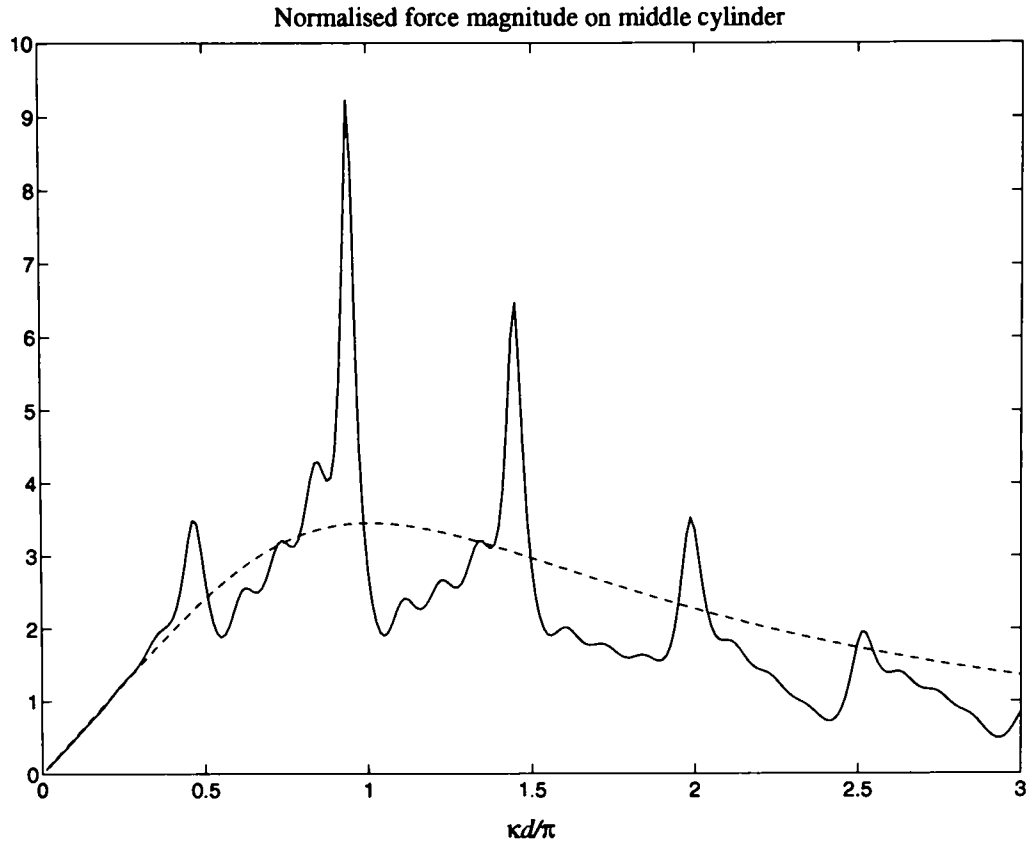

(a) $a/d = 1/4$

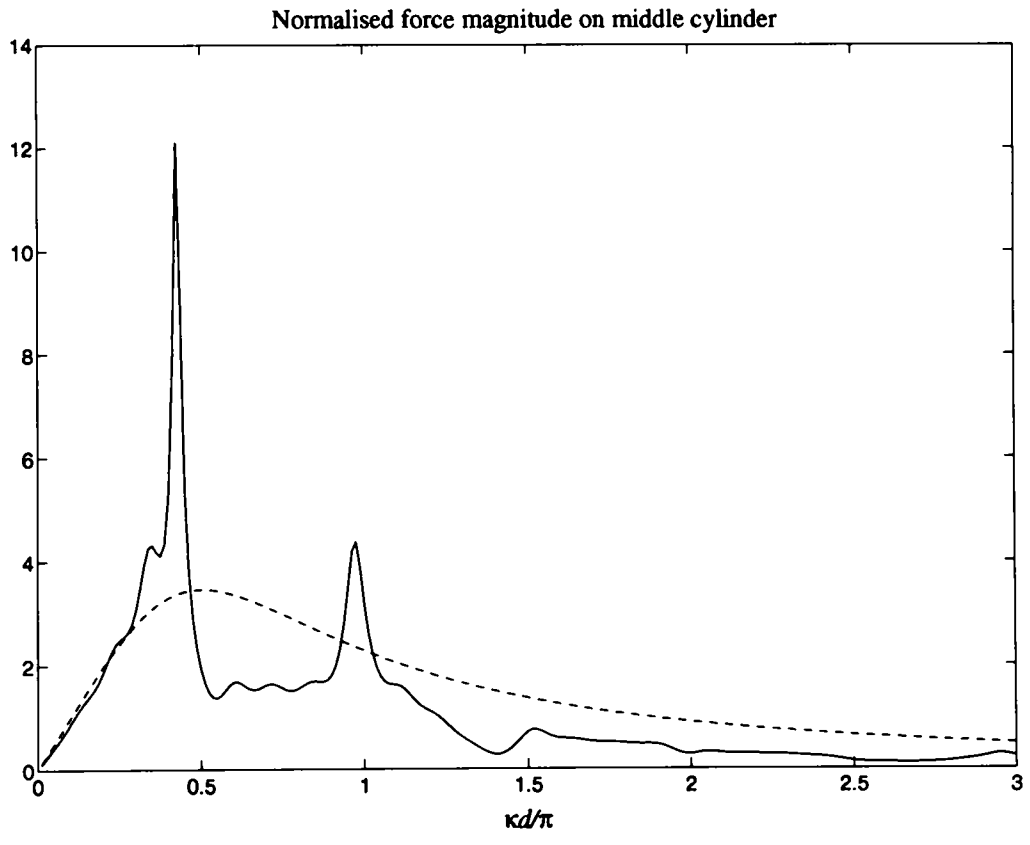

(b) $a/d = 1/2$

Figure 6.5: Normalised wave force amplitude acting on the middle cylinder in an array of nine (solid line) and comparison with the force on a single isolated cylinder (dashed line). The incident waves propagate in a direction parallel to the array (i.e. $\beta = 0$). These results were also given in Maniar and Newman (1997).

These plots illustrate the significance of the parameter κd, which relates the spacing between adjacent cylinders to the wavelength, with respect to wave interference. The most distinctive feature is a sequence of narrow peaks, with each peak occurring when κd is slightly less than $\pi/2$ times an integer. The largest peaks are approximately three times the force on a single isolated cylinder and it can be shown that this multiplicative factor increases with the number of cylinders in the array, N (Maniar and Newman (1997) and Walker and Eatock Taylor (2005)). These peak responses are studied further in this section.

As already mentioned, a connection has been identified between the peak forces acting on a finite linear array of cylinders in head waves and trapped waves around a corresponding cylinder in a channel. It is for this reason that the frequencies at which these large magnification effects occur for finite cylinder arrays are referred to as near-trapped mode frequencies. It is worth emphasising that a finite array of cylinders in open water excites the phenomenon described as near-trapping, not full trapping.

There are two types of trapped mode, namely Neumann trapped modes and Dirichlet trapped modes. The Neumann trapped modes, satisfying Neumann conditions on all solid boundaries, have been shown to exist for $0 < a/d < 1$. Physically, Neumann trapped modes describe an antisymmetric sloshing motion about the centre plane of a channel which is confined to the vicinity of the cylinder and decays rapidly down the channel. The second type, Dirichlet trapped modes, satisfy a Neumann condition of no normal flow through the cylinder surface and a Dirichlet condition on the channel walls. Dirichlet trapped modes have no obvious physical interpretation in the context of water waves in a channel, but are well documented in acoustical literature where they are termed acoustic resonances. The free surface responses associated with the corresponding phenomena of Neumann and Dirichlet near-trapped modes are examined below.

Most published research in this area (e.g. Maniar and Newman 1997) has concentrated on estimating hydrodynamic forces and it is only recently that the disturbance to the free surface resulting from wave diffraction around cylinder arrays has begun to be examined. Consequently, comparatively little surface elevation data have been published. Free surface elevation results in the local vicinity of a linear array of cylinders for incident regular waves are now presented.

For all free surface results presented in this section the normalised amplitude of the free surface elevation, $\mid \phi \mid = |\eta|/A$, is shown. Firstly, the free surface elevations on the upstream face of the first and middle cylinders in an array of nine (for $a/d = 1/4$) are plotted against $\kappa d/\pi$ (Figure 6.6). For comparison, the free surface elevation on the upstream face of a single

isolated cylinder is also plotted.

The plot for the middle cylinder can be compared with the force frequency response plot shown in Figure 6.5 (a). The plots bear considerable resemblance, both having narrow peaks with corresponding peaks occurring at the same frequencies. The largest deviations occur around the high and low frequency peaks ($\kappa d/\pi$=0.5 and 2.5) although it should be borne in mind that the two frequency responses would not be expected to be identical. Figure 6.6 plots the free surface elevation on the upstream face only (including all Fourier harmonics in the truncated form of Equation 3.16), whereas to calculate force one must consider the integrated effect of surface elevation around the circumference of the cylinder (to which only the terms $n = \pm 1$ contribute). For the isolated cylinder response, which is effectively plotted against $\kappa a/\pi$, as $\kappa a/\pi$ becomes large the normalised free surface elevation on the upstream face approaches two. This can be explained by imagining a fixed frequency incident wave (i.e. fixed κ) and then as $\kappa a/\pi$ increases, a increases and the cylinder begins to resemble a flat wall, hence resulting in a standing wave. One would expect similar behaviour for the first cylinder in the array of nine and this is shown to some extent in Figure 6.6, although peaks are of course present due to interaction effects with the other cylinders.

The free surface responses at Neumann and Dirichlet near-trapped modes are now examined

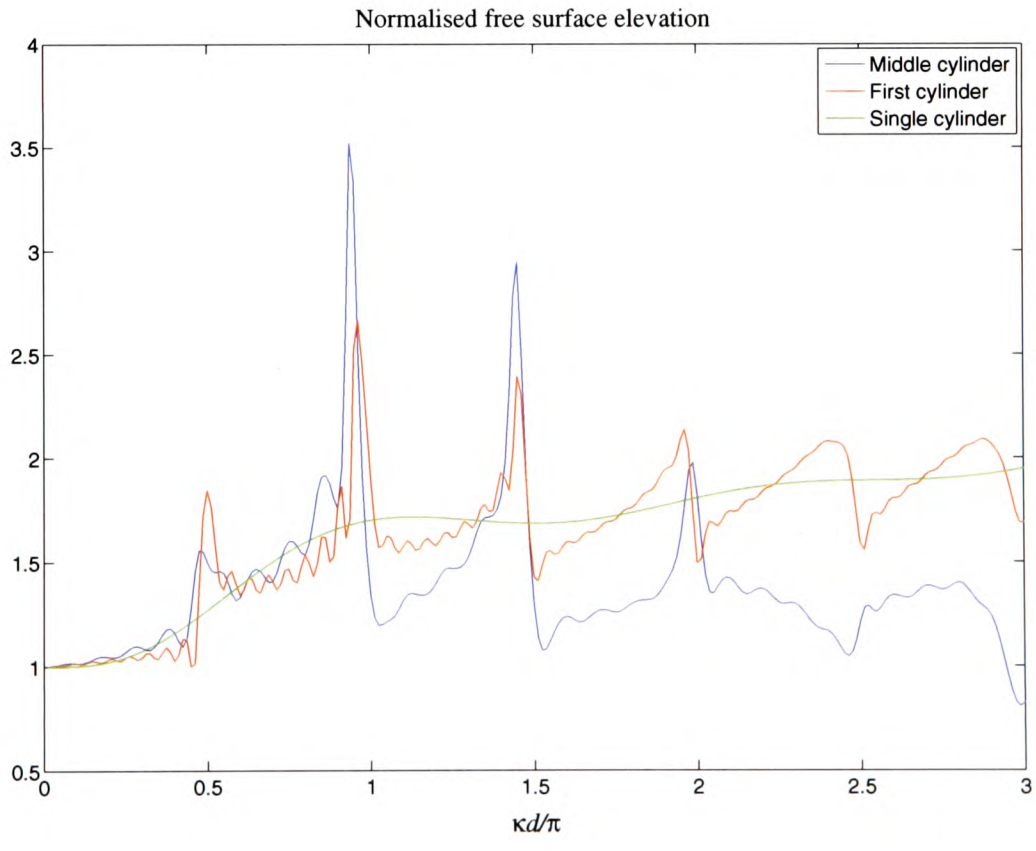

Figure 6.6: Normalised free surface elevation amplitude on the upstream face of the first and middle cylinders in an array of nine and comparison with the free surface elevation on the upstream face of a single isolated cylinder. $a/d = 1/4$. $\beta = 0$.

for $a/d = 1/2$ and $\beta = 0$. For this case the first and second largest peaks in Figure 6.5 (b) correspond to Neumann and Dirichlet near-trapped modes respectively for an array of nine cylinders. Maniar and Newman (1997) define the exact near-trapped mode frequencies for a number of array sizes, the smallest being $N = 10$. Therefore, Figure 6.7 shows the free surface elevation in the local vicinity of an array of 10 cylinders, each of radius 1m and centre-centre spacing of 4m ($a/d = 1/2$), for a Neumann near-trapped mode ($N = 10$, $\kappa d = 1.346352$). Contour and surface plots showing surface elevation are given together with a plot of surface elevation along the x-axis. Figure 6.8 shows similar plots for a Dirichlet near-trapped mode ($N = 10$, $\kappa d = 3.060920$).

The surface response for the Neumann near-trapped mode is found to increase towards the centre of the array, in agreement with force analysis undertaken by Maniar and Newman (1997). A curious observation for the Neumann near-trapped mode, which is most clearly shown in the plot of surface elevation along the x-axis, is that the normalised surface elevation remains high ($\mid \eta \mid /A \approx 1.71$) on the downstream face of the last cylinder. One would perhaps expect more sheltering and that $\mid \eta \mid /A < 1$, which is indeed the case for all other frequencies examined. However, for a Neumann near-trapped mode $\mid \eta \mid /A$ is found to remain greater than one for a distance of approximately 150m ($150a$) downstream of the last cylinder. It is known that the scattered wave amplitude far enough away from a body decays as $1/\sqrt{\kappa r}$, where r is the radial distance from the centre of the body. If one considers the cylinder array as a single body of length $2b$ and measures r from the centre of the array, the results suggest that as far out as $r = 10b$ the surface elevation still does not fall off fast enough to satisfy the $1/\sqrt{\kappa r}$ dependency. The cause of this behaviour is likely to be related to localised effects associated with the near-trapped mode.

The Dirichlet near-trapped mode corresponds to a less extreme free surface response than the Neumann near-trapped mode, with the peak elevation occurring in the first half of the array. The contour plot for the Dirichlet near-trapped mode almost suggests a discontinuity in behaviour in the space either side of the third and fourth cylinders, which is perhaps evidence of complex local effects away from the line of the cylinders.

A further observation relating to both near-trapped modes concerns the positioning of the free surface maximum relative to the upstream face of the first cylinder. Typically, one would expect to see a maximum coincident with the upstream face of the first cylinder, as is obviously the case for a single isolated cylinder, and this is observed for all κd values studied except the critical near-trapped mode values. Again, this departure from expectations can almost certainly be attributed to localised effects associated with the near-trapped modes.

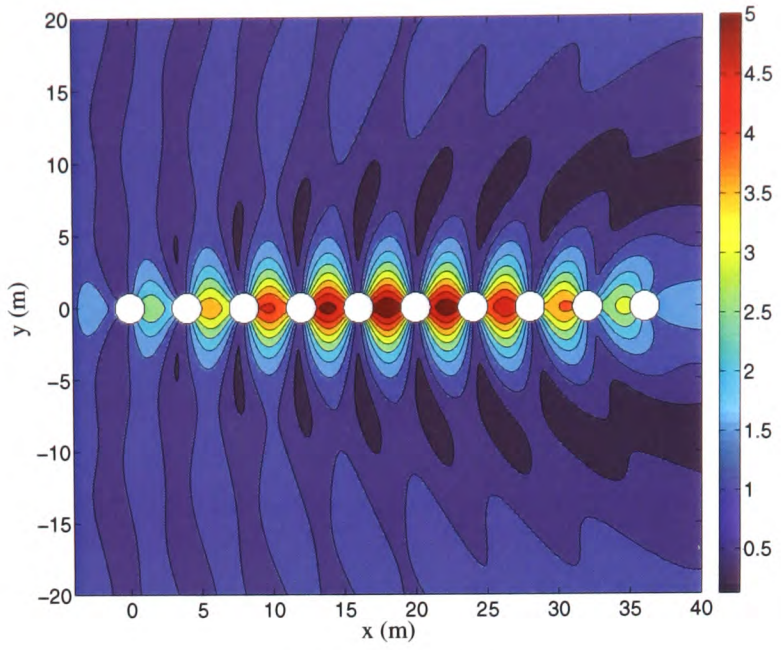

(a) Contour plot

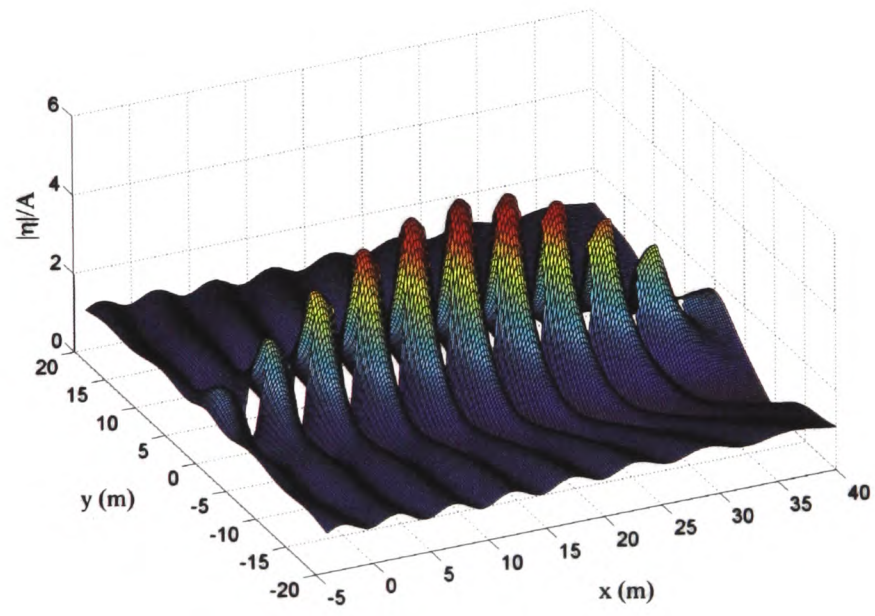

(b) Surface plot

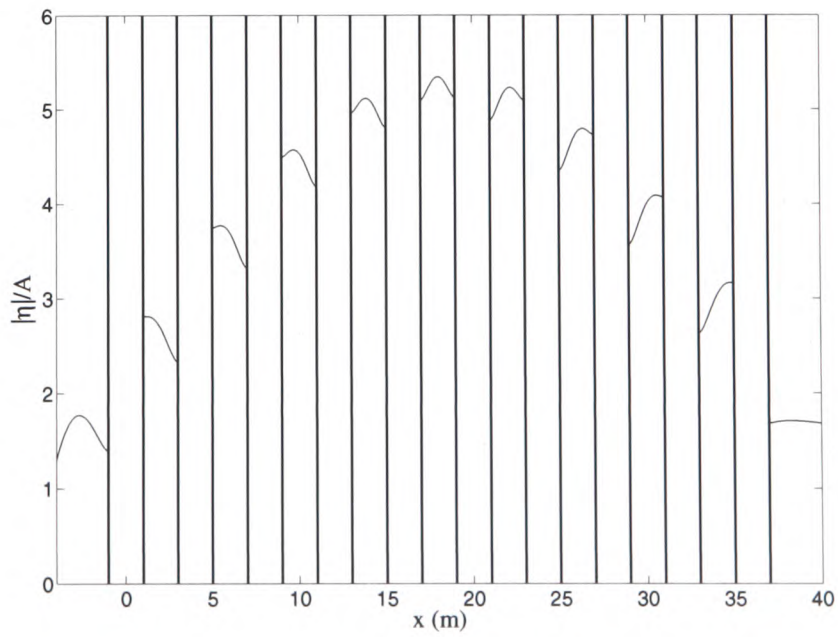

(c) Surface elevation along x-axis

Figure 6.7: Normalised free surface elevation amplitude in the vicinity of an array of 10 cylinders for the Neumann near-trapped mode: a=1m; $a/d = 1/2$; $\kappa d = 1.346352$; $\beta = 0$. Wavelength of incident waves = 9.4m.

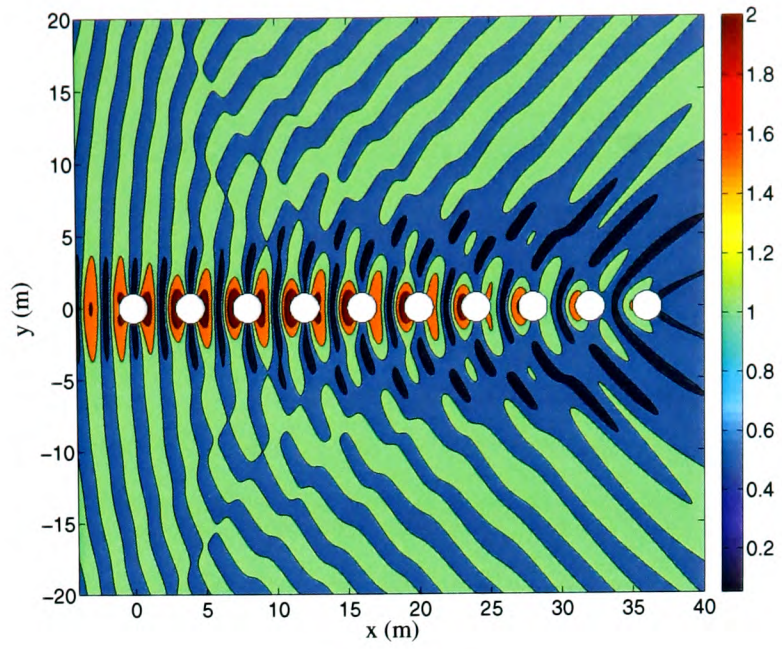

(a) Contour plot

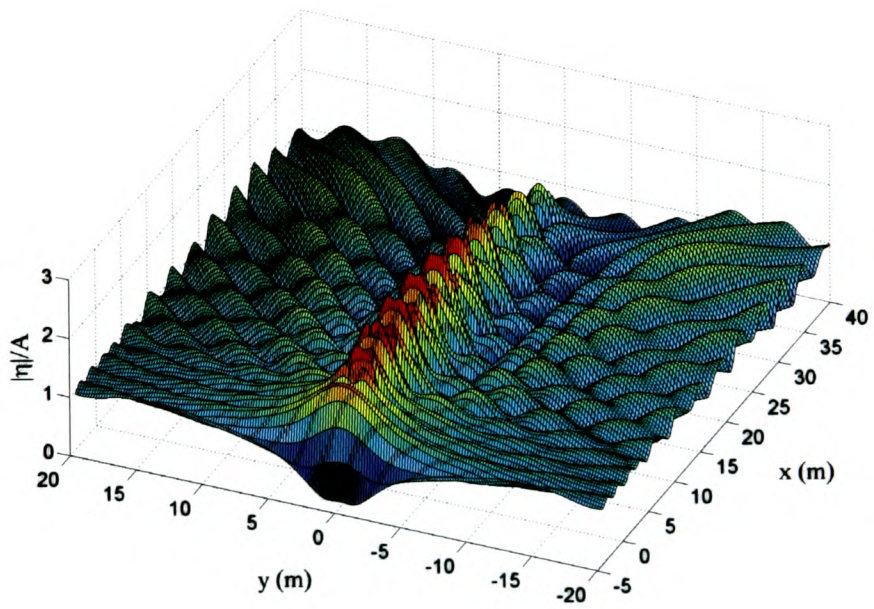

(b) Surface plot

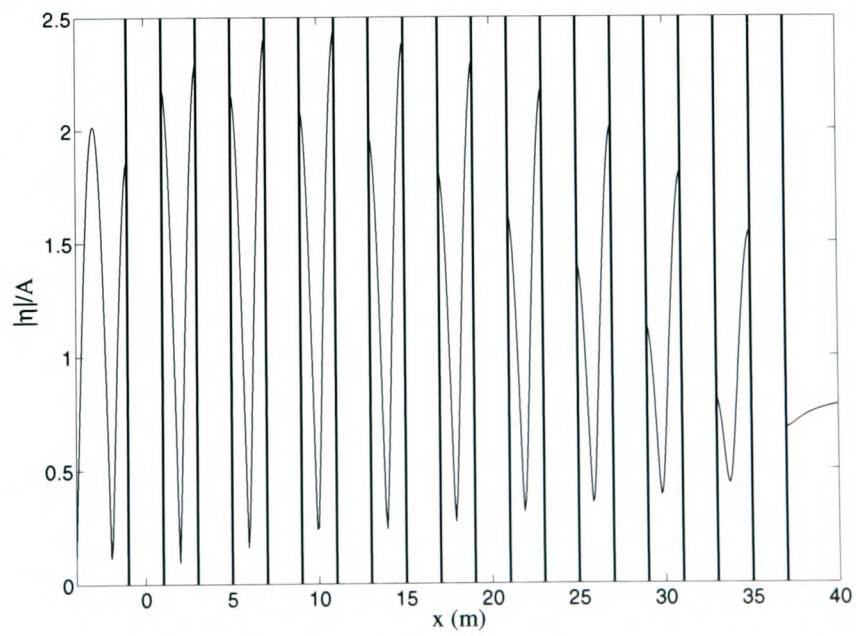

(c) Surface elevation along x-axis

Figure 6.8: Normalised free surface elevation amplitude in the vicinity of an array of 10 cylinders for the Dirichlet near-trapped mode: a=1m; $a/d = 1/2$; $\kappa d = 3.060920$; $\beta = 0$. Wavelength of incident waves = 4.1m.

A number of simulations have been studied in addition to the two near-trapped mode cases discussed thus far. In an attempt provide some insight into a more common non-resonant free surface disturbance, results are presented in Figure 6.9 for the conditions: $N = 10$, $a/d = 1/2$, $\kappa d = 2$, $\beta = 0$. Note that there are no significant magnifications of the free surface throughout the array and that a maximum coincides with the upstream face of the first cylinder.

The results presented in this section are drawn from a larger investigation of near-trapping for linear arrays of cylinders. The results and conclusions from this work are given by Walker and Eatock Taylor (2005). Some further conclusions that are of use to this thesis are: (1) the free surface magnification at near-trapping increases in approximate proportion to the size of the array (N); (2) as array size increases the force and free surface frequency response becomes more narrowly banded; (3) allowing the incident waves to propagate at non-zero incident angles results in reduced free surface magnifications and a broadening of the frequency response peaks.

It is unclear whether the large magnification effects associated with near-trapped modes would be observed in reality. Kagemoto et al. (2002) experimentally analysed near-trapped mode phenomena for linear arrays of cylinders and found that at near-trapping the magnification effects observed were substantially less than predicted by theory. Kagemoto et al. postulated that the observed discrepancy was likely to be due to dissipative effects taking place at the boundary layers around the cylinder walls.

In addition to dissipation effects, two further departures from the idealised conditions modelled, which would be expected to mitigate the considerable magnification effects predicted, are: (1) disorder in the array geometry (i.e. varying cylinder spacings and/or diameters) and (2) departure from the assumption of monochromatic incident waves. The implications of disorder have been considered by Duclos and Clément (2004), who showed that a small level of disorder (less than 0.5% of the cylinder spacing for the array they considered) is sufficient to substantially reduce the large forces associated with near-trapped modes. In Section 6.5 the second mitigating effect is considered, the fact that real ocean waves are not regular. In particular, the interaction of a NewWave with a cylinder array is considered.

6.4.2 LUNA GEOMETRY

Following on from the results presented in Section 6.4.1, the near-trapping of waves by arrays of four cylinders arranged at the vertices of a square or rectangle is now investigated. This is explored further in this section for the LUNA structure, by performing a search to identify

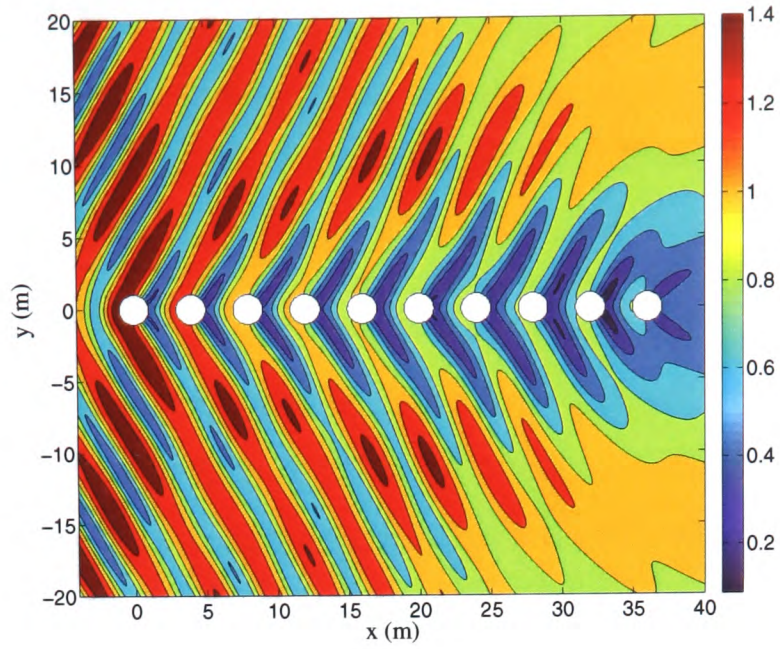

(a) Contour plot

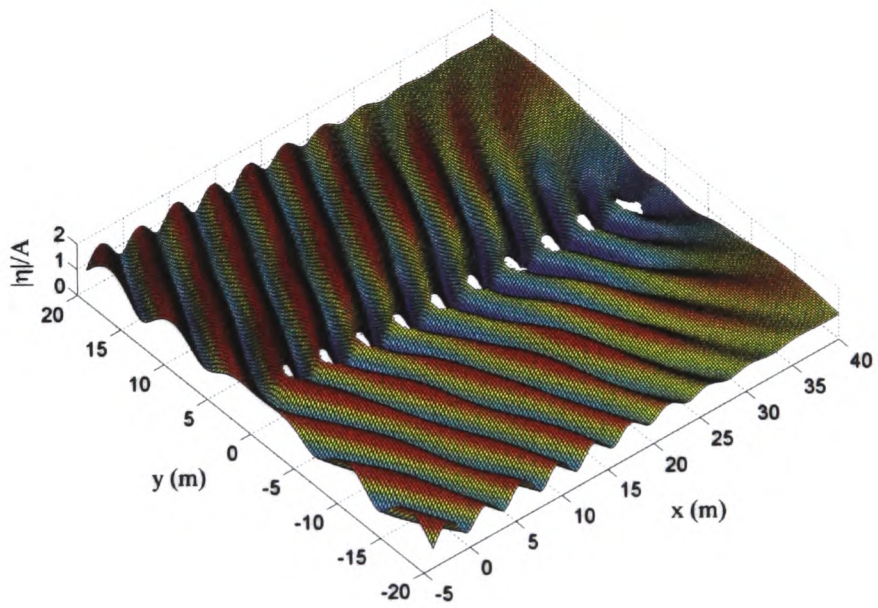

(b) Surface plot

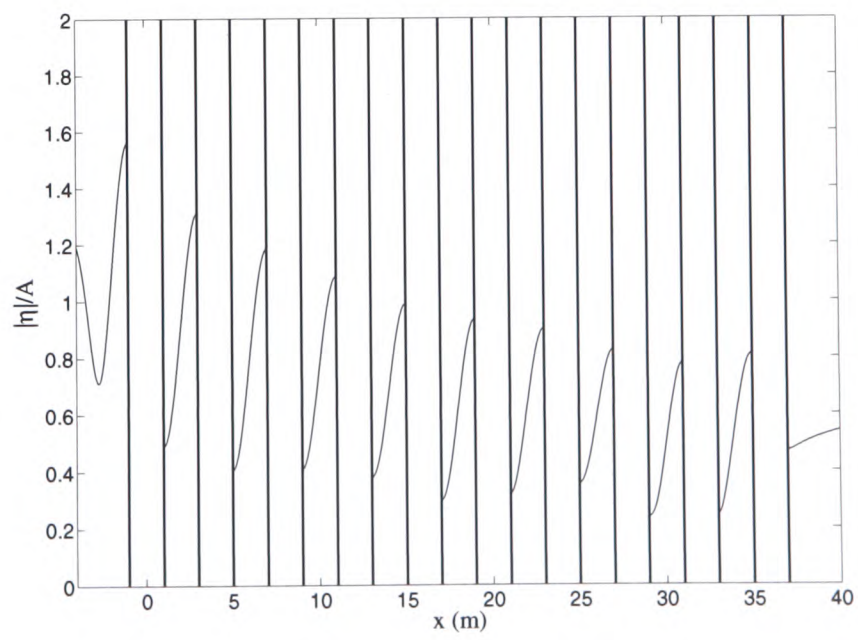

(c) Surface elevation along x-axis

Figure 6.9: Normalised free surface elevation amplitude in the vicinity of an array of 10 cylinders for: a=1m; $a/d = 1/2$; $\kappa d = 2$; $\beta = 0$. Wavelength of incident waves = 6.3m.

the largest linear surface magnifications occurring.

Unless otherwise stated, the linear analytical diffraction solution is used in this section to study wave interaction with the LUNA columns alone. DIFFRACT will be used towards the end of the section to study wave interaction with the entire structure and hence enable the effect of the caisson to be assessed.

The emphasis of this study is on the prediction of the most extreme surface magnifications ($|\eta|/A$) occurring anywhere in the vicinity of the LUNA structure. Therefore, the magnitudes and locations of the largest surface magnifications are first identified. Surface magnification frequency response functions are then computed at these specified locations, which can be used to assess the character of the frequency response peaks (e.g. how narrow the most extreme peaks are) and hence help determine the frequency resolution required for the consideration of incident NewWaves. Such guidance is particularly useful for the second order analysis of incident NewWaves, where the number of frequencies considered needs to be minimised to ease the computational burden.

Three incident wave directions are considered, namely $\beta = 0$ (along the x-axis), $\beta = 30$ degrees (which is approximately the angle subtended between the x-axis and a line joining the centres of two diagonally opposing columns) and $\beta = 90$ degrees (along the y-axis).

The frequency range 0-0.3Hz will be considered in this section. This frequency range obviously extends beyond the frequencies of practical interest, although it is hoped that the conclusions made here will help contribute to a more general understanding of near-trapping for the LUNA platform. For example, the higher frequency responses could potentially help to identify the existence of nonlinear near-trapped modes or be used in the design of a smaller scale platform with the same structural configuration.

In order to identify the magnitude and location of the largest linear surface magnifications, a 100m by 100m region around the LUNA structure is considered (-50m$<x<$50m, -50m$<y<$50m) and the linear diffracted wave field is computed throughout this region at x and y increments of 0.5m. Therefore, the surface magnification frequency response will be computed at 40,000 locations for each incident frequency and wave direction. It follows that the lowest frequency resolution possible must be used to help minimise the computation time. To help identify the lowest resolution capable of capturing the magnitude and shape of the response functions, such functions have first been computed at a number of locations around the structure using a range of frequency increments. It has been deemed that a frequency increment of 0.01Hz is sufficient for all locations considered.

Implementing the linear analytical diffraction solution for the above stated spatial and frequency resolutions, the magnitudes, locations and frequencies of the peak surface magnifications are given in Table 6.1. The largest magnification ($|\eta|/A = 3.27$) occurs between the two upstream cylinders for $\beta = 30$ degrees. It should be noted that if linear theory is used alone, each of the peak responses identified in Table 6.1 are not likely to be excited by a realistic sea state; if second or higher order contributions are considered, however, then these peaks may become significant for practical applications (see Chapter 7).

β (degrees)	$\|\eta\|_{max}/A$	f_{max} (Hz)	x_{max} (m)	y_{max} (m)
0	2.626	0.13	-36.5	0
30	3.267	0.23	-34.5	8
90	2.628	0.19	0	-2.5

Table 6.1: Magnitudes, locations and frequencies of the peak linear surface magnifications. Surface magnifications are given to three decimal places.

The frequencies recorded in Table 6.1 correspond to linear wavelengths of 99.58m, 30.83m and 45.60m for $\beta = 0$, 30 and 90 degrees respectively. The LUNA columns are positioned at the vertices of a rectangle with side lengths 68.1m (along the x-axis) and 40.5m (along the y-axis).

Surface magnification frequency response functions computed at the locations where the peak magnifications occur are shown in Figure 6.10 for each incident wave angle. Since only three specified locations are considered here, the computation time is not an important consideration and hence the functions are now computed using a frequency increment of 0.001Hz over the frequency range 0-0.3Hz. Using this increased frequency resolution the peak surface magnifications are found to be 2.649 ($\beta = 0$), 3.275 ($\beta = 30$ degrees) and 2.629 ($\beta = 90$ degrees), which occur at frequencies 0.126Hz, 0.226Hz and 0.184Hz. Comparing these values with the values in Table 6.1, it is clear that a frequency increment of 0.01Hz is sufficiently small to identify the largest magnifications.

The response functions for all wave angles are relatively flat for incident long waves ($f \leq\sim$ 0.08Hz) and have a series of peaks for shorter incident waves ($f >\sim 0.08$Hz). The response function corresponding to $\beta = 0$ is particularly frequency sensitive, exhibiting six energetic peaks in the studied frequency range. These peaks are likely to be caused by strong scattered wave interaction between the two upstream columns. Since the peak magnification possible from waves incident upon a flat wall is two, it seems reasonable to conclude that the largest peak magnifications observed in Figure 6.10 correspond to near-trapping. Indeed the response

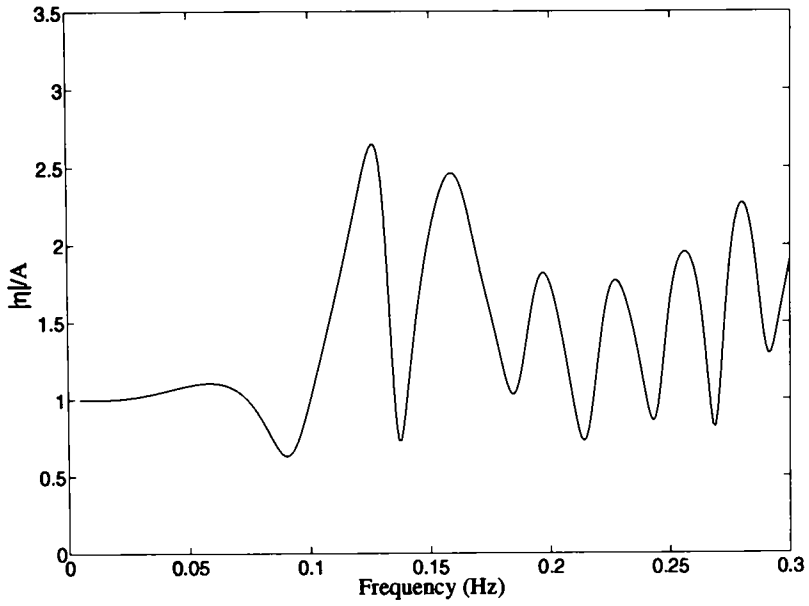

(a) $\beta = 0°$

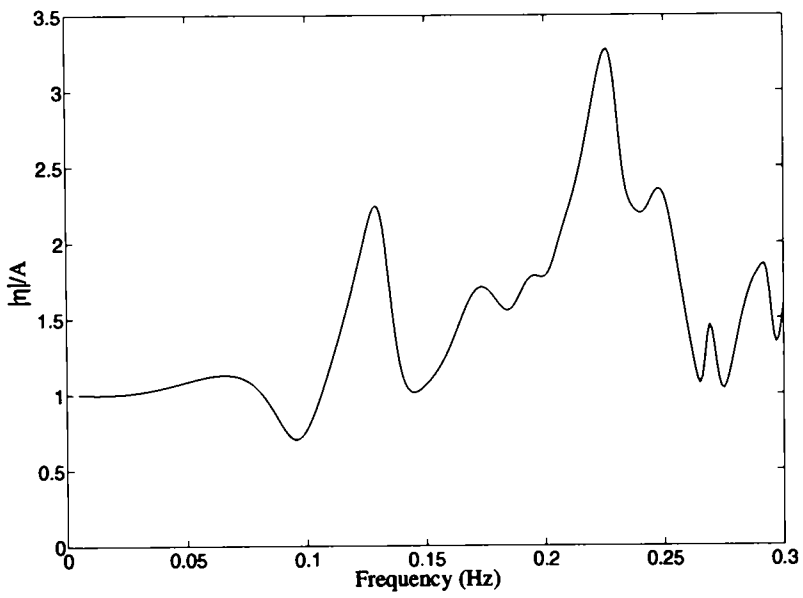

(b) $\beta = 30°$

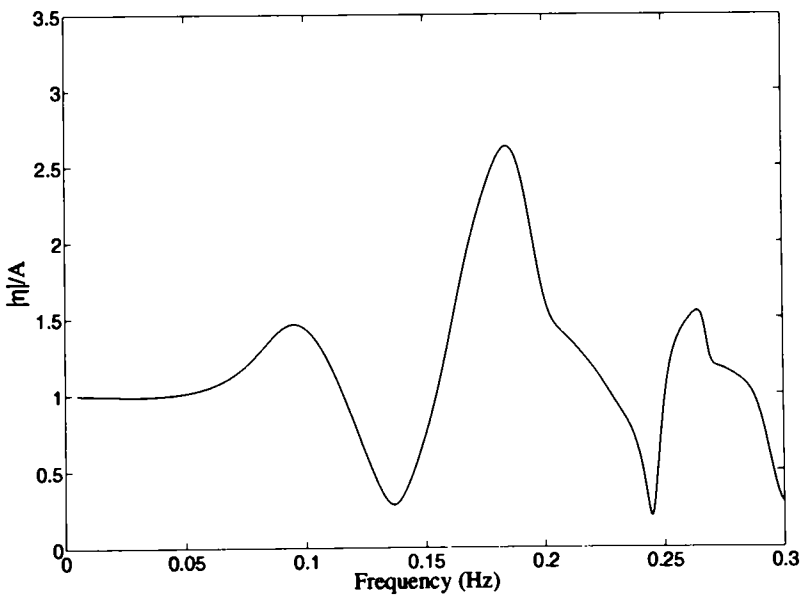

(c) $\beta = 90°$

Figure 6.10: Linear surface magnification frequency response functions computed at the locations where the peak magnifications occur.

functions show that for particular incident frequencies, wave interaction with an array of four cylinders arranged at the vertices of a rectangle can result in a considerable enhancement of the local free surface.

It is difficult to draw any direct comparisons between the free surface response functions for the LUNA structure and the response functions presented in this Chapter for linear arrays of nine cylinders. For linear arrays of cylinders, the peak responses become broader for smaller arrays and the peak magnitude is proportional to the array size (Walker and Eatock Taylor 2005). Walker and Eatock Taylor examined the surface response function for a linear array of three cylinders ($a/d = 1/4$) and found a peak linear magnification of 4.8, suggesting that a linear array of four cylinders would excite larger surface magnifications than an array of four cylinders arranged at the vertices of a rectangle. It would be interesting to generate results for a linear array of four cylinders with a diameter/spacing ratio comparable to the LUNA structure (using both the x and y spacings) to allow a direct comparison to be made. It is suspected that the regularity of the linear array would enable larger magnifications to develop.

Figures 6.11 to 6.13 show contour and surface plots of the surface elevation in the vicinity of the LUNA structure for each wave angle and frequency in Table 6.1. These plots clearly show the large magnifications associated with near-trapping at the locations identified in Table 6.1.

The largest surface magnifications identified in the above analysis for $\beta = 0$ and 30 degrees are 2.649 and 3.275 respectively, which both occur between the two upstream columns. The incident frequencies exciting these responses are 0.126Hz and 0.226Hz for $\beta = 0$ and $\beta = 30$ degrees respectively. It is suspected that these magnifications are primarily caused by wave interaction with the two upstream columns. To test this hypothesis the two downstream columns are removed and the maximum surface magnifications resulting from wave interaction with the two upstream columns alone are recorded (Table 6.2). As suspected, the majority of the surface magnification is caused by the incident waves interacting with the two upstream columns. The downstream columns are found to have a comparatively small yet appreciable effect. The presence of the two downstream columns has shifted the location of the peak surface magnification 9m downstream for $\beta = 0$ and has had little effect on the location of the largest magnification for β =30 degrees.

A further interesting exercise would be to investigate the effect the x-spacing of the columns has on the peak surface magnification. This work could potentially help to identify desirable rectangular array configurations, which minimise surface magnifications between the columns.

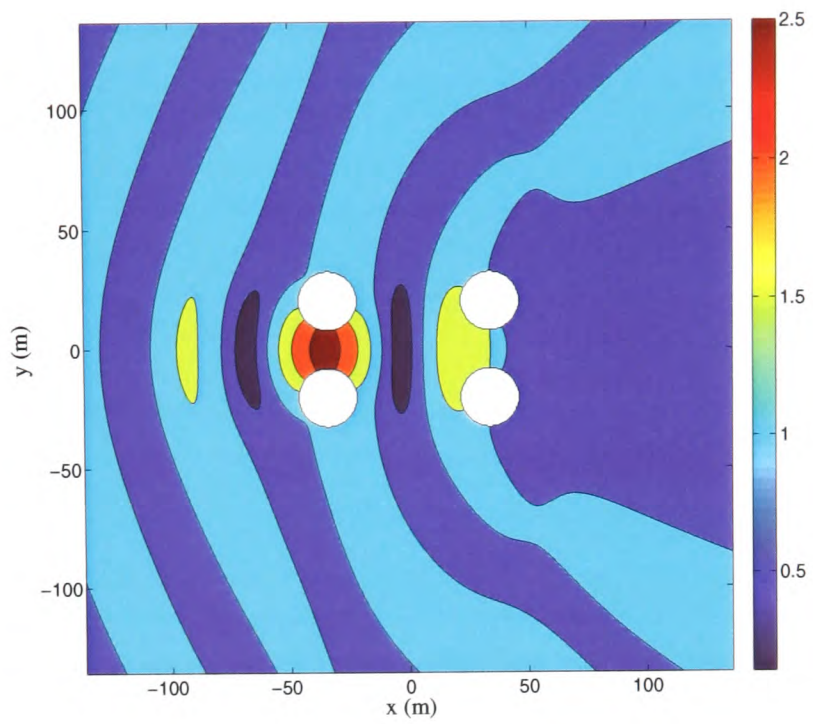

(a) Contour plot

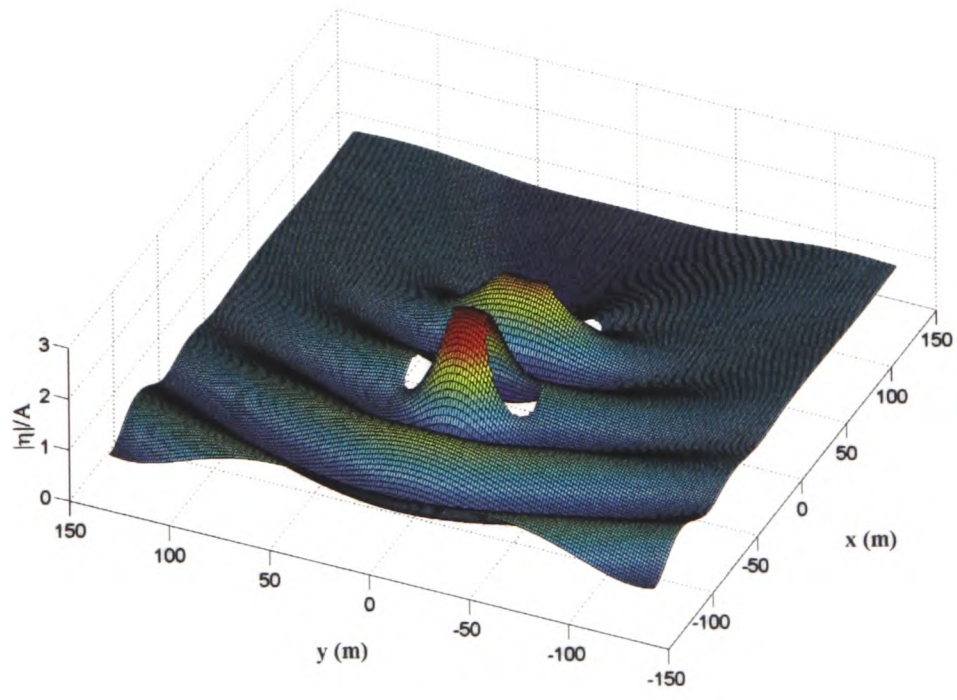

(b) Surface plot

Figure 6.11: Surface elevation around the LUNA structure at near-trapping. $\beta = 0^{o}$, $f =$ 0.126Hz.

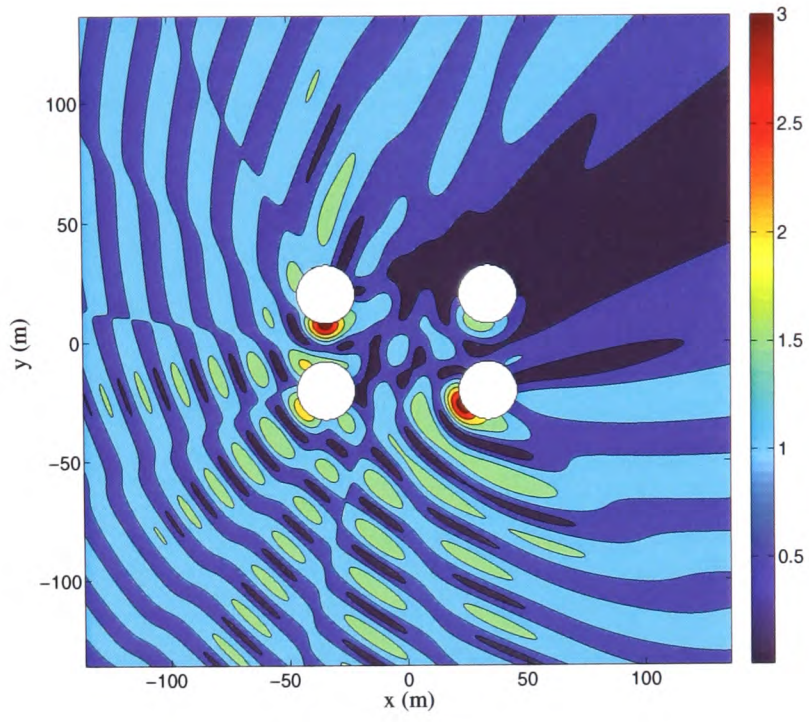

(a) Contour plot

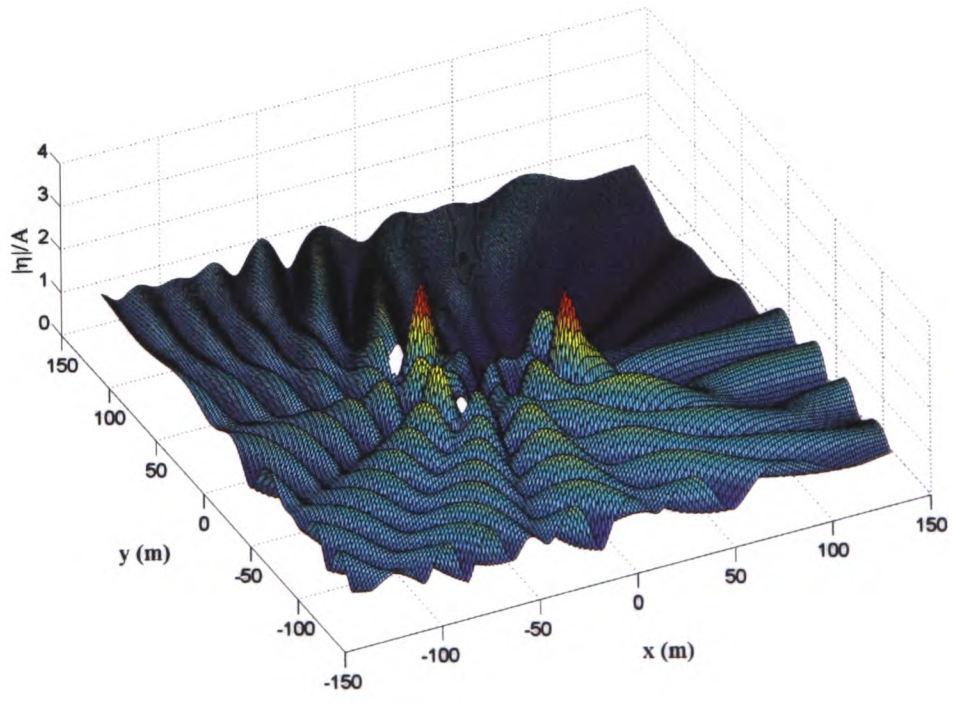

(b) Surface plot

Figure 6.12: Surface elevation around the LUNA structure at near-trapping. $\beta = 30^{o}$, $f = 0.226$Hz.

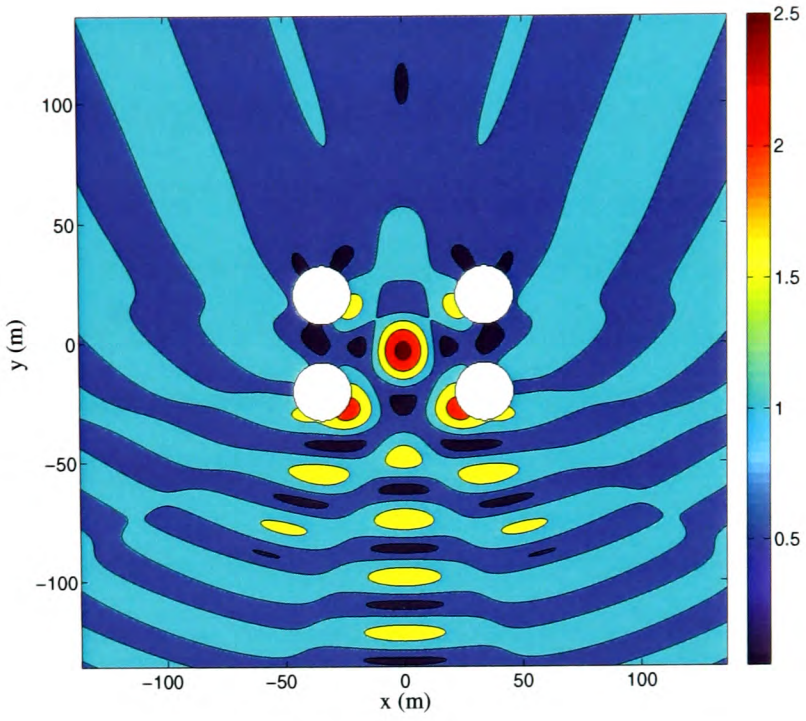

(a) Contour plot

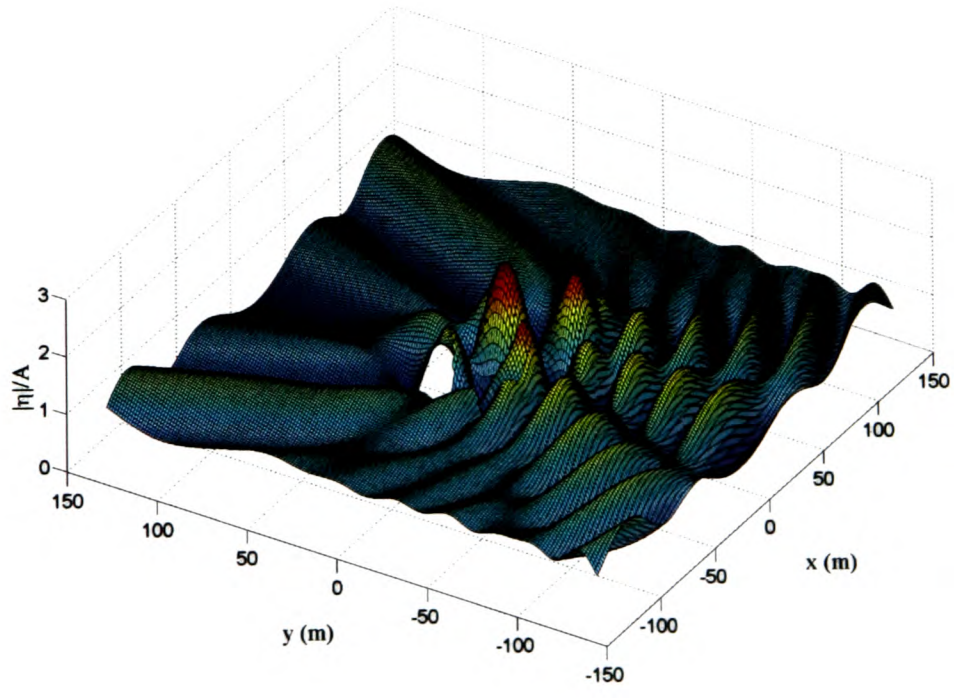

(b) Surface plot

Figure 6.13: Surface elevation around the LUNA structure at near-trapping. $\beta = 90^{o}$, $f = 0.184$Hz.

β (degrees)	Incident frequency (Hz)	$\lvert\eta\rvert_{max}/A$	x_{max} (m)	y_{max} (m)
0	0.126	2.013	-45.5	0
30	0.226	2.769	-35.5	8

Table 6.2: Magnitudes and locations of the peak linear surface magnifications resulting from wave interaction with the two upstream columns of the LUNA structure. Surface magnifications are given to three decimal places.

The effect of the caisson on the linear surface frequency response function at the point where the largest linear surface magnification occurs for $\beta = 0$, (x, y)=(-36.5,0), is now assessed. DIFFRACT is used to generate a similar response function to that shown in Figure 6.10 (a) for wave interaction with the entire LUNA structure (caisson with four columns mounted on top). The effect of the caisson on near-trapping is assessed. In particular, the effect on the magnitude and frequency of the response peaks is investigated.

It is noted that wave interaction with the caisson could possibly move the location of the maximum surface magnification in $x - y$ space, although this effect is not investigated here. Unfortunately the DIFFRACT code restricts the number of points that can be considered on the free surface and so attention is restricted to the point identified using the analytical solution. It is thought that useful insight into the effect of the caisson on near-trapping can be sought by considering this point alone.

To minimise the computational burden whilst retaining a sufficiently fine frequency resolution a frequency increment of 0.003Hz is used to generate the numerical results. For comparison with the analytical solution, a frequency range 0-0.3Hz is again considered.

It is useful and interesting to first compare the frequency response functions computed using analytical diffraction theory and the numerical code DIFFRACT for the four LUNA columns alone. This comparison is presented in Figure 6.14 for $\beta = 0$ at point (-36.5,0). There is excellent agreement between the two solution methods for frequencies less than approximately 0.2Hz. Above this frequency there is some mismatch between the magnitudes of the peaks and troughs, although the frequencies of the peaks and troughs remain in good agreement. For the highest frequency peak (at ~ 0.28Hz) the numerical solution predicts a double peak. These discrepancies at high frequency are not likely to be caused by an insufficiently fine mesh in the numerical solution. The smallest linear wavelength considered (corresponding to 0.3Hz) is 17.3m and the largest elemental lengths used on the body surface mesh are 5m and 10m for elements near the free surface and sea bed respectively. That said, it is noted that near-trapping (if that is what these peaks are) is a very sensitive phenomenon, linked to small values of the determinant of the governing linear equations; small errors in the linear

coefficients could lead to large errors in the solution.

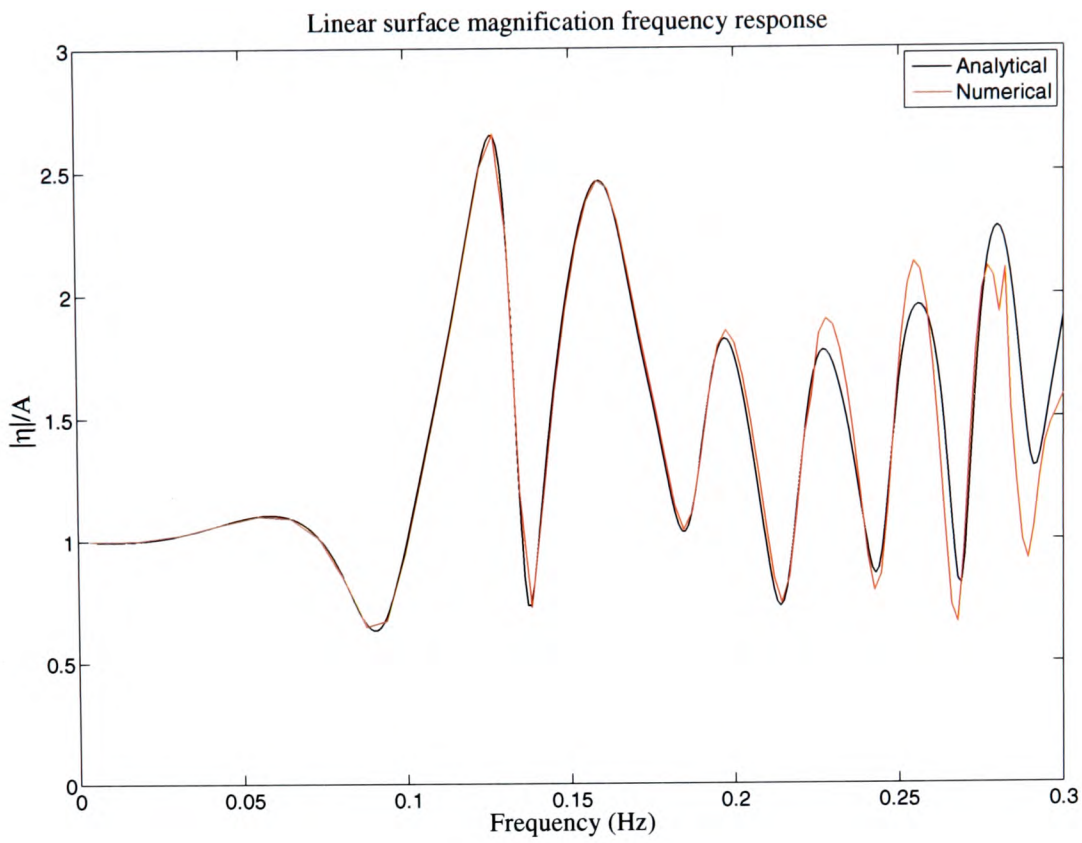

Figure 6.14: Comparison between frequency response functions computed using linear analytical diffraction theory and the numerical code DIFFRACT at the point (-36.5,0). $\beta = 0$.

The effect of the LUNA caisson on the $\beta = 0$ linear surface response function at point (-36.5,0) is shown in Figure 6.15. As was found in Section 6.3, Figure 6.15 shows the effect of the caisson to be dependent on the frequency of the incoming waves. For long waves (frequency $< \sim 0.01$Hz) and short waves (frequency $> \sim 0.14$Hz) the effect of the caisson is negligible and there is a relatively narrow range of frequencies where the caisson has an appreciable effect on the linear surface magnification. In this frequency range the caisson appears to alter the magnitude of the response function only and is not found to have a significant effect on the frequency of the peaks and troughs. The largest increase in surface magnification caused by the caisson at point (-36.5,0), which can be identified from the data presented in Figure 6.15, is 19.4% at a frequency of 0.093Hz.

In Section 6.3 the effect of caisson height on waves of frequency 0.07Hz was investigated. The results and subsequent discussion presented in Section 6.3 are entirely consistent with the results shown in Figure 6.15. For example, the effect of the caisson at point (-36.5,0) for waves of frequency 0.07Hz is found to be very small, which is shown both in Figure 6.4 and Figure 6.15.

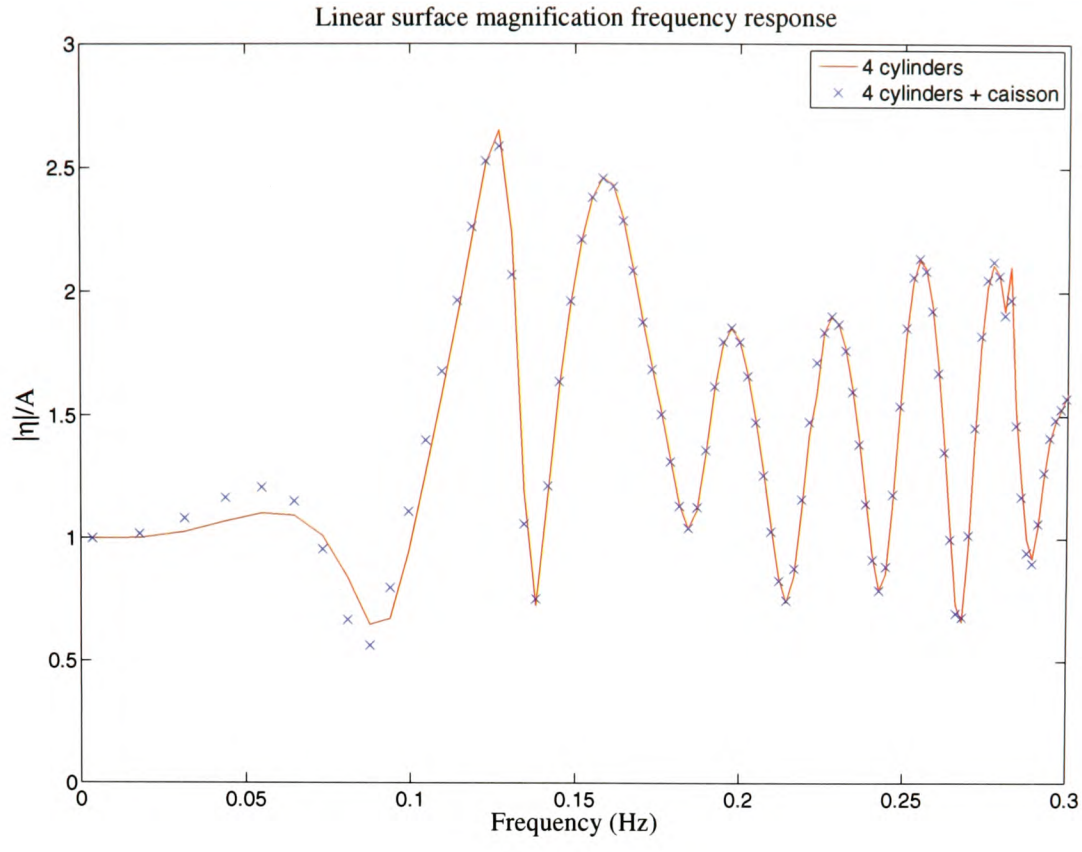

Figure 6.15: Effect of the LUNA caisson on linear near-trapping at point (-36.5,0). $\beta = 0$. Both cases are computed using DIFFRACT.

The above analysis indicates that the presence of a caisson can cause an appreciable enhancement of the free surface for a limited range of frequencies. A caisson is also found to have a negligible effect on the near-trapped frequencies caused by wave interaction with the columns. This suggests that for structures consisting of columns mounted on a subsurface caisson, useful information on the near-trapping characteristics for the structure can be obtained by studying wave interaction with the columns alone. Despite this, depending on the size of the caisson and the local sea environment, an additional free surface enhancement factor associated with wave interaction with the caisson should be incorporated for airgap design.

6.5 Incident NewWaves

In an attempt to model the interaction of extreme ocean waves with offshore structures, the diffraction analysis is now extended to cover incident NewWaves (e.g. isolated wave groups). The majority of published research on wave diffraction by cylinder arrays is for regular waves and to the author's knowledge, no data other than that given by Walker and Eatock Taylor (2005), have been published for NewWaves incident upon linear arrays of cylinders; only limited data for single cylinders and groups of four cylinders arranged at the vertices of a square are available. Some of the results from the study carried out by Walker and Eatock

Taylor are presented in this section. All results in this section are produced using the linear analytical diffraction solution.

The Pierson-Moskowitz spectrum (Pierson and Moskowitz 1964) is used to produce an incident wave field that is representative of a realistic extreme storm wave. There are a number of definitions for this spectrum depending on the sea state parameters chosen to define the spectrum; see for example Ochi (1998), who defines the spectrum in terms of the significant wave height and peak frequency. The following definition in terms of the significant wave height, H_s, and zero mean crossing period, T_z, is used in this section:

$$S(\omega) = \frac{H_s^2}{8\pi^2 T_z^4} \left(\frac{2\pi}{\omega}\right)^5 \exp\left[-\frac{1}{\pi}\left(\frac{2\pi}{T_z\omega}\right)^4\right] \tag{6.1}$$

For wave diffraction by linear arrays of cylinders a sea state characterised by H_s=12m and T_z=10s is investigated. These values are typical for storm conditions. Using published statistical relationships (Faltinsen 1990) a realistic extreme crest amplitude of 13m is computed for this sea state, which will be used as the linear NewWave amplitude, A_{nw}.

The Pierson-Moskowitz spectrum for the conditions defined above is shown in Figure 6.16 and a NewWave profile based on this spectrum is shown later in Section 6.5.1.

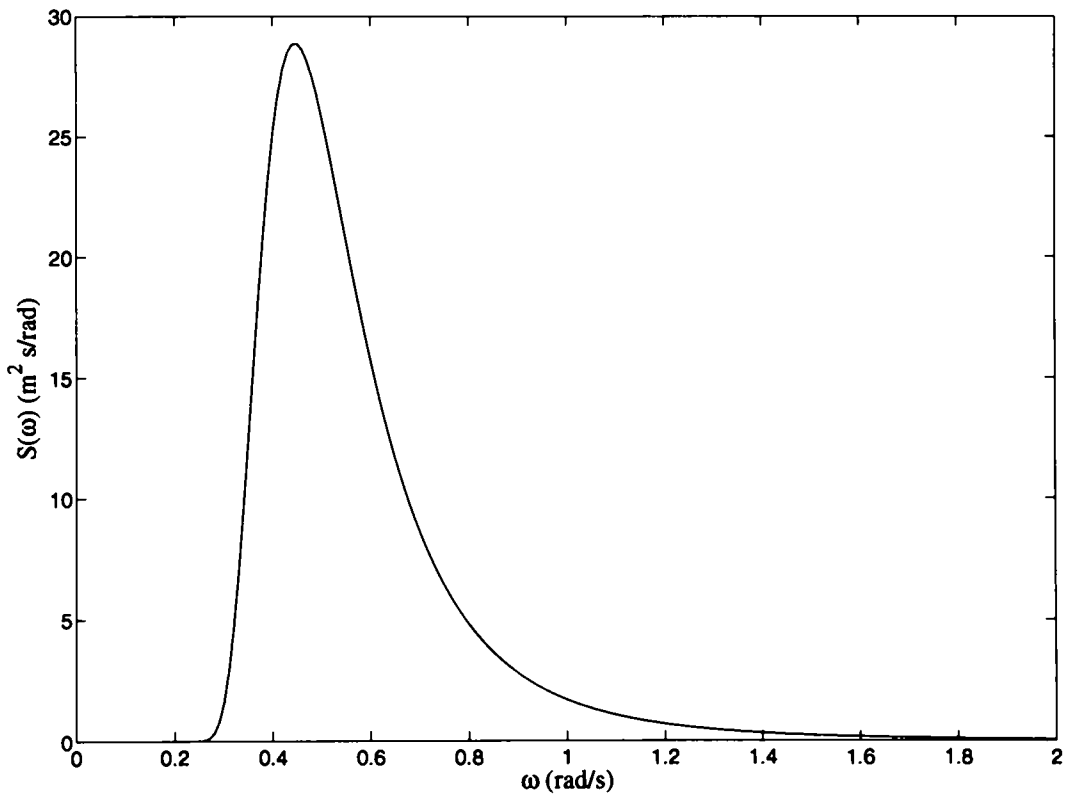

Figure 6.16: Pierson-Moskowitz spectrum for a sea-state characterised by H_s=12m and T_z=10s.

For wave diffraction by the LUNA columns a significant wave height of 9.9m and a zero mean crossing period of 11.1s are used, which correspond to realistic conditions for the location of the LUNA platform. A linear NewWave amplitude, A_{nw}, of 11m is used for this sea state.

The NewWave formulation (Equation 2.2 Section 2.2 Chapter 2) is implemented using a standard FFT algorithm, in which a Nyquist frequency of ω_{nf}=1.405rad/s is assumed for the studied sea states. For frequencies larger than this, a spectral density of zero has been used for padding up to the maximum frequency of $\omega_{max} = 2\omega_{nf}$=2.81rad/s. This ensures no corruption of the spectrum at high frequencies (i.e. no aliasing). The wave energy spectrum is divided into 200 frequency components (i.e. $d\omega$=0.01405rad/s), which produces accurate results whilst retaining a manageable computation time.

Nonlinear interactions between waves at different frequencies are not accounted for in linear diffraction theory and so it is relatively straightforward to obtain a linear diffraction solution for incident NewWaves. This is achieved by the linear superposition of the diffracted wave field for each frequency component of the incident wave. Therefore, from Equations 2.2 and 2.73, the free surface elevation resulting from the diffraction of an incident NewWave is given by:

$$\eta_D(x,y,\tau) = \frac{\alpha}{\sigma^2}\sum_{n=1}^{N} C_n \,\Re\left\{\phi_n(x,y)e^{-i(\kappa_n x_0+\omega_n \tau)}\right\} \tag{6.2}$$

where $\tau = t - t_0$ and $X = x - x_0$, with the focus event occurring in the y-plane at (x_0, y, t_0). The incident angle (β) is taken to be zero for each frequency component of the incident wave and the diffraction coefficient for the n^{th} spectral component is ϕ_n, which is obtained using the linear analytical diffraction solution in this section.

For incident regular waves at near-trapping, the large magnifications in force and free surface elevation that result could have serious practical implications for very large column-supported floating structures. However, the bandwidths of these magnification effects were found to be quite narrow, especially for large arrays, and so it would seem likely that the integrated effects over a continuous spectrum would not be severe. This hypothesis is tested in this section by studying NewWaves incident upon large linear arrays of cylinders and the LUNA cylinder configuration.

To allow comparison with some of the results produced for incident regular waves, both force and free surface elevation results are presented for linear arrays of cylinders and free surface elevation results alone are presented for the LUNA structure.

6.5.1 LINEAR ARRAYS

The cylinder radius, a, and cylinder spacing, $2d$, used in this section are 15m and 120m respectively ($a/d = 1/4$). It is thought that these values represent a realistic geometric configuration for a column supporting structure. Note that the separation of the cylinders is approximately equal to the crest-trough separation of the NewWave in space - i.e. for a NewWave focused on the second cylinder, the first and third cylinders will coincide approximately with the deepest troughs of the NewWave.

Force results are presented first before moving on to consider free surface elevations. There are obviously many test simulations that can be run (e.g. focusing the NewWave at different points in space etc.) and the aim here is to present results that provide a useful insight into the interaction of NewWaves with a linear array of cylinders.

All analysis here assumes deep water. For this assumption to be valid, the water depth, $h >$ (maximum wavelength)/2. Hence, by identifying the lowest significant frequency component associated with the discretised spectrum (Pierson-Moskowitz), it has been decided to use h=500m for all test cases in this section.

Figure 6.17 shows the force time history for a single isolated cylinder of radius 15m with a NewWave focused on its upstream face at time $t = 0$. Because force is approximately in phase with the local horizontal acceleration, the maximum force occurs when the wave slope is close to its maximum. Therefore one would not expect the maximum force to occur at time $t = 0$. In addition, a small phase shift from the time of maximum wave slope is introduced by diffraction effects. The maximum force magnitude on the cylinder is 164.1MN.

A linear array of three cylinders is next considered. The force pattern resulting from a NewWave being focused on the upstream face of each cylinder in turn is examined. Table 6.3 gives the initial force (i.e. at $t = 0$) and maximum force magnitude at any time on each cylinder.

Focused Cylinder	Initial Force (MN)			Maximum force magnitude (MN)		
	Cyl. 1	Cyl. 2	Cyl. 3	Cyl. 1	Cyl. 2	Cyl. 3
1	89.9	2.9	-26.4	166.3	151.2	133.6
2	-65.1	98.0	1.1	155.8	168.5	145.9
3	58.1	-69.7	101.9	137.9	160.2	166.4

Table 6.3: Initial force and maximum force magnitude results for a NewWave incident upon a three-cylinder array. The focused cylinder is the cylinder that the NewWave is focused on.

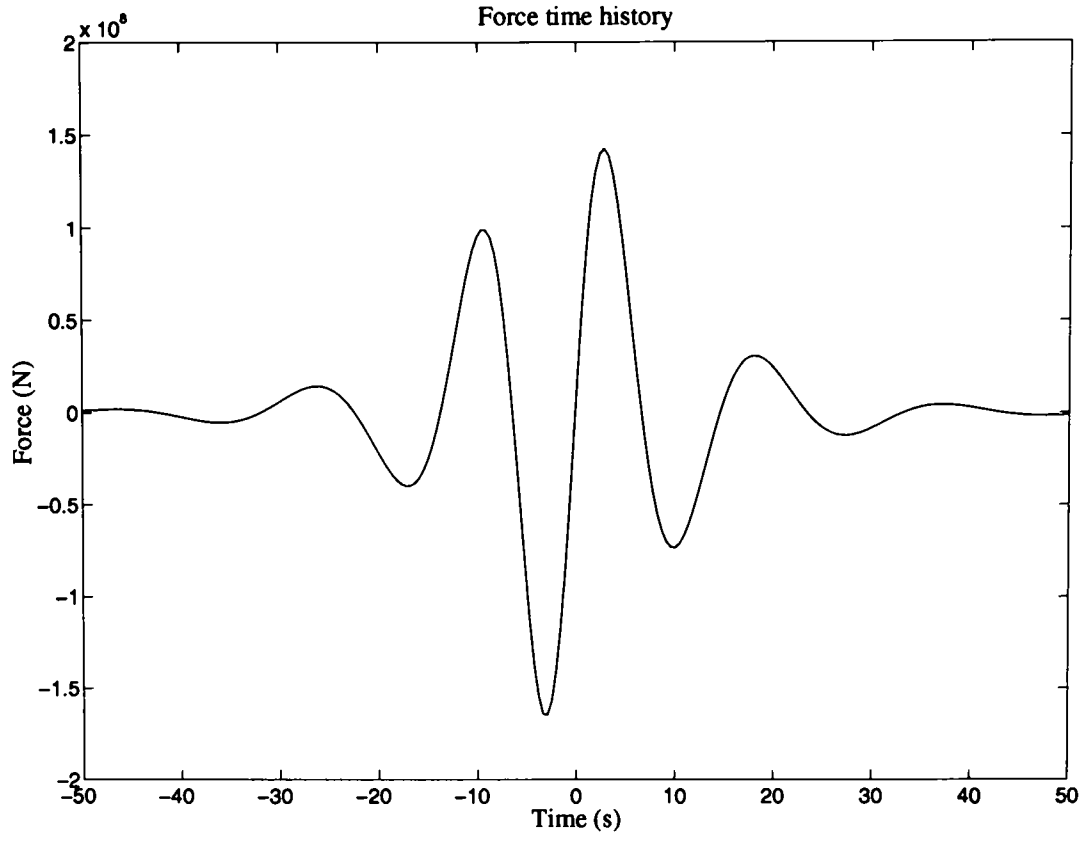

Figure 6.17: Force time history for a single isolated cylinder with a NewWave focused on its upstream face at time $t = 0$.

As one would expect, the cylinder that has the NewWave focused on its upstream face (referred to as the focused cylinder) experiences the largest loads, both initially and over an extended time period. The differences between the forces on the cylinders for each test case are comparatively large initially although as time progresses each cylinder experiences a force greater than its initial value. For each of the three cases considered, the maximum force magnitude experienced by the focused cylinder is only marginally greater than that experienced by a single isolated cylinder (=164.1MN). The largest force magnification occurs when the NewWave is focused on the second cylinder, where the maximum force magnitude experienced by the focused cylinder is 2.7% greater than that on a single isolated cylinder.

Larger arrays of cylinders are now examined in an attempt to establish whether this force magnification increases with array size, as it does for regular waves. Figure 6.18 shows results for arrays of 10, 25, and 50 cylinders. In each case, one of the central cylinders has been chosen as the focused cylinder. Both initial forces and maximum force magnitudes at any time have been plotted throughout the array.

These results show how interaction effects between the cylinders for large arrays strongly influence the resulting force on each cylinder. In none of the cases studied does the maximum force magnitude occur on the focused cylinder and for the 25 and 50 cylinder arrays, the focused cylinder does not even experience the largest initial force. The maximum force mag-

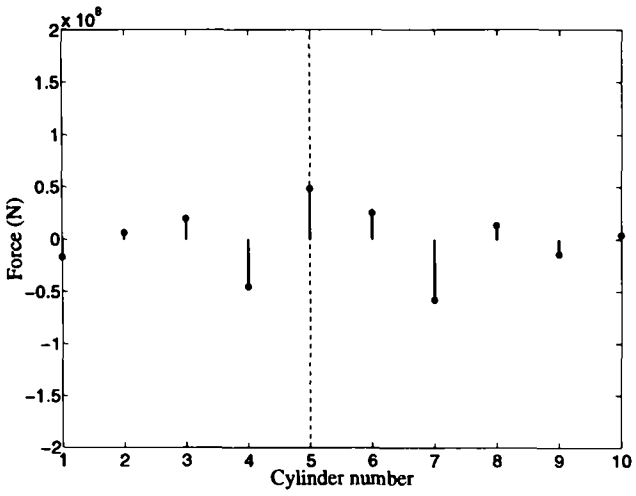

(a)

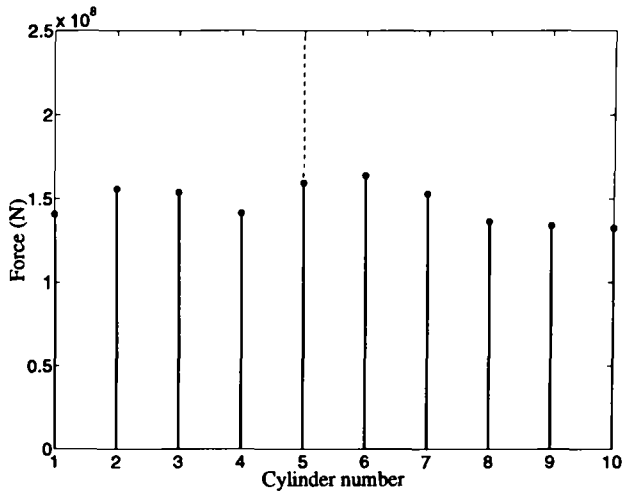

(b)

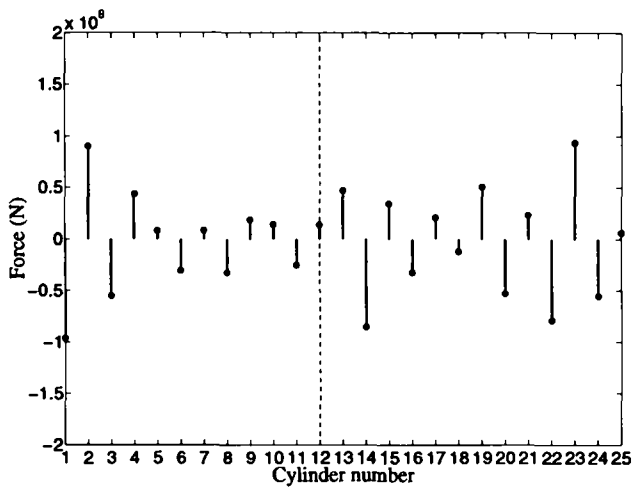

(c)

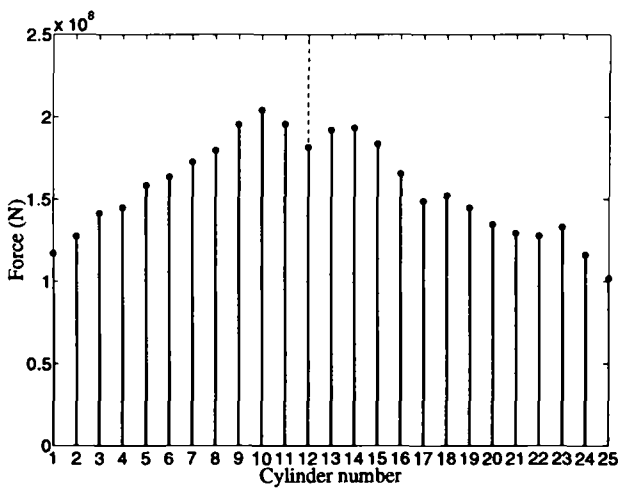

(d)

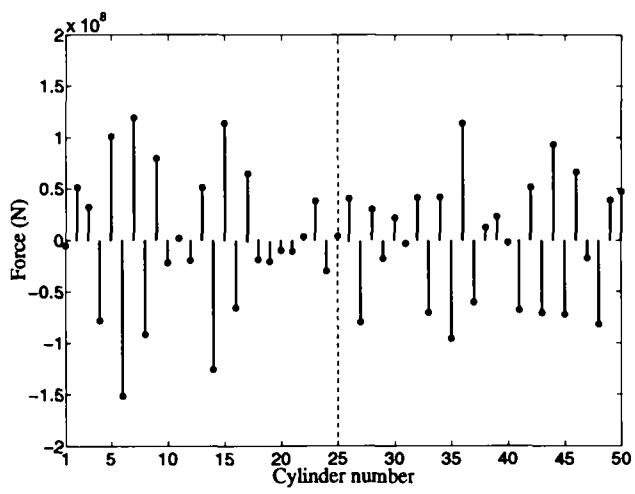

(e)

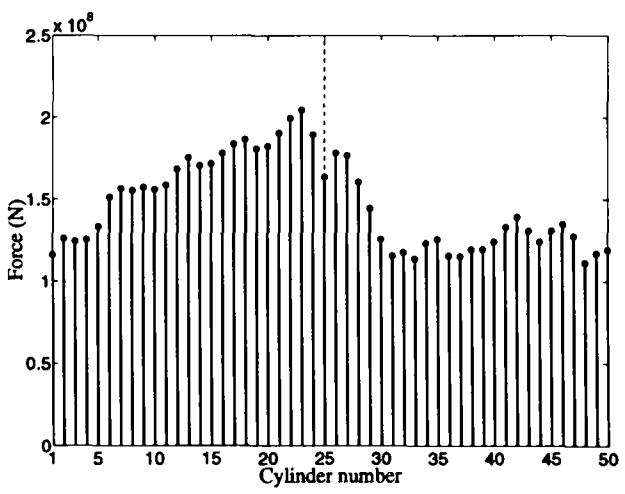

(f)

Figure 6.18: Initial force and maximum force magnitude on each cylinder in arrays of 10, 25 and 50 cylinders. A vertical dashed line shows the cylinder on which the NewWave is focused. a=15m, $2d$=120m ($a/d = 1/4$). (a), (c), (e): Initial force. (b), (d), (f): Maximum force magnitude

nitude for the 10-cylinder array is comparable to that for a single isolated cylinder, although the 25 and 50 cylinder arrays exhibit some degree of force magnification. The maximum force magnitudes for both the 25 and 50 cylinder arrays ($\sim$ 205MN) are approximately 25% greater than that on a single isolated cylinder. It would be difficult to draw any definite conclusions from these results alone as it is overwhelmingly likely that a different focus point will result in an increased cylinder loading. However, the results presented certainly suggest that the large force magnifications observed at critical wavenumbers for regular waves are not so severe when integrated over a continuous spectrum. This is what one would expect considering the narrow banded nature of the near-trapping peaks shown in Section 6.4.

The maximum force magnitude plots presented in Figure 6.18 could be useful for design purposes. One useful design exercise would be, perhaps, to identify the largest force acting on any cylinder, determine the time at which this occurs, and then compute the force on all other cylinders at this time.

The maximum force distribution possible as a result of NewWave loading could be sought by systematically focusing the NewWave at incremental positions along the x-axis. However, further insight into the maximum force distribution could be obtained without the need for such lengthy computation from the data presented in Figure 6.18. One would simply need to note the time at which the maximum cylinder force occurred, determine the position of the NewWave crest at this time, and finally compute all forces again for the NewWave focused at this position. This will almost certainly result in an increased force distribution.

The free surface elevation resulting from the diffraction of the same incident NewWave is now investigated. Firstly, a NewWave focused on a single isolated cylinder of radius 15m is considered. Figure 6.19 shows the free surface elevation along the x-axis at time $t = 0$ and a time history of the free surface elevation on the upstream face of the cylinder. In both cases the incident and total wave fields are shown. The maximum surface elevation is found to almost coincide with the focus time $t = 0$, indicating that diffraction effects introduce only a small phase shift ($\sim$ 1.6 seconds).

Following a similar sequence of investigation to that for force above, a three-cylinder array is now considered. Figure 6.20 presents plots of free surface elevation along the x-axis at time t=0 for the NewWave focused on each cylinder in turn.

The surface elevation on the upstream face of the focused cylinder for each case presented in Figure 6.20 is: (a) 15.5m; (b) 16.4m; (c) 17.2m. These values are comparable to the surface elevation on the upstream face of a single isolated cylinder (16.8m). The plots shown in

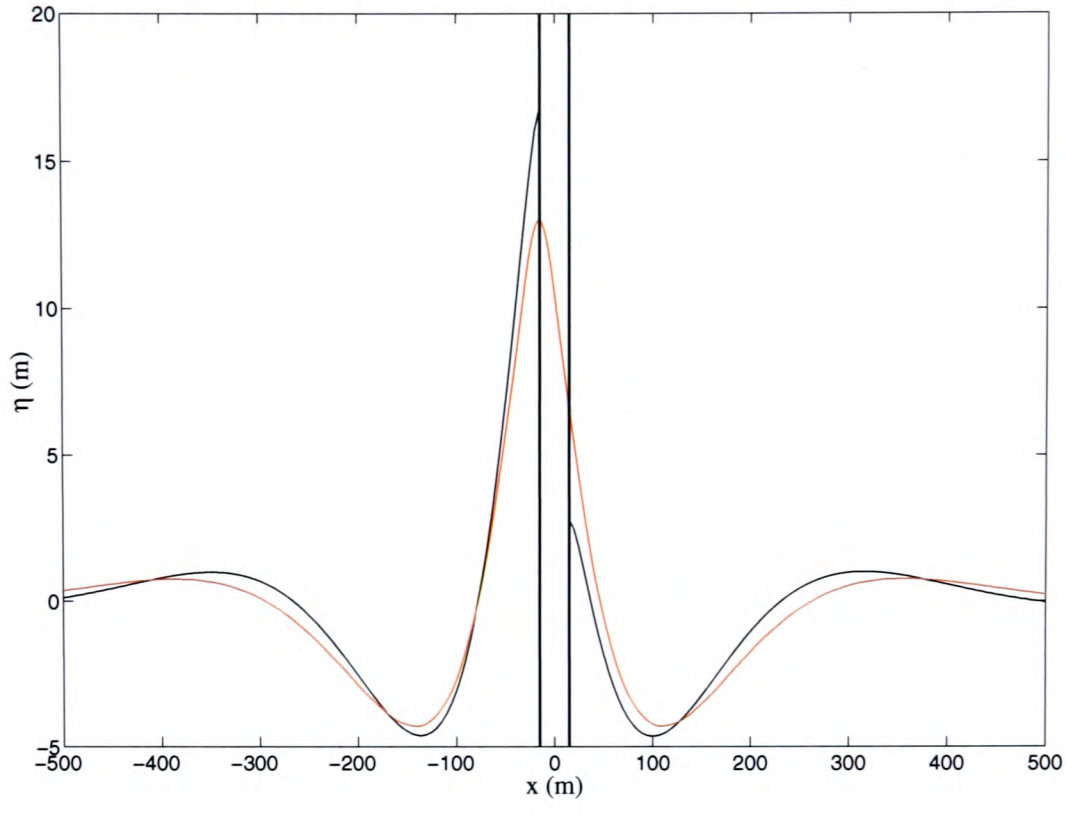

(a) Initial free surface elevation along x-axis

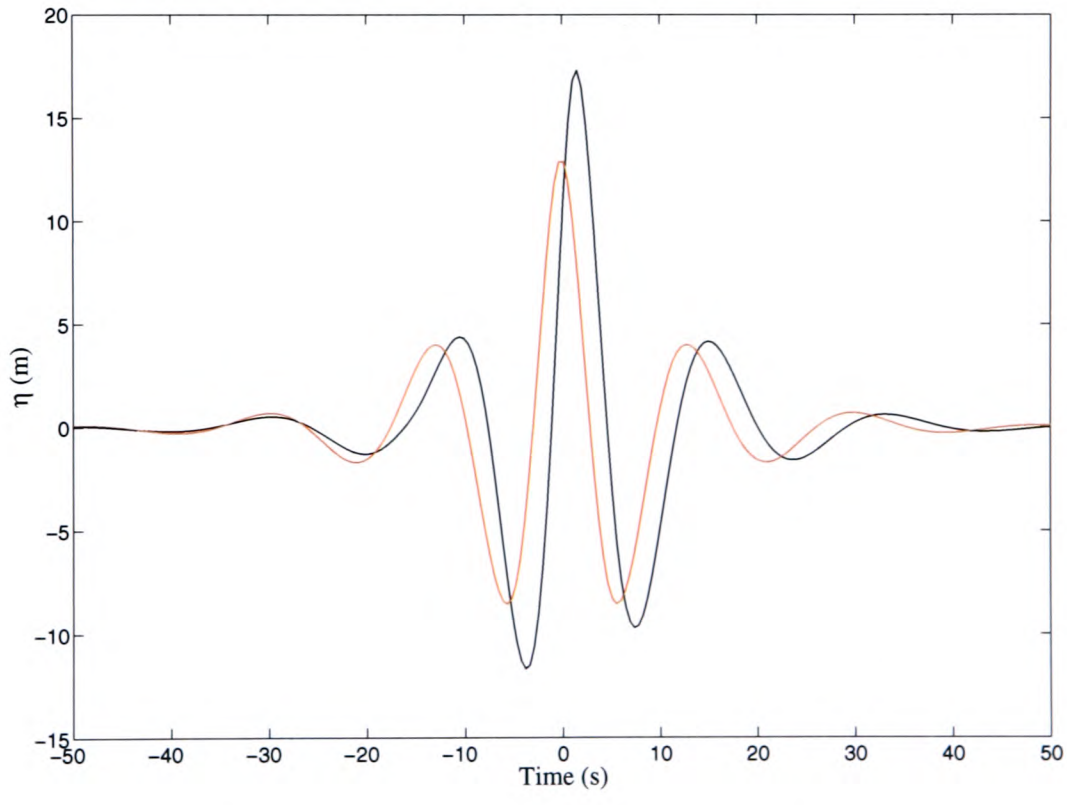

(b) Free surface elevation time history on upstream face

Figure 6.19: Free surface elevation resulting from a NewWave incident upon a single isolated cylinder (black line). a=15m. The incident NewWave is also shown (red line). The vertical solid lines on plot (a) represent the cylinder walls.

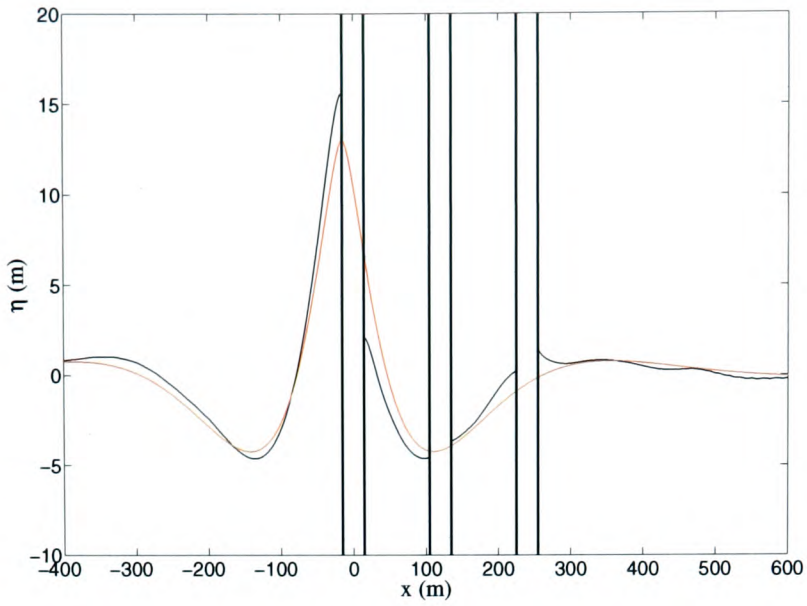

(a) NewWave focused on first cylinder

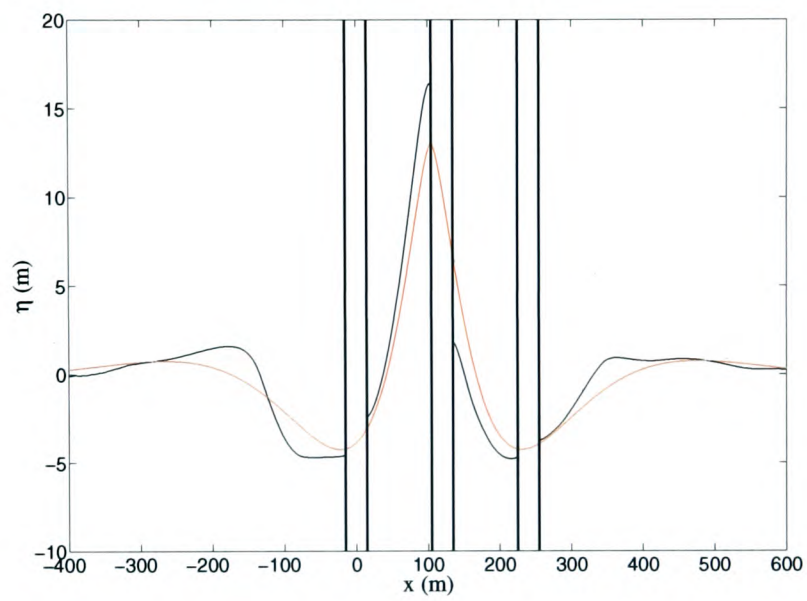

(b) NewWave focused on second cylinder

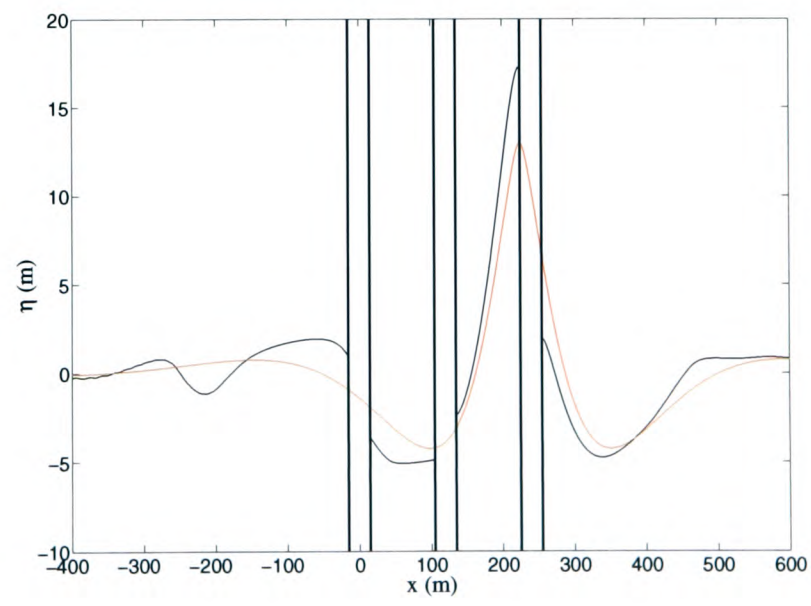

(c) NewWave focused on third cylinder

Figure 6.20: Free surface elevation resulting from a NewWave incident upon a three-cylinder array (black line). a=15m, $2d$=120m (a/d=1/4). The incident NewWave is also shown (red line). The vertical solid lines represent the cylinder walls.

Figure 6.20 are largely consistent with the force values given in Table 6.3. Note that the initial force on the second cylinder, when a NewWave is focused on the first, is positive even though the wave elevation on the downstream face of the second cylinder appears slightly greater than that on its upstream face. This is again because the elevation incorporates all Fourier harmonics whereas the force only depends on the terms $n = \pm 1$.

Similar results to those shown in Figure 6.20 have been produced for an array of 10 cylinders with $a/d = 1/4$ and no significant magnifications of the free surface have been noted.

It would be interesting to investigate a NewWave, composed of components from the same spectrum, incident upon a more closely spaced array of cylinders (e.g. $a/d = 1/2$). The radius and spacing values studied here (a=15m, $2d$=120m) are of more practical interest and hence the reason for including this configuration.

The spectrum studied in this section was chosen as it provides an accurate representation of a realistic sea state. However, it would also be useful to investigate the diffraction magnification effects for a spectrum with a peak frequency corresponding to one of the near-trapping frequencies identified in Section 6.4.1 for $a/d = 1/4$ (Figure 6.5). An incident NewWave based on such a spectrum is likely to result in larger magnifications than those noted thus far. Furthermore, for a spectrum with a peak frequency corresponding to a near-trapping frequency, it would be useful to investigate the effect the bandwidth of the spectrum has on extreme magnifications. The Pierson-Moskowitz spectrum considered in this section is relatively broad banded and so it would be interesting to consider a JONSWAP spectrum for varying bandwidths.

6.5.2 LUNA GEOMETRY

Firstly in this section the free surface diffraction effects resulting from focusing an incident unidirectional NewWave at a specific location along the x-axis, x_0, are studied. Results for a NewWave focused on the upstream columns (x_0=-34.05m) and at the centre of the structure (x_0=0) are presented. Since the most extreme surface elevations beneath the LUNA structure are of most interest for airgap design, a novel approach proposed by Ohl et al. (2001b) for computing the maximum possible free surface elevation in the vicinity of an array of cylinders is then developed for the linear diffraction of an incident NewWave.

A sea-state characterised by Hs=9.9m and Tz=11.1s, corresponding to storm conditions at the location of the LUNA platform, is now investigated. A NewWave amplitude, A_{nw}, of 11m is used, which is a realistic extreme crest amplitude for this sea state. For all results presented in this section, the linear diffracted wave field in the vicinity of the LUNA structure

is computed at 0.1m x and y increments.

Figures 6.21 and 6.22 show contour and surface plots for the linear elevation in the vicinity of the LUNA columns for an incident unidirectional NewWave with x_0=-34.05m and x_0=0 respectively. For each case the peak elevation (η_{max}), corresponding surface magnification (η_{max}/A_{nw}) and the location at which it occurs (x_{max}, y_{max}) are given in Table 6.4. The magnifications recorded are much smaller than those computed for the diffraction of regular waves by the LUNA columns at near-trapping (Table 6.1). It is clear from the surface plots in Figures 6.21 and 6.22 that diffraction effects for the particular NewWave considered are small.

x_0	η_{max}	η_{max}/A_{nw}	x_{max}	y_{max}
-34.05	11.54	1.05	-36.1	$\pm$44.3
0	12.61	1.15	-2.0	$\pm$18.4

Table 6.4: Peak linear surface elevations and their locations for a NewWave incident upon the LUNA structure. Peak elevations are given to two decimal places.

The maximum surface elevation resulting from the linear diffraction of an incident NewWave is now investigated. For this purpose, an expression is derived that allows the maximum possible free surface elevation at a given point (x, y) to be calculated.

If the amplitude of each spectral component in Equation 6.2 is fixed, then a random phase angle, ζ_n, can be introduced to enable the free surface elevation for an imperfectly focused NewWave to be calculated. This gives:

$$\begin{aligned}\eta_D(x,y,\tau) &= \frac{\alpha}{\sigma^2}\sum_{n=1}^{N} C_n \,\Re\left\{\phi_n(x,y)e^{-i(\kappa_n x_0+\omega_n\tau-\zeta_n)}\right\} \\ &= \frac{\alpha}{\sigma^2}\sum_{n=1}^{N} C_n \,\Re\left\{\phi_n(x,y)e^{-i(\kappa_n x_0+\omega_n\tau)}e^{i\zeta_n}\right\} \qquad (6.3)\end{aligned}$$

such that $0 \leq \zeta_n \leq 2\pi$ and $\mid e^{i\zeta_n} \mid = 1$.

There exists a value of this phase angle, ζ_n, that allows the diffraction coefficient for each component to reach its maximum value, $\mid \phi_n(x,y) \mid$, at the same position and time. This phase angle is $\zeta_n^{'}$ where:

$$e^{i\zeta_n^{'}} = e^{i\kappa_n x}\frac{\mid \phi_n(x,y) \mid}{\phi_n(x,y)}. \qquad (6.4)$$

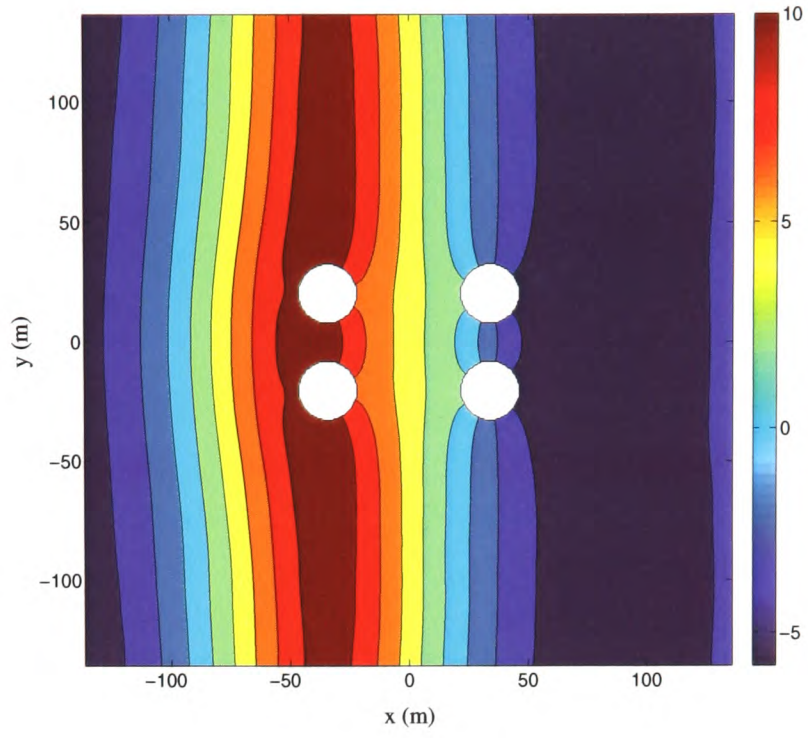

(a) Contour plot

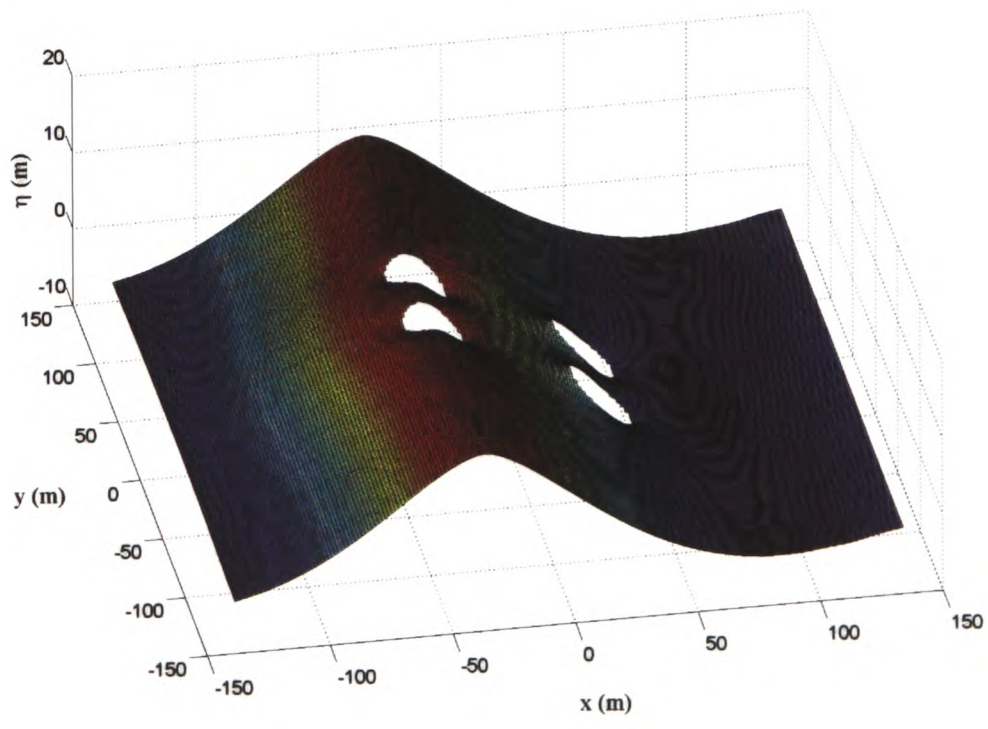

(b) Surface plot

Figure 6.21: Surface elevation around the LUNA structure for an incident NewWave focused on the upstream columns (x_0=-34.05m). $t = t_0 = 0$.

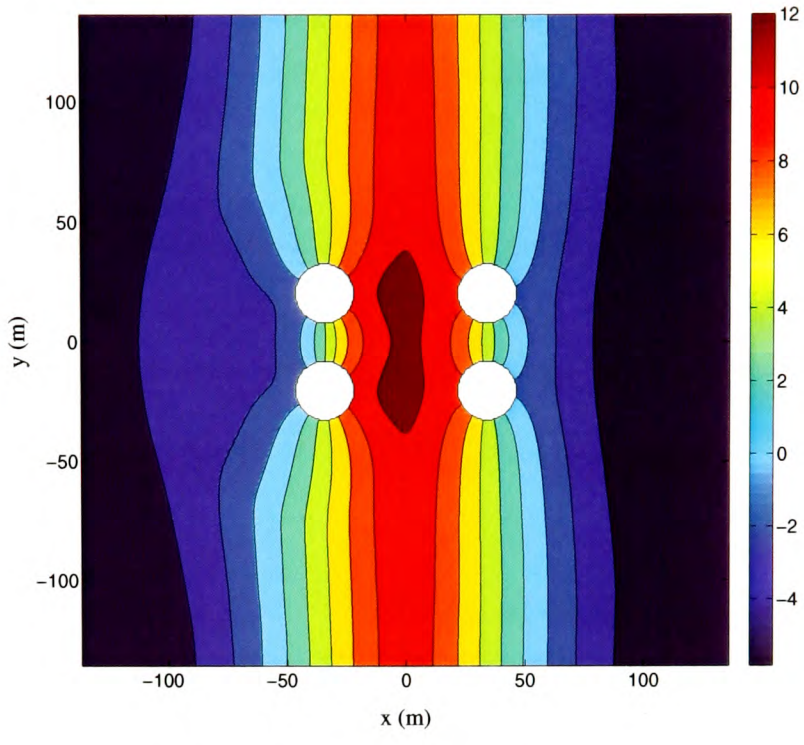

(a) Contour plot

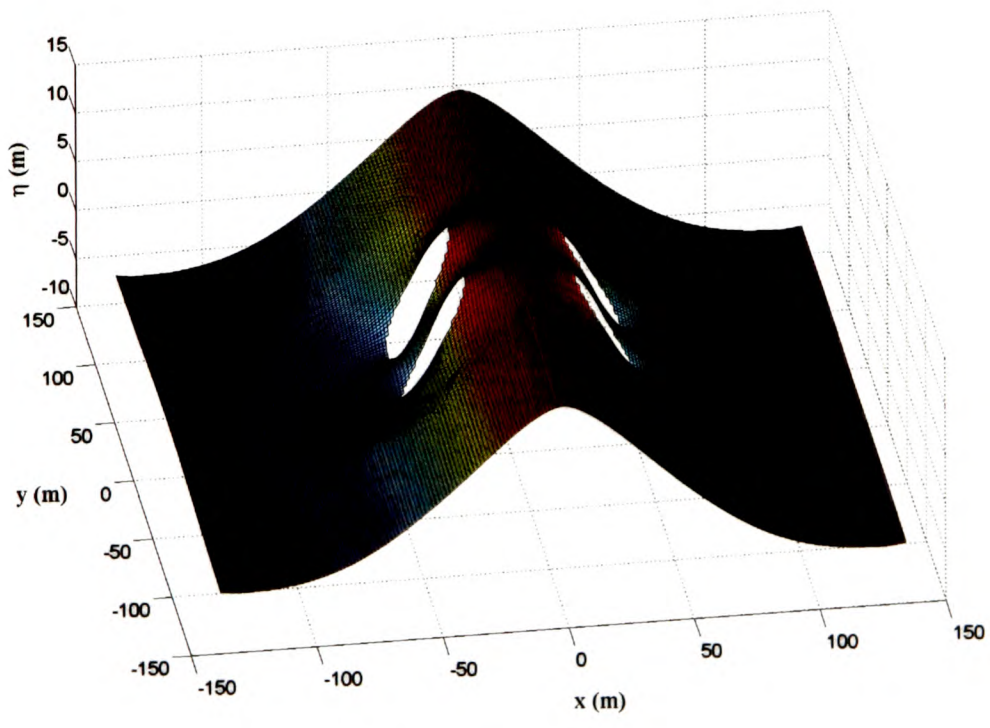

(b) Surface plot

Figure 6.22: Surface elevation around the LUNA structure for an incident NewWave focused at the centre of the structure (x_0=0). $t = t_0 = 0$.

Substituting Equation 6.4 into Equation 6.3 produces the phase-modified NewWave:

$$\eta_D(x,y,\tau) = \frac{\alpha}{\sigma^2}\sum_{n=1}^{N} C_n \,\Re\left\{ \mid \phi_n(x,y) \mid e^{-i(\kappa_n X + \omega_n \tau)} \right\}, \tag{6.5}$$

where $X = x - x_0$. If the point of computation is then assumed to be the focused point, with $x = x_0$ and $t = t_0$ such that $X = 0$ and $\tau = 0$, Equation 6.5 becomes:

$$\eta_M(x,y) = \frac{\alpha}{\sigma^2}\sum_{n=1}^{N} C_n \mid \phi_n(x,y) \mid . \tag{6.6}$$

Equation 6.6 allows the computation of the maximum possible free surface elevation at a given point (x, y) for the linear diffraction of an incident NewWave (of fixed amplitude components but arbitrary phasing).

As noted by Ohl et al. (2001b), for the relatively simple case of a single cylinder, the diffracted extreme crests from Equation 6.2 will equal the maximum free surface elevations from Equation 6.6. However, for multiple cylinder arrays interaction effects between the cylinders become critical and diffraction phase shifting defocuses the incident extreme waves. Therefore the maximum elevations around the LUNA structure computed using Equation 6.6 will be larger than those predicted using Equation 6.2 (Table 6.4).

Equation 6.6 is used to produce Figure 6.23, which shows contour and surface plots of the maximum possible free surface elevation in the vicinity of the LUNA columns for the NewWave considered in this section. The maximum possible surface elevation is 14.53m, which corresponds to a 32% magnification of the NewWave amplitude. This extreme magnification occurs on the upstream faces of the two front columns.

Larger surface magnifications are indeed now computed in comparison to those recorded in Table 6.4, although they are still considerably smaller than the surface magnifications associated with near-trapping for incident regular waves.

A number of further linear results, in addition to those presented in this section, have been produced for NewWaves incident upon the LUNA columns. The effect of H_s and T_z on the diffracted wave field have been examined, and the contributions to the total surface magnifications from the upstream and downstream columns have been computed.

It would be interesting to study the diffraction of a NewWave embedded into a random background and observe the effect of the random background on peak surface magnifications. This can be achieved using the so-called constrained NewWave, which embeds an extreme crest

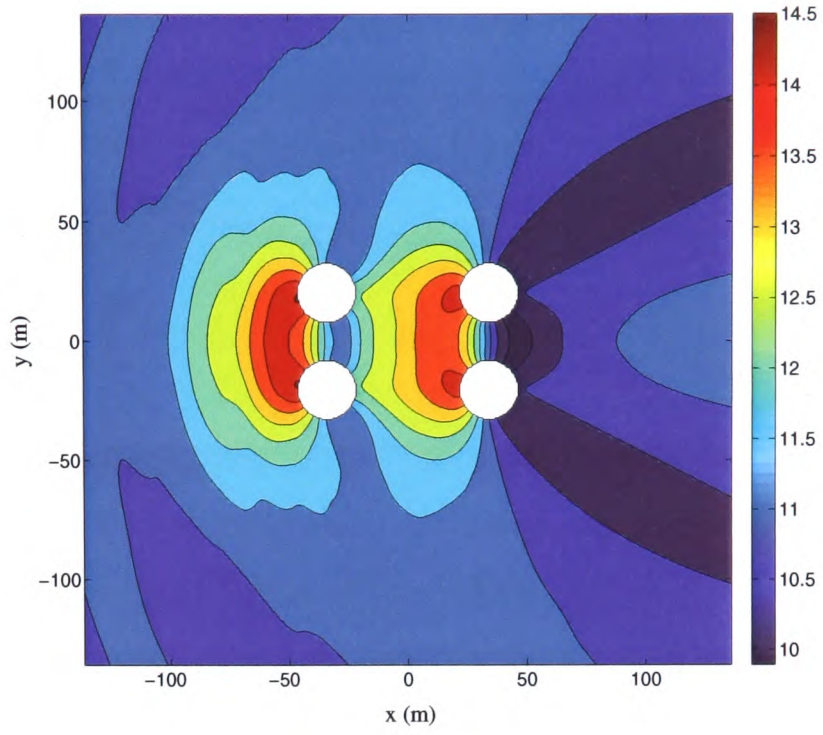

(a) Contour plot

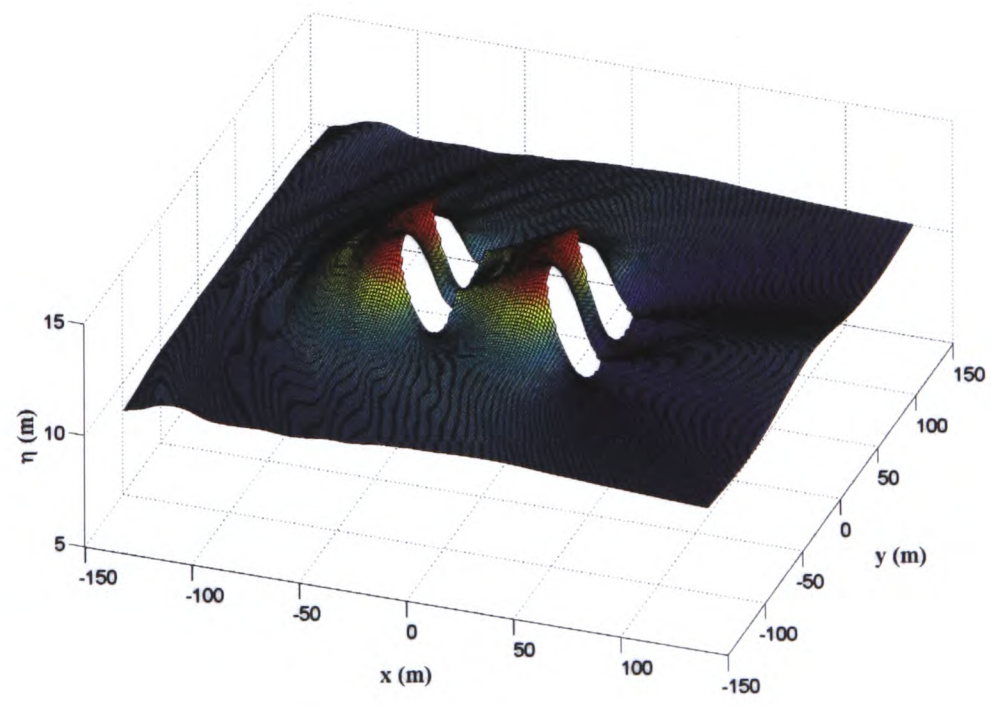

(b) Surface plot

Figure 6.23: Maximum possible surface elevation around the LUNA structure for an incident NewWave.

into a random sequence in such a way that the overall sequence is almost indistinguishable from a purely random occurrence of a large wave. Taylor, Jonathan, and Harland (1997) outline a procedure for achieving this.

As suggested for diffraction by a linear array of cylinders, it would be useful to examine the surface magnification effects resulting from an incident NewWave based on a JONSWAP spectrum. In Chapter 7 diffraction results for an incident NewWave based on a Gaussian spectrum, which has been fitted to a JONSWAP peak, are presented for the LUNA structure (four columns mounted on a caisson).

6.6 Directionally spread incident waves

Real seas are, of course, directionally spread and the importance of multidirectional wave effects to the accurate prediction of surface elevations around a diffracting body is widely recognised. Buldakov et al. (2004) studied the diffraction of a directionally spread focused wave group by a single bottom mounted cylinder, and found the diffracted wave field for the directionally spread case to be qualitatively similar to that of the unidirectional case except with smaller amplitudes. Indeed, it is commonly perceived by the offshore industry that the most extreme diffraction magnification effects result from an incident unidirectional wave field. However, although this may be true for many structures, here it is postulated that the effect of directional spreading is dependent upon the structural configuration and that in some cases directional spreading may lead to an enhancement of the diffracted free surface. For example, the LUNA columns have x and y spacings of 2.8 and 1.7 column diameters respectively, and so for waves incident along the x-axis the close proximity of the two upstream columns would restrict wave energy passing between them, which in turn may limit the peak magnifications achieved between the columns. In this case, spreading the incident wave field would allow increased wave energy to pass between the upstream and downstream columns and that could possibly lead to increased magnifications between the columns.

The effect of directional spreading on the linear surface magnification in the vicinity of the LUNA structure is now investigated. Incident regular waves are first considered and then incident NewWaves. Wave interaction with the columns alone is studied using the linear analytical diffraction solution.

Wave directionality is introduced by considering a directional spectral density function, which is defined as:

$$S(f,\theta) = S(f)G(\theta,f) \tag{6.7}$$

where $S(f)$ is the one-dimensional spectral density function and $G(\theta, f)$ describes how the energy at frequency f is distributed with angle θ. It follows from the definition of G that:

$$\int_{-\pi}^{+\pi} G(\theta,f)\mathrm{d}\theta = 1. \tag{6.8}$$

In this study directional spreading is introduced into the incident wave field using a wrapped normal spreading function, given by (Tucker and Pitt 2001):

$$G(\theta,f) = \frac{1}{\psi\sqrt{2\pi}} \exp\left[\frac{-(\theta-\theta_M)^2}{2\psi^2}\right] \quad \text{for } -\infty < (\theta-\theta_M) < \infty \tag{6.9}$$

where ψ is the spreading angle and θ_M is the mean wave direction, which can both be functions of frequency, f. In practical engineering applications it is common to simplify such a frequency dependent spreading function by assuming that ψ and θ_M are independent of frequency. This simplified approach is based on integrated parameters such as an averaged spreading angle, and is implemented in this section.

Spreading angles, ψ, from 0 to 45 degrees for 5-degree increments are considered and a mean wave direction, θ_M, of 0 degrees is used. The incident wave energy is spread over nine direction components between -2.5ψ and +2.5ψ. Tests have been carried out to ensure that nine direction components are sufficient to capture the spread nature of the incident wave field defined by $G(\theta, f)$. A regular wave frequency of 0.08Hz is examined, which corresponds to the period used for the experimental regular wave tests (T=12.7s).

There is clearly a considerable computational burden associated with the diffraction of a directionally spread wave field, especially for incident NewWaves, and hence the spatial resolution considered is restricted to a 100m by 100m region around the LUNA structure (-50m< x <50m, -50m< y <50m) and the linear diffracted wave field is computed at 0.5m x and y increments. Therefore, a total of 360,000 linear diffraction coefficients must be computed for each frequency and spreading angle.

The maximum linear surface magnification ($|\eta|_{max}/A$) and the location at which it occurs (x_{max}, y_{max}) are noted for each spreading angle in Table 6.5. Contrary to the above postulation, as the degree of wave spreading is increased the maximum linear surface magnification occurring anywhere in the vicinity of the structure reduces. From the spatial resolution con-

sidered, the location of the peak response is found to be reasonably insensitive to the degree of spreading; the location is shifted upstream by only 1.5m as the spreading angle increases from 0 to 45 degrees. The table also shows that the solutions computed for the directionally spread waves approach the corresponding unidirectional solution as the spreading angle is reduced.

ψ (degrees)	$\lvert\eta\rvert_{max}/A$	x_{max} (m)	y_{max} (m)
0	1.502	3.5	0
5	1.499	3.5	0
10	1.491	3.5	0
15	1.478	3.0	0
20	1.463	3.0	0
25	1.447	3.0	0
30	1.431	2.5	0
35	1.416	2.5	0
40	1.403	2.0	0
45	1.392	2.0	0

Table 6.5: Magnitudes and locations of the maximum linear surface magnifications around the LUNA structure for incident directionally spread regular waves. Surface magnifications are given to three decimal places.

From Section 6.3 it can be inferred that the caisson will have an appreciable effect on the total linear diffracted wave field for incident regular waves at f=0.08Hz. Therefore, it would be interesting to repeat the above analysis at f=0.08Hz using DIFFRACT for wave interaction with the entire LUNA structure. A number of frequencies have been considered in this study for wave interaction with the columns alone, including frequencies for which the effect of the caisson is deemed negligible, and the peak surface magnifications are still found to reduce as the spreading angle is increased.

The diffraction of an incident directionally spread NewWave field by the LUNA structure is now considered. A NewWave based on a Pierson-Moskowitz spectrum with H_s=9.9m and T_z=11.1s is again used, together with a linear NewWave amplitude, A_{nw}, of 11m.

An incident directionally spread NewWave can be described as a superposition of monochromatic waves of different frequencies approaching the structure from different directions. The principal difference between a directionally spread NewWave and the unidirectional analogue is the reduction of wave amplitude in the transverse (along crest) direction. This amplitude reduction becomes larger for larger spreading angles. The spatial profile of a directionally spread NewWave based on the frequency spectrum and spreading function considered in this section is shown in Figure 6.24 for a spreading angle of 30 degrees.

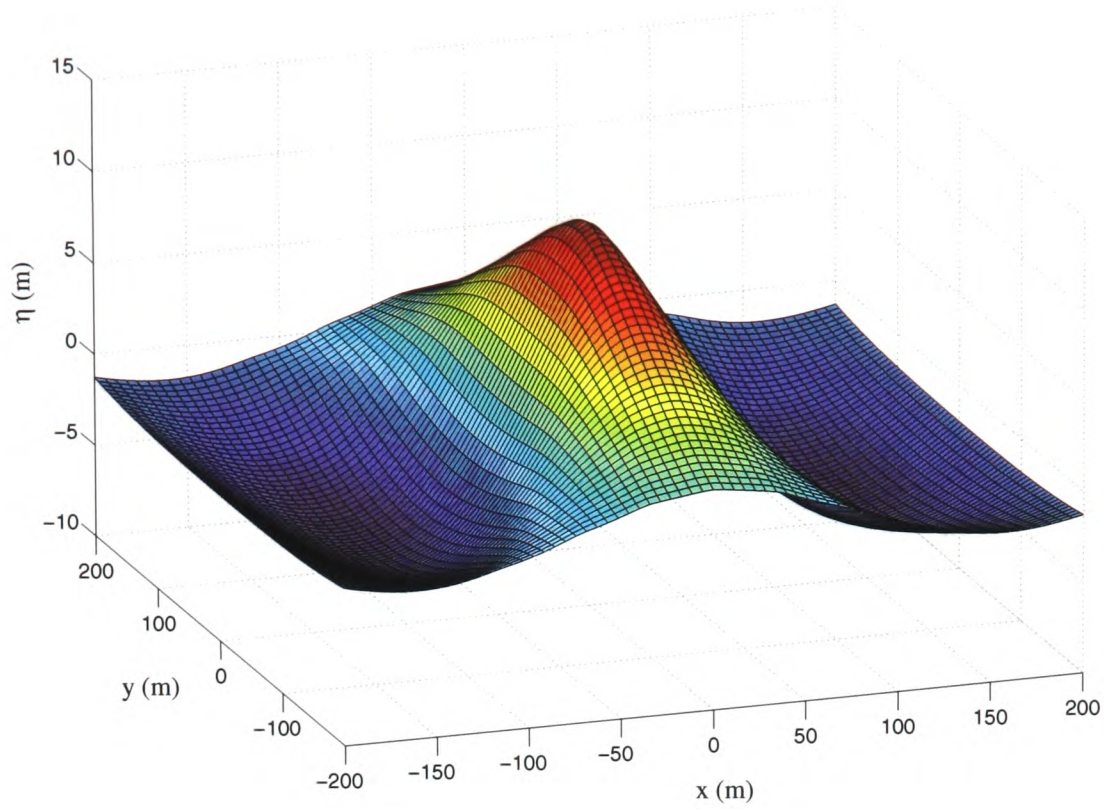

Figure 6.24: Spatial profile of a directionally spread NewWave. $\psi = 30°$.

As for the regular wave analysis, a mean wave direction of 0 degrees and spreading angles from 0 to 45 degrees are considered. Because the linear diffraction of a directionally spread NewWave involves the linear superposition of diffraction coefficients for each frequency and direction, there is a considerable computational burden associated with this calculation. In an effort to minimise the computation time whilst retaining accurate results, the number of frequencies considered has been reduced from 200 (used for the unidirectional calculations) to 50. Following tests at particular points around the structure, it has been found that the reduction in the number of frequency components has a very small effect on the resultant diffracted wave field.

Equation 6.6 is used to compute the maximum possible surface magnification at each location around the structure. For each spreading angle the peak elevation (η_{max}), corresponding surface magnification (η_{max}/A_{nw}) and the location at which it occurs (x_{max}, y_{max}) are given in Table 6.6.

Increasing the spreading angle is again found to reduce the peak surface magnifications; increasing the spreading angle from 0 to 45 degrees reduces the peak magnification by 6%. The effect of directional spreading on the locations of the peak magnifications is small, with the peak magnifications in each case occurring close to the upstream faces of the two front columns.

ψ (degrees)	η_{max} (m)	η_{max}/A_{nw}	x_{max} (m)	y_{max} (m)
0	14.532	1.32	-46.5	±18
5	14.519	1.32	-46	±18
10	14.466	1.32	-46	±18
15	14.382	1.31	-46	±18
20	14.276	1.30	-46	±18
25	14.158	1.29	-46	±17.5
30	14.034	1.28	-46	±17.5
35	13.907	1.26	-46	±17
40	13.778	1.25	-45.5	±16.5
45	13.652	1.24	-45.5	±16.5

Table 6.6: Magnitudes and locations of the maximum linear surface magnifications around the LUNA structure for an incident directionally spread NewWave. Surface magnifications are given to three decimal places.

Therefore, based on linear diffraction theory alone, an incident unidirectional wave field is found to excite the largest magnifications around the LUNA structure. However, the second order diffraction of a directionally spread wave field should also be investigated before any definitive conclusions are drawn on this matter.

The effects of directional spreading identified from the experimental wave tank tests are discussed in Chapter 8 Section 8.3.5.

6.7 Conclusions

The analytical and numerical linear diffraction solutions implemented in this study have been extensively verified against published data before being used to investigate the linear diffraction effects around arrays of bottom mounted columns and the LUNA structure.

The numerical diffraction solution was used to examine the effect of caisson height on the linear diffracted wave field in the vicinity of the LUNA structure. The effect of caisson height was found to be dependent on the frequency of the incident waves and the location around the structure.

The diffraction of regular waves incident upon linear arrays of columns and the LUNA configuration of columns was studied. Large magnifications in force and free surface elevation were found to exist for incident regular waves at critical frequencies, which could have serious practical implications for column-supported structures. However, the bandwidths of these magnification effects were found to be quite narrow, especially for large arrays of columns, and so the integrated effects over a continuous spectrum are not likely to be severe. The

analysis presented in this chapter for NewWaves incident upon arrays of columns supports this.

The effects of directionally spreading an incident wave field on the diffracted wave field around the LUNA structure were explored. The linear results presented suggest that a unidirectional wave field will excite the largest magnifications around the LUNA structure.

Many further linear diffraction results have been generated in addition to those presented in this Chapter, some of which have already been discussed. One set of results not mentioned thus far examines transients in wave diffraction for arrays of cylinders. For example, the time needed to build up the large free surface magnifications between the cylinders at near-trapping has been investigated by considering an incident wave field generated by a piston wavemaker (Joo et al. 1990). This work is outlined by Eatock Taylor et al. (2006).

Chapter 7

Second order diffraction results

7.1 Introduction

Second order water wave diffraction results generated using DIFFRACT are presented and discussed in this chapter. Firstly, a description of the meshing scheme implemented in the numerical solution procedure is given, followed by a discussion on convergence testing in achieving reliable second order results.

For the case of incident monochromatic waves, the second order wave field in the vicinity of the LUNA structure is investigated and comparisons are made with the linear wave field. The phenomenon of near-trapping at second order and the effect of a caisson on the second order wave field are also investigated. Progressing towards a more realistic representation of the ocean surface, the second order sum and difference contributions for incident bichromatic waves are compared against published data. Finally, a NewWave incident upon the LUNA structure is considered.

Further second order results for the LUNA structure are presented in Chapter 8, where comparisons are made with the experimental data.

7.2 Meshing

The boundary element method implemented by DIFFRACT requires the surface of the diffracting body to be discretised into a number of elements (or panels). The following information is defined for the body surface mesh:

1. The number of planes of symmetry used.
2. The number of elements used.
3. The number of nodes used.

4. The coordinates of each node (Cartesian or polar coordinates can be used).

5. A unit vector normal to the body surface at each node.

6. The number of nodes surrounding each element.

7. The ordering of the nodes and vectors around each element.

This information is provided for the full body surface for zero planes of symmetry, for half of the body surface for one plane of symmetry and for quarter of the body surface for two planes of symmetry. It is noted that for nodes along edges between two surfaces (e.g. along the edges between the horizontal top and vertical sides of a rectangular box caisson) there will be two normal vectors associated with each node.

In addition to the body surface, a mesh for the inner water free surface (i.e. the free surface in the space occupied by the body) and the outer water free surface (i.e. the free surface around the body) must also be created. Information (2), (4) and (6) from the list above is required on the free surface.

A number of mesh generation programs are available to create such meshes. However, because of the specific format requirements of the DIFFRACT input mesh files and to have full flexibility over all meshing parameters to help achieve convergence, a new meshing program has been developed for wave diffraction by a bottom mounted single cylinder, an array of bottom mounted cylinders and an array of cylinders mounted on a rectangular subsurface caisson. The meshing program, which is implemented using MATLAB, uses quadrilateral elements on the body surface and outer free surface and quadrilateral and triangular elements on the inner free surface.

For the diffracting bodies considered in this chapter, namely a single cylinder, four cylinders arranged at the vertices of a square mounted on the sea bed and four cylinders arranged at the vertices of a rectangle centrally mounted on a rectangular caisson, two planes of symmetry can be used to generate the mesh. This greatly simplifies the meshing scheme and reduces the total number of elements required to achieve convergence. The meshes shown in this section are for quarter of the solution domain.

The array sizes defined within the DIFFRACT code restrict the mesh sizes that can be implemented in the numerical procedure. The critical meshing limits for this study are: (1) the body surface mesh can have a maximum of 1500 nodes and 1500 vectors; (2) the outer free surface mesh can have a maximum of 500 elements.

Figure 7.1 shows the body surface mesh and free surface meshes for wave diffraction by a single cylinder with $h/a = 3$. The number of elements used in Figure 7.1 has been chosen for illustrative purposes only. The elemental radial length in the outer free surface mesh increases gradually with increasing distance from the cylinder and the elemental vertical length in the body surface mesh increases with increasing distance from the free surface. The purpose of varying elemental length (controlled by a fixed factor) is to maximise the number of elements (for a specified total number of elements) close to the body and near the free surface where the potential will exhibit the most rapid change.

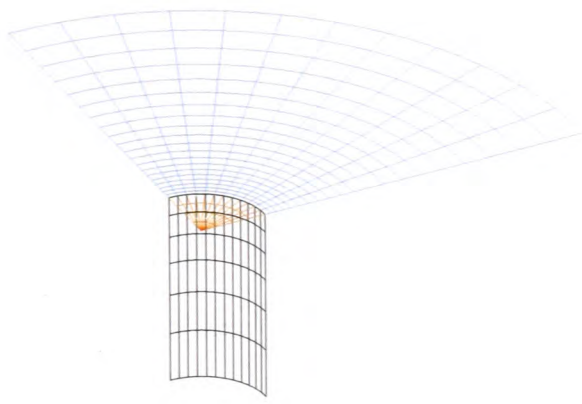

(a) Complete mesh

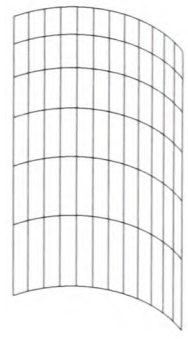

(b) Body surface mesh

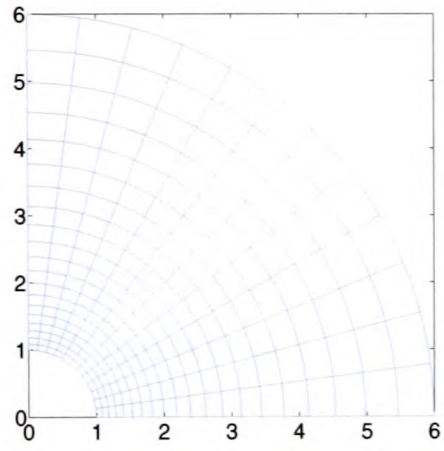

(c) Outer free surface mesh

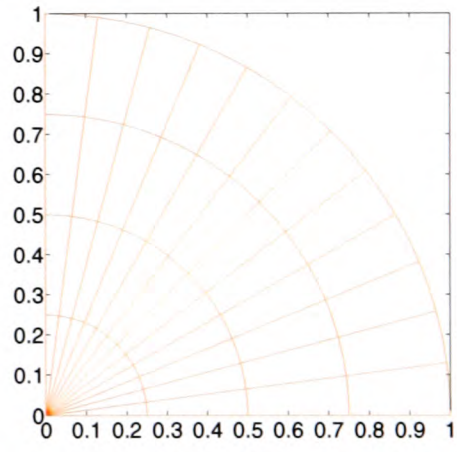

(d) Inner free surface mesh

Figure 7.1: Mesh for a single cylinder ($h/a = 3$).

The following meshing parameters are varied when testing for convergence or attempting to achieve convergence in a shorter time:

- The number of radial elements in the inner and outer free surface meshes.
- The number of circumferential elements.
- The variation of the elemental radial length with distance from the diffracting body in the outer free surface mesh.

- The variation of the elemental vertical length with distance from the free surface in the body surface mesh.

The required size of the outer free surface mesh and its effect on the convergence properties of the second order calculation are not well understood. Chau (1989) recommended that the outer radius (R_{out}) must be at least twice the water depth to achieve convergence for a fixed diffracting body. Following a number of tests using the DIFFRACT code for bichromatic waves, Kernot (1995) concluded that R_{out} should be at least as large as the larger wavelength. These two statements should only serve as guidelines in the present study as the conclusions made by Chau and Kernot are founded on a limited number of test cases and the required size of the outer free surface is likely to depend on the specific diffracting body considered.

The body surface mesh and free surface meshes for a four-cylinder array are now discussed. Figure 7.2 shows the body surface mesh and free surface meshes for wave diffraction by an array of four bottom mounted cylinders arranged at the vertices of a square ($a = 1$, $R = 4$, $h = 3$). The mesh shown in Figure 7.2 is used later in this chapter to achieve converged results for an incident wave field defined by $\kappa a = 0.468$ and $\beta = \pi/4$.

For the LUNA structure, where the cylinders are arranged at the vertices of a rectangle, it becomes more difficult to achieve convergence at second order. The principal reason for this is the difficulty associated with creating an outer free surface mesh with desirably shaped quadrilateral elements (e.g. with aspect ratios $\leq\sim 2$) around the full circumference of the cylinder. For example, in each quadrant the elements in the region between the cylinder and the closest axis become long and thin. Also, the elements along the x and y axes closest to the circular boundary are very skewed and are thought to cause the Jacobian in the numerical procedure (see Appendix A) to become ill-conditioned. In an effort to alleviate these problems the spacings of the nodes along the x and y axes are increased with increasing x and y. The elemental radial length in the outer free surface mesh is again increased with increasing distance from the cylinder and the elemental vertical length in the body surface mesh is increased with both the distance from the free surface and the distance from the caisson top in order to provide smaller elements closer to the free surface and caisson, which is where the change in potential is likely to be greatest. The elements on the caisson are regularly spaced.

Figure 7.3 shows the body surface mesh and free surface meshes for wave diffraction by the LUNA structure. Following extensive convergence testing involving approximately 100 different meshes, the mesh shown in Figure 7.3 is found to provide the best convergence

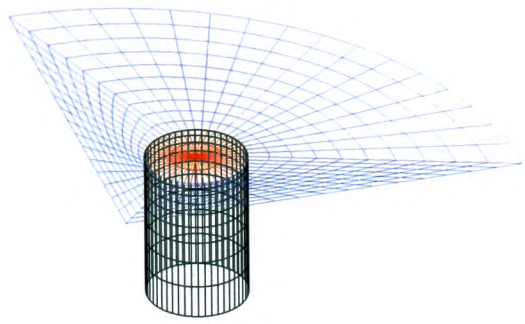

(a) Complete mesh

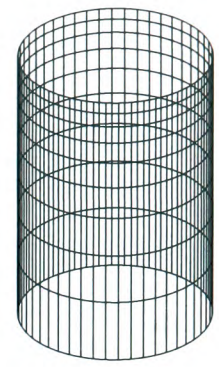

(b) Body surface mesh

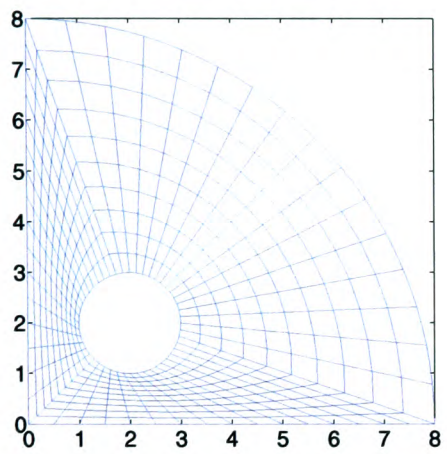

(c) Outer free surface mesh

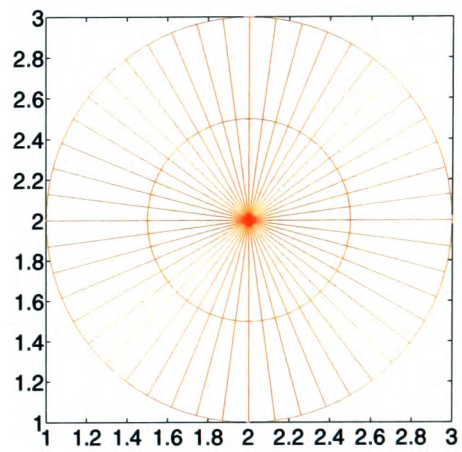

(d) Inner free surface mesh

Figure 7.2: Mesh for an array of four bottom mounted cylinders arranged at the vertices of a square ($a = 1$, $R = 4$, $h = 3$).

properties for the particular meshing scheme implemented and for the limits on the mesh size given above. Improved convergence properties at higher frequencies could be achieved by altering the DIFFRACT code to allow an increased number of elements/nodes to be used in the meshing and/or using both triangular and quadrilateral elements in the outer free surface mesh. It is clear from Figure 7.3 that it becomes very difficult to achieve desirably shaped quadrilateral elements across the entire free surface for an array of four cylinders arranged at the vertices of a rectangle, especially with the additional restriction on the allowable number of elements imposed by DIFFRACT. Teigen and Trulsen (2001) used WAMIT and its incorporated meshing facility to study second order wave diffraction by an array of four bottom mounted cylinders and made use of both triangular and quadrilateral elements in the outer free surface mesh.

7.3 Convergence

The ability to achieve converged second order results is dependent on both the structural configuration considered and the frequency content of the incident wave field.

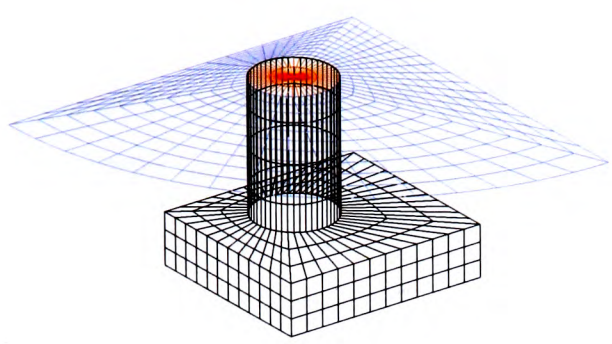

(a) Complete mesh

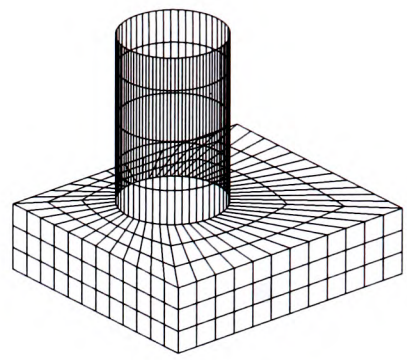

(b) Body surface mesh

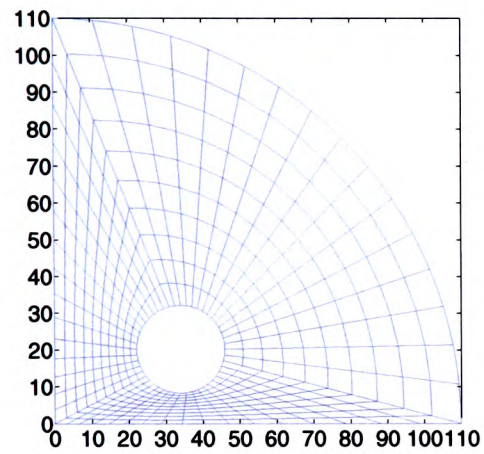

(c) Outer free surface mesh

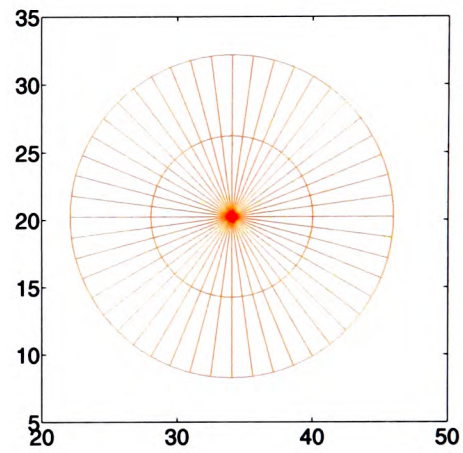

(d) Inner free surface mesh

Figure 7.3: Mesh for the LUNA structure.

As already discussed, using the meshing scheme described in Section 7.2 it becomes difficult to achieve desirably shaped quadrilateral elements on the outer free surface for an array of four cylinders arranged at the vertices of a rectangle. This problem is exacerbated for the LUNA geometry, where two pairs of cylinders are very close together. It is for this reason, coupled with the fact that DIFFRACT enforces a limitation on the number of nodes that can be used in the outer free surface mesh, that an array of four cylinders arranged at the vertices of a square has been studied in this chapter in addition to the LUNA structure. This will allow a wider range of frequencies to be examined and will hence provide a greater insight into the second order surface elevation characteristics around a four-cylinder structure.

Following extensive convergence testing for the LUNA geometry, it has been found that it becomes very difficult to achieve converged second order results for incident frequencies above 0.132Hz (corresponding to a wavenumber of 0.07m^{-1}). This is achieved using the mesh shown in Figure 7.3. Therefore, it is possible to produce converged results for the experimental regular wave frequency (0.08Hz) and for the linear near-trapping frequency (0.126Hz) although the consideration of an incident NewWave composed of components across a JONSWAP spectrum, which is the spectrum used to generate the irregular waves in the

model tests, is not possible. Therefore an incident NewWave based on a Gaussian spectrum is considered.

The development of a new mesh generator for the outer free surface incorporating triangular elements as well as quadrilaterals could help improve convergence for the LUNA structure. However, the use of triangular elements may increase the number of nodes used on the free surface and hence the benefits of such a mesh generator may only be realised if the maximum number of nodes allowed by DIFFRACT was increased.

Extensive convergence tests have been carried out for all of the results presented in this chapter and the author is confident that the results give an accurate representation of the second order wave field.

7.4 Incident regular waves

Firstly in this section second order results generated by DIFFRACT for regular waves incident upon a four-cylinder array are verified against published data. Following these tests, the second order surface elevation in the vicinity of the LUNA structure is examined and the relative significance of the linear and second order contributions is commented upon. The existence of a near-trapping phenomenon at second order is then examined for both an array of four cylinders arranged at the vertices of a square and the LUNA structure. Finally, the effect of a caisson on the second order diffracted wave field is investigated.

Further second order surface elevation results for regular waves incident upon the LUNA structure are presented in Chapter 8, where comparisons are drawn with the experimental data. In Chapter 8 conclusions are made on the accuracy of diffraction theory at predicting real wave measurements beneath the LUNA structure.

The notation used for the components of second order surface elevation is defined in Section 2.4.1 Chapter 2.

7.4.1 Solution verification

As outlined in Chapter 3, DIFFRACT has been extensively verified for second order wave diffraction by a single cylinder and ship shaped bodies. However, the code has not previously been used to generate wave elevation results for four-cylinder arrays and hence verification checks are needed for this geometry before proceeding. Therefore, second order results generated by DIFFRACT for the case of regular waves incident upon a four-cylinder array are verified against published data for the sum (potential and quadratic) contribution and an

analytical solution for the difference (quadratic) contribution.

The second order sum wave runup amplitude around a four-cylinder array has been computed and compared against results produced by Malenica et al. (1999), who used a semi-analytical approach. An array of four cylinders arranged at the vertices of a square is considered ($R = 4a$, $h = 3a$) and the incident wave field is defined by $\kappa a = 0.468$ and $\beta = 45$ degrees. The cylinders are numbered in a clockwise sense, starting with the cylinder at the location (x, y)=$(R/2, R/2)$ and the incident waves propagate in the positive x-direction. The quadratic difference component of the second order solution ($\eta_q^{(2-)}$ in Equation 2.75 Section 2.4 Chapter 2), which is a constant for monochromatic waves, is not considered by Malenica et al. Figure 7.4 shows the non-dimensional sum components of the second order wave runup amplitude around each cylinder. These results show excellent agreement with those produced by Malenica et al. and hence confirm the accuracy of DIFFRACT at computing second order sum components. Figure 7.4 will be referred to again in Section 7.4.3 as part of an investigation into second order near-trapping.

It is relatively straightforward to compute the second order quadratic difference component for incident monochromatic waves using Equation 2.78 (Section 2.4 Chapter 2) and the Linton and Evans linear diffraction solution (outlined in Chapter 3) to calculate the first order potential. This has been carried out for the test case studied by Malenica et al. (defined above) and the results are compared with the corresponding component computed by DIFFRACT in Figure 7.5. The analytical solution is found to be in good agreement with the numerical solution and hence the accuracy of DIFFRACT at computing the full second order runup around a four-cylinder array subject to incident regular waves has been confirmed.

For the consideration of airgap design, one is not only interested in the surface runup around the cylinders, but also surface elevations away from the cylinders. Unfortunately there are few, if any, published second order results available detailing the surface elevation between the cylinders of a four-cylinder array at frequencies for which DIFFRACT can achieve convergence at second order. However, previous use of DIFFRACT indicates that if accurate results have been produced on the surface of a diffracting body, then accurate results will also be produced away from the body. Both second order sum and difference surface elevation results computed by DIFFRACT have been compared with corresponding components computed using a semi-analytical solution (developed by E.V. Buldakov at Oxford) for a number of points in the vicinity of a single cylinder. Close agreement was found between the two sets of results for both incident regular waves and focused wave groups. In addition, Zang et al. (2003) used DIFFRACT to study the second order surface elevation on and around a ship shaped body

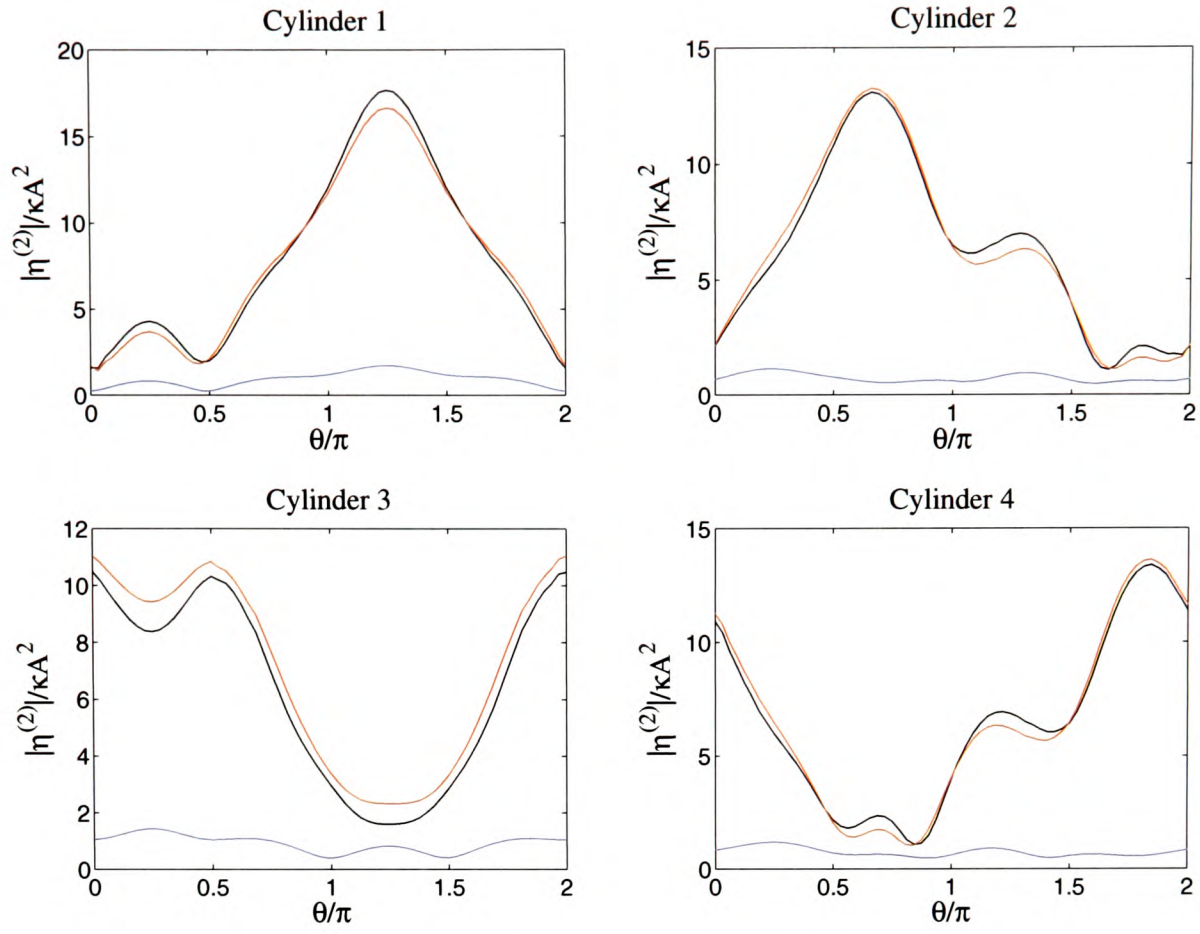

Figure 7.4: Non-dimensional sum components of the second order wave runup amplitude for regular waves incident upon an array of four cylinders arranged at the vertices of a square. $R = 4a$, $h = 3a$, $\kappa a = 0.468$ and $\beta = 45$ degrees. Black line: $|\eta^{(2+)}|/\kappa A^2$; red line: $|\eta_p^{(2+)}|/\kappa A^2$; blue line: $|\eta_q^{(2+)}|/\kappa A^2$. Positive θ is measured anti-clockwise from the positive x-axis.

and found excellent agreement with experimental wave tank data.

A simple test to check the accuracy of DIFFRACT at predicting second order results between the cylinders of a four-cylinder array is to plot the second order surface response along lines joining the surfaces of two cylinders. The end values on such plots, which give the runup on the cylinders, are known and hence one can check that the surface variation along each line approaches these two end values in a reasonable manner. This test has been undertaken for the Malenica et al. (1999) test case for all possible pairs of cylinders. For each cylinder pair, the runup values computed on the cylinders suggest that the results between the cylinders are realistic.

Following the successful verification of DIFFRACT results on the surface of each cylinder and the indication from the above tests and previous work that accurate results are also computed away from the cylinders, the DIFFRACT code can now be used with confidence to study second order diffraction of regular waves by four-cylinder arrays.

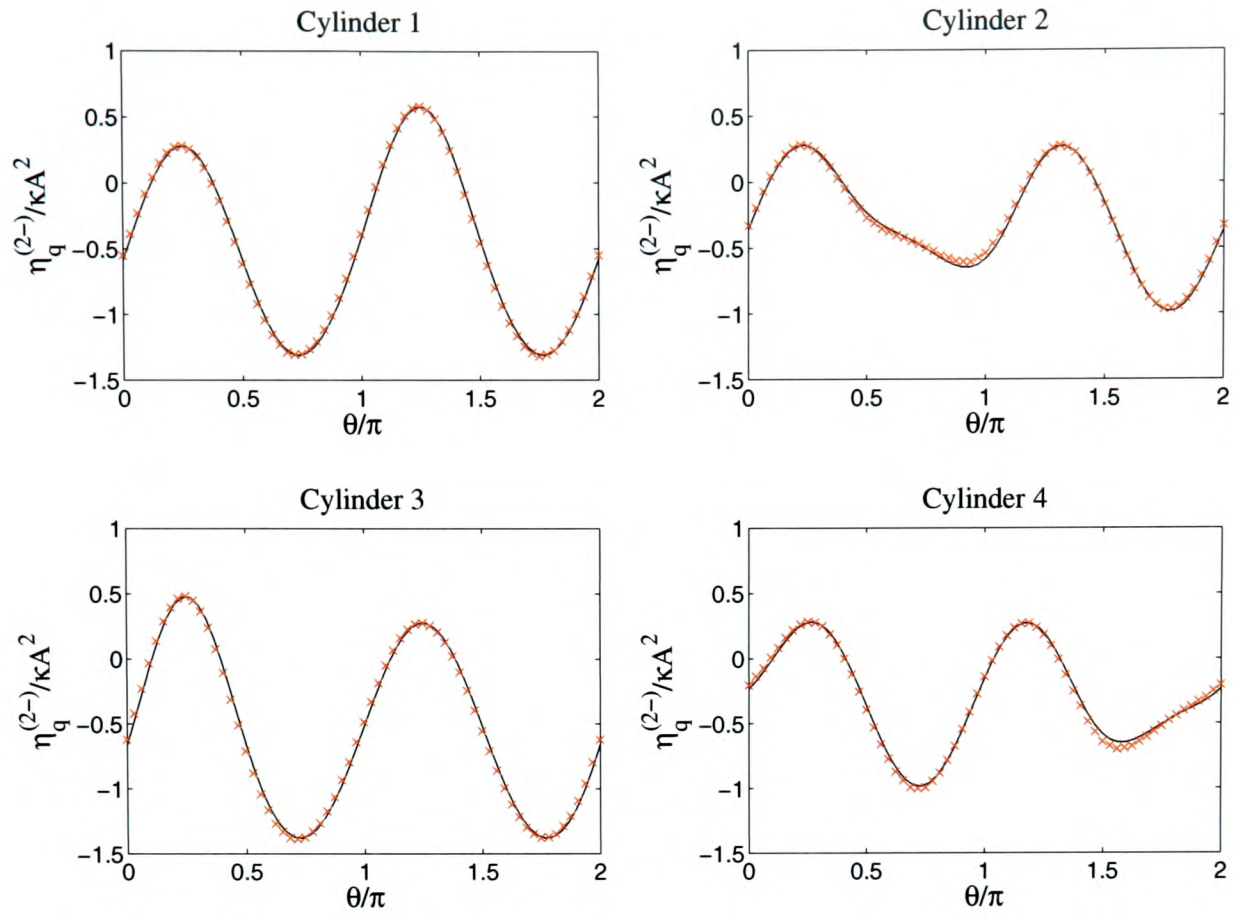

Figure 7.5: Non-dimensional difference quadratic component of the second order wave runup amplitude for regular waves incident upon an array of four cylinders arranged at the vertices of a square. $R = 4a$, $h = 3a$, $\kappa a = 0.468$ and $\beta = 45$ degrees. Black solid line: analytical solution; red crosses: numerical DIFFRACT solution. Positive θ is measured anti-clockwise from the positive x-axis.

7.4.2 Second order surface elevation

This section presents second order surface elevation results around each cylinder of the LUNA structure and along the x and y axes for incident regular waves with T=12.7s, corresponding to the experimental regular wave frequency (f = 0.079Hz) studied in Chapter 8. The purpose of this section is to illustrate the relative significance of the linear and second order contributions and hence comparisons are made with linear results.

Figures 7.6 and 7.7 show the non-dimensional linear and second order sum runup amplitudes respectively. The time-independent contribution ($\eta_q^{(2-)}$) around each cylinder is shown in Figure 7.8. The cylinders are numbered in a clockwise sense, starting with the cylinder at the location (x, y)=(68.1/2, 40.5/2) and the incident waves propagate in the positive x-direction. Positive θ is measured anti-clockwise from the positive x-direction.

The maximum linear and second order sum runup values occur at different locations around each cylinder and the variation of the time-independent term around the cylinders is similar to the linear variation. The largest linear runup occurs on the inside face of each cylinder

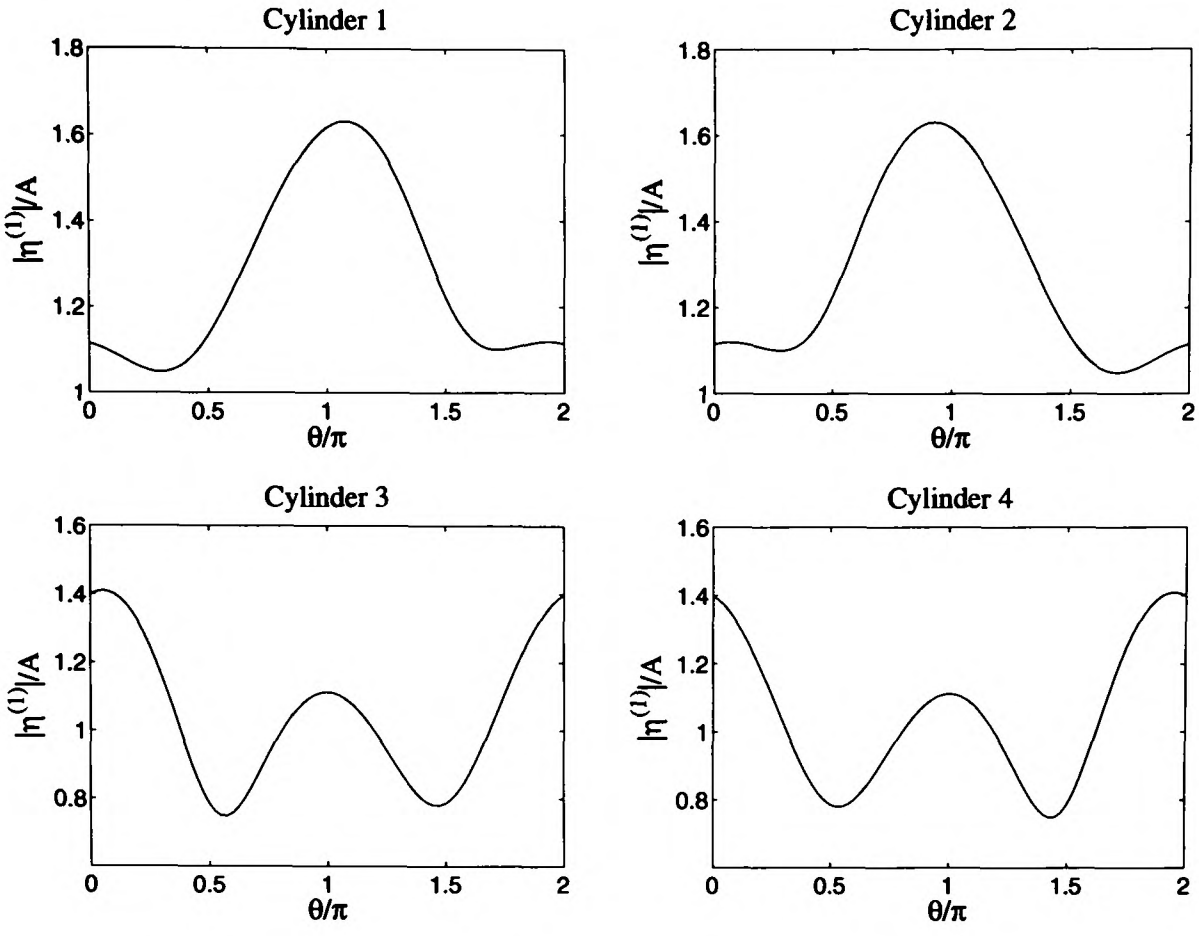

Figure 7.6: Non-dimensional linear wave runup amplitude for regular waves incident upon the LUNA structure. T=12.7s ($\kappa = 0.0278\text{m}^{-1}$). $\beta = 0$.

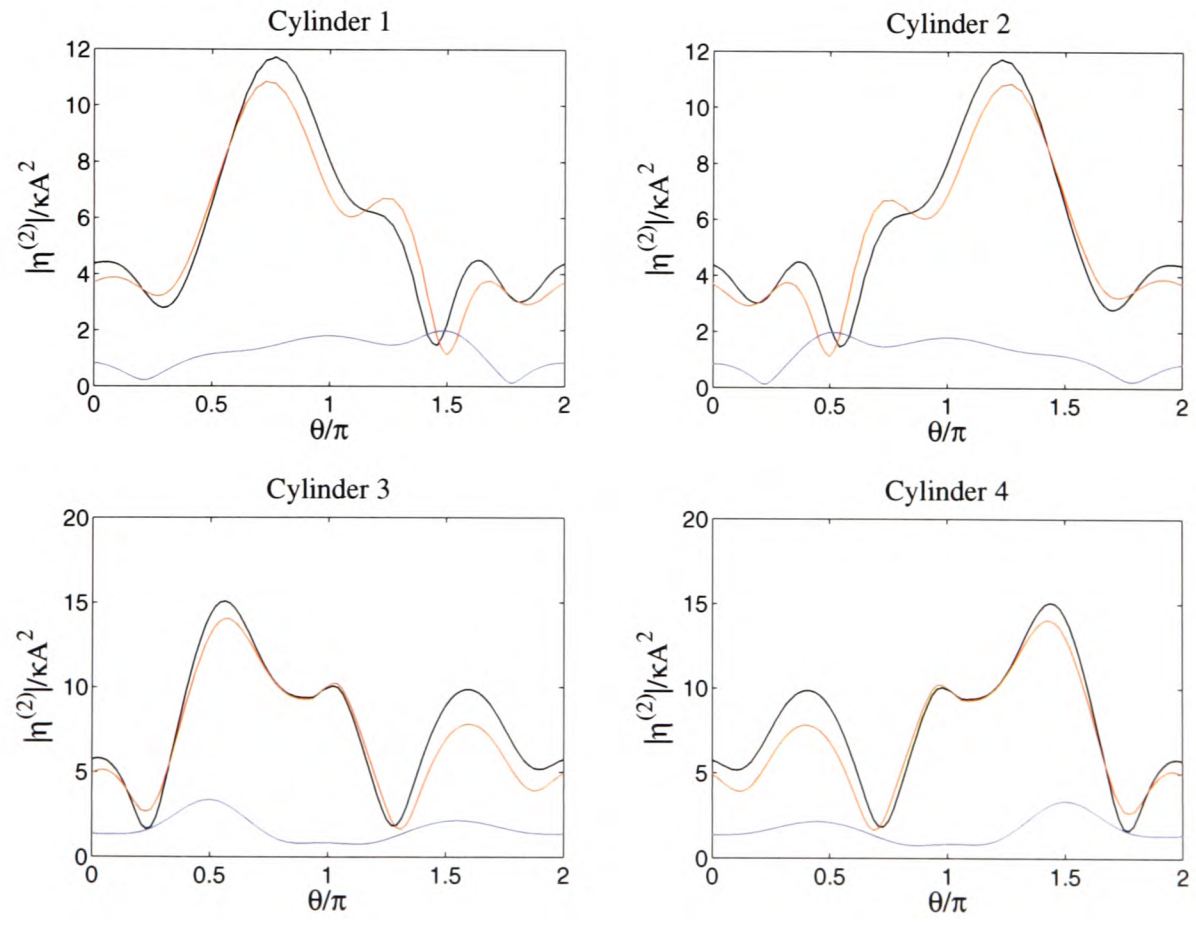

Figure 7.7: Non-dimensional sum components of the second order wave runup amplitude for regular waves incident upon the LUNA structure. T=12.7s ($\kappa = 0.0278\text{m}^{-1}$). $\beta = 0$. Black line: $|\eta^{(2+)}|/\kappa A^2$; red line: $|\eta_p^{(2+)}|/\kappa A^2$; blue line: $|\eta_q^{(2+)}|/\kappa A^2$.

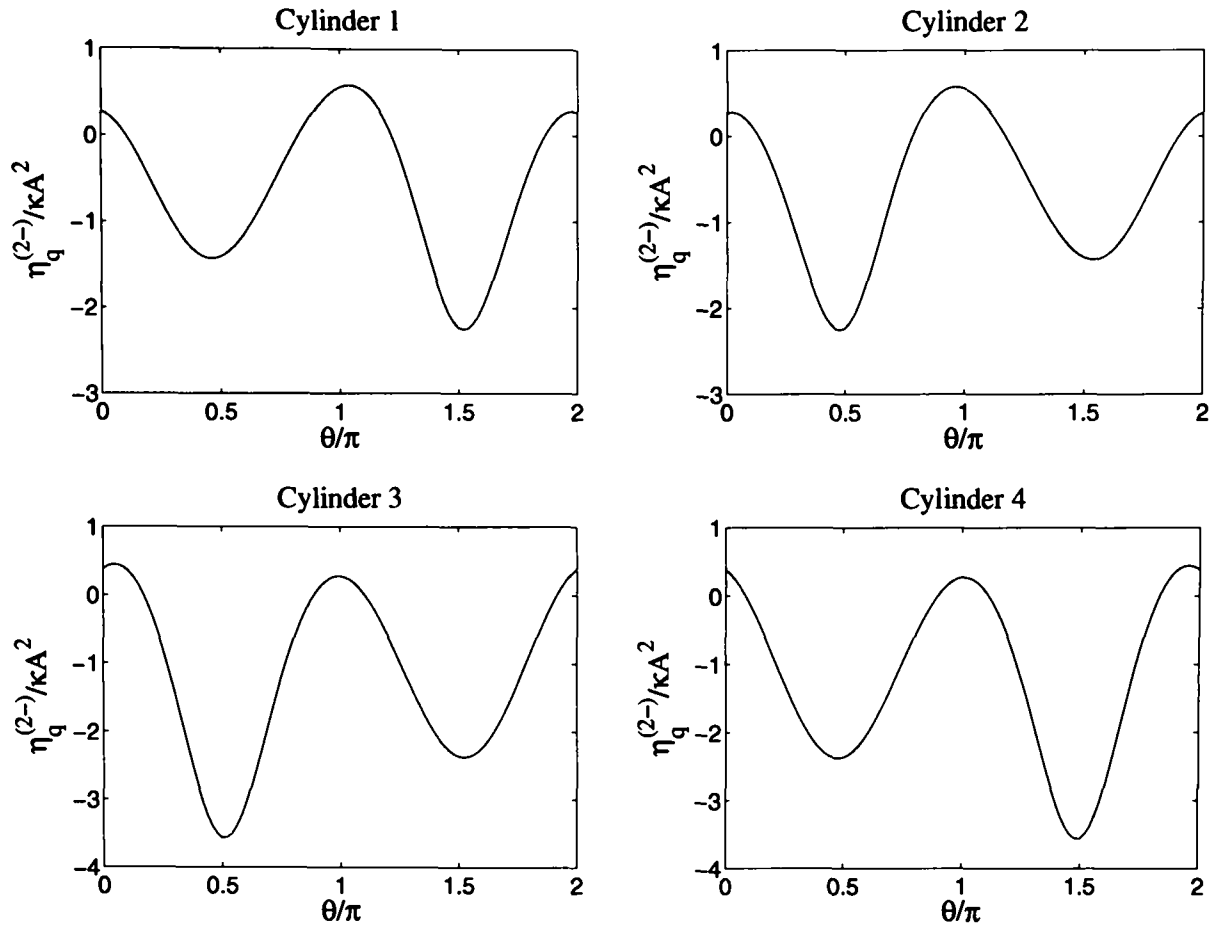

Figure 7.8: Non-dimensional difference quadratic component of the second order wave runup for regular waves incident upon the LUNA structure. T=12.7s ($\kappa = 0.0278\text{m}^{-1}$). $\beta = 0$.

($\theta = \pi$ for cylinders 1 and 2 and $\theta = 0$ for cylinders 3 and 4) and is equal to $1.63A$ for cylinders 1 and 2 and $1.41A$ for cylinders 3 and 4. The largest second order sum runup occurs between the two upstream cylinders (cylinders 3 and 4) and is equal to $15.05\kappa A^2$, corresponding to $2.09A$ for H=10m waves and $2.93A$ for H=14m waves, which are the two wave heights used in the model tests. Hence the second order contributions are found to be very large and exceed the peak linear elevations in the region between the two upstream cylinders (for the two experimental wave heights).

Previous work studying the wave field in the vicinity of a diffracting body suggests that the time-independent contribution, $\eta_q^{(2-)}$, exhibits a set-up (i.e. has a positive value) close to a diffracting body. This has been observed for wave diffraction from arrays of cylinders and ship-shaped bodies; see for example Zang et al. (2006). It is therefore perhaps surprising that no appreciable set-up is observed close to the LUNA cylinders.

The results presented in Figures 7.6 to 7.8 are compared with experimental wave measurements in Section 8.4 Chapter 8; the ability of diffraction theory to reproduce real wave measurements and the complications associated with making comparisons with real wave data are discussed.

The second order wave field along the x and y axes is now examined. Figures 7.9 and 7.10 show the second order sum (potential, quadratic and total) and difference (quadratic) contributions respectively.

The magnitude of the second order sum contribution along the x-axis is considerable, reaching peak values between the upstream and downstream cylinders and at the centre of the structure. The largest non-dimensional second order sum elevation ($|\eta^{(2+)}|/\kappa A^2$) occurs between the two front cylinders and is equal to 13.91. From the linear surface elevation frequency response function between the two front cylinders shown in Figure 6.10 (a) Chapter 6, it is clear that the second order sum terms have excited a double frequency ($2 \times 0.079 = 0.158$Hz) resonance; the second largest peak in Figure 6.10 (a) occurs at 0.159Hz. Therefore the extreme sum magnifications observed in this region are not surprising.

The large sum magnifications between the upstream and downstream cylinders are associated with appreciable positive (i.e. set-up) time-independent difference contributions, $\eta_q^{(2-)}$. Between the upstream cylinders $\eta_q^{(2-)}/\kappa A^2$ reaches a value of 2.00, which corresponds to $\eta_q^{(2-)} = 0.28A$ and $0.39A$ for wave heights $H = 10$m and 14m respectively. Therefore, the second order difference contribution has a considerable effect on the total wave field around the LUNA structure and so should not be neglected during design.

This is a very useful conclusion, as the difference contribution can be computed directly from the first order potential for monochromatic incident waves, and hence an improved prediction (compared with that given by linear diffraction theory alone) of the required airgap beneath a four-column structure can be achieved without the need for computing the second order diffraction potential. That said, although the offshore industry currently only consider incident regular wave fields prior to model testing, it is hoped that this work and associated research will lead to the consideration of more realistic incident wave fields, which require the computation of the first and second order potentials to generate the difference response.

The total second order sum contribution, $\eta^{(2+)}$, along the x-axis is compared with real wave measurements in Section 8.4 Chapter 8.

It would be interesting to investigate the effect incident wave height has on the location of the extreme surface magnifications in the vicinity of the LUNA structure. This is pursued to a limited extent in Chapter 8 using the $H = 10$m and $H = 14$m experimental wave data.

The results presented in this section show that the magnitudes of the second order contributions (sum and difference) to the overall diffracted wave field are considerable, suggesting that

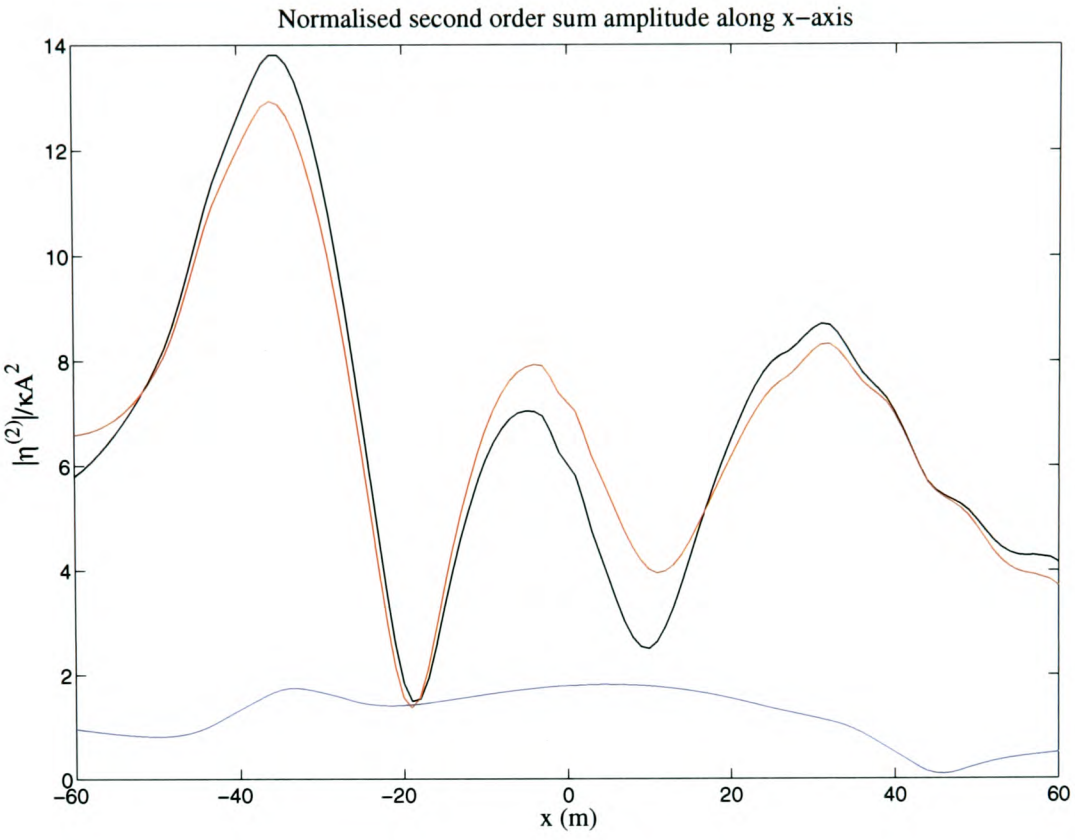

Figure 7.9: Non-dimensional sum components of the second order wave amplitude along the x and y axes for regular waves incident upon the LUNA structure. T=12.7s ($\kappa = 0.0278\text{m}^{-1}$). $\beta = 0$. Black line: $|\eta^{(2+)}|/\kappa A^2$; red line: $|\eta_p^{(2+)}|/\kappa A^2$; blue line: $|\eta_q^{(2+)}|/\kappa A^2$.

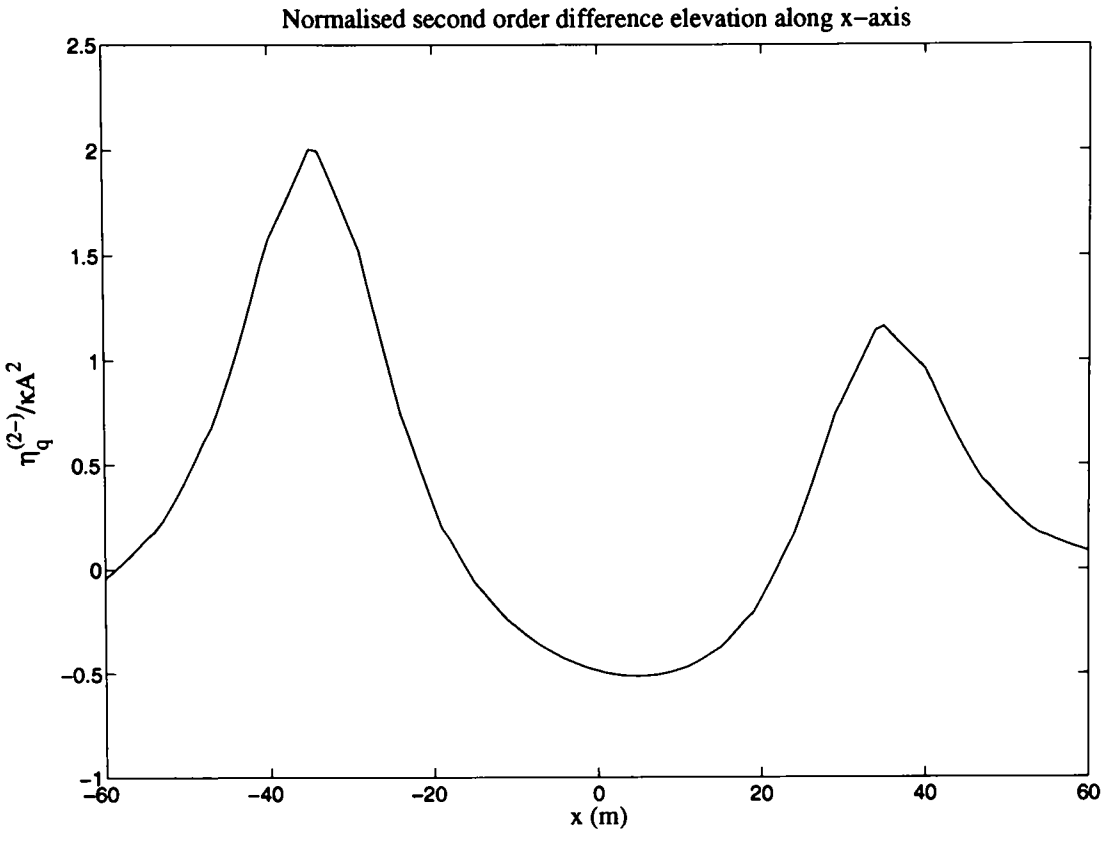

Figure 7.10: Non-dimensional difference quadratic component of the second order elevation along the x and y axes for regular waves incident upon the LUNA structure. T=12.7s ($\kappa = 0.0278\text{m}^{-1}$). $\beta = 0$.

they should not be neglected in design. The significance of the second order contributions in the quest to reproduce real wave measurements is addressed in Chapter 8.

7.4.3 NEAR-TRAPPING

The phenomenon of linear near-trapping has been studied by Evans and Porter (1997) for the four-cylinder configuration considered in Section 7.4.1. Malenica et al. (1999) extended this study to explore the possibility of near-trapping at second order for the same cylinder configuration.

Following on from this work, the array of bottom mounted cylinders defined by $R = 4a$ and $h = 3a$ will again be considered in this section. To allow comparison with results generated by Malenica et al. (1999) an incident wave angle (β) of 45 degrees is investigated. Further results in addition to those produced by Malenica et al. are presented and additional conclusions concerning the character of the free surface response at near-trapping are discussed. Finally, working within the limitations of the DIFFRACT code, second order near-trapping is explored for the LUNA structure.

By studying the linear forces on each cylinder, Evans and Porter (1997) found that the peak linear force on each cylinder occurs at approximately the same wavenumber, namely $\kappa a \approx 1.66$, and they concluded that this wavenumber corresponds to the phenomenon of a linear near-trapping mode. For $\kappa a = 1.66$, Evans and Porter found the largest surface elevation occurring in the vicinity of the cylinder array to be approximately 3.5 times the incident wave amplitude. To help illustrate the character of the linear surface elevation response around the cylinders for this mode, the linear surface magnification frequency response is computed at ten points in the vicinity of the array. For this near-trapped mode the largest linear magnifications occur on or close to the cylinder surfaces and hence all except one of the points considered lie on the cylinder surfaces. The ten points considered are shown in Figure 7.11 and the linear response functions are shown in Figure 7.12.

With the exception of point 1, which lies at the centre of the array, Figure 7.12 shows that the largest surface magnifications around each cylinder all occur at approximately $\kappa a = 1.66$. The largest linear magnification in the vicinity of the four-cylinder array occurs at point 3, where $|\eta|/A = 4.48$ at $\kappa a = 1.69$. Therefore, perhaps predictably, for a particular near-trapped mode, the maximum force and free surface magnification will not necessarily occur at exactly the same frequency.

To help illustrate the linear surface response in the vicinity of the four cylinders at this near-trapped mode ($\kappa a = 1.69$ for maximum surface elevation), contour and surface plots

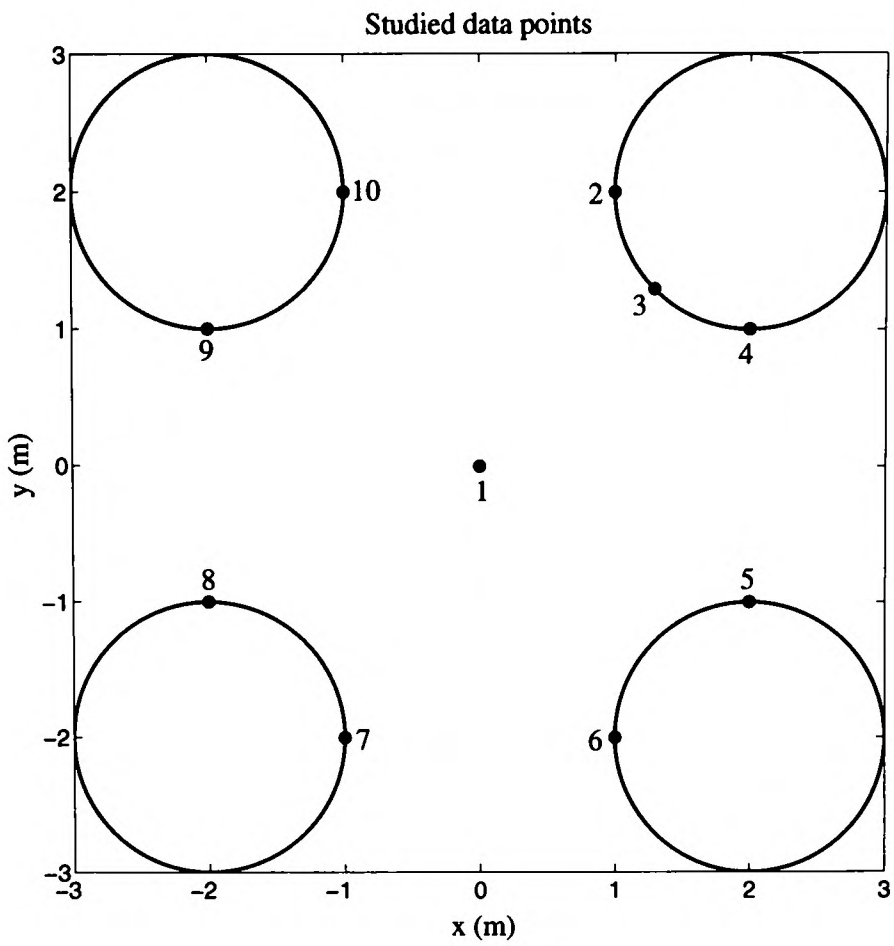

Figure 7.11: Considered points around a four-cylinder array.

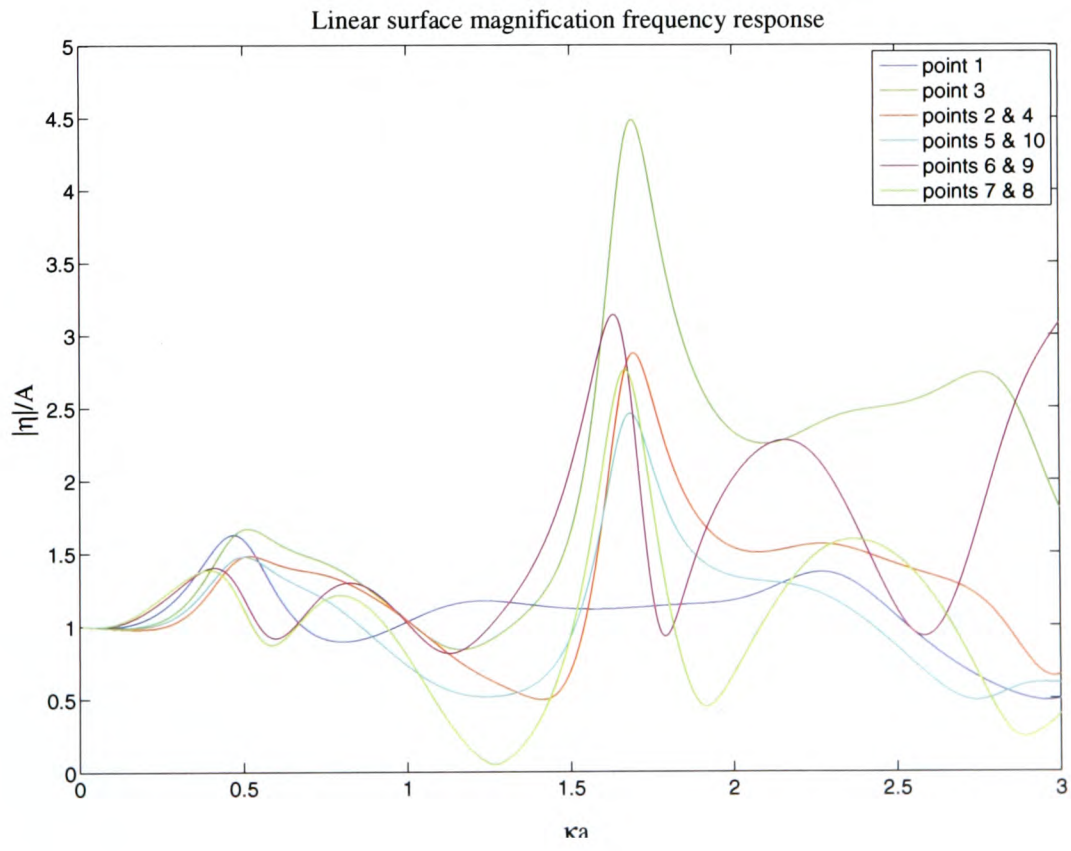

Figure 7.12: Linear surface magnification frequency response functions at 10 points around a four-cylinder array. $R = 4a$, $h = 3a$ and $\beta = 45$ degrees.

showing free surface elevation are presented in Figure 7.13. It is clear from this figure that the most extreme surface magnifications occur on or close to the surface of the cylinders and the surface magnifications midway between the cylinders are relatively small. The largest surface elevation, which occurs on the inside surface of cylinder 1 (at point 3 in Figure 7.11), is also clearly shown.

For $\kappa a = 1.66$, Malenica et al. observed that although the linear elevation was greatly enhanced around the cylinders the total second order surface elevation was not particularly large. It should be noted that the amplitudes of the individual second order sum components, η_q^{2+} and η_p^{2+}, are large around the cylinders at this frequency but the relative phasing between the two components is such that the total second order sum elevation is not large.

By examining the surface elevation response at $\kappa a = 0.468$, which corresponds to half the near-trapping frequency identified by Evans and Porter ($\kappa a = 1.66$) for this water depth, the first order elevation around the cylinders is found to be unremarkable whereas the second order potential term, η_p^{2+}, becomes very large. This very significant observation (first noted by Malenica et al.) suggests that near-trapping of the second order wave occurs when its frequency coincides with the linear near-trapping frequency. This effect results in the η_p^{2+} term dominating the second order wave, as is illustrated in Figure 7.4 (Section 7.4.1).

Malenica et al. considered a further non-trapping incident frequency, namely $\kappa a = 0.755$ (corresponding to two thirds of the near-trapping frequency), and found no large magnifications at first or second order.

In an effort to provide further insight into the second order surface response between the cylinders at second order near-trapping ($\kappa a = 0.468$, $\beta = 45$ degrees), a normalised plot of the second order sum response along the x-axis (which is identical to the plot along the y-axis for this particular geometry and incident wave angle) is given in Figure 7.14. Results are computed at 0.25m increments along the x-axis.

For the linear near-trapped mode at κa=1.66 (or κa=1.69 to achieve maximum elevation) the largest linear surface magnifications occur around the cylinders and the linear surface response in the region between the cylinders is comparatively small. Figures 7.4 and 7.14 show that the second order diffracted wave field exhibits similar spatial variation when the system is excited with a second order wave at a frequency corresponding to this linear near-trapping frequency.

In order to allow further comparison between the spatial profiles of the second order wave field at second order near-trapping and the linear wave field at linear near-trapping, Figure 7.15

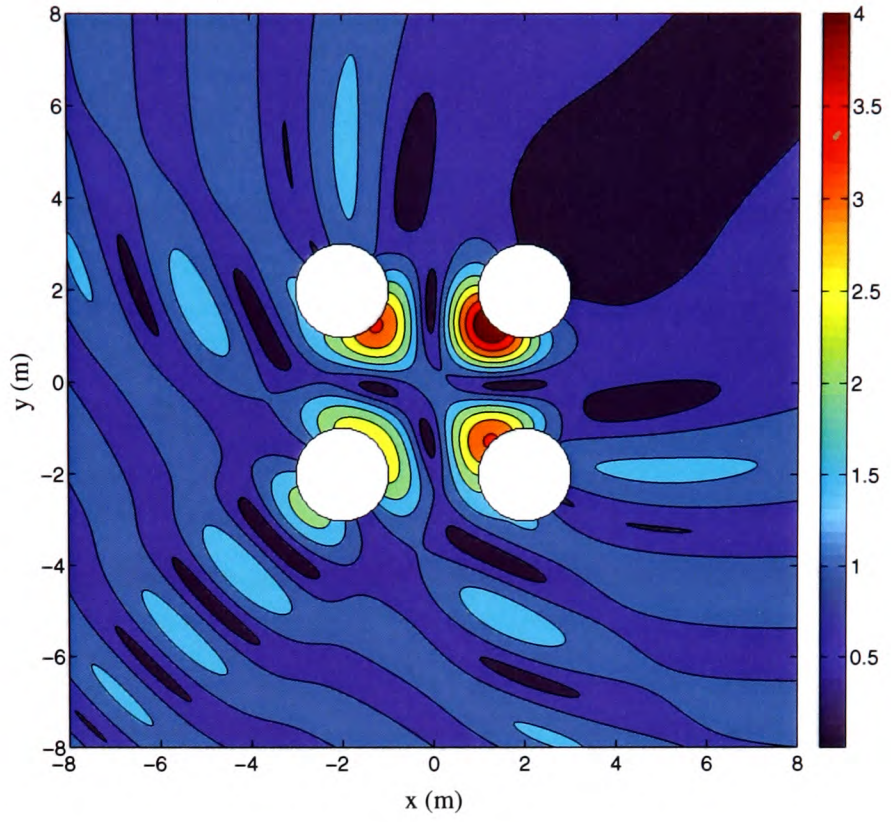

(a) Contour plot

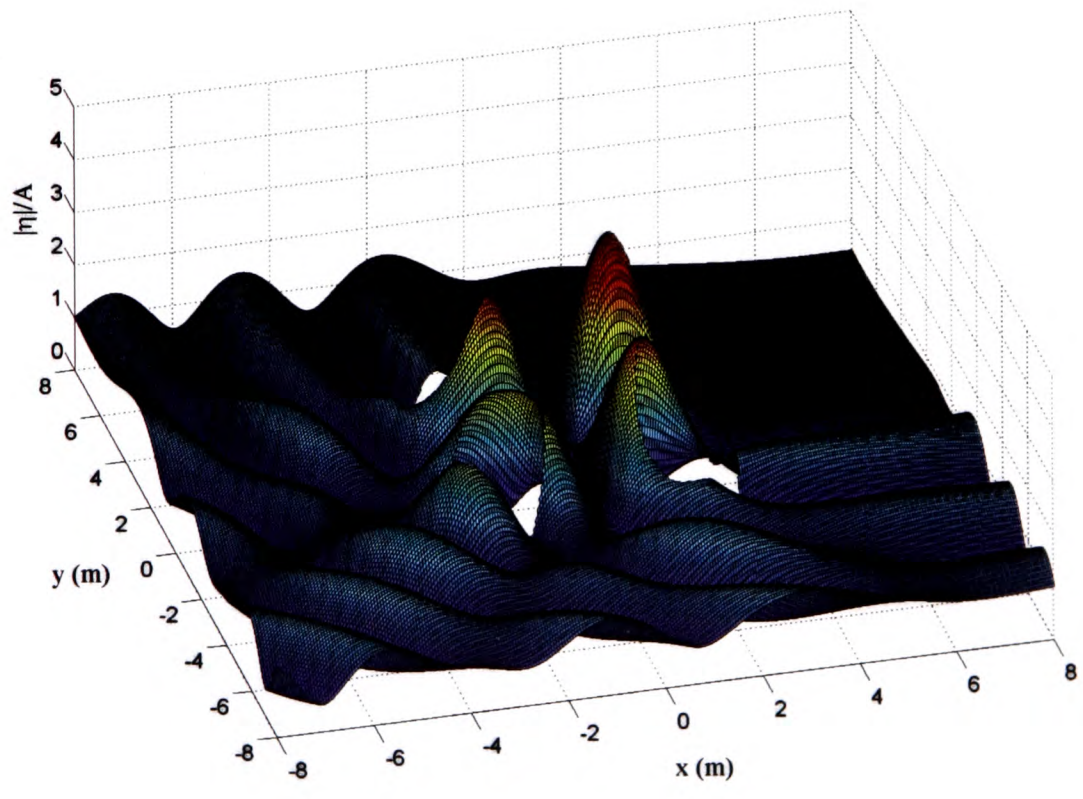

(b) Surface plot

Figure 7.13: Linear surface elevation around a four-cylinder array at near-trapping. $R = 4a$, $h = 3a$, $\kappa a = 1.69$ and $\beta = 45$ degrees.

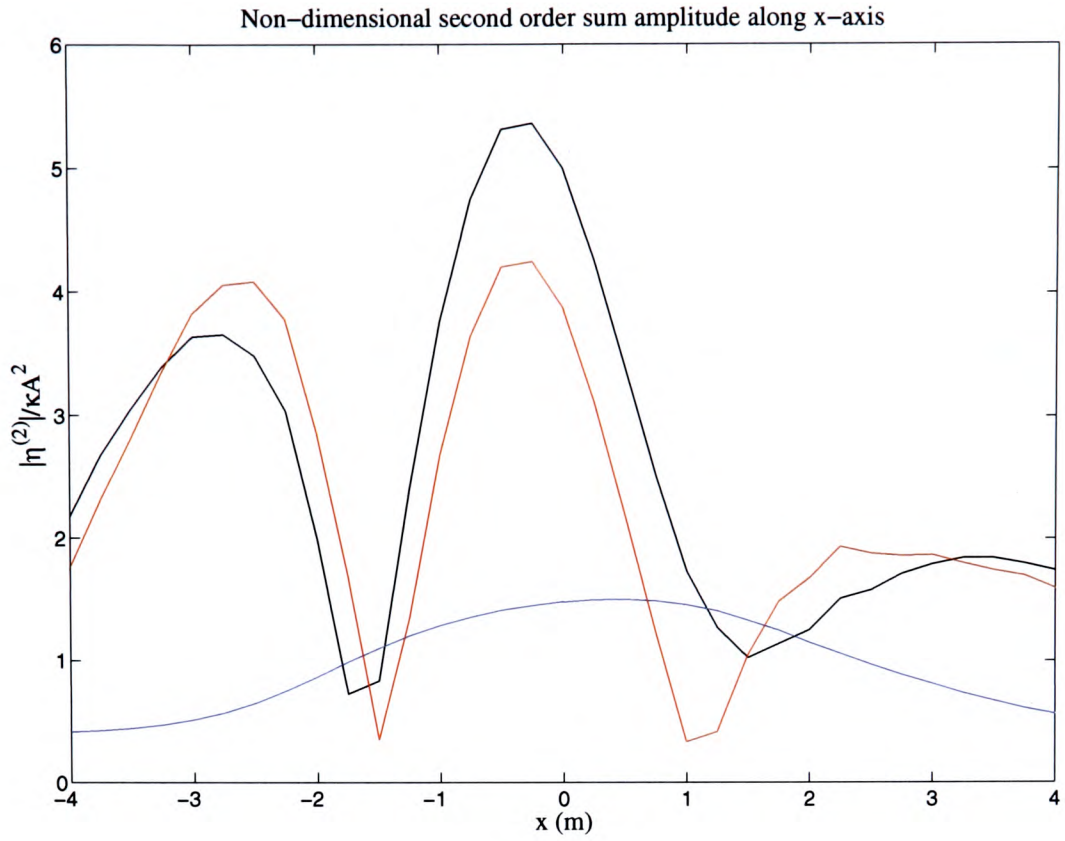

Figure 7.14: Non-dimensional sum components of the second order wave amplitude along the x-axis for regular waves incident upon an array of four cylinders arranged at the vertices of a square. $R = 4a$, $h = 3a$, $\kappa a = 0.468$ and $\beta = 45$ degrees. Black line: $|\eta^{(2+)}|/\kappa A^2$; red line: $|\eta_p^{(2+)}|/\kappa A^2$; blue line: $|\eta_q^{(2+)}|/\kappa A^2$.

shows the linear elevation along the x-axis at linear near-trapping (κa=1.66). The spatial variations of the total second order sum and linear profiles shown in Figures 7.14 and 7.15 are remarkably similar, with the peaks and troughs occurring at the same locations. The main difference between the two profiles is that the linear response increases with increasing distance upstream ($x <\sim -3.5$m) whereas the second order response reduces upstream away from the structure.

The largest magnification of the second order sum wave at second order near-trapping (κa=0.468) occurs at point 3 (Figure 7.11), which is the same point where the largest linear magnification occurs for linear near-trapping, and is equal to $17.65\kappa A^2$ (see Figure 7.4). For realistic ocean waves a κA value of 0.25 is reasonable, suggesting that the largest magnification of the second order sum wave at second order near-trapping is approximately $4.41A$, which is comparable to the peak linear magnification of $4.48A$ at linear near-trapping. Therefore, for the particular near-trapped phenomena considered, the magnitudes and spatial variations of the linear wave field at linear near-trapping and the second order sum wave field at second order near-trapping show close agreement. This is a significant observation and suggests that useful information on extreme second order responses can be obtained by studying linear near-trapping.

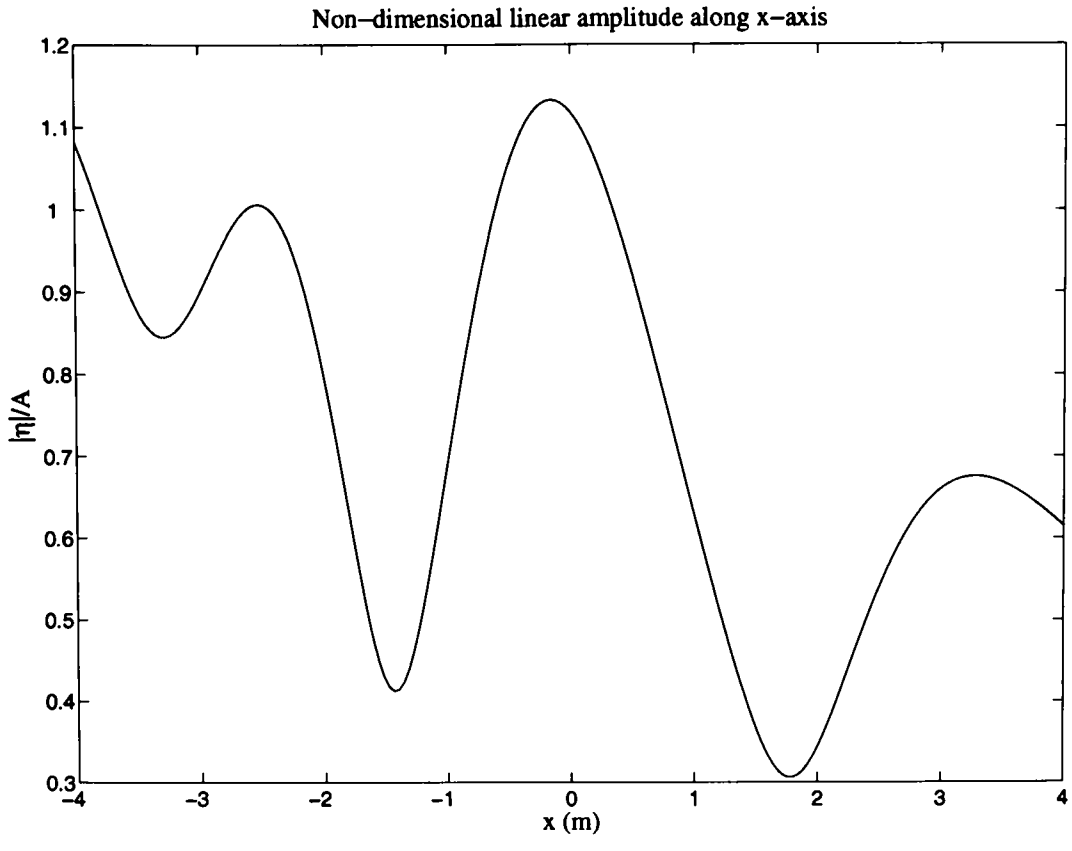

Figure 7.15: Non-dimensional linear wave amplitude along the x-axis for regular waves incident upon an array of four cylinders arranged at the vertices of a square. $R = 4a$, $h = 3a$, $\kappa a = 1.66$ and $\beta = 45$ degrees.

It follows that the preliminary design of a multi-column offshore structure should include the selection of a suitable configuration of columns so that energy from the surrounding wave environment is small at both the linear, and second order, near-trapped frequencies. This would help to avoid large diffraction magnifications of the free surface in the vicinity of the structure and can be achieved using linear diffraction theory alone.

Second order free surface frequency response plots have been computed for the studied array at various locations on the cylinder surfaces. Peaks in the responses are found to arise at $\kappa a \approx 0.45$. However, because of the computational burden associated with the second order calculation, a limited number of frequencies were considered and hence it is not possible to accurately identify second order near-trapping frequencies from these plots.

The existence of a second order near-trapped mode for the LUNA structure is now examined. From the linear surface elevation frequency response function shown in Figure 6.10 (a) Section 6.4.2 Chapter 6, a linear near-trapped mode is found to be excited at 0.126Hz ($\kappa = 0.0641\text{m}^{-1}$) for waves incident along the x-axis (i.e. $\beta = 0$). This mode was identified by considering a point along the x-axis between the two upstream cylinders (x=-36.5m, y=0), which is where the largest linear surface magnification in the vicinity of the structure occurs for $\beta = 0$.

The observations noted above for an array of four bottom mounted cylinders arranged at the vertices of a square suggest that the LUNA structure will excite a second order near-trapped mode at half the linear near-trapping frequency, namely 0.063Hz ($\kappa = 0.0202\text{m}^{-1}$).

From Figure 6.11 Section 6.4.2 Chapter 6, the largest linear surface magnifications in the vicinity of the LUNA structure for $f = 0.126$Hz and $\beta = 0$ occur between the upstream and downstream cylinders and the peak value lies on the x-axis. It follows from the above observations for an array of four bottom mounted cylinders that, when the second order wave is excited at the linear near-trapping frequency, one may expect the largest second order surface magnifications to also occur between the upstream and downstream cylinders. Therefore, examining linear and second order elevations along the x-axis should allow similarities between linear and second order near-trapped modes to be identified. Figures 7.16 and 7.17 show the linear and second order sum (potential and quadratic) surface elevations along the x-axis for $f = 0.126$Hz and $f = 0.063$Hz respectively. In agreement with previous findings for an array of four bottom mounted cylinders, the following conclusions can be made from Figures 7.16 and 7.17 for the LUNA structure:

1. When the LUNA structure is subject to incident waves at half the linear near-trapping frequency, the linear magnifications are comparatively small and the second order sum magnifications are large. This corresponds to a near-trapping phenomenon associated with the second order wave.

2. At linear near-trapping the amplitudes of the individual second order sum components, η_q^{2+} and η_p^{2+}, are large but the relative phasing between the two components is such that the total second order sum elevation is comparatively small.

3. The spatial variation of the second order wave field at second order near-trapping is similar to the spatial variation of the linear wave field at linear near-trapping, both fields reaching comparable peak values along the x-axis between the upstream and downstream cylinders.

The results and observations in this section suggest that if a linear near-trapped mode can be identified for a multi-column structure then a near-trapping phenomenon associated with the second order wave will also exist at half the linear near-trapping frequency. For structures such as LUNA, which have large closely spaced cylinders, the second order contributions to the overall diffracted wave field can be considerable and hence the design of such a structure should avoid exciting both linear and second order near-trapped modes. Although near-trapping is a phenomenon associated with monochromatic incident waves, which are obviously

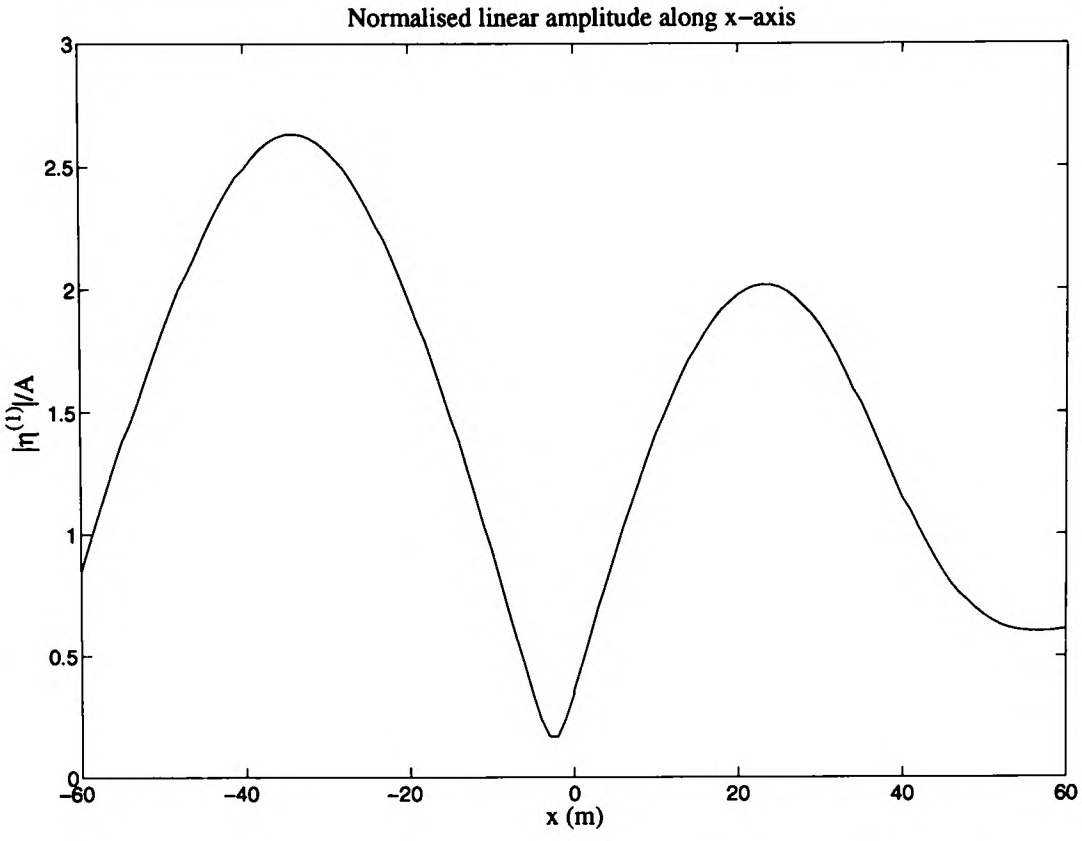

Figure 7.16: Non-dimensional linear and second order sum amplitudes along the x-axis for regular waves incident upon the LUNA structure. f=0.126Hz ($\kappa = 0.0641\text{m}^{-1}$). $\beta = 0$. For the second order plots: black line $|\eta^{(2+)}|/\kappa A^2$; red line $|\eta_p^{(2+)}|/\kappa A^2$; blue line $|\eta_q^{(2+)}|/\kappa A^2$.

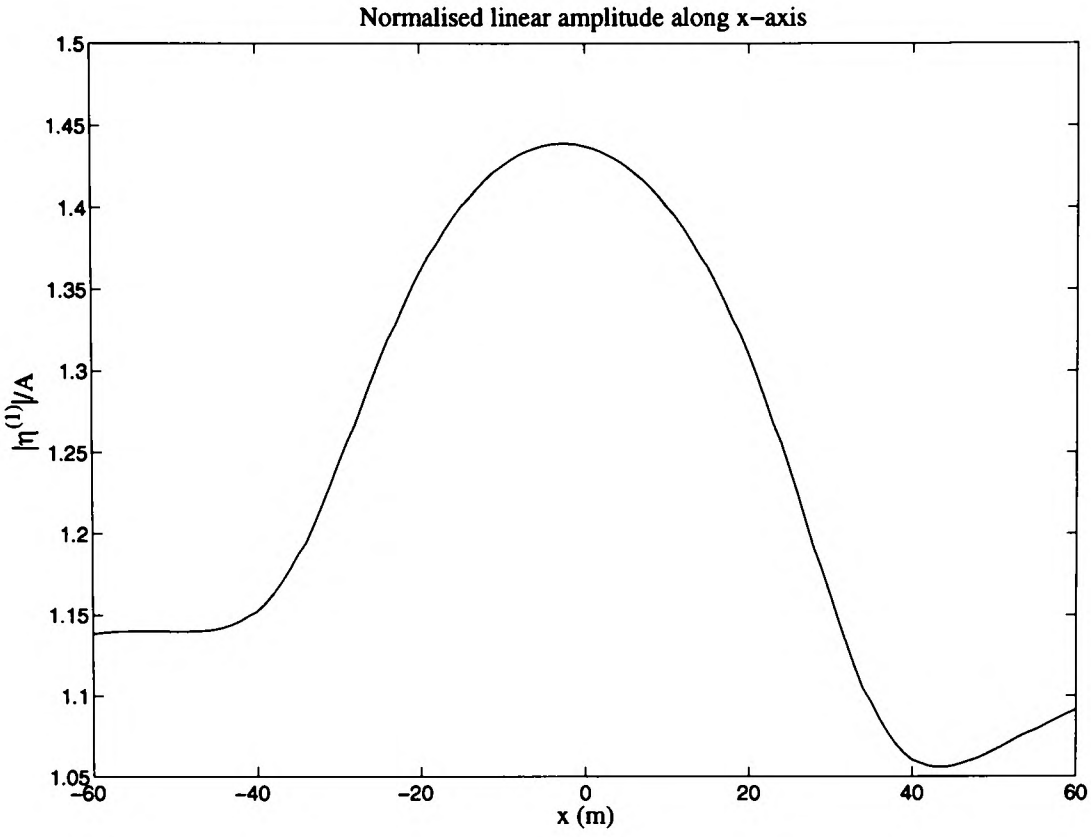

Figure 7.17: Non-dimensional linear and second order sum amplitudes along the x-axis for regular waves incident upon the LUNA structure. f=0.063Hz ($\kappa = 0.0202\text{m}^{-1}$). $\beta = 0$. For the second order plots: black line $|\eta^{(2+)}|/\kappa A^2$; red line $|\eta_p^{(2+)}|/\kappa A^2$; blue line $|\eta_q^{(2+)}|/\kappa A^2$.

not an accurate representation of an ocean surface, it is still important to avoid significant energy from the local sea environment (e.g. close to the peak of the sea spectrum) being concentrated around one of these critical frequencies.

In Section 6.4.2 Chapter 6 the effect of the caisson on peak linear magnification values was found to be very frequency dependent and hence its effect on linear near-trapping will depend on the geometrical configuration of the cylinders. Figure 6.15 in Section 6.4.2 shows that the LUNA caisson has no significant effect on the linear magnification at the linear near-trapping frequency (f = 0.126Hz) although it appreciably increases the linear magnification at the second order near-trapping frequency (f = 0.063Hz). Therefore, the effect of the caisson could potentially blur the distinction between the relative sizes of the linear and second order surface magnifications at linear and second order near-trapping. Fortunately, the effect of the LUNA caisson on near-trapping is sufficiently small to allow a second order near-trapped mode to be identified. The effect of the caisson on the second order diffracted wave field is considered in the next section.

7.4.4 Effect of caisson

The effect of caisson height, h_c, on the second order surface elevation in the vicinity of the LUNA structure is now examined. To allow comparisons to be made with the first order results presented in Chapter 6 Section 6.3, a regular wave frequency of 0.07Hz (corresponding to the peak period for the 100-year sea state) and an incident wave angle (β) of 0 are considered.

Wave interaction with the LUNA structure is investigated for six caisson heights, namely h_c = 0m, 5m, 10m, 15m, 20m and 25m, where h_c = 0m obviously corresponds to wave interaction with the four cylinders alone. For each caisson height the normalised second order (sum and difference) surface elevation along the x-axis is computed at 5m increments for -60m< x <60m (almost extending along the full x-length of the caisson, 121.03m), which provides sufficient accuracy and a reasonable computation time. The effect of the caisson beyond this x-range is not important for airgap design.

Considerable effort has been made to ensure that converged second order results have been computed. Ten body surface meshes have been constructed for each caisson height, in addition to ten outer free surface meshes. The element sizes, shapes and aspect ratios have been carefully chosen for the considered structural geometry and incident wave frequency. The second order surface elevation along the x-axis and the second order runup around the cylinders show little deviation for each mesh, suggesting that converged results have been

achieved.

Normalised sum potential, sum quadratic and difference quadratic components of second order surface elevation along the x-axis are plotted in Figure 7.18 for each caisson height. The total second order sum contribution (potential + quadratic) is also plotted in Figure 7.18. From this figure it is clear that increasing caisson height increases the second order sum elevation along the x-axis. Furthermore, increasing caisson height increases the difference quadratic elevation in the region between the cylinders and reduces it at the centre of the structure.

Caisson height has a considerable effect on the second order sum diffracted wave field, altering both the magnitude and, to a lesser extent, the location of the peak responses. As was found at first order, the peak second order sum response ($|\eta^{(2+)}|/\kappa A^2$) is both increased and shifted slightly downstream by an increase in caisson height. For each caisson height the peak second order sum response occurs near the two back cylinders.

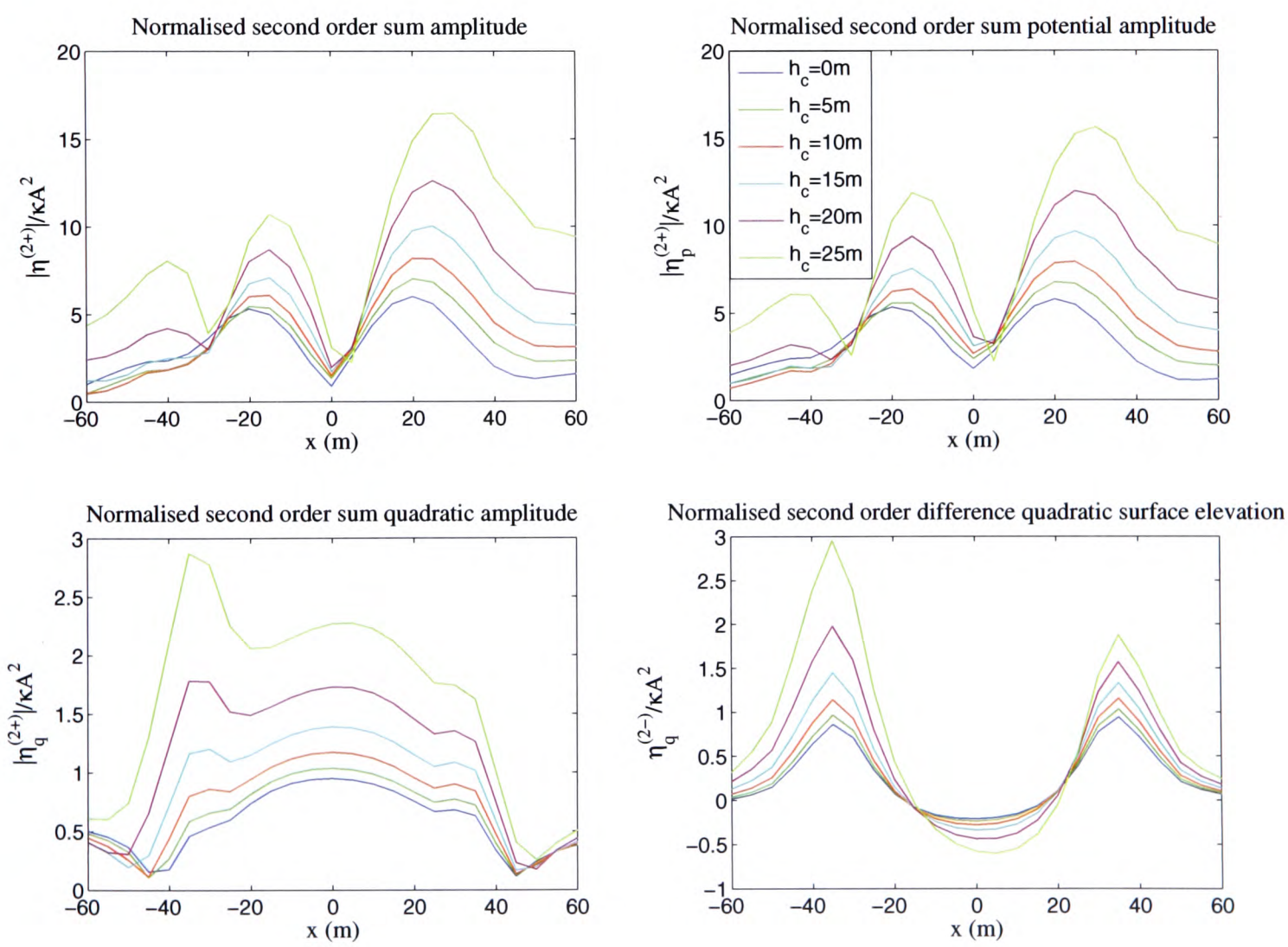

Figure 7.18: Effect of LUNA caisson height (h_c) on the second order surface elevation along the x-axis.

Newman (1990) studied second order wave diffraction at large depths and found that for sufficiently large depths, the second order potential will dominate the first order component. This implies that the second order potential decreases more slowly with depth than the first order potential, suggesting that the presence of a caisson will have a larger effect on the total second order wave field than the linear field. This is confirmed in Figure 7.18 for the sum contribution, where a caisson height of 15m, which is the actual LUNA caisson height, increases the peak second order sum response ($|\eta^{(2+)}|/\kappa A^2$) by 67.2% (from 6.00 to 10.03), compared to a 18.9% increase in the peak linear response.

For a caisson height of 15m, wave-caisson interaction effects increase the peak sum potential response ($|\eta_p^{(2+)}|/\kappa A^2$) by 67.2% (from 5.79 to 9.68) and increase the peak sum quadratic response ($|\eta_q^{(2+)}|/\kappa A^2$) by 46.3% (from 0.95 to 1.39). The potential component, which is computed from the second order potential, is considerably larger than the quadratic component at most points along the x-axis and hence dominates the total second order sum wave field.

For monochromatic incident waves the difference contribution has only a constant time-independent quadratic component, which is computed directly from the first order potential. The peak second order difference responses occur between the upstream and downstream cylinders and are found to be very dependent on caisson height. The LUNA caisson (h_c=15m) increases the peak difference response ($\eta_q^{(2-)}/\kappa A^2$) by 68.6%, from 0.86 to 1.45. Considering that the difference quadratic component is computed from the first order potential and the fact that the presence of a caisson has a comparatively small effect on the first order potential, it may seem surprising that the caisson has such a large effect on this time-independent term. However, the difference quadratic component is dependent on the derivative of the first order potential with respect to the vertical coordinate, z (Equation 2.78, Section 2.4.1 Chapter 2), and a rectangular caisson will cause a large change in vertical fluid velocity.

It should be noted that the effect of the caisson on the second order wave field is likely to be frequency dependent, as was found in Chapter 6 for the first order wave field.

7.5 Incident NewWaves

The diffraction of an isolated wave group (e.g. NewWave) is directly relevant to modelling the interaction of extreme ocean waves with offshore structures. Various forms of semi-empirical sea-state spectra, such as Pierson-Moskowitz (Pierson and Moskowitz 1964) and JONSWAP (Hasselmann et al. 1973), are available to create the incident wave field.

In the LUNA model tests the irregular waves were synthesised to match a JONSWAP spectrum, which is defined by:

$$S(f) = \alpha g^2 (2\pi)^{-4} f^{-5} \exp\left[-\frac{5}{4}\left(\frac{f}{f_p}\right)^{-4}\right] \gamma^{\exp -\frac{(f-f_p)^2}{2\sigma^2 f_p^2}} \tag{7.1}$$

where α is a factor depending on wind speed and fetch and:

g = gravity

f_p = peak frequency

γ = peak enhancement factor

$\sigma = 0.07$ for $f \leq f_p$ and 0.09 for $f > f_p$.

In the irregular wave experiments α=1, f_p=0.07Hz and γ=2.

Because of the convergence limitations of the DIFFRACT code (Section 7.3) it is not possible to study a NewWave composed of components across a JONSWAP spectrum. However, the majority of the energy of this spectrum is concentrated in a narrow range of frequencies around its peak, and so a useful insight into the interaction of extreme waves with the LUNA structure can still be obtained by modelling only the components close to the peak. This is achieved by computing a NewWave based on a Gaussian spectrum, defined by:

$$S(f) = \frac{1}{\sqrt{\pi}\Delta} \exp\left[-\frac{(f-f_p)^2}{\Delta^2}\right] \tag{7.2}$$

where Δ defines the bandwidth of the spectrum. A value of 0.0115 is used for Δ, which allows the Gaussian spectrum to approximate the shape of the JONSWAP peak with γ=2 (Figure 7.19).

The purpose of this section is to improve our understanding of the second order diffraction of an incident NewWave and not to provide design results for the LUNA structure. Therefore, working within the limitations of the DIFFRACT code, it is perfectly acceptable to study a NewWave based on a Gaussian spectrum even though it is not representative of the local sea environment.

Because of the considerable computational burden associated with the second order calculation, the number of frequency components used must be kept to a minimum. Therefore, the NewWave model considered in this section will be composed of nine equispaced frequency components in the frequency range from 0.05Hz to 0.09Hz (with the peak frequency lying midway between these two cut-off values). Using this frequency resolution, the total com-

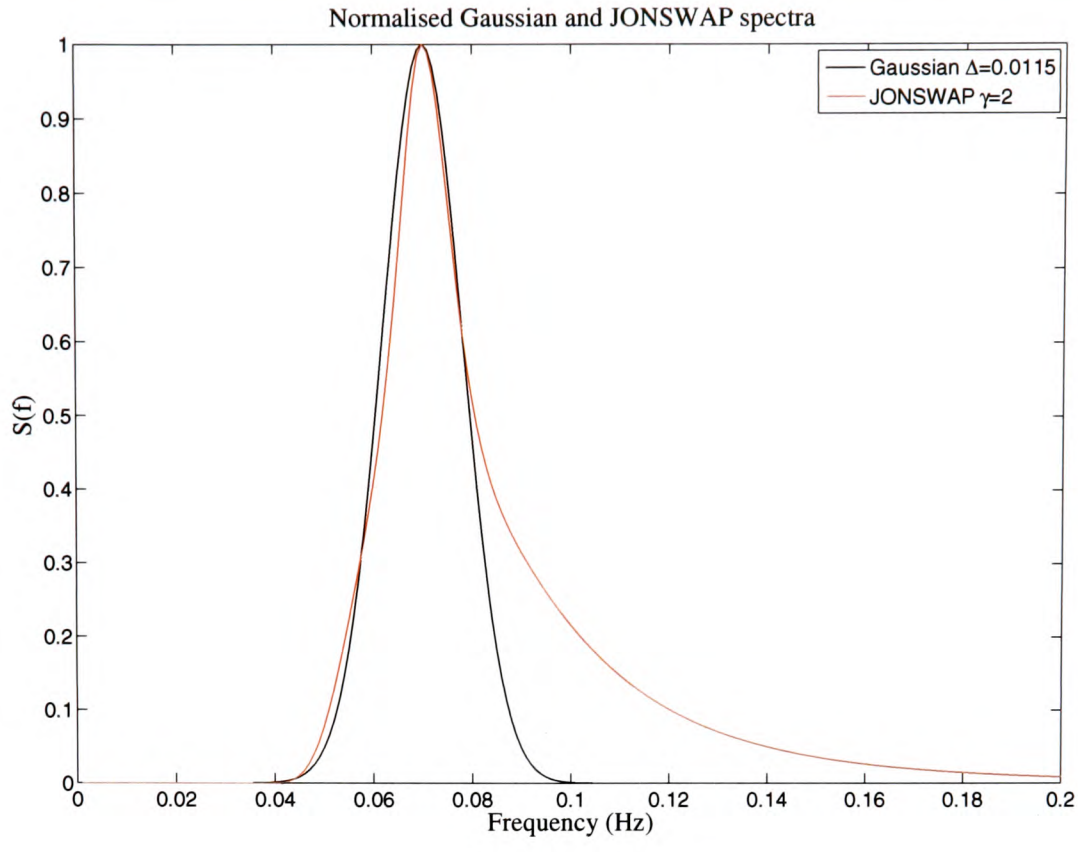

Figure 7.19: A Gaussian model for the peak of a JONSWAP spectrum with a peak enhancement factor (γ) of 2. The spectra have been normalised such that the peak values are 1.

putation time for the complete second order diffraction calculation is approximately 4 weeks (using a 3GHz processor and 1GB of RAM).

A NewWave time history based on the Gaussian spectrum and the frequency resolution defined above is shown in Figure 7.20.

The second order diffraction analysis yields a sum and difference quadratic transfer function (QTF) for each frequency pair (45 frequency pairs in total), which describe the second order sum and difference interaction between the two frequency components. The QTFs are used to construct the second order solution for a specified incident wave field.

In order to check whether nine frequency components are sufficient to capture the salient features of the second order response, surface plots showing the variation of the second order QTFs, $Q^{\pm}$, with the frequencies of the interacting wave components have been produced for a number of points in the vicinity of the LUNA structure. For all points considered, both close to the cylinders (front and back) and near the centre of the structure, the QTFs show relatively smooth variation with frequency, suggesting that a sufficiently fine frequency resolution has been used. As an illustration of the plots produced, Figure 7.21 shows surface plots of the real and imaginary components of the sum and difference QTFs for a point at the centre of the structure (x=0,y=0).

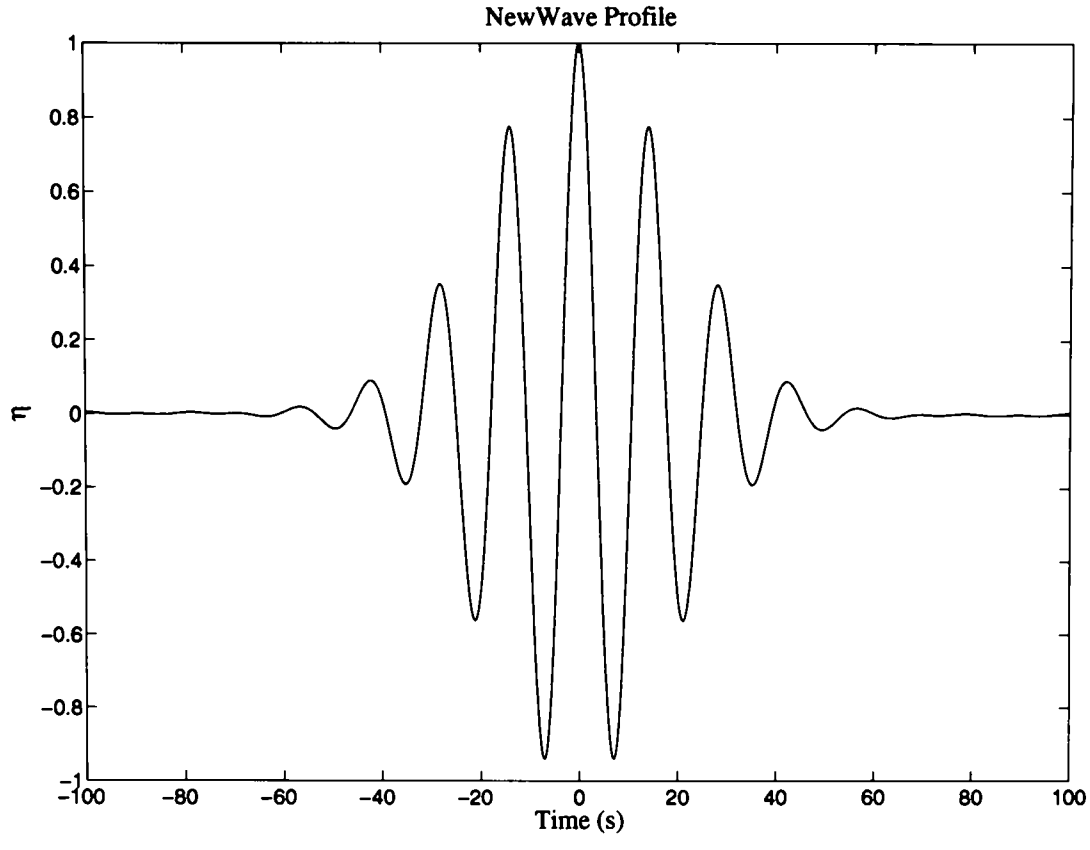

Figure 7.20: NewWave profile based on a Gaussian spectrum. The profile has been normalised such that the peak value is 1.

The second order sum QTFs are smooth across the entire frequency domain whereas the rate of change of the difference QTFs increases close to $f_1 = f_2$. This effect is most pronounced in the real components of the difference QTFs. Therefore, as an additional check on the accuracy of the computed difference QTFs, the complex values corresponding to monochromatic wave interaction (i.e. the QTFs along the $f_1 = f_2$ diagonal) have been compared against values computed using the linear analytical solution (Section 3.2 Chapter 3) and Equation 2.78 (Section 2.4 Chapter 2). Even though the linear analytical solution does not take account of the caisson, good agreement has been found between the analytical and numerical solutions. Furthermore, four additional frequency components have been considered between 0.05Hz and 0.06Hz, namely 0.0517Hz, 0.0534Hz, 0.0567Hz and 0.0584Hz, in order to confirm the frequency variation close to $f_1 = f_2$. The variation of the difference QTFs computed at these additional frequencies is in agreement with the results shown in Figure 7.21 - e.g. plotting the $\mathrm{Re}(Q^-)$ along a line perpendicular to the $f_1 = f_2$ diagonal reveals the ridge.

The surface plots shown in Figure 7.21 for a point at the centre of the structure are representative of the QTF variation for most points; the sum QTF exhibiting smooth variation across all frequencies and the real component of the difference QTF showing more rapid change close to $f_1 = f_2$.

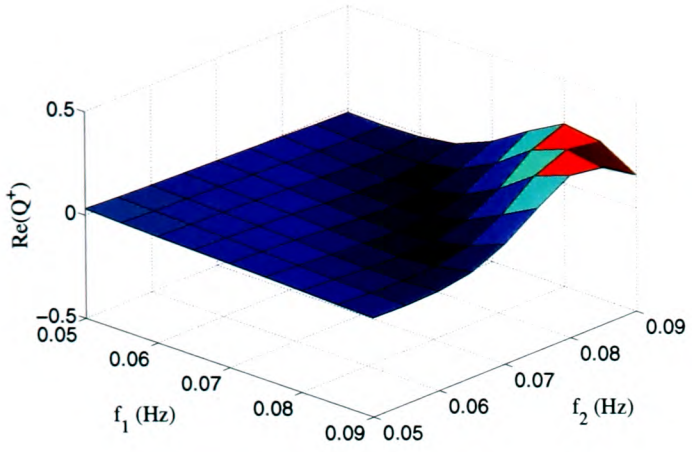

(a) $\mathrm{Re}(Q^+)$

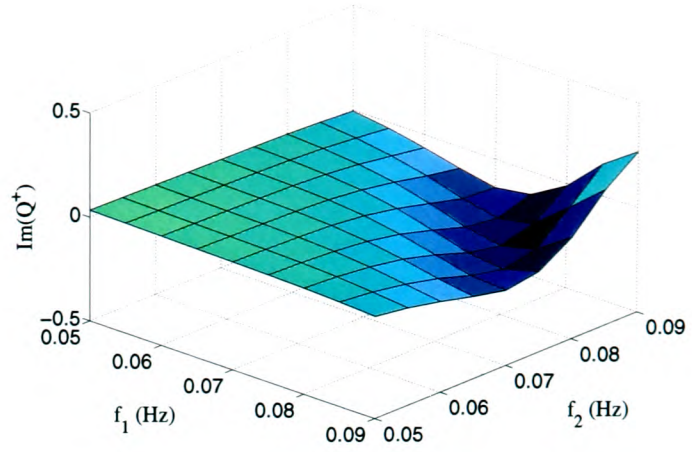

(b) $\mathrm{Im}(Q^+)$

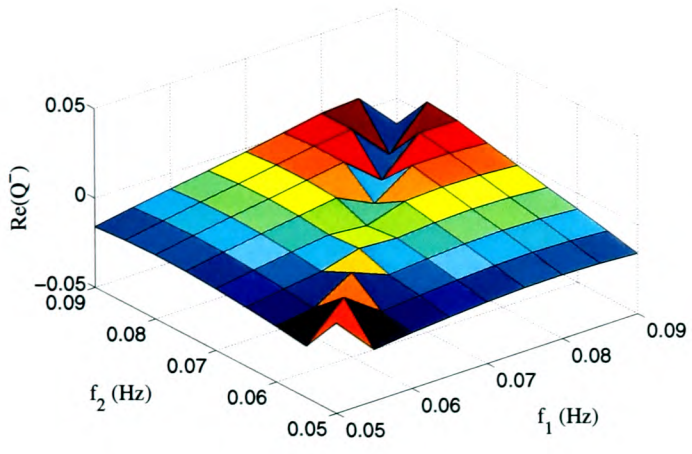

(c) $\mathrm{Re}(Q^-)$

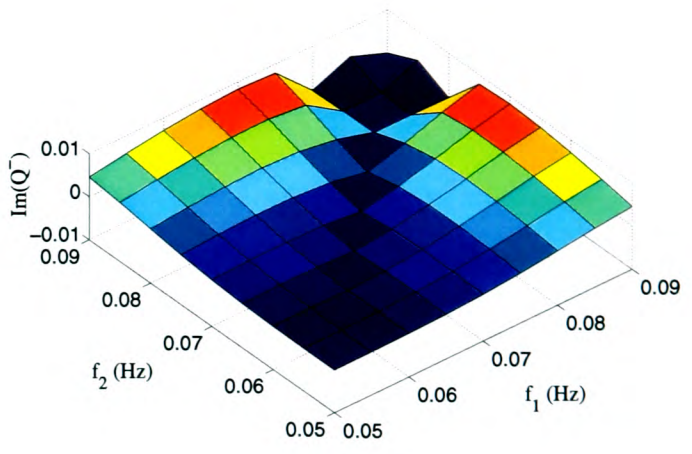

(d) $\mathrm{Im}(Q^-)$

Figure 7.21: Surface plots of the QTFs, $Q^{\pm}$, for a point at the centre of the LUNA structure.

7.5.1 Solution verification

Previous application of DIFFRACT for second order diffraction of focused wave groups is limited to single cylinders and ship shaped bodies. In order to illustrate the accuracy of the meshing schemes implemented in the present study and to extend the application of DIFFRACT to multiple cylinder arrays for incident wave fields composed of more than one frequency component, this section presents results for bichromatic waves incident upon a single cylinder and a four-cylinder array and compares them with published data.

To the author's knowledge, at the time of writing this thesis the only published surface elevation data available for bichromatic waves incident upon a body are for single cylinders and only hydrodynamic force data are available for multiple cylinder arrays. Therefore surface elevation results in the vicinity of a single cylinder and hydrodynamic forces on a four-cylinder array are considered in this section.

Kim and Yue (1990) considered the second order diffraction of unidirectional bichromatic waves ($\beta = 0$ for both wave components) by a uniform bottom mounted vertical circular

cylinder of radius a and depth $h = a$. Using a semi-analytical approach Kim and Yue computed the second order sum and difference runup profiles around the circumference of the cylinder for the frequency pair $(\kappa_1 a, \kappa_2 a) = (1.536, 1.709)$, where κ_1 and κ_2 are the linear wavenumber values for the two incident components. Note that Kim and Yue define the incident frequency pair as $(\nu_1 a, \nu_2 a) = (1.4, 1.6)$, where ν_1 and ν_2 are deep water wavenumber values. The second order runup computed by Kim and Yue for θ between 0 and π is accurately reproduced using DIFFRACT in Figure 7.22. Both $|\eta_{p12}^{(2\pm)}|/A_1 A_2$ and $|\eta_{q12}^{(2\pm)}|/A_1 A_2$ are plotted in Figure 7.22, where A_1 and A_2 are the amplitudes of the two incident wave components and the subscript '12' refers to the wave-wave interaction term (wave self interaction terms are not plotted).

The verification of second order hydrodynamic forces on an array of four bottom mounted vertical circular cylinders in bichromatic waves is now considered. The only published results available for bichromatic waves incident upon a four-cylinder array are provided by Moubayed and Williams (1995), who used a semi-analytical approach to study the problem for a number of frequency pairs. Moubayed and Williams considered an array of four cylinders arranged at the vertices of a square of side length $R = 5a$ and depth $h = 4a$.

Because of the convergence limitations of DIFFRACT it is not possible to produce converged second order results for the majority of the frequencies considered by Moubayed and Williams. Fortunately it was possible to produce almost converged results for the lowest two frequency components, which have corresponding non-dimensional linear wavenumbers $\kappa_1 a = 1.0$ and $\kappa_2 a = 1.2$; these are essentially deep water values for the configuration considered. The calculation did, however, take approximately 200 hours to complete and convergence was not achieved for a number of nodes on the free surface. A comparison between the forces generated using DIFFRACT and those produced by Moubayed and Williams for two incident wave angles ($\beta = 0$ and 45 degrees) is given in Table 7.1. The second order force components on cylinder 1 (centred at $x = y = +2.5a$) due to the first order potential ($F_q^{2\pm}$) and second order potential ($F_p^{2\pm}$) are recorded in Table 7.1. Despite the convergence problems encountered in the numerical solution, good agreement is found between the two sets of results.

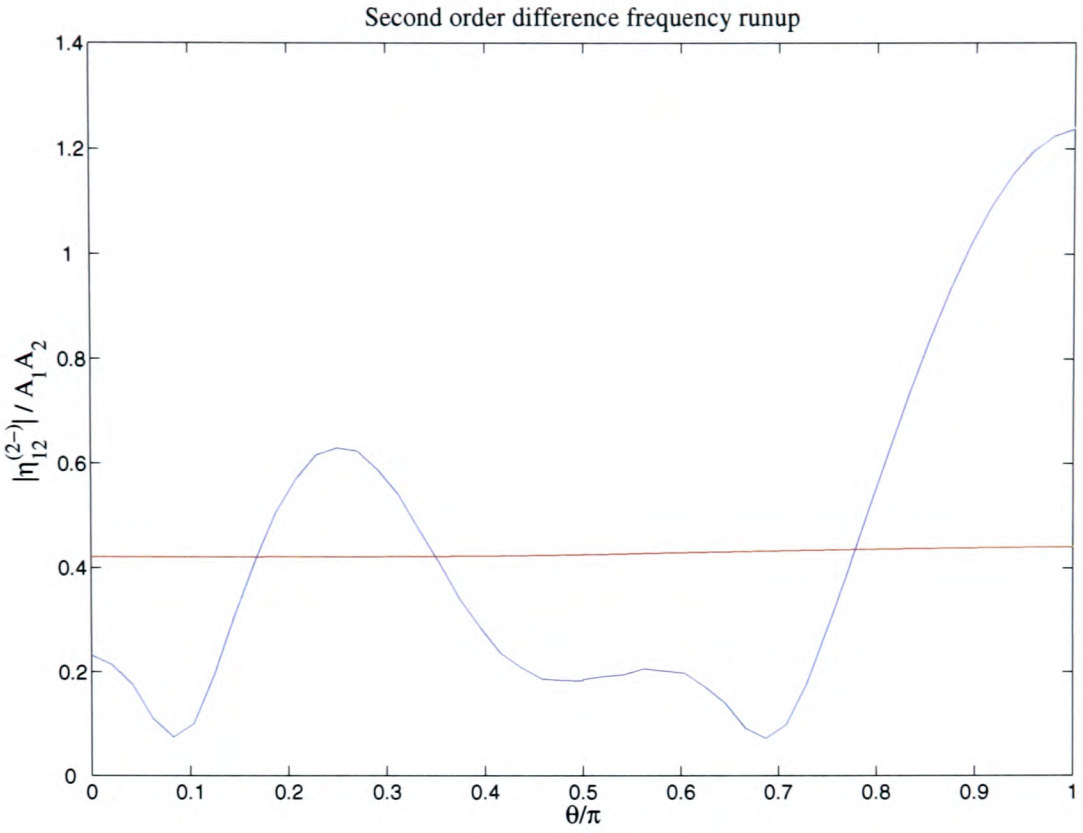

Figure 7.22: Second order runup around a single cylinder for incident bichromatic waves. $(\kappa_1 a, \kappa_2 a) = (1.536, 1.709)$. $h/a = 1$. Red line: $|\eta_{p12}^{(2\pm)}|/A_1 A_2$; blue line: $|\eta_{q12}^{(2\pm)}|/A_1 A_2$. Positive θ is measured anti-clockwise from the positive x-axis.

	β (degrees)	F_q^{2-}	F_p^{2-}	F_q^{2+}	F_p^{2+}
Force in x-direction					
DIFFRACT	0	0.470	0.309	1.322	3.321
Moubayed and Williams	0	0.469	0.289	1.324	3.314
Force in y-direction					
DIFFRACT	0	0.075	0.029	0.716	1.743
Moubayed and Williams	0	0.077	0.022	0.717	1.739
Force in x-direction					
DIFFRACT	45	0.261	0.175	1.010	2.046
Moubayed and Williams	45	0.266	0.163	1.008	2.035

Table 7.1: A comparison between second order sum and difference frequency force magnitudes on cylinder 1 generated by DIFFRACT and those produced by Moubayed and Williams (1995). Bichromatic incident waves: $\kappa_1 a = 1.0$ and $\kappa_2 a = 1.2$. The forces are non-dimensionalised by $\rho g a A_1 A_2$. Forces are given to three decimal places

The frequency components used to generate the NewWave in Section 7.5.2 are all below the maximum frequency for convergence and hence the computation time should be shorter and the accuracy improved for each frequency pair compared to the above case.

The second order diffracted wave field resulting from an incident NewWave will consist of components spread across a number of frequencies and the mesh used to generate the numerical results must achieve convergence for all frequencies. For such calculations it is often difficult to create a mesh for the free surface that can achieve convergence at both the difference and sum frequencies. In particular, difficulty was experienced achieving convergence for the difference frequency calculation where, in general, the smaller the difference frequency the larger the required numerical integration region. An excessively large numerical integration region is obviously not desirable for the sum calculation where it is necessary to keep the mesh sufficiently fine in order to achieve convergence. This problem was exacerbated for the DIFFRACT code because of the limit on the number of elements that can be used in the free surface mesh. However, following extensive convergence testing for the considered incident NewWave, the author is confident that the results presented for a Gaussian spectrum are accurate.

7.5.2 Second order surface elevation

Following the verification of the DIFFRACT code for multiple incident frequencies, the code is now used to investigate the surface elevation around the LUNA structure for an incident NewWave.

A unidirectional NewWave is considered in this section with all constituent wave components propagating along the x-axis ($\beta = 0$). A NewWave amplitude, A_{nw}, of 11m is used, which is a realistic maximum crest amplitude for a storm in the Sea of Okhotsk near Sakhalin Island and is the value used in Chapter 6 for the study of the linear diffraction of a NewWave by the LUNA structure.

For an incident NewWave, the wave spectrum (a Gaussian spectrum here) is represented by a discrete set of monochromatic waves which have amplitudes defined by Equation 2.2 (Section 2.2 Chapter 2). The second order solution is formulated as a sum of the QTFs for all frequency pairs weighted by the corresponding wave amplitudes. This approach is outlined by Eatock Taylor and Fonquernie (2001).

Firstly in this section, the magnitudes of the second order sum and difference contributions to the total surface elevation, defined by:

$$|\eta^{(2\pm)}| = \sum_{m=1}^{N}\sum_{n=1}^{N} A_m A_n |Q_{mn}^{\pm}| \tag{7.3}$$

are examined. For the particular NewWave considered in this section nine frequency components are used (N=9). Here A_m are the component wave amplitudes and $Q_{mn}^{\pm}$ are the quadratic transfer functions generated by DIFFRACT. These magnitude results are relatively straightforward to compute and give an indication of the size of the second order contributions obtainable for some unspecified combination of phases. It is important to note that Equation 7.3 does not provide the magnitude of the response when all of the wave components come into phase, as is the case when plotting the magnitude of the linear response.

The magnitudes of the sum and difference contributions to the total runup around cylinders 1 and 4 are shown in Figure 7.23. The incident NewWave is focused at $x_0 = 0$.

The magnitude of the second order sum contribution, $|\eta^{(2+)}|$, obtainable for some combination of phases, is found to be very large around the cylinders, reaching peak values of 26.0m and 23.3m for cylinders 1 and 4 respectively. Considering the incident NewWave amplitude is 11m, these runup values show that diffraction effects can result in a significant magnification of the free surface close to the cylinders. The potential component of the sum contribution,

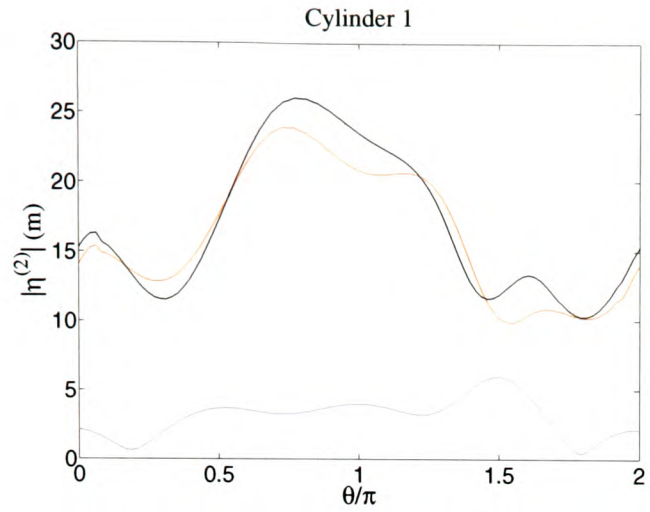

(a) Second order sum

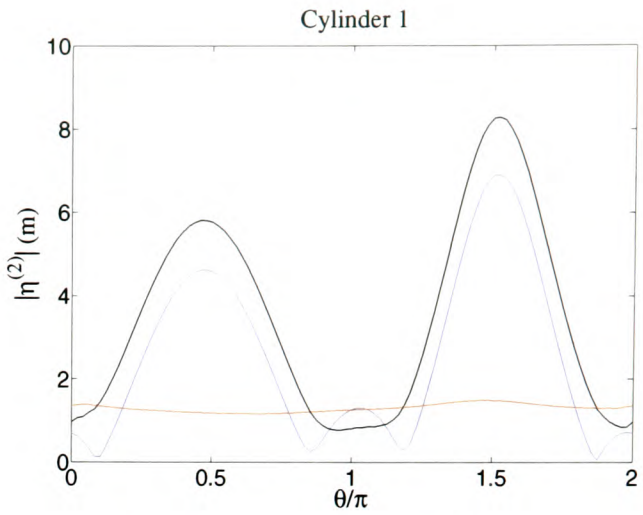

(b) Second order difference

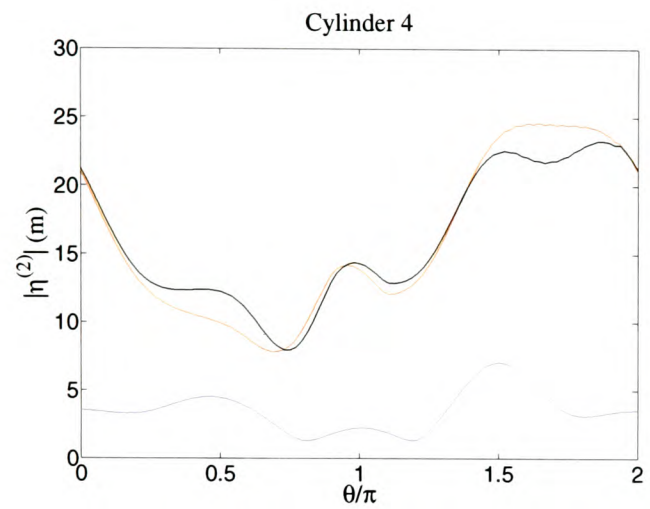

(c) Second order sum

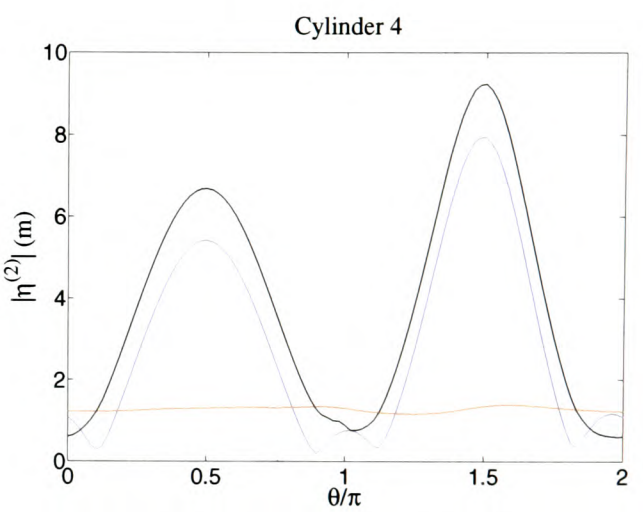

(d) Second order difference

Figure 7.23: Magnitudes of the sum and difference contributions to the total runup around cylinders 1 and 4. Black line: $|\eta^{(2\pm)}|$; red line: $|\eta_p^{(2\pm)}|$; blue line: $|\eta_q^{(2\pm)}|$. Positive θ is measured anti-clockwise from the positive x-axis.

$\eta_p^{(2+)}$, dominates the response and hence suggests that a second order near-trapped mode has possibly been excited. This possibility could be explored further through an examination of the linear surface elevation frequency response functions close to the cylinders. With reference to response data already presented, the linear surface elevation frequency response function between the two front cylinders (given in Figure 6.10 (a) Chapter 6) shows that the largest linear responses, which perhaps correspond to linear near-trapping, occur at 0.126Hz and 0.159Hz. These frequencies correspond to second order near-trapped frequencies of 0.063Hz and 0.080Hz, which both lie close to the peak of the considered Gaussian spectrum. In fact, the peak frequency of the Gaussian spectrum ($f_p = 0.07$Hz) equals half the frequency of the trough separating the largest two linear peaks. Therefore, it seems likely that the large sum elevations observed are the result of exciting two second order (double frequency) near-trapped modes.

Although smaller than the sum contribution, the difference contribution can still represent a

significant proportion of the total runup, especially between the front and back cylinders. The largest difference magnitudes, $|\eta^{(2-)}|$, around cylinders 1 (8.3m) and 4 (9.2m) in Figure 7.23 correspond to 75.5% and 83.6% of the incident NewWave amplitude respectively. Also, as one would expect for the difference contribution, the low frequency response is dominated by the quadratic contribution, $\eta_q^{(2-)}$

The wave field away from the surface of the cylinders along the x and y axes is now considered. Figure 7.24 plots the magnitude of the second order sum and difference elevations along the x and y axes using Equation 7.3, together with the magnitude of the linear elevation for comparison.

The magnitude of the linear elevation reaches a peak value of 17.0m near the centre of the structure whereas the magnitudes of the second order sum and difference elevations reach peak values between the front and back cylinders. For some combination of phases, the sum elevation exceeds the linear elevation between the front and back cylinders, attaining a peak magnitude of 27.4m between the back cylinders, which is 2.5 times the incident NewWave amplitude. The peak difference magnitude is equal to 5.6m and occurs between the two front cylinders.

Figures 7.23 and 7.24 show that the second order contributions to the diffracted wave field for an incident NewWave are considerable and, depending on the phasing, can exceed the linear contributions.

It would also be useful to plot the peak surface elevation response (positive or negative) at each point around the cylinders and along the x and y axes, which would require the computation of the surface elevation time history at each point. This is pursued to some extent below where surface elevation time histories are computed at three points around the LUNA structure.

The total surface elevation time history (correct to second order) is defined by:

$$\eta(t) = \Re\left[\sum_{n=1}^{N} A_n L_n \mathrm{e}^{-i\omega_n t} + \sum_{m=1}^{N}\sum_{n=1}^{N} A_m A_n \left(Q_{mn}^{+}\mathrm{e}^{-i(\omega_m+\omega_n)t} + Q_{mn}^{-}\mathrm{e}^{-i(\omega_m-\omega_n)t}\right)\right] \quad (7.4)$$

where t is time, N=9 and L_n are the linear transfer functions generated by DIFFRACT. Figures 7.25 and 7.26 show time histories predicted by linear and second order diffraction theories for a point midway between the two front cylinders, a point at the centre of the structure and a point midway between the two back cylinders. Figure 7.25 shows the second

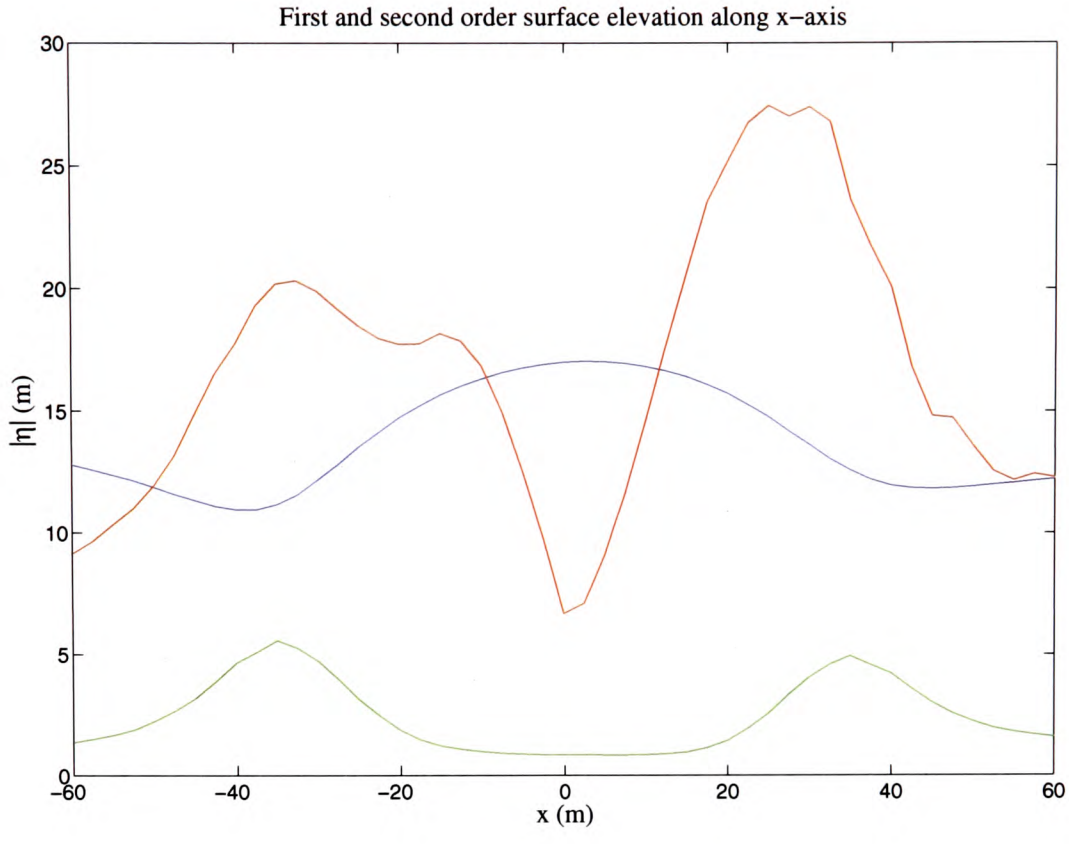

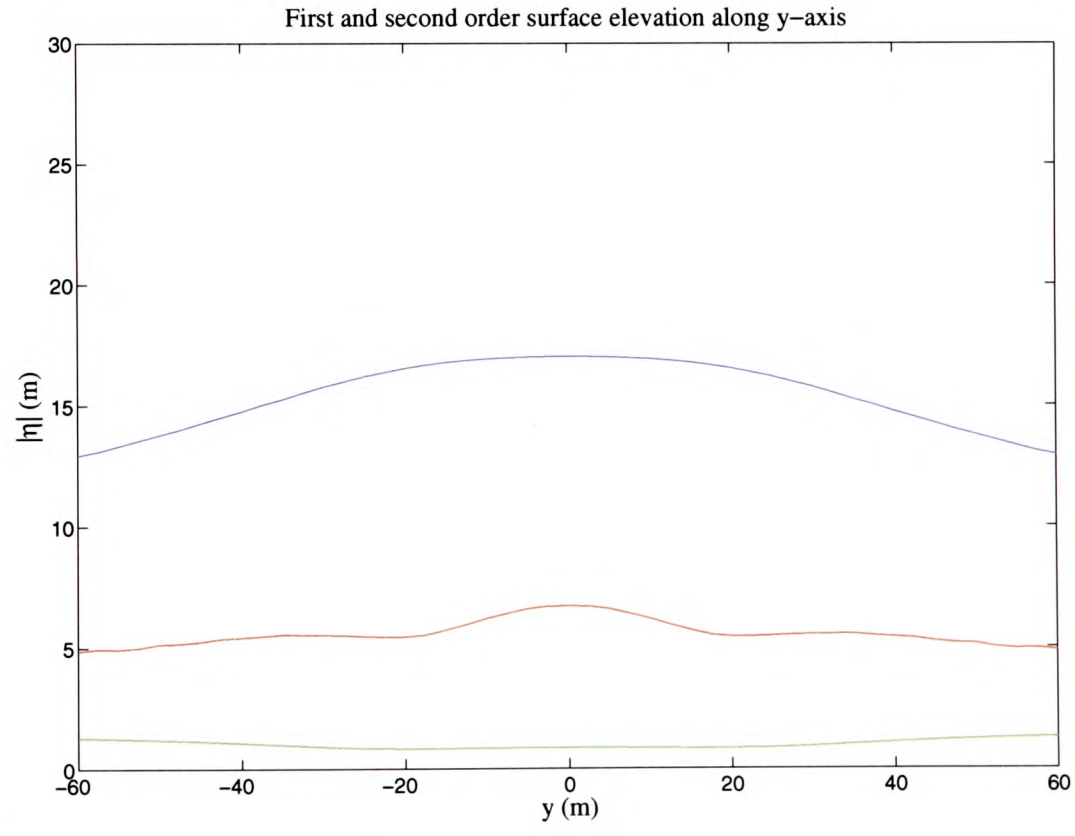

Figure 7.24: Magnitudes of the linear and second order contributions along the x and y axes. Blue line: $|\eta^{(1)}|$; red line: $|\eta^{(2+)}|$; green line: $|\eta^{(2-)}|$.

order sum and difference time histories and Figure 7.26 shows the linear and total second order (sum + difference) time histories together with the overall (first + second order) time histories, $\eta^{(1+2)}$. The incident NewWave is focused at $t_0 = 0$.

The second order contributions (sum and difference) are found to be comparatively small at the centre of the structure, where the majority of the response is predicted well by linear diffraction. The second order contributions become more significant between the front and back cylinders, considerably altering the surface elevation time histories predicted by linear diffraction. Dominating sum contributions result in large higher frequency peaks in the overall time histories between the front and back cylinders. The largest overall surface elevations, $\eta^{(1+2)}$, between the front and back cylinders are 23.9m and 34.3m respectively, which build up after the focus time. The growth of the second order sum contributions after the focus time, particularly between the two front cylinders, is perhaps associated with the growth of a near-trapped mode response, which is known to take time to build up (see Eatock Taylor et al. (2006)).

A curious feature of the second order time histories between the front and back cylinders is the fact that the responses do not seem to settle to zero elevation. Figure 7.25 shows that this is caused by the difference contributions, which decay very slowly with time after the group has passed. This slow decay is surprising and is perhaps a manifestation of the resonant surface responses between the cylinders. Alternatively, there could be a convergence problem with the difference calculation between the cylinders. An investigation into this anomalous behaviour is not pursued here.

A further interesting observation is that the large troughs observed between the front and back cylinders (e.g. $\eta = -30.4$m between the back cylinders) are close to the top of the LUNA caisson. It seems likely that if a larger NewWave amplitude is considered then the resultant troughs in these regions may interact with the top of the caisson. This could leave the top of the caisson exposed to slam loading, which would have large implications for the structural design of the caisson.

The diffraction magnification effects predicted in this section are considerably larger than those recorded in Chapter 6 Section 6.5.2 for the linear diffraction of a NewWave based on a Pierson-Moskowitz spectrum. In Chapter 6 the incident NewWave did not excite a linear near-trapped mode and since only linear components were considered, the diffracted free surface around the structure was not particularly extreme. However, as demonstrated in this section, when second order components are considered the total diffracted wave field can be significantly magnified if sufficient energy excites a second order near-trapped mode. This

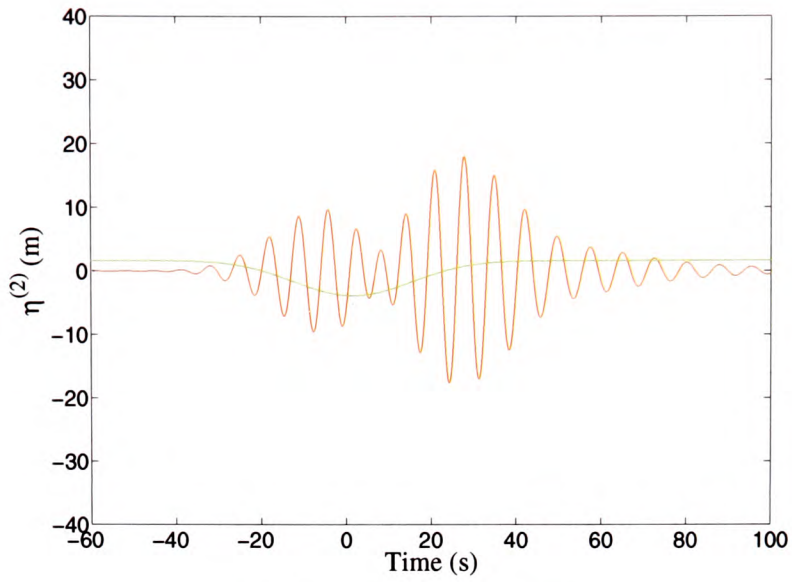

(a) Between front columns

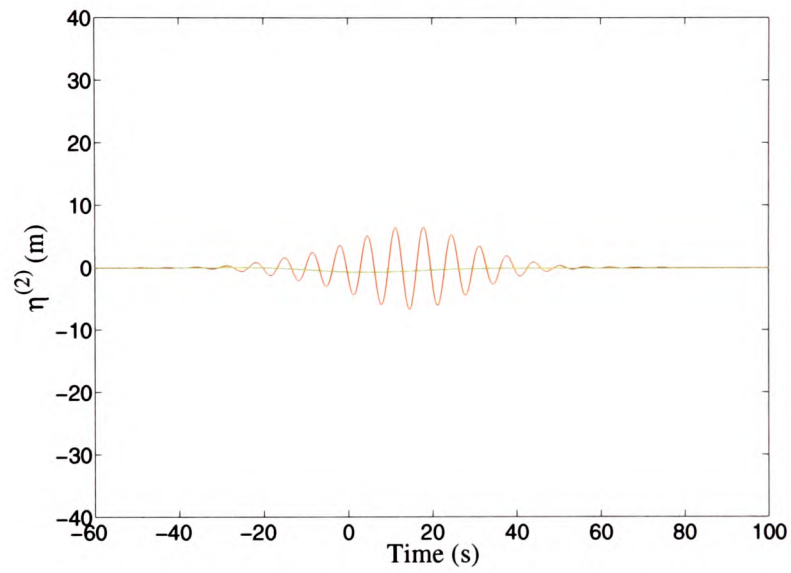

(b) Centre of structure

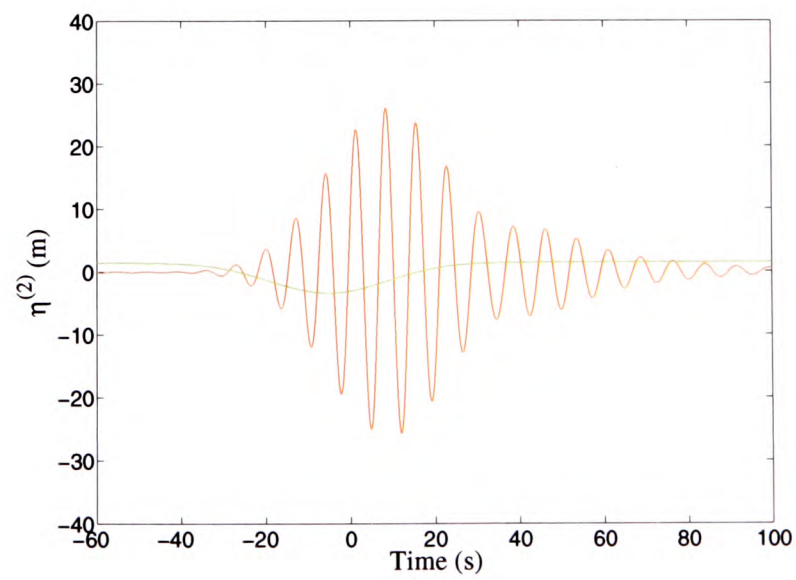

(c) Between back columns

Figure 7.25: Surface elevation time histories. Red line: $\eta^{(2+)}$; green line: $\eta^{(2-)}$.

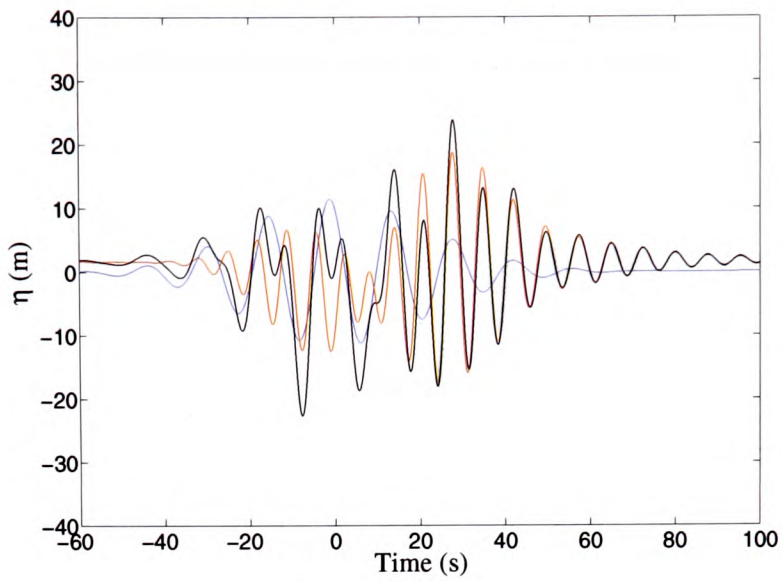

(a) Between front columns

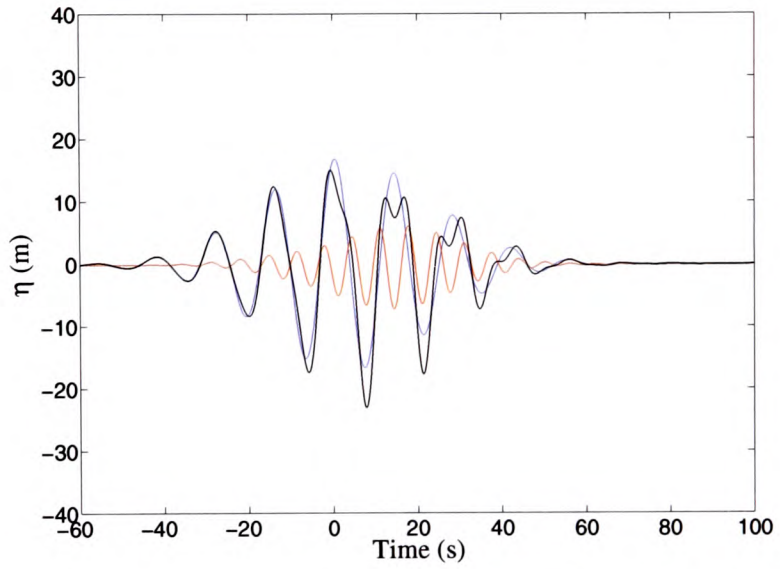

(b) Centre of structure

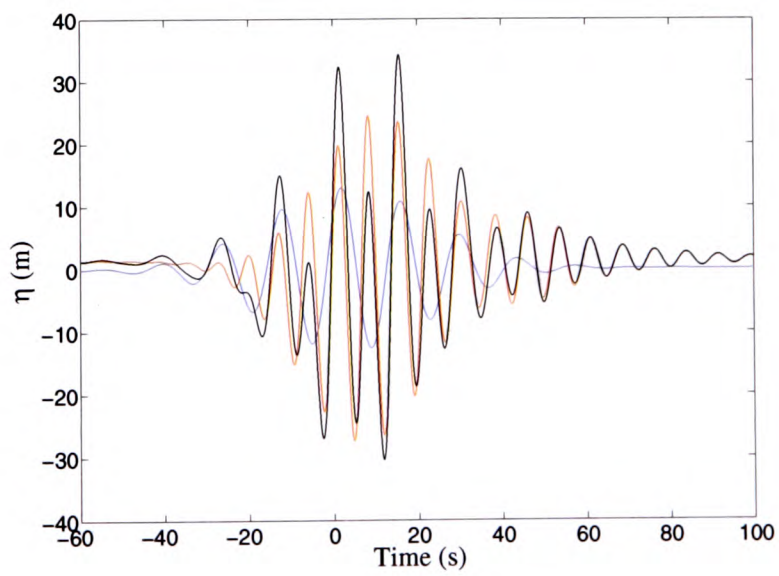

(c) Between back columns

Figure 7.26: Surface elevation time histories. Black line: $\eta^{(1+2)}$; red line: $\eta^{(2)}$; blue line: $\eta^{(1)}$.

reinforces the argument, made in Section 7.4.3, that an offshore structure should be designed so that the local wave energy spectrum does not excite linear or second order near-trapped modes.

Comparisons with wave data are needed to determine whether the magnitudes and locations of the extreme elevations predicted in this section occur in reality. Unfortunately, no model test data for incident NewWaves are available.

It would be interesting to investigate the effect the number of frequency components has on the second order results for an incident NewWave. This can be pursued to some extent using the QTFs already computed by considering only the first, third, fifth, seventh and ninth frequency components.

7.6 Conclusions

The efficiency and accuracy of the DIFFRACT code at second order has been established through systematic convergence testing and comparisons with available published data for both incident monochromatic and bichromatic waves.

The second order surface elevation in the vicinity of the LUNA structure has been examined for the experimental regular wave frequency. The magnitudes of the second order contributions (sum and difference) to the overall diffracted wave field were found to be considerable.

The study of near-trapping in Chapter 6 has been extended in this chapter to explore the possibility of near-trapping at second order. Working within the limitations of the DIFFRACT code, second order near-trapping has been studied for an array of four bottom mounted cylinders arranged at the vertices of a square and the LUNA structure. The results presented suggest that near-trapping of the second order wave occurs when its frequency coincides with the linear near-trapping frequency. Furthermore, the second order wave field at second order near-trapping was found to be remarkably similar to the linear wave field at linear near-trapping, suggesting that useful information on extreme second order responses can be obtained by studying linear diffraction alone.

The effect of caisson height on the second order surface elevation in the vicinity of the LUNA structure was investigated. Through comparison with linear results in Chapter 6, the presence of a caisson was found to have a larger effect on the second order wave field than the linear field.

Finally, the diffraction of an incident NewWave by the LUNA structure was studied. The

second order elevations around the structure were found to be very large and were thought to be caused by second order near-trapping.

Chapter 8

Experimental data analysis

8.1 Introduction

The wave data from the diffraction experiments described in Chapter 4 are analysed in this Chapter. Both the undisturbed (i.e. no model) and model test data are considered in an effort to improve current understanding of extreme water waves and to establish the effectiveness of diffraction theory for modelling real wave-structure interaction.

The analysis carried out in Chapter 5 on the Draupner field data was restricted by the comparatively small number of waves ($\sim$ 100) in each data set. The irregular wave data sets analysed in this chapter contain many more waves, approximately 1000 waves during each three hour test period, and so errors arising from statistical variability of the data are greatly reduced. Therefore, the undisturbed irregular wave data are first analysed in this chapter using the analysis tools developed in Chapter 5. In addition, the effect of directional spreading on the magnitude of the second order sum contribution is investigated for the undisturbed data.

Once the wave conditions at the test site have been established, the model test irregular wave data are analysed and comparisons are made with the undisturbed data analysis in order to assess the nature of the diffraction effects on the incident wave field. The ability of linear diffraction theory to predict measured diffracted wave spectra in the vicinity of the LUNA structure is investigated for incident irregular waves. An approach to identify the linear frequency range of the model test irregular wave data, based on the coherence function between the undisturbed and diffracted wave records, is proposed. First and second order diffraction transfer functions are incorporated into the surface response statistics (SRS) method of Tromans and Vanderschuren (1995). The SRS method is used to compute crest elevation statistics beneath the LUNA structure corresponding to given probabilities of exceedance,

and comparisons are made with measured wave data. Furthermore, the effects of directional spreading on the measured diffracted wave field around the LUNA structure are investigated.

Finally, comparisons between measured surface elevations in the vicinity of the LUNA structure and linear and second order diffraction solutions are made for incident regular waves. Conclusions on the ability of diffraction theory to reproduce real wave measurements are made.

8.2 Undisturbed data

For all undisturbed data analysis undertaken in this chapter, with the exception of the directional spreading calculations carried out in Section 8.2.8, the undisturbed unidirectional irregular wave data set is considered (Data Set 3, Table 4.2, Section 4.6 Chapter 4). For the consideration of directional spreading, the undisturbed multidirectional irregular wave data set is used (Data Set 4, Table 4.2, Section 4.6 Chapter 4). The target met-ocean conditions for these two data sets are given in Section 4.6 Chapter 4.

8.2.1 Variability between probes

Before proceeding to analyse the undisturbed waves, the variability of the wave conditions at the test site is assessed. As described in Section 4.5 Chapter 4, wave conditions at the centre and around the perimeter of the test site were measured using an array of nine wave probes. The spectra for all probe locations show little variation, with the peak period, T_p, and significant wave height, H_s, closely matching the target wave conditions. Computed values of T_z, T_p and H_s at each probe location are given in Table 8.1. The mean T_p and H_s values are 14.3s and 9.9m respectively, which exactly match (to one decimal place) the target values. The T_p values have a range of 0.6s (4% of the target value) and the H_s values have a range of 0.6m (6% of the target value). Considering the numerous inaccuracies present in any experimental undertaking, it is concluded that there is comparatively little variability between the wave probes at the test site; each probe is able to reproduce the target wave conditions with sufficient accuracy. Wave probe 10, which is located at the centre of the test site, is used for all subsequent undisturbed data analysis.

Wave probe	T_z (s)	T_p (s)	H_s (m)
6	11.0	14.5	9.8
7	11.5	14.1	10.1
8	11.0	14.5	9.7
9	11.2	14.5	10.0
10	11.2	13.9	9.5
11	11.1	14.5	9.8
12	11.1	14.5	10.1
13	11.0	14.5	9.9
14	11.2	14.1	10.0

Table 8.1: Computed T_z, T_p and H_s values for each undisturbed wave probe at the test site. All values are given to one decimal place.

8.2.2 Wave profiles

Average large crest and trough profiles, together with their linear and second order contributions, are considered in this section. The average linear crest profile can be computed using Equation 5.1, defined in Section 5.4 Chapter 5. Similarly, from a consideration of a Stokes water wave expansion, it can be shown that the even harmonics (which will be dominated by the second order contribution) can be readily extracted from a wave record using the expression:

$$\eta_{even} = \frac{\eta_C + \eta_T}{2} \tag{8.1}$$

where η_C is the average large crest profile (crest elevation taken as positive) and η_T is the average large trough profile (trough depression taken as negative). Average large crest and trough profiles, computed using the largest 25% of crests and troughs, together with the average linear and second order large crest profiles, computed using Equations 5.1 and 8.1, are shown in Figure 8.1. The second order difference contribution is filtered out of the data to obtain the linear and second order profiles.

As one would expect for real water waves, the crests are higher and spikier and the troughs are less deep and more rounded; the average peak crest elevation is 5.65m and the average peak trough depression is 4.62m. The linear contribution is found to dominate the average large crest profile close to $t = 0$; at $t = 0$ the average linear large crest amplitude is 5.13m and the average second order large crest amplitude is 0.52m (10.1% of the linear amplitude).

In order to most effectively illustrate the apparent asymmetry between crests and troughs in the wave data, Figure 8.2 plots ordered crest elevation against ordered trough depression in an exactly analogous manner to that used in Chapter 5. Predictably, crest-trough asymmetry

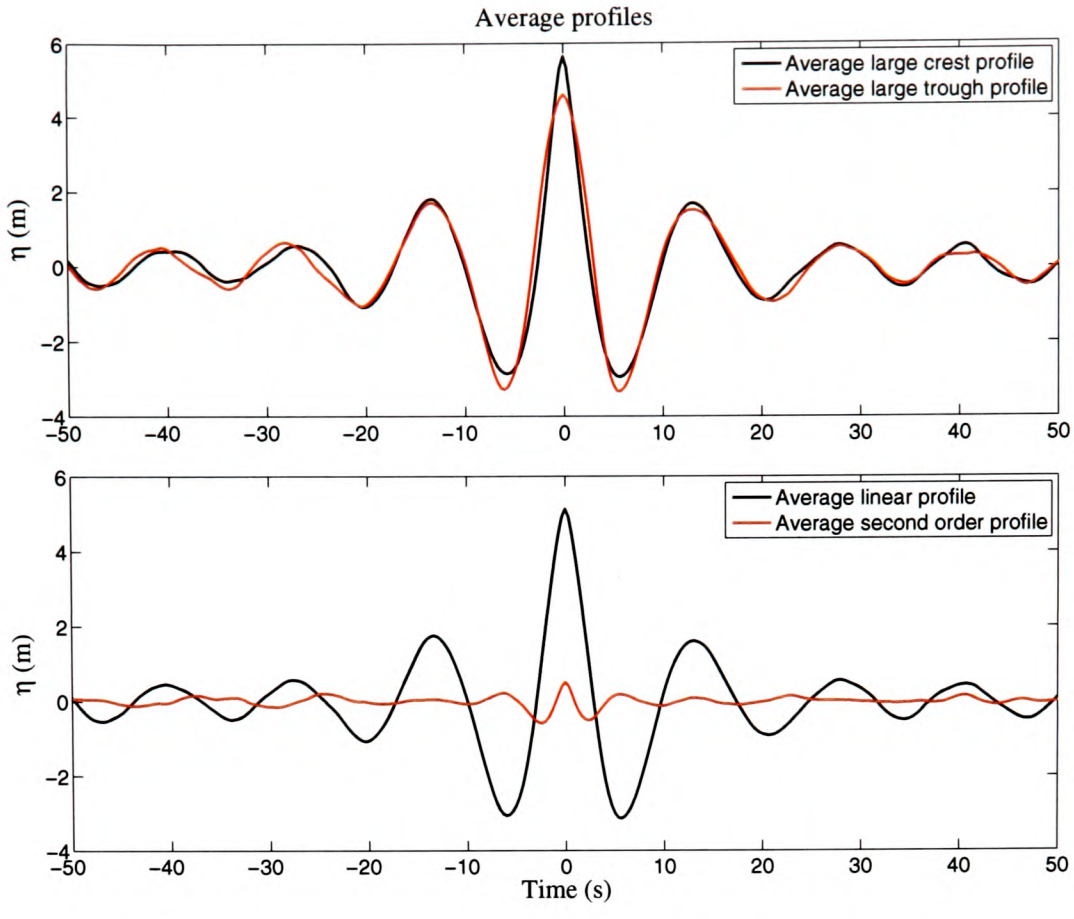

Figure 8.1: Average large crest and trough profiles, together with the average linear and second order large crest profiles for the undisturbed irregular wave data.

increases as the size of the crests and troughs increases. The advantage of presenting such results for the experimental data rather than the Draupner data is that there are many more instances of large waves in the data, and hence towards the top end of each ordered data set there is considerably less sample variability on the mean properties.

Similar plots to those generated in this section will be produced in Section 8.3.1 for the model test data. This will enable the effect of diffraction on wave steepness, wave asymmetry and the relative sizes of the linear and second order contributions to be examined.

8.2.3 Second and third order corrections

Stokes-type corrections are now used to approximate the second and third order sum contributions to the undisturbed wave record. The technique used (described fully in Section 5.5 Chapter 5) involves estimating the linear contribution by accounting only for the second order corrections, and then performing a search to the find the value of the second order sum coefficient, S_{22}, that sets the skewness of the linearised time series to zero. Therefore, the linear time series is approximated as:

$$\eta_L(t) \approx \eta(t) - \frac{S_{22}}{h}\left(\eta(t)^2 - \eta_H(t)^2\right) \tag{8.2}$$

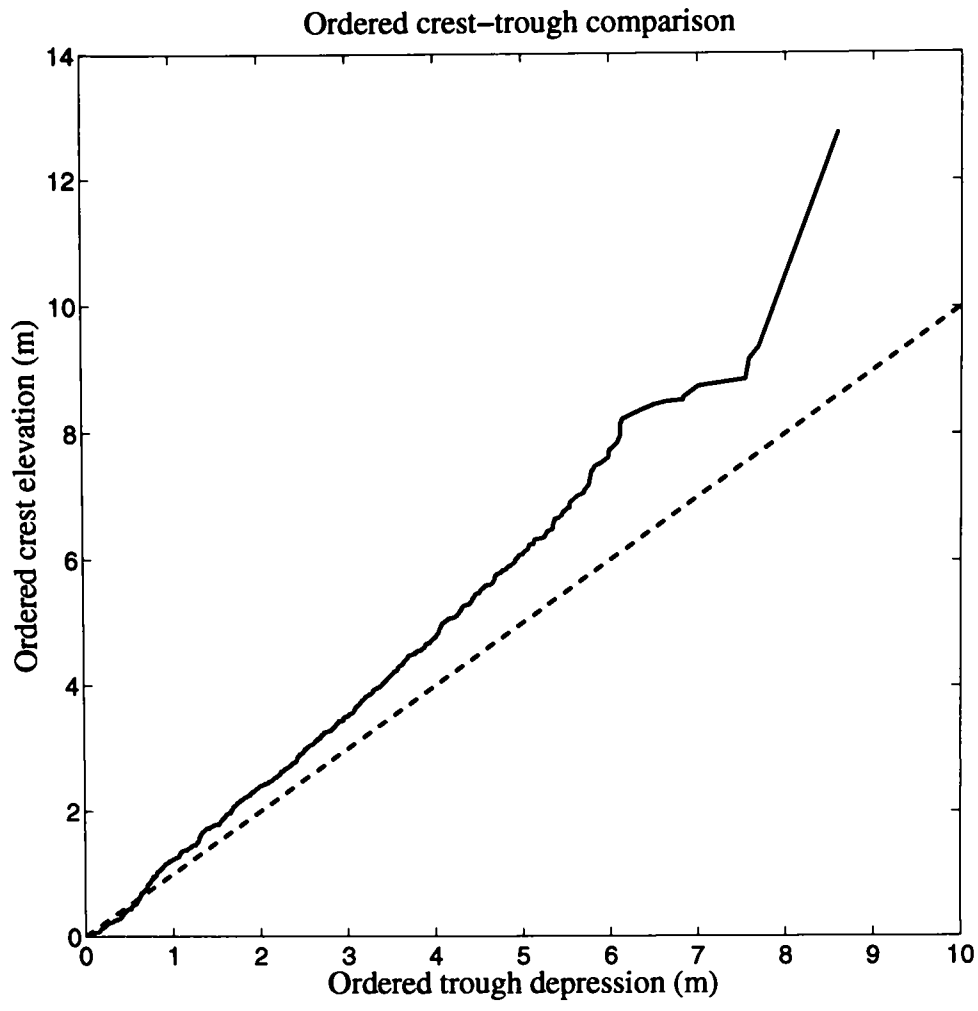

Figure 8.2: Ordered crest elevation plotted against ordered trough depression for the undisturbed irregular wave data.

where $\eta(t)$ is the high-pass filtered wave data, obtained using a suitable cut-off frequency (found through a spectral decomposition of the signal) to remove the second order difference contribution.

For the Draupner data it was not possible to assess how variable the computed value of S_{22} was because there were insufficient waves in each data set. However, using the undisturbed experimental data this issue can now be addressed. The undisturbed wave record is divided into 10 sections each containing approximately 100 waves, and a S_{22} value is computed for each section. The values of S_{22} computed for each section are given in Table 8.2.

Section number	S_{22} for zero skewness
1	1.318
2	1.594
3	1.057
4	0.728
5	1.047
6	0.956
7	1.408
8	1.217
9	0.972
10	1.084

Table 8.2: Table of second order coefficient values computed using ten samples of 100 waves from the undisturbed irregular wave data. S_{22} values are given to three decimal places.

The range of S_{22} values computed is 0.728-1.594 and the mean value calculated across all 10 sections is 1.138. The range of S_{22} values found here clearly indicates that 100 waves is insufficient to reliably determine the magnitude of the second order sum coefficient. The value of S_{22} is now computed across different numbers of waves in an effort to further investigate the size of the wave record needed to obtain representative S_{22} values. The S_{22} values computed using different numbers of waves are given in Table 8.3.

Number of waves	S_{22} for zero skewness
200	1.466
300	1.247
400	1.126
500	1.137
1000	1.132

Table 8.3: Second order coefficient values computed using different numbers of waves from the undisturbed irregular wave data. S_{22} values are given to three decimal places.

From Table 8.3 and the mean value computed from Table 8.2, it is clear that a S_{22} value of approximately 1.13 is representative of the wave conditions in the undisturbed irregular wave data. Table 8.3 also suggests that 300 waves are insufficient to reliably compute S_{22}. Therefore, based upon the results presented here alone, it seems reasonable to conclude that at least 400-500 waves are needed to accurately compute the magnitude of the second order sum coefficient. However, noise in the experimental data, such as reflections in the wave tank, may affect the computation of the second order sum coefficient and so the results in this section should not be used to infer any definite conclusions for the Draupner field data. Random wave simulations could be used to investigate this further.

The more waves considered in the determination of S_{22}, the more representative the value

will be of the actual wave conditions. For this reason a S_{22} value of 1.132 (corresponding to the value computed using 1000 waves) is used in subsequent calculations. Figure 8.3 shows surface elevation histograms for the measured high-pass filtered wave record (η) and the linearised wave record (η_L) obtained using Equation 8.2 and $S_{22} = 1.132$. The histograms are plotted together with their reflections about the origin to help illustrate the degree of skewness present in the data. The plots have been smoothed using a 29-point running average.

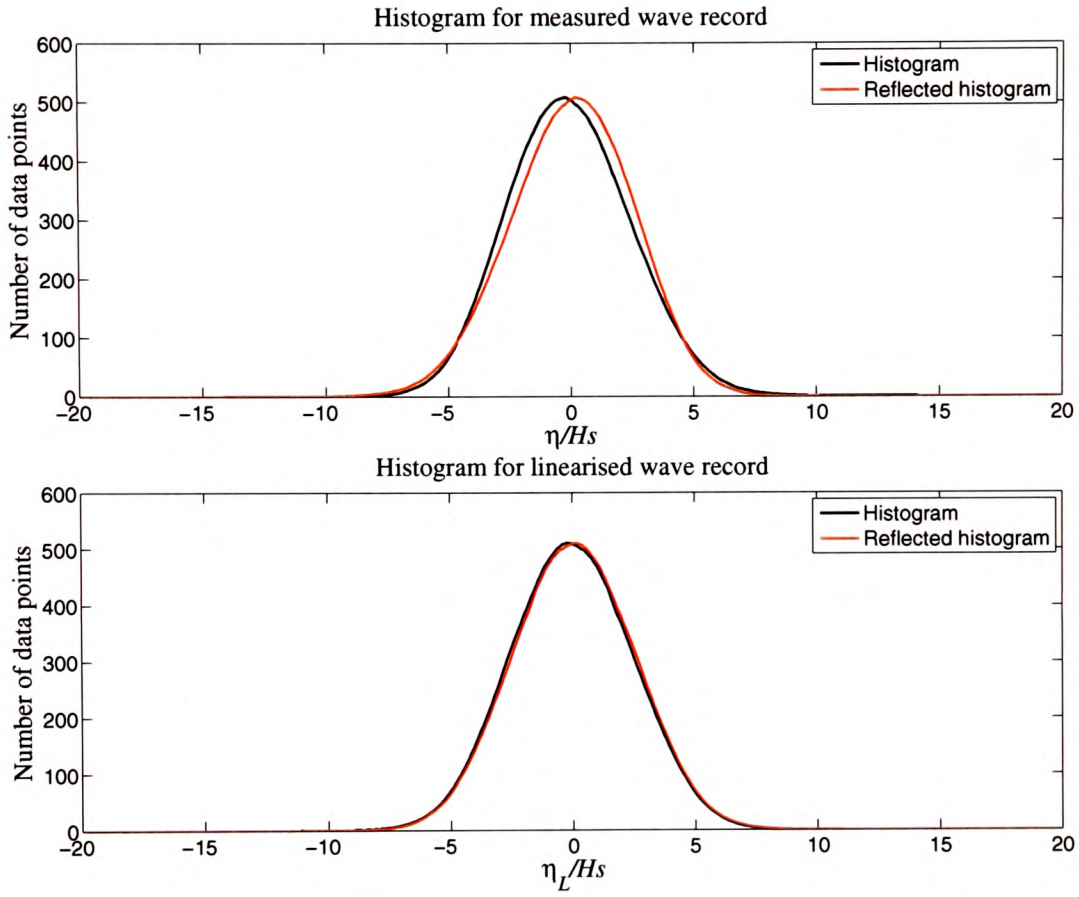

Figure 8.3: Surface elevation histograms for the measured high-pass filtered wave record (η) and the linearised wave record (η_L).

The histogram and its reflection overlie each other almost exactly for the linearised data, indicating that little skewness remains in the data. As a further illustration of the degree of skewness remaining in the linearised data, Figure 8.4 plots ordered crest elevation against ordered trough depression for the linearised wave record. Approximately 1000 crests and troughs are plotted in Figure 8.4, most of which show little asymmetry. The slight deviation from zero skewness found for crest and trough magnitudes above ~7.5m is the result of the second and third largest crests and troughs only. Hence, with the exception of two slightly skewed results, the magnitudes of ordered linearised crest height and trough depression are comparable over the full range of wave heights.

The magnitude of the third order sum coefficient, S_{33}, is now sought using the procedure outlined in Section 5.5 Chapter 5. Figure 5.7 in Chapter 5 plots the variation of the re-

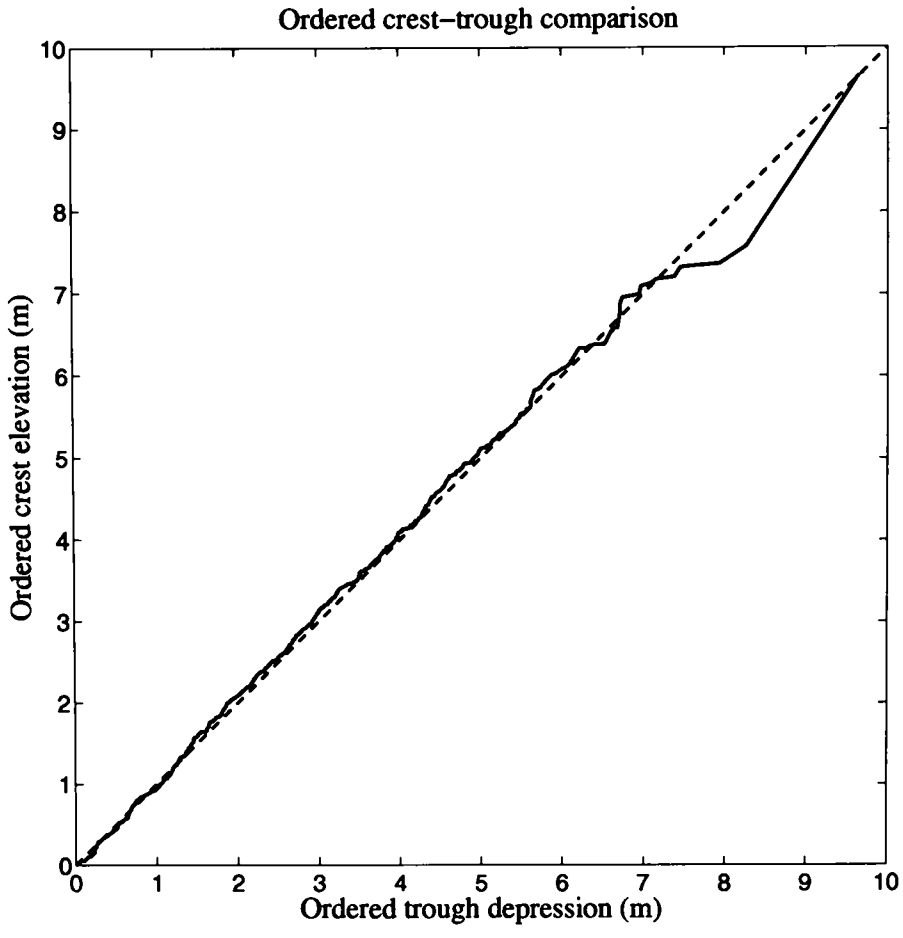

Figure 8.4: Ordered crest elevation against ordered trough depression for the linearised wave record.

formulated Stokes coefficients, S_{22} and S_{33} (defined in Section 2.5 Chapter 2), against κh, together with two horizontal lines corresponding to values of S_{22} that set the skewness of the two Draupner wave records to zero. A similar plot for the undisturbed data is shown in Figure 8.5, where the horizontal line corresponding to $S_{22} = 1.132$ now lies slightly above the minimum of the S_{22} curve, suggesting two suitable values of κh (found at the intersections of the horizontal line and the S_{22} curve) for the computation of S_{33}. The values of κh at the points of intersection are 1.34 and 1.90, which both lie close to the minimum of the S_{22} curve ($\kappa h = 1.60$). As noted in Chapter 5 for the Draupner data, close to the minimum of the S_{22} curve the second and third order coefficients are relatively insensitive to κh for this particular water depth (53.13m) and hence, similar to the Draupner data analysis, a κh value of 1.60 is again used here for the evaluation of the second and third order coefficients.

Using equations 2.81 and 2.83 (Section 2.5 Chapter 2) with $\kappa h = 1.60$, the coefficients S_{22} and S_{33} are found to be 1.10 and 1.57 (both to two decimal places). Note the excellent statistical accuracy of the S_{22} value computed from 1000 waves; to one decimal place the values (1.132 and 1.10) are identical. Therefore, the first three terms in the Stokes water wave expansion for the undisturbed irregular wave data can be approximated as:

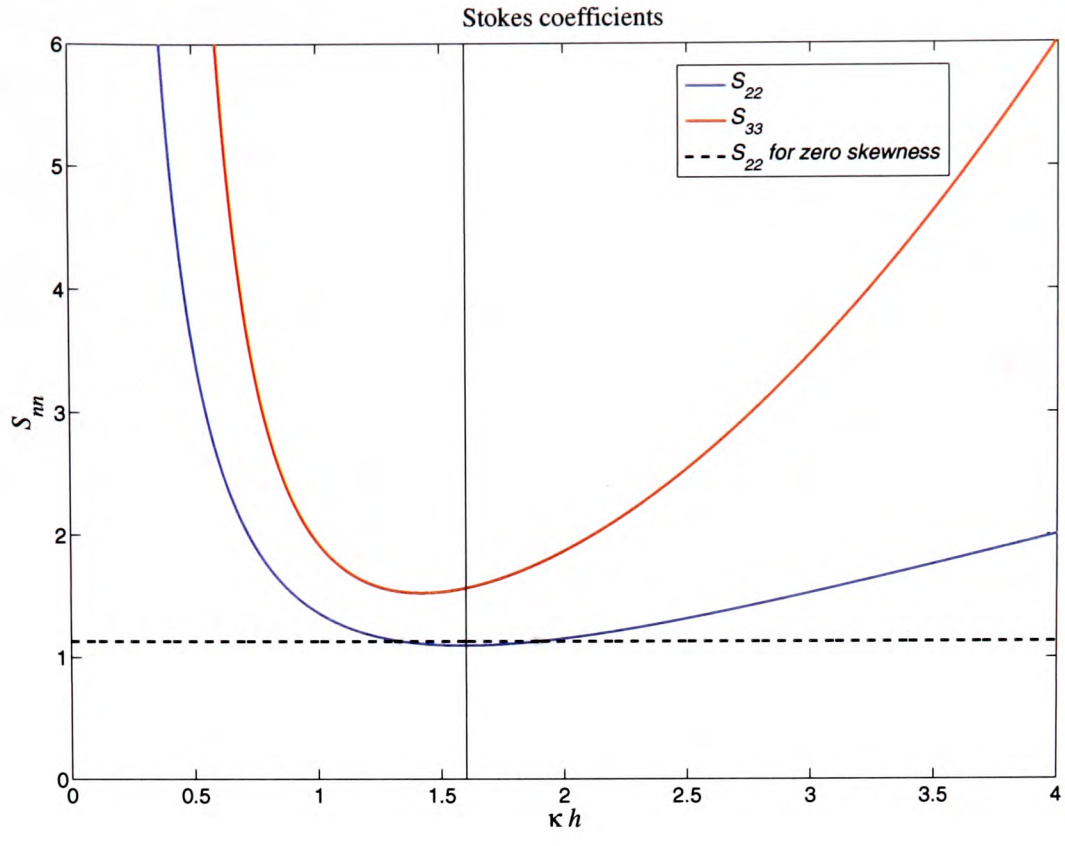

Figure 8.5: Stokes second and third order sum coefficients, S_{22} and S_{33}, plotted against κh. A horizontal line is shown corresponding to the S_{22} value computed for zero skewness. A vertical line is drawn at $\kappa h = 1.60$.

$$\eta(t) = a\cos\phi(t) + \frac{1.10}{53.13}a^2\cos 2\phi(t) + \frac{1.57}{53.13^2}a^3\cos 3\phi(t). \tag{8.3}$$

The effect of directional spreading on the value of S_{22} is explored in Section 8.2.8.

The second and third order sum contributions to the largest three waves in the undisturbed data are now investigated. The sum contributions are approximated using Equations 5.4 and 5.5, defined in Chapter 5, together with the S_{22} and S_{33} coefficients computed above using $\kappa h = 1.60$. For clarity, these approximations are given again below:

$$\eta_{2+} = \frac{S_{22}}{h}\left(\eta_L^2 - \eta_{LH}^2\right) \tag{8.4}$$

$$\eta_{3+} = \frac{S_{33}}{h^2}\eta_L\left(\eta_L^2 - 3\eta_{LH}^2\right). \tag{8.5}$$

The linearised wave record, η_L, in these approximations is computed using Equation 8.2 together with the second order sum coefficient found for zero skewness. Figure 8.6 plots the local time histories for the largest three waves in the undisturbed data with their second and third order sum contributions. The time history of each wave has been time shifted so that

the peak crest elevation occurs at $t = 0$. The waves have been labelled 'Wave 1', 'Wave 2' and 'Wave 3' to allow comparisons to be clearly made with filtered nonlinear contributions discussed later in this Chapter.

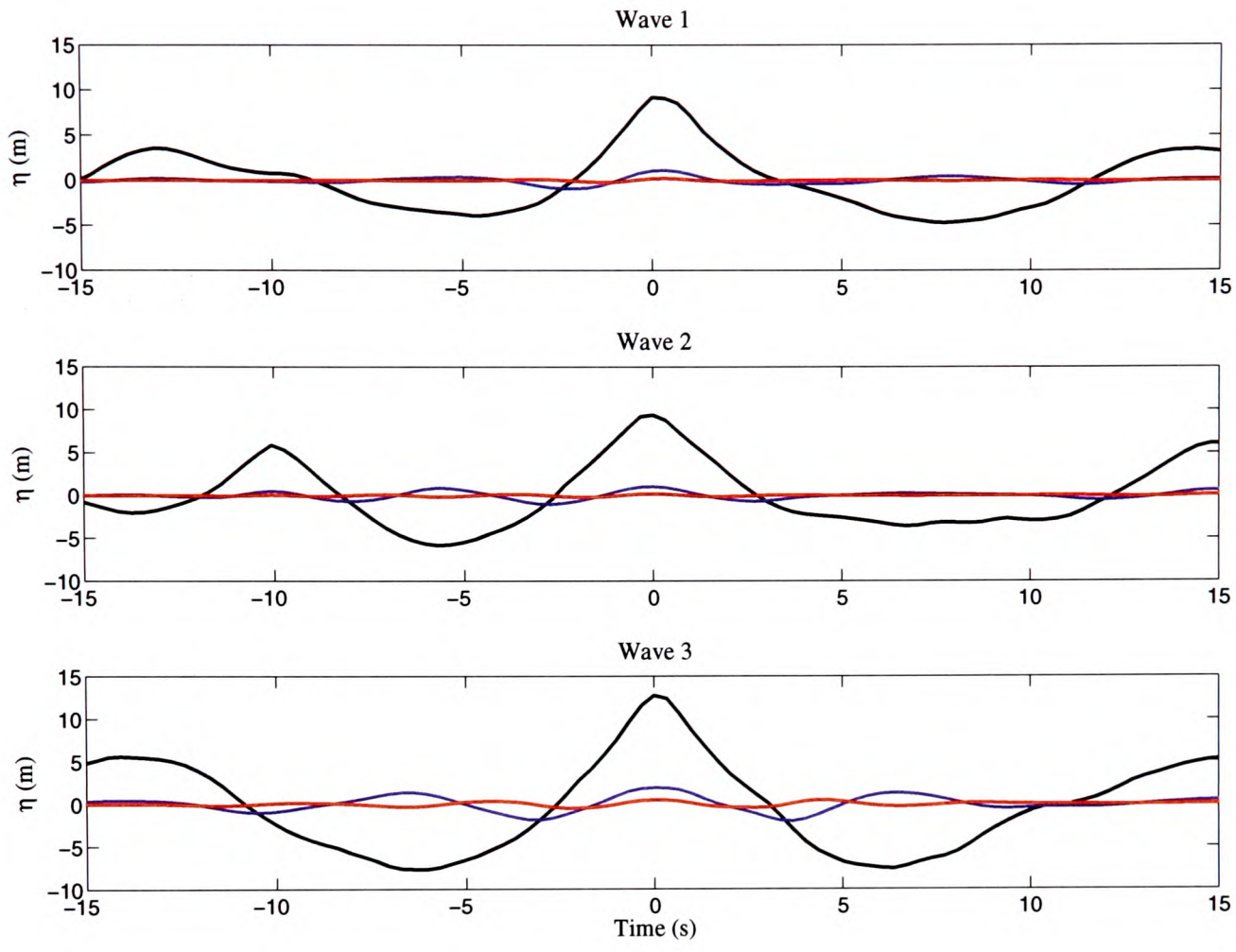

Figure 8.6: Time histories for the three largest waves in the undisturbed irregular wave data (black lines) and their second and third order sum contributions (blue and red lines respectively).

The peak crest elevations for each wave and their second and third order sum contributions (at $t = 0$) are are given in Table 8.4.

Wave	Peak crest elevation (m)	η_{2+} (m)	η_{3+} (m)
1	9.18	1.07	0.19
2	9.37	1.05	0.20
3	12.76	1.93	0.50

Table 8.4: Peak crest elevations for the three largest waves in the undisturbed irregular wave data and their second and third order sum contributions. All values are given to two decimal places.

For Wave 1 and Wave 2, which are of comparable amplitude, the second and third order sum contributions constitute approximately 11% and 2% of the total crest elevation respectively.

As one would expect, for the larger amplitude Wave 3, the second and third order sum contributions make up a larger proportion of the total crest elevation, approximately 15% and 4% respectively. If higher harmonic contributions are assumed to be insignificant, then one can conclude that the remainder of the crest amplitude is linear (87% for Wave 1 and Wave 2; 81% for Wave 3).

The relative magnitudes of the linear and nonlinear contributions to crest height are assessed again in Section 8.3 for waves close to the model structure.

8.2.4 NewWave comparison

The ability of NewWave to model the largest waves in the experimental data is now assessed. Figure 8.7 compares the linear NewWave profile with the odd-harmonics profile, η_{odd}, and the fifth order NewWave profile with the average large crest profile (averaged over the largest 25% of waves). The linear and fifth order NewWave profiles, as well as the odd-harmonics profile, are generated using techniques outlined in Chapters 2 and 5. The linear NewWave and odd-harmonics profiles have been normalised such that the peak crest elevations equal one. A linear NewWave amplitude of 5.10m is used for the generation of the fifth order NewWave profile, as this corresponds to a fifth order corrected amplitude of 5.65m, matching the amplitude of the average large crest profile. The comparisons shown in Figure 8.7 do not incorporate any representation of the second order difference contribution.

The generation of the fifth order NewWave uses Stokes' fifth order wave theory (Section 2.5 Chapter 2), requiring the computation of a set of nonlinear coefficients using some predetermined κh value. For the undisturbed data studied here, a number of κh values could potentially be used for the evaluation of these coefficients: the κh values implied by the zero skewness calculation ($\kappa h = 1.34, 1.90$); the κh value corresponding to the minimum of the S_{22} curve ($\kappa h = 1.60$); the κh value corresponding to the zero mean crossing period, $T_z = 11.2s$ ($\kappa h = 1.81$); the κh value corresponding to the peak period, $T_p = 14.3s$ ($\kappa h = 1.24$). However, as noted previously, the second and third order coefficients, which are the dominant nonlinear coefficients, are relatively insensitive to κh in the range $1.2 \leq \kappa h \leq 2$. Higher order coefficients are more variable in this range (see Figure 2.1 Section 2.5 Chapter 2) although their magnitudes are comparatively small. The fifth order NewWaves generated using each of the κh values above show no noticeable differences and hence any one of the values can be used for a graphical comparison with the experimental data; the fifth order NewWave shown in Figure 8.7 was generated using $\kappa h = 1.60$.

The agreement between the linear NewWave profile and the odd-harmonics profile (which is

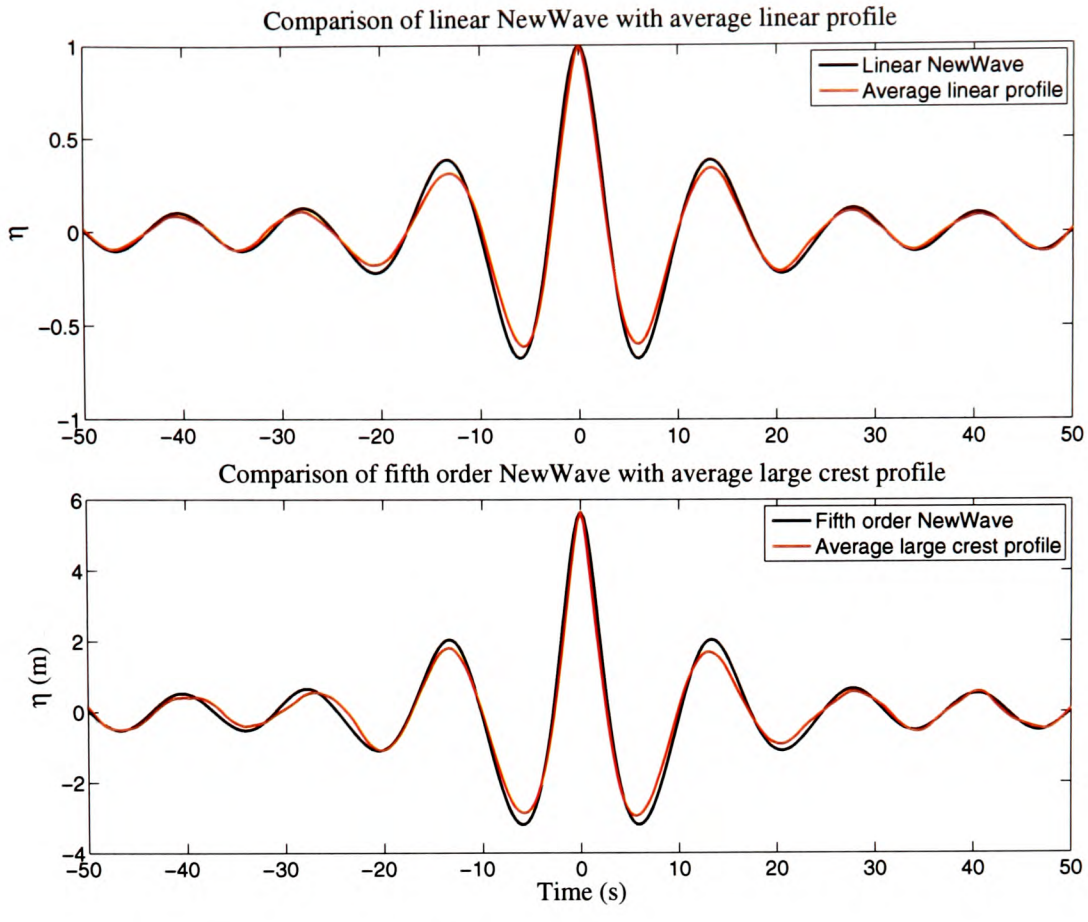

Figure 8.7: Comparisons between NewWave profiles (linear and fifth order) and the undisturbed irregular wave data.

approximately the average linear profile) is better than that found for the Draupner field data (see Figure 5.4 in Chapter 5). This is likely to be because of the increased number of waves averaged over for the experimental data, hence reducing statistical variability. As found for the Draupner data, the third order harmonic contribution retained in the odd-harmonics profile causes the central peak to be slightly narrower than predicted by the linear NewWave model.

The fifth order NewWave profile shows good agreement with the average large crest profile although the troughs either side of the peak crest are predicted to be too deep; the actual trough depths are 2.86m and 2.95m whereas the fifth order NewWave prediction is 3.20m. This observation was also noted for the Draupner data and suggests that the fifth order NewWave is slightly too narrow banded. The probable cause of this discrepancy is third order wave-wave interactions occurring in real wave data, resulting in a broadening of the local spectra around each large wave occurrence and hence a spread of energy. Gibbs (2004) identified such spectral broadening for deep water waves and a similar phenomenon is thought to exist for shallower water. Nevertheless, the comparisons shown in Figure 8.7 suggest that NewWave is a good wave model for undisturbed large wave occurrences.

8.2.5 Spectral decomposition

The second order difference, second order sum, and third order sum contributions are now extracted from the undisturbed wave data in order to assess the range of frequencies over which each nonlinear contribution is significant. Equations 5.4, 5.5 and 5.10 defined in Chapter 5, provide approximations for the temporal contributions to the second order sum, third order sum, and second order difference contributions respectively. The linearised time series, η_L, in these equations is computed using Equation 8.2 and $S_{22} = 1.132$. Fourier transforming each approximation provides estimates for the isolated spectral contributions. True power values are not of interest and so the vertical scale for each spectrum is normalised such that the maximum peak for each is unity. Figure 8.8 shows the total wave spectrum and estimated spectra for the second order difference, second order sum and third order sum contributions. The spectra have been smoothed using a 39-point running average (corresponding to a frequency window of 0.0036Hz) to help reveal the underlying spectral shapes. The running average used here does not cause any appreciable broadening of the spectra. Significant low frequency spectral peaks, which are most likely associated with sloshing modes set up in the wave tank, have been removed from the second order difference spectrum; the lowest frequency spectral components have been set to zero.

This approach has again been a success here, as it was for the Draupner data, clearly identifying the range of frequencies over which each nonlinear contribution is significant. Figure 8.8 can be used to identify suitable cut-off frequencies for extracting nonlinear contributions by filtering, which will be pursued further in sections 8.2.6 and 8.2.7. Similar spectral plots to those shown in Figure 8.8 will be produced in Section 8.3.2 for the model test data, allowing the effect of diffraction on the frequency spread of each contribution to be assessed.

8.2.6 Second order difference contribution

The second order difference contributions to the largest three waves in the undisturbed wave data (Waves 1, 2, and 3 discussed in Section 8.2.3) are now investigated. From Figure 8.8 a cut-off frequency of 0.04Hz is found to be reasonable for the extraction of the second order difference contribution by low-pass filtering the data. Time series plots for the three largest waves in the undisturbed data are produced again in Figure 8.9 alongside their second order difference contributions.

The second order difference contributions to Waves 1, 2 and 3 (at $t = 0$) are -0.03m, +0.03m and -0.89m respectively. As one would expect for a free undisturbed wave, the largest wave, Wave 3, has an unambiguous set-down associated with it. The set-down has a magnitude

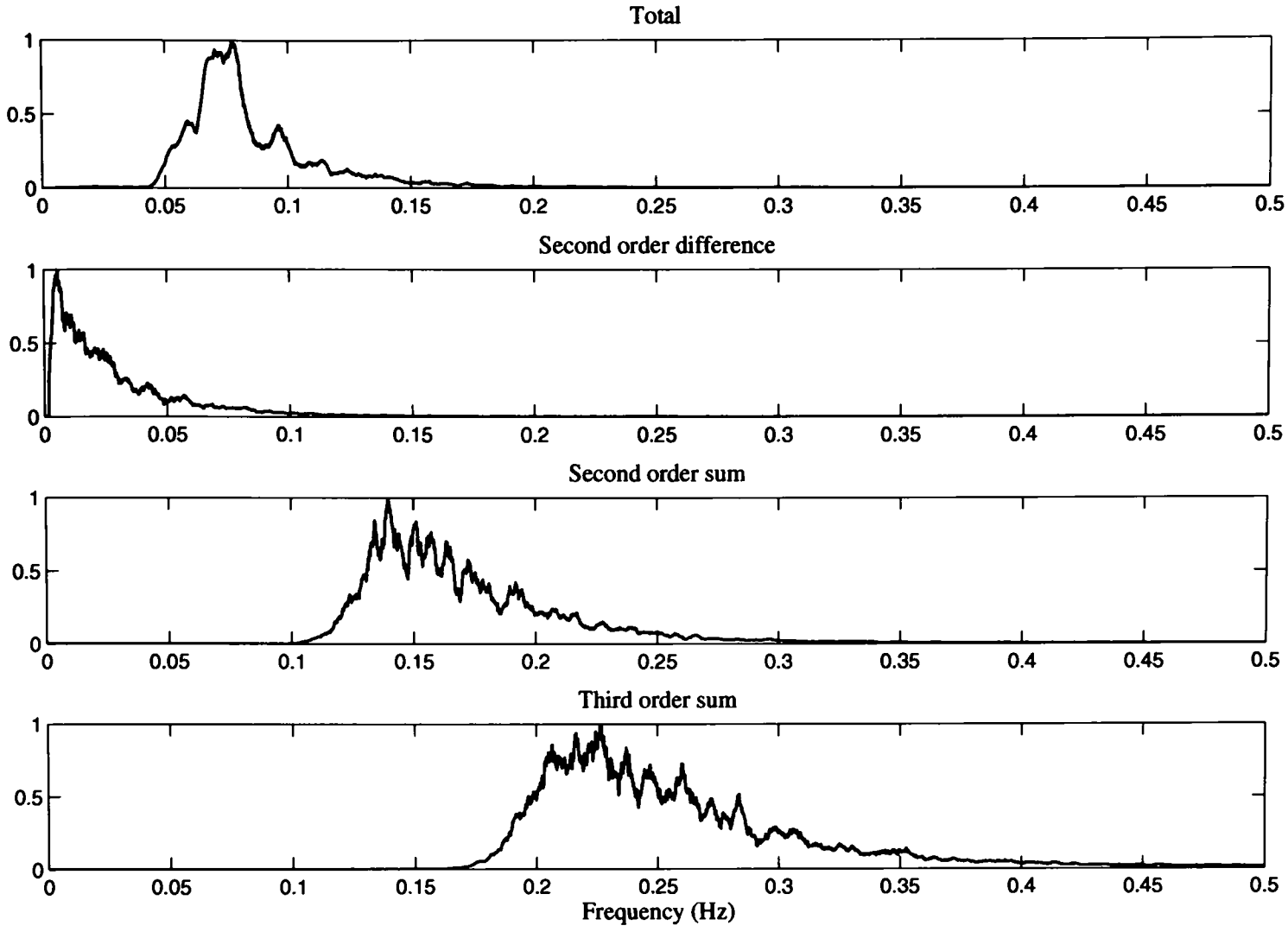

Figure 8.8: Normalised power spectra for the undisturbed irregular wave data.

equal to 7% of the total crest amplitude and is found to be a robust feature of the wave, remaining for progressively lower cut-off frequencies. The small set-up associated with Wave 2 can almost certainly be attributed to long wave reflections from the end of the tank. The reflection coefficients quoted in Chapter 4 for the wave absorber at the end of the tank ($\sim 2-6\%$) are very unlikely to be true for the long second order difference waves, which are notoriously difficult to absorb. Hence a significant proportion of the low frequency wave energy is reflected back along the tank and interacts with the incident wave field. The reflection of long waves is also likely to be the cause of the very small set-down associated with Wave 1.

The observations here highlight one of the principal difficulties associated with carrying out wave tank tests and subsequent data analysis, namely long wave reflections. Obviously, unlike waves in tank tests, a large free wave group on the open sea, where there are no physical boundaries to cause reflections, should always have a set-down associated with it.

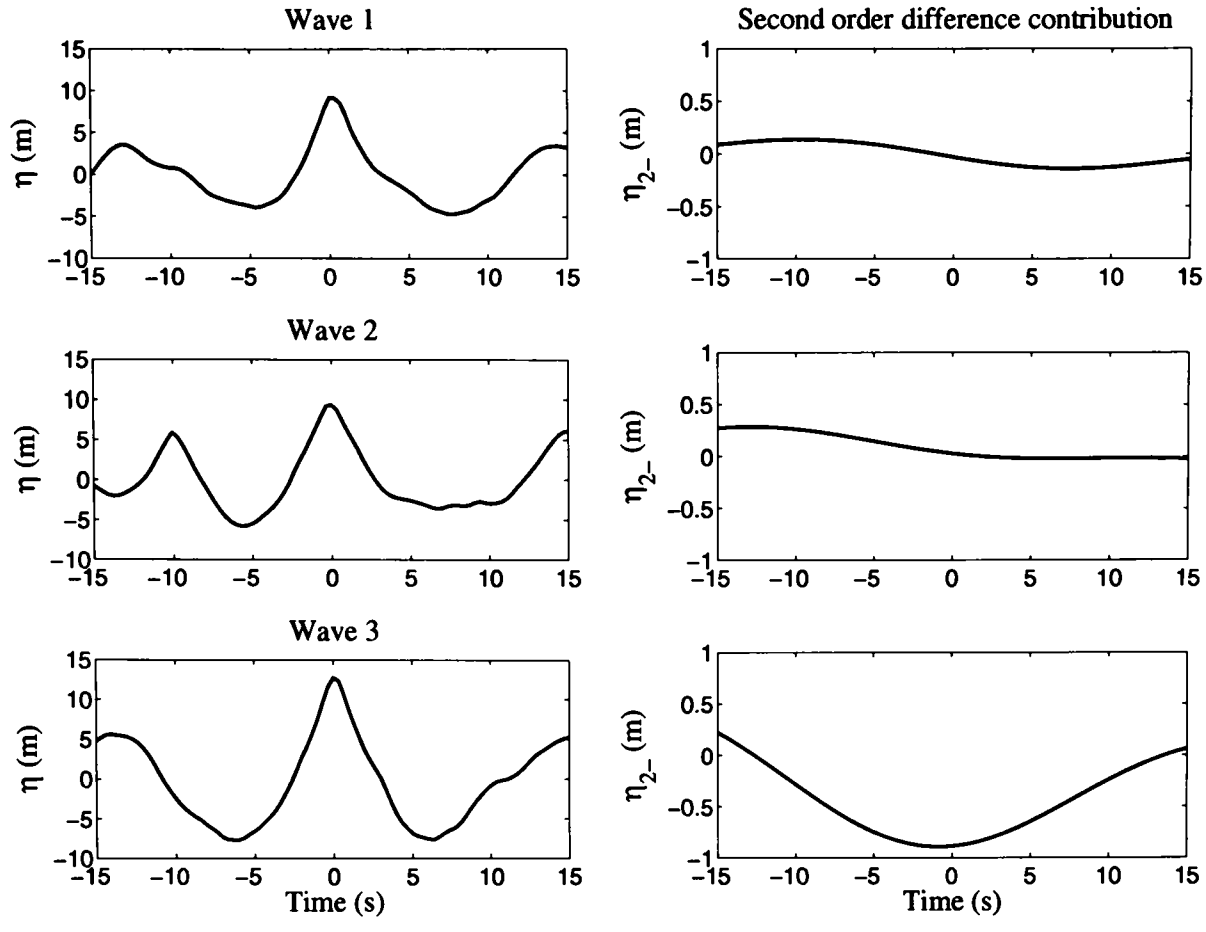

Figure 8.9: Time histories for the three largest waves in the undisturbed irregular wave data set alongside their second order difference contributions.

8.2.7 High frequency contributions

From the spectral decomposition of the data carried out in Section 8.2.5, it is found that the high frequency contributions (i.e. everything above linear) can be extracted by high-pass filtering the data at 0.12Hz. Figure 8.10 shows the time histories for the three largest waves in the undisturbed data alongside their high frequency contributions. The high frequency contributions to Waves 1, 2 and 3 are 3.73m, 3.12m and 3.97m respectively, corresponding to 40.6%, 33.3% and 31.1% of the total crest amplitudes.

Comparing these high frequency contributions with the second and third order sum contributions given in Table 8.4, it is possible to estimate the cumulative magnitude of all other high frequency nonlinear contributions above third order. These magnitudes are found to be 2.47m, 1.87m and 1.54m for Waves 1, 2 and 3 respectively. From an inspection of the spectra given in Figure 8.8, these large high order harmonics are unexpected. The most likely explanation is that some high frequency linear components have passed through the filter.

8.2.8 Directional spreading

The effect of directional spreading on the size of the second order sum contribution is now investigated. On the open sea, wave spreading is usually measured by directional wave buoys

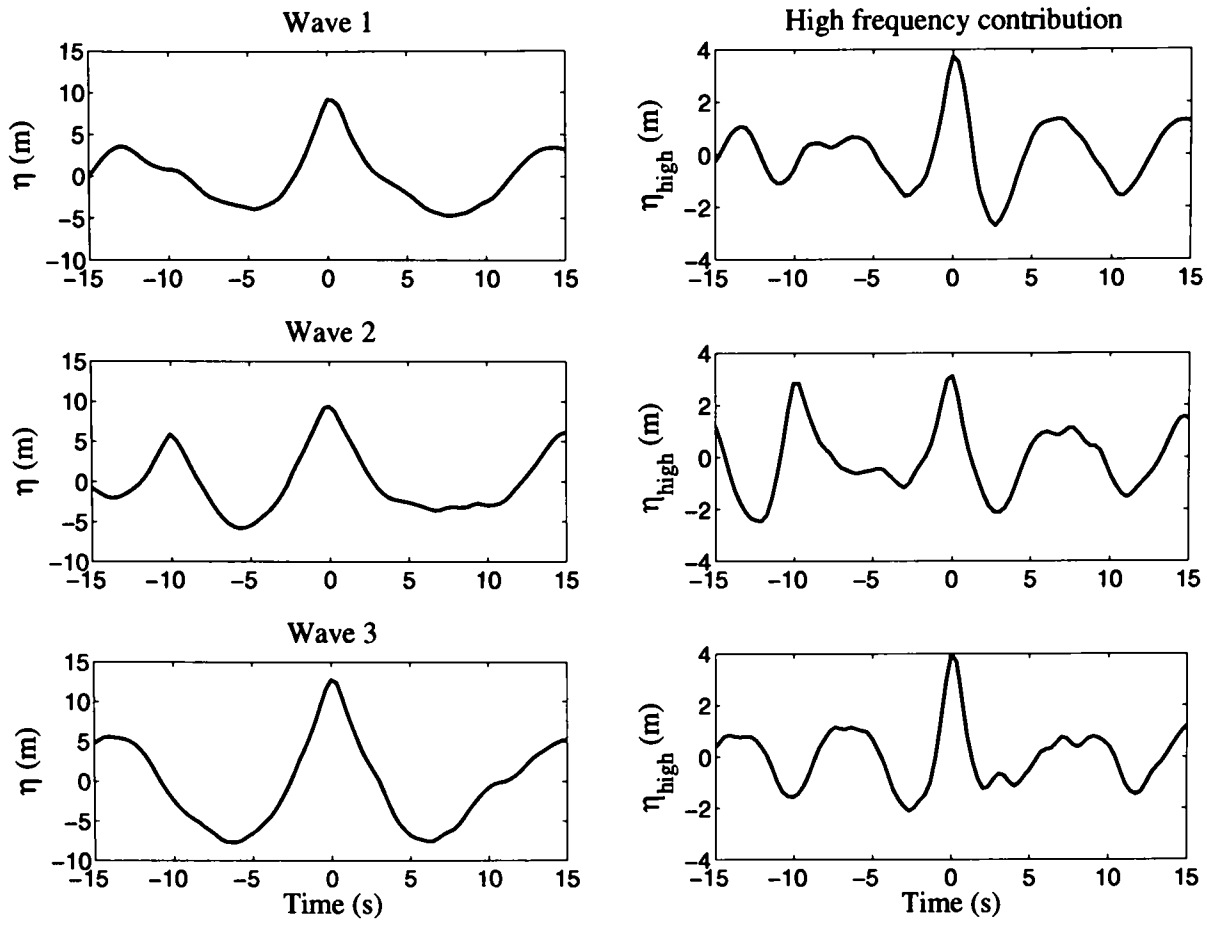

Figure 8.10: Time histories for the three largest waves in the undisturbed irregular wave data alongside their high frequency contributions.

that move in the plane of the free surface in two directions, as well as moving vertically as waves pass by. In contrast, a fixed Eulerian sensor, such as the capacitance wave probes used to record the experimental data studied in this chapter, record only the vertical surface elevation time history at a fixed point. The aim in this section is to investigate a possible technique for estimating the directional spreading of a wave field from a single surface elevation time series. Although perhaps not directly relevant to the overall project brief, namely to guide airgap design, the estimation of directional spreading from a fixed Eulerian sensor could be useful to the offshore industry and so is pursued here.

If the wave motion is modelled by linear theory alone then obviously it is not possible to extract any information on directional spreading from a single time series. However, if the nonlinear contributions to the wave motion are considered, then although it is not possible to infer the mean wave direction, it may be possible to estimate the average spreading of a wave field about its mean direction. Both the second order sum and difference contributions are dependent upon the directionality of the wave field (see Equations 2.104 and 2.105 Section 2.6 Chapter 2), although only the sum contribution is considered here for estimating directional spreading. It is possible that a similar technique using the magnitude of the second order difference contribution could be used to try to estimate directional spreading.

For the unidirectional wave data the second order sum coefficient, S_{22}, was estimated to be 1.132 (computed over the full three hour wave record). This coefficient was computed by linearising the data (accounting only for the second order contributions) and searching for the value of S_{22} that sets the skewness of the linearised data to zero. An exactly analogous procedure is now applied to the undisturbed multidirectional irregular wave data (Data Set 4, Section 4.6 Chapter 4), which has identical target met-ocean conditions as the unidirectional wave data apart from the introduction of directional spreading. Data Set 4 was synthesised using a cosine-power directional spreading function (Equations 4.3 Section 4.6 Chapter 4) that produced a wave field in which the wave directions have a standard deviation of approximately 15 degrees and the maximum wave angles all lie within 45 degrees of the mean direction.

Considering the full three hour time series (containing approximately 1000 waves), the value of S_{22} resulting in zero skewness for the multidirectional data is found to be 1.126, corresponding to a reduction of only 0.5% from the unidirectional value. To two decimal places the magnitude of the second order sum coefficients for the unidirectional and multidirectional wave records are identical. Therefore, the two undisturbed irregular wave data sets studied in this chapter suggest that it is not possible to use the magnitude of the second order sum contribution to estimate the degree of spreading in a wave field. However, before any definite conclusions can be drawn on this matter it is obviously necessary to consider further data, and this has been done by Taylor et al. (2005). By studying both experimental wave tank data and field data recorded by a fixed Eulerian sensor, Taylor et al. demonstrated that it is possible to use the size of the second order sum contribution to approximately measure the average spreading of a wave field.

8.3 Model test data: Incident irregular waves

The diffraction effects resulting from the undisturbed irregular waves (studied in Section 8.2) interacting with the LUNA model structure are now investigated. For all model test irregular wave data analysis undertaken in this section, with the exception of the directional spreading analysis carried out in Section 8.3.5, the unidirectional irregular wave data (Data Set 7, Table 4.2, Section 4.6 Chapter 4) are considered. This data set comprises waves with the same met-ocean conditions as the undisturbed unidirectional waves studied in Section 8.2 and so comparisons can be drawn between the undisturbed waves and the same waves as they interact with the structure. For the consideration of directional spreading, the multidirectional irregular wave data (Data Set 8, Table 4.2, Section 4.6 Chapter 4) are used.

For the LUNA model tests, 26 wave probes were deployed to measure the wave conditions in

the local vicinity of the model; the layout of these probes is given in Figure 4.3 Chapter 4. For the purposes of airgap design it is important to consider the wave probes recording the maximum free surface elevation measurements. However, to rigorously assess the validity of the diffraction solutions at reproducing the measured diffracted wave field, wave probes positioned at a number of locations around the structure must be considered, rather than restricting attention to wave probes in one specific region where the most extreme free surface magnification effects occur. With this in mind, five wave probes have been selected for analysis in this section. To help select these wave probes, the peak free surface elevation recorded by each probe has been identified and plotted in Figure 8.11; values are not plotted for probes 2, 3, 6 and 26 because these record waves overtopping the concrete columns.

The largest wave measurements are found to occur in the vicinity of the downstream columns (probes 19, 22, 23, 24, and 25), at the centre of the four columns (probe 11) and between the two upstream columns (probe 8). The smallest measurements were recorded downstream of the structure (probe 16) and between the upstream and downstream columns (probe 17). Some insight into the comparative free surface magnifications around the structure can be gained using Figure 8.11 together with the plot of probe locations given in Figure 4.3 Chapter 4.

The most extreme free surface elevations are recorded by wave probes 23 and 24, which record

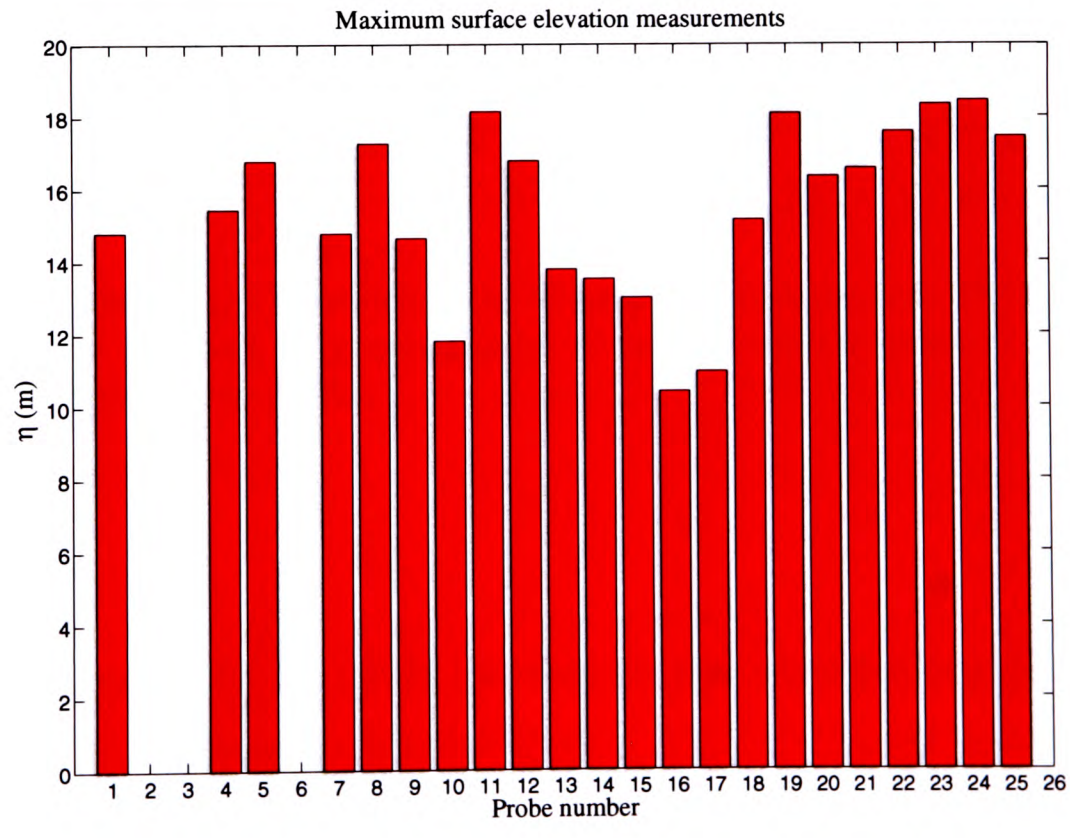

Figure 8.11: Maximum surface elevation measurements recorded by the model test wave probes.

peak values of 18.34m and 18.44m respectively. The next five largest surface elevations were measured by wave probes 11 (18.14m), 19 (18.09m), 22 (17.58m), 25 (17.43m) and 8 (17.26m). Wave probes 23, 24 and 25 are located in the same region adjacent to one of the downstream columns and hence only one of these probes is considered, namely probe 24, which records the largest wave crest. The other probes cited above are evenly distributed around the structure and so provide a suitable group of probes for consideration in this section. For all unidirectional model test data analysis wave probes 8, 11, 19, 22 and 24 are considered. The locations of these wave probes in relation to the four concrete columns are shown in Figure 8.12 together with the coordinates of each probe.

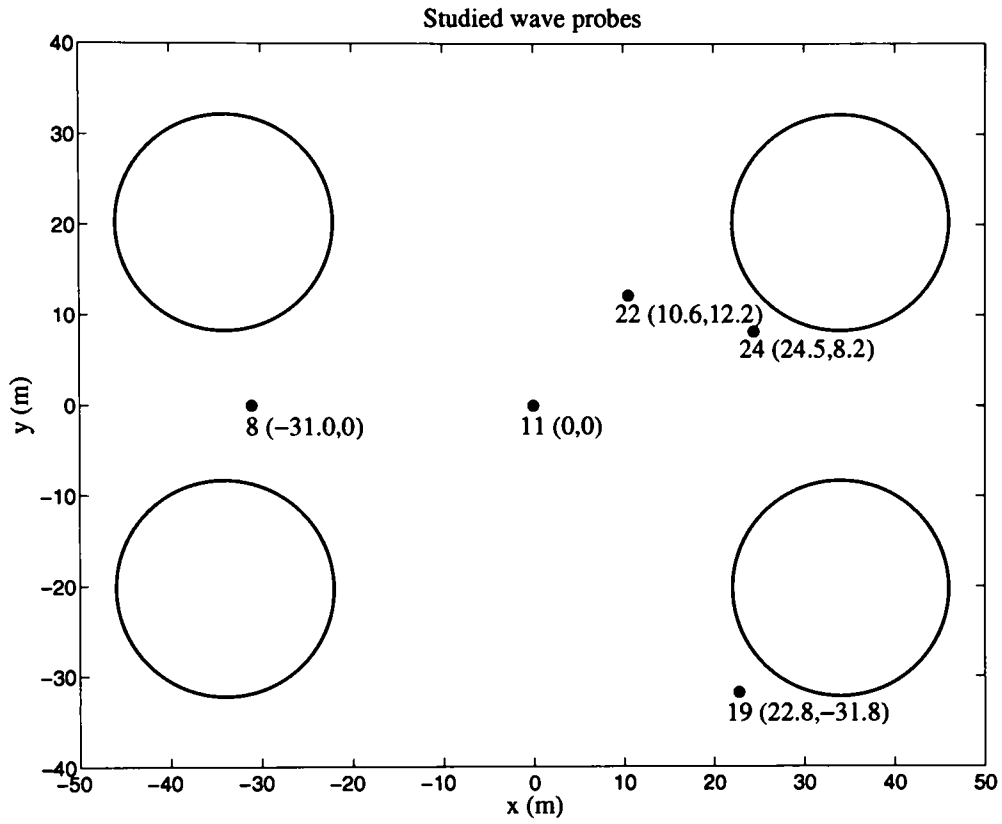

Figure 8.12: Plot showing the locations of the five studied wave probes. The large circles show the LUNA concrete columns. The coordinates of each probe are given in metres. Incident waves propagate from left to right.

8.3.1 Wave profiles

The average wave profiles for the model test data are now examined and compared with the undisturbed profiles. For comparison with Figure 8.1, Figure 8.13 plots the average large crest and trough profiles, computed using the largest 25% of crests and troughs, and Figure 8.14 plots the average linear and second order large crest profiles, computed using Equations 5.1 and 8.1. Plots are produced for the five studied wave probes. The number of waves averaged over for the computation of these profiles is dependent on the interaction of the incident and

scattered wave fields at the location of the probe and hence is different for each probe.

As found for the undisturbed data, the crests are, on average, larger and steeper than the troughs. The crests and troughs are found to be particularly steep for wave probe 8, which is located between the two closely spaced upstream columns. This is likely to be caused by scattered waves emanating out from the two columns, resulting in a dramatic steepening of the waves midway between the columns. This effect is observed in the video footage recorded during the tests. The presence of the model increases the average crest and trough magnitudes for all probes from the undisturbed values.

The linearisation undertaken to produce the average linear crest profiles has not been successful for all probes. For example, higher frequency energy is clearly included in the probe 8 profile. Similarly, it is probable that the average second order profiles incorporate higher order even harmonics. However, the linear and second order crest profiles shown here will still be dominated by the linear and second order contributions respectively, and hence provide some indication of the relative sizes of the contributions.

To aid a quantitative comparison between profiles, average large crest, trough, linear crest and second order crest magnitudes are given in Table 8.5 for the model test data. Comparing the average crest and trough magnitudes with those found for the undisturbed data, the presence of the model is found to magnify wave asymmetry. The wave data recorded by probe 19 is found to be the most asymmetric, with the average crest magnitude being 64.8% larger than the average trough magnitude. Hence, predictably, the same wave data also incorporates the largest second order component, comprising 19.6% of the total crest magnitude. With the exception of probe 11, the relative size of the second order contribution has increased for each probe from the value recorded for the undisturbed wave data. For probe 11 it is possible that wave-wave interactions have combined at this location to cancel out some of the second order contribution. Although it is clearly difficult to draw definite conclusions from these profiles alone, it seems certain that the higher order harmonics (second order and above) have become more dominant as a consequence of the waves interacting with the model structure.

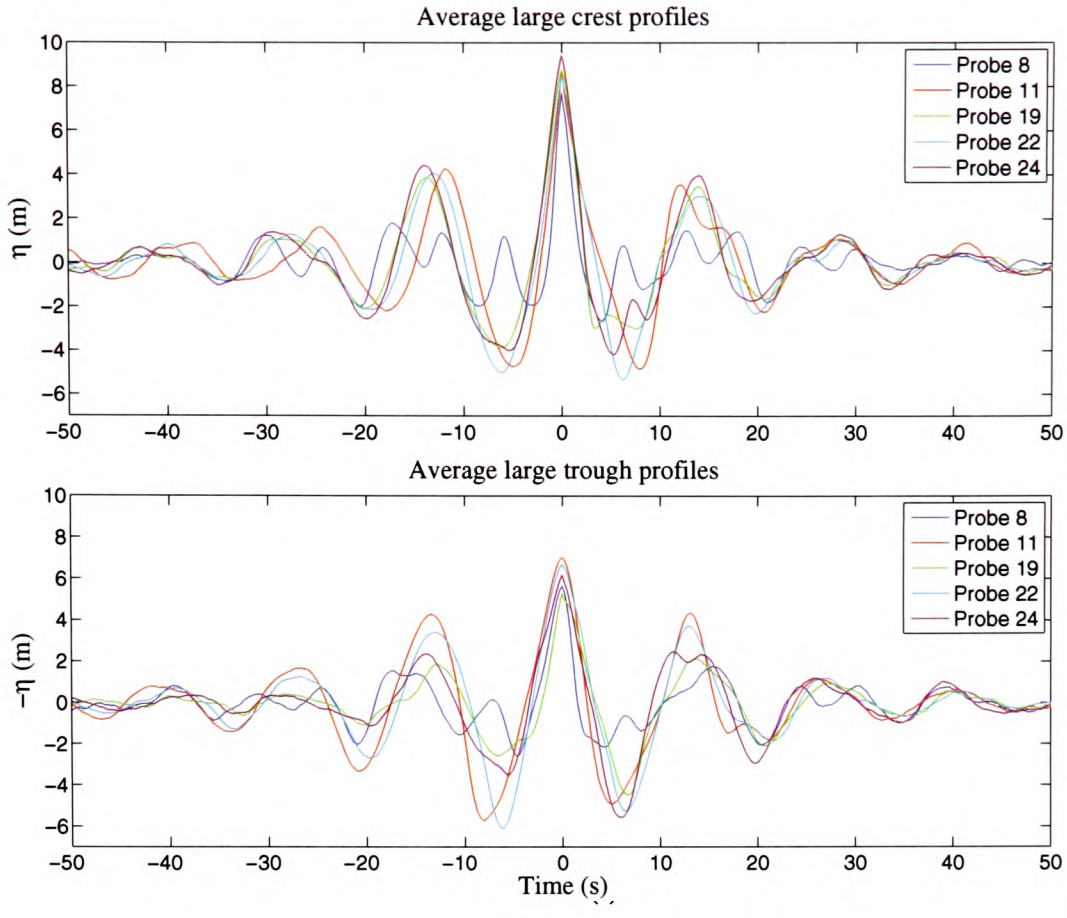

Figure 8.13: Average large crest and trough profiles for the model test data.

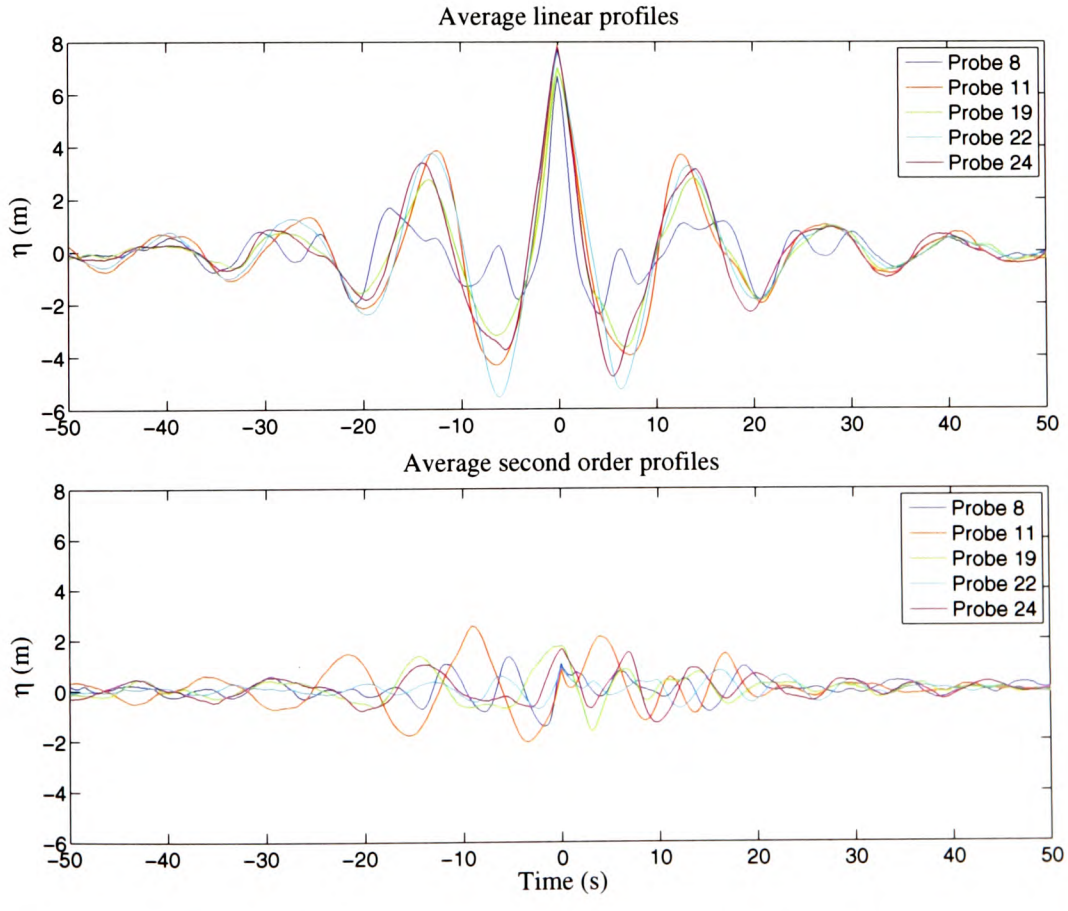

Figure 8.14: Average linear and second order large crest profiles for the model test data.

Wave probe	η_C (m)	η_T (m)	η_L (m)	η_2 (m)
8	7.73	5.65	6.69	1.04
11	8.66	7.04	7.85	0.81
19	8.75	5.31	7.03	1.72
22	8.49	6.71	7.60	0.89
24	9.42	6.20	7.81	1.61

Table 8.5: Average large crest (η_C), trough (η_T), linear crest (η_L) and second order crest (η_2) magnitudes for the model test data. All values are given to two decimal places.

To provide an improved illustration of the asymmetry of the waves, ordered crest elevation is plotted against ordered trough depression for all five wave probes in Figure 8.15. As the size of the crests and troughs increases, crest-trough asymmetry is found to increase for all probes. Probe 19 records the most asymmetric wave data, which is in agreement with the average profiles given in Figure 8.13. Comparing Figure 8.15 to Figure 8.2, it is clear that the waves in the vicinity of the model structure are more asymmetric than those in the undisturbed wave field.

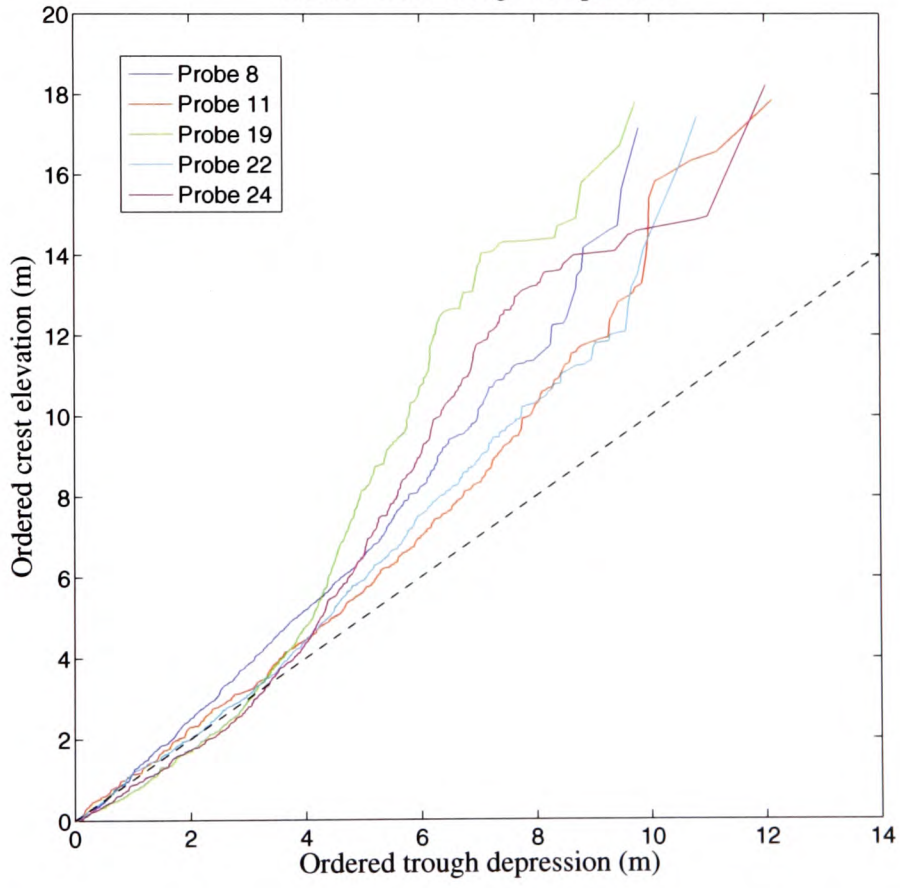

Figure 8.15: Ordered crest elevation plotted against ordered trough depression for the model test data.

8.3.2 Spectral decomposition

Using the narrow-banded approach outlined in Section 8.2.5, the second order difference, second order sum and third order sum contributions are now extracted from the model test

data. Since the model test data has not been linearised, as was done for the undisturbed data (by removing the second order contributions), the nonlinear contributions here are approximated using the measured wave record, η, instead of the linearised wave record, η_L, in Equations 5.4, 5.5 and 5.10. This should have a small effect on the frequency range of the nonlinear contributions, which is being solely investigated here.

For each wave probe, the nonlinear spectra and the total measured spectrum are shown in Figure 8.16. The spectra have been smoothed using a 195-point running average (corresponding to a frequency window of 0.018Hz) and have been normalised such that the maximum peak for each is unity. A 195-point average has been chosen solely for the purposes of achieving reasonably smooth spectra. It has been found that the value of 'n' used in the n-point average has a small effect on spectral broadening and hence comparisons can still be made with the undisturbed spectra, which were computed using a 39-point running average (corresponding to a frequency window of 0.0036Hz). Low frequency spectral peaks associated with sloshing modes have been removed from the second order difference spectra.

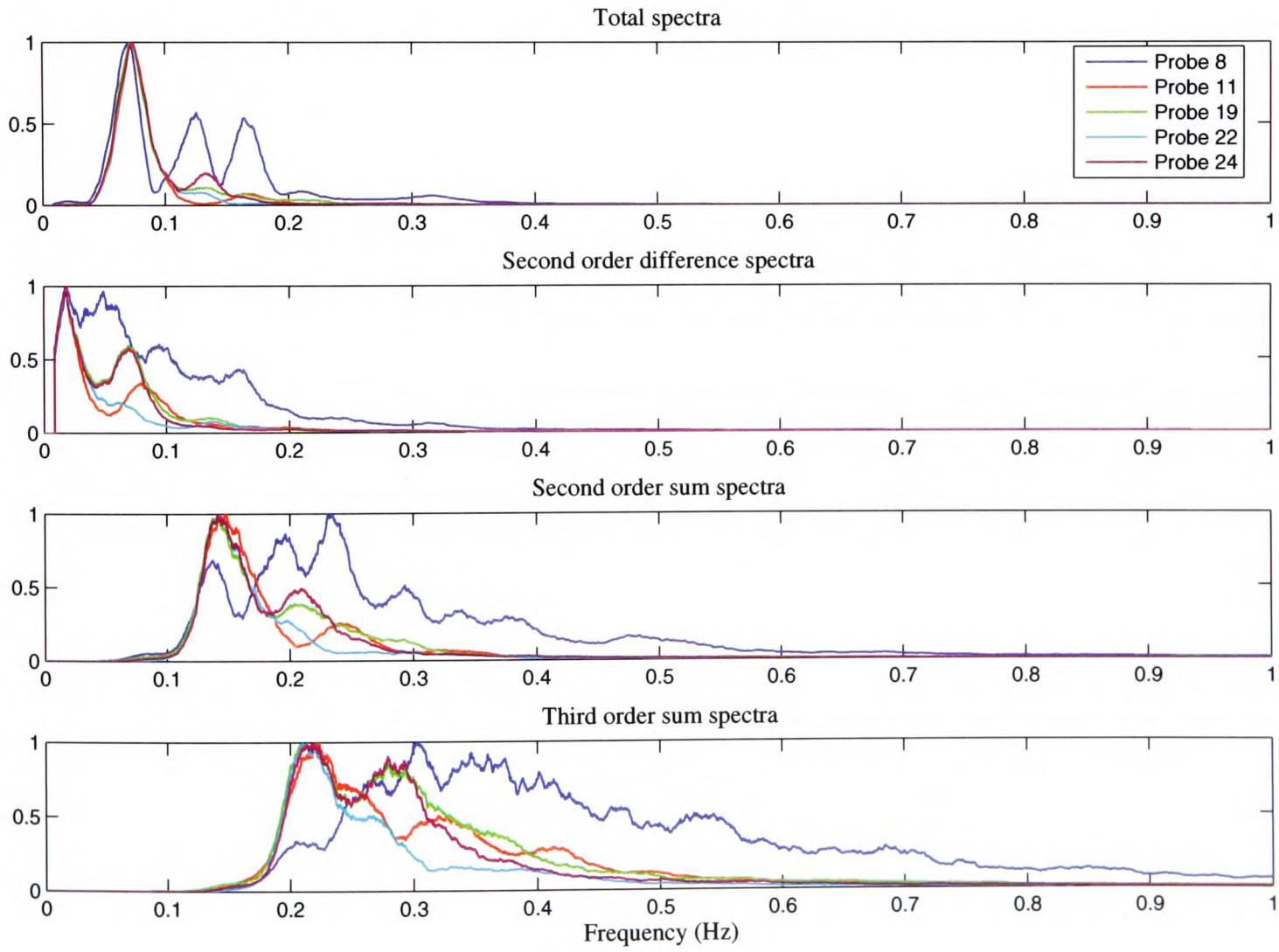

Figure 8.16: Normalised power spectra for the model test data.

Comparison of the spectra in Figure 8.16 with corresponding spectra for the undisturbed data (Figure 8.8) allows the effect of diffraction on the frequency spread of each contribution to be assessed. The spectra shown here are markedly different to those computed for the undisturbed data, with the most prominent differences being observed for probe 8. Examining the total spectra, the model test data is found to be more broad-banded than the undisturbed data, with energy being shifted to higher frequencies. This is most evident for probe 8, where multiple high frequency peaks can be identified. The second order difference contribution is no longer localised to low frequencies (e.g. <0.05Hz for the undisturbed data); significant energy has spread to the linear frequency range and above for all probes. The second and third order sum contributions now extend over much broader ranges of frequencies principally because of a shift of energy to higher frequencies.

It must be borne in mind that the approach adopted here is a narrow-banded approximation and so the applicability of the approach for the model test data is uncertain. In addition, the total measured wave record is used to approximate the nonlinear contributions, which will introduce further error - e.g. the third order sum contribution (3-3) is likely to include third order difference contribution (3-1) and the relative sizes of the sum and difference contributions depends on the magnitude of the nonlinearities in the measured record.

Because of the possible scope for inaccuracy, it is difficult to judge how well the approach has worked for the model test data. The spectra shown in Figure 8.16 suggest that diffraction effects cause a broadening of the total and nonlinear spectra, making it more difficult to extract the nonlinear contributions from the data by filtering. High frequency contributions (above linear) could possibly be extracted by high-pass filtering at ~0.1Hz. However, it would be very difficult to identify a cut-off frequency for the extraction of the second order difference contribution by low-pass filtering; a frequency would need to be identified that maximises the second order difference components and minimises the linear components passing through the filter.

Because of the difficulties associated with identifying cut-off frequencies for the extraction of nonlinear contributions by filtering, this is not undertaken for the model test data.

8.3.3 Linear diffraction

The ability of linear diffraction theory to predict real diffracted wave spectra in the vicinity of the LUNA structure is now investigated. To this end, comparisons are made between the diffracted spectra measured by the considered wave probes and those predicted using linear analytical diffraction theory (described in Section 3.2 Chapter 3). Also, the coherence

function between the incident and diffracted wave fields is used to try to identify the linear frequency range for each probe.

The linear analytical diffraction solution is used in this section because of its ease and speed of computation. The effect of the caisson on the results is discussed, although is not investigated further using DIFFRACT.

The linear amplification factor, ϕ (defined in Section 3.2 Chapter 3), is used to transform the measured incident (i.e. undisturbed) spectrum, S_i, into a diffracted spectrum, S_d, using:

$$S_d(x, y, \omega_n) = \phi_n^2(x, y) \times S_i(\omega_n). \tag{8.6}$$

Figure 8.17 shows the measured incident spectrum together with comparisons between the measured diffracted spectra for each considered probe and the diffracted spectra predicted by linear diffraction theory (Equation 8.6). The measured spectra have been smoothed using a 195-point running average (corresponding to a frequency window of 0.018Hz) to help reveal the underlying spectral shapes.

With the exception of probe 8, the predominantly linear peak (at $\sim$ 0.07Hz), which from here on is referred to as the linear peak, has been under predicted by linear analytical diffraction theory. This is perhaps due to wave interaction with the caisson, which has not been accounted for in the analytical solution. In Chapter 6 the LUNA caisson was found to have an appreciable effect on the diffracted wave field for incident regular waves at 0.07Hz, increasing the surface magnification in some regions and reducing it in others. The discrepancy could also be due to the occurrence of waves over-topping the concrete columns (which project 7.07m above mean sea level), which is captured in the video footage recorded during the tests and is not accounted for in the diffraction solution. Probes 11, 19, 22 and 24 are located downstream of the front two columns and hence the measurements recorded by these probes are likely to be most affected by over-topping. For probe 8, which is located between the two front columns where over-topping perhaps has a smaller effect, the linear peak is reproduced well by linear diffraction theory.

The low prediction of the linear peak is most notable for probe 24, which is located adjacent to one of the steel columns supporting the deck structure. The diffraction solution implemented here does not incorporate the steel columns and hence any diffraction effects resulting from the interaction of waves with these columns are not accounted for. The video footage recorded during the tests clearly shows wave runup around the steel columns. However, due to the

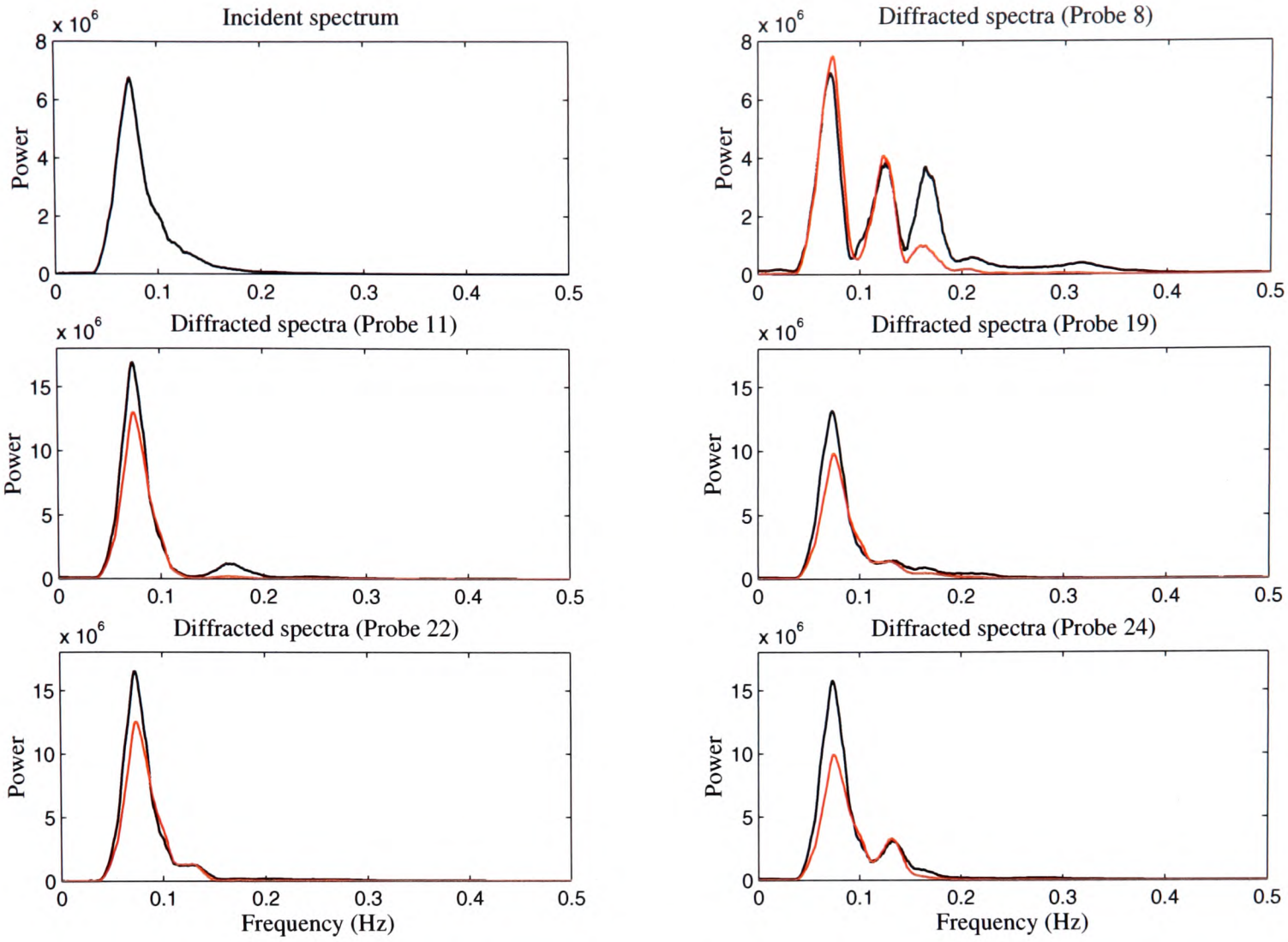

Figure 8.17: Comparison between measured diffracted spectra (black lines) and diffracted spectra computed using linear diffraction theory (red lines). The incident spectrum is also shown.

relatively small diameter of the steel columns compared to the most energetic wavelengths, the effect of the columns on the incident wave field is not likely to be the sole cause of the low prediction found in Figure 8.17. A further factor possibly causing the low prediction of the linear peak is nonlinear effects not included in a linear solution, such as third order wave-wave interactions.

The measured diffracted spectra show increases in energy (from the undisturbed values) at approximately twice the peak frequency of the incident spectrum. It would perhaps seem reasonable to assume that these peaks are due to second order sum effects although with the exception of probe 11, these peaks are predicted very well by linear diffraction theory; for probe 11 the peak is still predicted although its magnitude is too small. For probe 8, the third and fourth measured peaks at approximately 0.16Hz and 0.21Hz (three times the incident peak frequency) are also predicted by linear diffraction theory, although the energy is much lower than is measured.

In summary, the spectral shapes for each probe are reproduced well by linear diffraction theory although the predicted energy contents of the diffracted wave fields are lower than are measured. The additional measured energy is likely to be the result of wave interaction with the caisson, waves over-topping the concrete columns, the influence of the steel columns supporting the deck structure and nonlinear wave-wave interactions.

A useful extension to this work would be to produce the diffracted spectra predicted using the numerical linear diffraction solution, DIFFRACT, which would allow the effect of the caisson to be assessed. It would also be useful to compute the second order diffracted spectra using DIFFRACT to allow the effect of nonlinearities to be examined. However, the excessive computation time associated with the second order calculation at each frequency and the convergence problems encountered at second order at higher frequencies would greatly hinder such a calculation using DIFFRACT. It is noted that computation time and convergence may not be so inhibitive using alternative diffraction codes.

The linear transfer functions, ϕ, used to produce the diffracted spectra in Figure 8.17 are now compared directly with the measured linear transfer functions. The measured transfer functions are computed using (Bendat and Piersol 2000):

$$\phi(\omega) = \frac{S_{id}(\omega)}{S_i(\omega)} \tag{8.7}$$

where S_{id} is the cross-spectral density function between the incident and diffracted data. Note that Equation 8.7 is a complex-valued relation, which can provide both magnitude and phase information although here only the magnitude of the transfer function is considered. The cross-spectral density function can be defined by:

$$S_{id}(\omega) = I^*(w) \times D(w) \tag{8.8}$$

where I is the Fourier transform of the incident wave record, D is the Fourier transform of the diffracted wave record, and '*' denotes a complex conjugate. The incident and diffracted wave data are recorded using different sampling rates and hence cubic spline interpolation is used to provide additional data points in the incident record, which is sampled at a slower rate. To help assess the amount of temporal and spectral averaging that should be applied to the data, a linear transfer function is initially computed between two undisturbed wave probes, namely probes 9 and 10, which are located 2.2m apart (100m full scale). Such a transfer function should obviously average unity over all frequencies and various averaging

schemes have been applied to the undisturbed data to help identify what level of averaging best achieves this predictable result.

The following averaging is used: (1) the undisturbed and diffracted time series are divided into 25 equal sections each with a duration of approximately seven minutes; (2) 25 incident spectral density functions and 25 cross-spectral density functions are computed; (3) the incident and cross-spectral density functions are averaged over all sections; (4) the averaged incident and cross-spectral density functions are averaged in the frequency domain using a 9-point running average; (5) the time and frequency averaged incident and cross-spectral density functions are used to compute the linear transfer function.

Figure 8.18 shows comparisons between the measured linear transfer functions for each studied wave probe and the linear transfer functions computed using linear diffraction theory over the frequency range 0.02-0.16 Hz. Good agreement is found between the measured and computed transfer functions, with the majority of the measured trends across the considered frequency range being predicted well by linear diffraction theory. There are of course some discrepancies, most notably the peaks predicted by linear diffraction theory at ~ 0.13Hz for probes 19, 22 and 24 that are not found in the measured data. To ensure that this is not a consequence of the averaging applied to the data, the same measured results have been computed using less averaging and the peaks are again found to be absent. A further mismatch is found for probe 8 where linear diffraction theory over predicts the measured peak amplification at ~ 0.13Hz by 51%. Discrepancies such as those noted here are likely to be the result of nonlinear wave-wave interactions. In addition, the equations used to compute the measured transfer functions (8.7 and 8.8) apply only to ideal linear systems that exhibit no nonlinear characteristics. Hence, because the experimental data is inherently nonlinear the measured transfer functions computed are not truly linear.

Due to the presence of significant nonlinear contributions, the spectral decomposition carried out in Section 8.3.2 did not clearly identify the linear frequency range for each probe. In an effort to help clarify the linear frequency range, the coherence function between the incident and diffracted wave records is now computed. The coherence function is equal to unity for a constant parameter ideal linear system. Hence by identifying the range of frequencies over which this function is approximately equal to unity allows the linear frequency range to be estimated. The coherence function, γ_{id}, is given by (Bendat and Piersol 2000):

$$\gamma_{id}^2(\omega) = \frac{|S_{id}(\omega)|^2}{S_i(\omega)S_d(\omega)}. \tag{8.9}$$

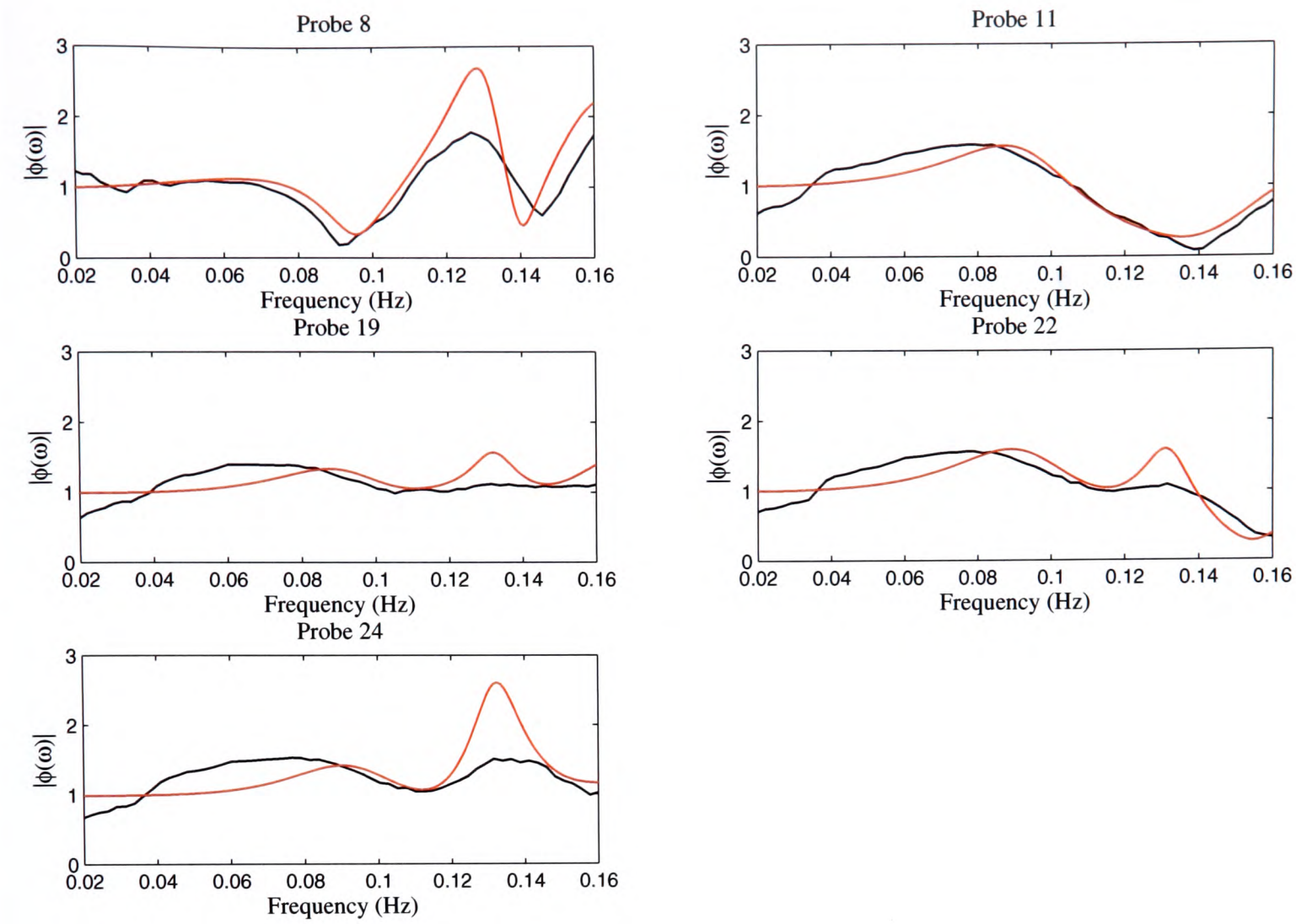

Figure 8.18: Comparison between measured linear transfer functions (black lines) and linear transfer functions computed using linear diffraction theory (red lines).

Implementing the same level of averaging as outlined for the computation of the linear transfer functions, the coherence function for each probe is plotted in Figure 8.19. Assuming that any significant disparity from unity is caused by nonlinearities in the data, the linear frequency ranges for probes 8, 11, 19, 22 and 24 respectively are found to be approximately: 0.04-0.08Hz; 0.04-0.11Hz; 0.04-0.12Hz; 0.04-0.11Hz; 0.04-0.11Hz. It is perhaps not surprising that probe 8, which incorporates considerable nonlinear components, has the smallest linear frequency range.

8.3.4 The surface response statistics method

The first and second order diffraction transfer functions, computed in Section 7.5 Chapter 7 for the LUNA structure for nine frequencies, are now incorporated into the surface response statistics (SRS) method of Tromans and Vanderschuren (1995). Extreme surface elevation statistics are computed at two locations around the structure, namely (0,0) and (24.5,8.2), which correspond to the locations of measurement probes 11 and 24 respectively. Comparisons

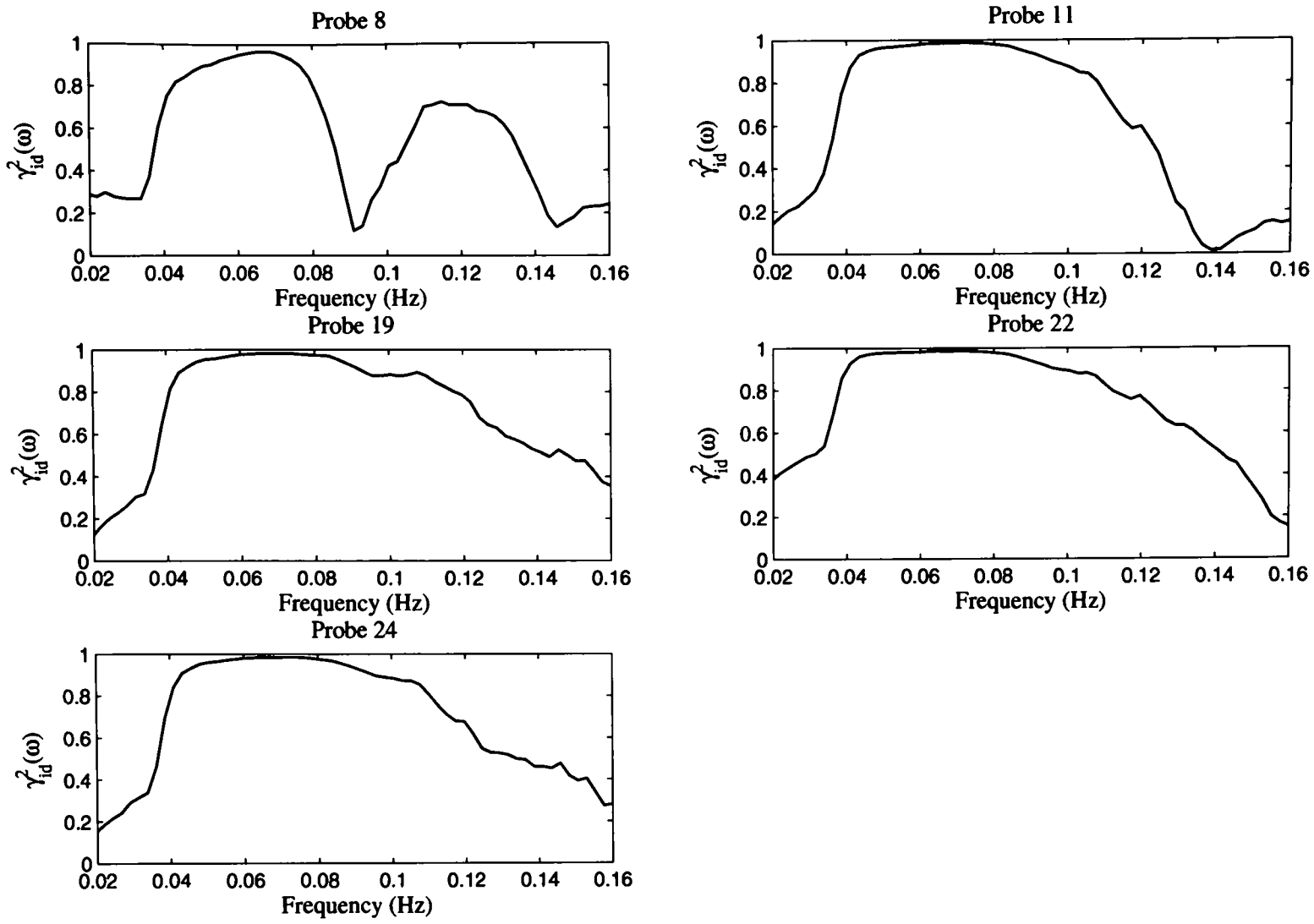

Figure 8.19: Coherence functions between the incident and diffracted wave records.

are made between the measured crest elevations at these locations and the values predicted by the SRS method.

The SRS method assumes that there is an underlying linear random Gaussian process. The spectrum of this process is discretised into a large number of frequency components. Each component represents a narrow-banded random process itself, and is independent of the properties of the other components. The interaction of the wave field with a structure can be described by a summation of the interactions of each of these linear components. For linear interaction, only linear transfer functions are needed for this summation.

The SRS method also assumes that the linear process is modified by second order interactions between the narrow-banded components. Second order interactions, of course, require quadratic transfer functions between pairs of linear components, and so are more complicated. In principle, higher order interactions could be included in the SRS method but higher order diffraction transfer functions are not commonly available.

Since the frequency components represent narrow-banded linear random processes, they have

Gaussian statistics. The SRS method works in the probability domain and the probability structure of the entire wave field corresponds to a Gaussian hill in multi-dimensional probability space. Each of the frequency components is Gaussian with zero mean and known variance, specified by the spectrum of the wave field. Hence the multi-dimensional Gaussian hill for the entire process is centred on the origin; the most likely instantaneous value of the wave field is zero.

A particular value of system response then becomes a multi-dimensional surface in the same probability space. There are many possible combinations of the linear wave components that give rise to the same value of system response and, of these combinations, the point on the response surface closest to the origin corresponds to the most probable point, and is known as the 'design point' in reliability theory.

The aim of the SRS method is to assess the probability of exceedance of a given level of system response in a specified period (usually expressed as a return rate). This probability corresponds to the proportion of the volume of the Gaussian hill outside the chosen response surface. In principle, to evaluate this volume would require a large multi-dimensional integral. However, in first order reliability theory the volume of the hill outside the response surface is approximated by replacing the actual curved response surface with a plane that is tangential to this surface at the design point. This greatly simplifies the integration. Although only an approximation, first order reliability estimates become increasingly accurate the further the design point is away from the origin. Previous experience suggests that responses at 10^{-2} and 10^{-3} levels are sufficiently extreme for first order reliability estimates to be accurate (Tromans and Vanderschuren 1995).

It follows that the determination of the response statistics is reduced to a search in probability space for the design point. This is achieved using a Lagrange multiplier method and is included in code developed by Dr. Peter Tromans at Ocean Wave Engineering. Since the search is in probability space, it is much faster than conventional time domain simulation of random waves. The method has already been used in several ocean engineering applications - e.g. Tromans and van Dam (1996) and Tromans and Taylor (1998). Here the SRS method is used to deduce crest elevations beneath the LUNA structure corresponding to given probabilities of exceedance.

For the irregular wave data studied in this thesis (Data Set 7, Table 4.2, Section 4.6 Chapter 4), which is associated with a return period of 100 years and is based on a JONSWAP spectrum ($\gamma = 2$, f_p=0.07Hz and H_s=9.9m), the largest elevations measured during the three-hour test period are 18.14m (probes 11) and 18.44m (probe 24). The linear and quadratic

diffraction transfer functions from the analysis reported in Chapter 7 were supplied to Dr. Peter Tromans, who ran his code for the LUNA case. For an incident wave field based on the above JONSWAP spectrum, the surface elevations computed by the SRS method (provided by Dr. Peter Tromans) are given in Table 8.6, together with measured crest elevations.

Exceedance prob.	η (m) (SRS method)		η (m) (measured)	
	Probe 11	Probe 24	Probe 11	Probe 24
10^{-1}	8.75	8.61	8.8	9.8
10^{-2}	13.50	13.06	13.5	13.8
10^{-3}	17.87	17.04	18.1	18.4

Table 8.6: Crest elevations beneath the LUNA structure corresponding to given probabilities of exceedance. Values from the SRS method are given to two decimal places and measured values are given to one decimal place.

The linear and second order contributions to the total crest elevations (computed using the SRS method) are given in Table 8.7.

Probe	Exceedance prob.	$\eta^{(1)}$	$\eta^{(2)}$	$\eta^{(2+)}$	$\eta^{(2-)}$
11	10^{-1}	7.54	1.21	1.32	-0.11
11	10^{-2}	9.85	3.65	3.85	-0.20
11	10^{-3}	11.50	6.37	6.64	-0.27
24	10^{-1}	7.10	1.51	1.66	-0.15
24	10^{-2}	9.73	3.33	3.58	-0.25
24	10^{-3}	11.84	5.20	5.53	-0.33

Table 8.7: Linear and second order contributions to the crest elevations computed using the SRS method. Values are given to two decimal places.

As one would expect, Tables 8.6 and 8.7 show that the second order contributions to the total surface elevation become more significant as the probability of exceedance reduces. For wave crests corresponding to the 10^{-3} exceedance probability, the second order terms constitute 35.6% and 30.5% of the total elevation for probes 11 and 24 respectively. It would also be interesting to investigate the size of the third order terms, although this would require third order diffraction transfer functions, which are not readily available.

Considering that the diffraction transfer functions inputted into the SRS method do not account for white water activity or waves over-topping the concrete columns (which were observed in the model tests and are discussed further in Section 8.4), the close agreement found with the measured data for both probes is encouraging. The agreement was particularly good for probe 11, where the SRS method predictions were within 0.6% and 1.3%

of the measured values for the 10^{-1} and 10^{-3} exceedance probabilities respectively, and the prediction for the 10^{-2} exceedance probability was equal to the measured value! The slightly larger differences (between prediction and measured) found for probe 24, which is close to one of the downstream columns, can probably be attributed to waves over-topping the concrete columns, which will modify the wave field from that predicted by diffraction theory.

The work presented in this section introduces a very useful design methodology for the offshore industry. To the author's knowledge, this study is the first to combine diffraction analysis with the SRS method to produce realistic extreme surface elevation statistics.

8.3.5 Effects of directional spreading on the diffracted wave field

The effects of directional spreading on the magnitude and location of the most extreme free surface magnifications beneath the LUNA structure are now investigated for incident irregular waves. For this purpose, the magnitudes and locations of the five most extreme crests are recorded for the multidirectional wave data and are compared with similar results obtained for the unidirectional wave data. One multidirectional data set is available (Data Set 8, Table 4.2, Section 4.6 Chapter 4), which represents a wave field with wave directions having a standard deviation of approximately 15 degrees and the maximum wave angles are all within 45 degrees of the mean direction.

Table 8.8 records the five largest crest elevations for the unidirectional and multidirectional irregular wave data. The largest five crest measurements for the multidirectional wave field all occur in the vicinity of the downstream columns; the largest three crest elevations are recorded by wave probes 23, 24 and 25, which are all located in the same region directly adjacent to the inside surface of one of the downstream columns. This region was also found to record the most extreme surface elevations for the unidirectional data. The largest crest is recorded by wave probe 24 for both the unidirectional and multidirectional data and has increased by 5.1% as a result of directional spreading. The remaining four multidirectional peak crest elevations are comparable to the unidirectional values although two of the values are recorded in different locations. For the unidirectional wave field two of the five largest crests are recorded at probes 11 and 22, which are both located away from the columns. Directional spreading has the effect of reducing the largest crests at these probes and hence results in the largest crests all occurring adjacent to the downstream columns.

Wave-structure interaction calculations carried out during the preliminary design of an offshore platform are commonly only undertaken for a unidirectional wave field, as this is regarded as the critical incident wave field. Indeed, the linear directional spreading analysis

carried out in Section 6.6 Chapter 6 suggested that directionally spreading a wave field from its unidirectional state results in reduced peak crest elevations. However, the experimental data examined here for the LUNA structure shows that directional spreading has resulted in increased free surface magnification around the downstream columns. Therefore, for this particular structural geometry, the analysis undertaken suggests that nonlinear effects may give rise to increased surface magnifications when the incident wave field becomes spread. Such nonlinear effects are likely to be considerable in the vicinity of the downstream columns, where two large diameter columns are positioned close together. It is unfortunate that further multidirectional data is not available, as it would be useful to study the magnification effects for varying degrees of spreading.

Data Set	Probe	η_{max} (m)
7	24	18.44
7	23	18.34
7	11	18.14
7	19	18.09
7	22	17.58
8	24	19.38
8	25	18.44
8	23	18.37
8	20	18.00
8	19	17.59

Table 8.8: Maximum surface elevations recorded in the vicinity of the LUNA structure for the unidirectional (Data Set 7) and multidirectional (Data Set 8) irregular wave data. All values are given to two decimal places.

8.4 Model test data: Incident regular waves

In order to assess the validity of using diffraction solutions for airgap design, comparisons are now made with experimental regular wave (i.e. monochromatic wave) data for the LUNA structure. Since only one frequency is being considered the computation time is not critical and so the numerical diffraction solution is used here to model wave interaction with the columns and caisson. The results presented in this section are taken from an investigation into airgap design carried out by Walker et al. (2006).

Comparisons are made between the measured surface magnifications in the vicinity of the structure and those predicted by linear and second order diffraction theories. Through comparing experimental data with diffraction solutions, the ultimate aim is to address the following key question: if you do not carry out model tests then can you rely upon linear and second order diffraction solutions to accurately guide airgap design? Progress towards a definitive

answer to this question is pursued in this section.

Firstly, the experimental data recorded along the centreline of the structure is spectrally decomposed (using a band-pass filter) into linear ($\eta^{(1)}$) and second order sum ($\eta^{(2)}$) components and compared with corresponding components computed by DIFFRACT. Obviously it is relatively easy to extract linear and nonlinear components from measured regular wave data by filtering because the individual components are well separated in frequency. Wave probes 4, 7-9 and 11-16 provide an array of ten measurement probes along the centreline of the structure, starting at the up-wave end of the model (see Figure 4.3 Section 4.5 Chapter 4). Wave measurements from two regular wave tests are available, namely Data Set 5 and Data Set 6 (Table 4.2 Section 4.6 Chapter 4). The wave period for each test is 12.7s, corresponding to a frequency of 0.079Hz, and the wave heights are 10m (Data Set 5) and 14m (Data Set 6). Linear and second order sum comparisons along the centreline of the structure are shown in Figures 8.20 and 8.21 where the DIFFRACT solution has been computed at 5m increments. The linear and second order components have been non-dimensionalised by dividing by the undisturbed linear amplitude, A, and κA^2 respectively. In these figures the waves pass the structure from left to right.

For the specific structure and wave conditions considered in this study, a number of numerical meshes have been used to test the convergence properties of the second order solution. Following these tests the author is satisfied that the results presented are an accurate representation of the wave field predicted by diffraction theory. The body surface, internal water plane and outer free surface meshes used to generate the results in this section for LUNA are shown in Figure 7.3 Chapter 7.

Figure 8.20 shows that the measured trend in linear surface magnification along the centreline has been reproduced well by linear diffraction theory. The measured peak surface magnifications, recorded near the centre of the structure (x=0), closely agree with that predicted by linear diffraction; the predicted value lies midway between the measured peaks for the two wave heights. The most notable discrepancies occur in the vicinity of the platform columns. The measured minima between the two front columns ($x \approx -30$m) are further downstream than predicted by linear diffraction. This shifting of the minimum near the two front columns was also identified by Ohl et al. (2001a) for a square array of bottom-mounted circular columns. Downstream of the back columns ($x >\sim 40$m), the measured linear magnification continues to decrease whereas diffraction theory predicts a gradual increase in linear magnification. The dissipation of energy due to wave breaking could be the cause of this, which is obviously not incorporated into a diffraction solution.

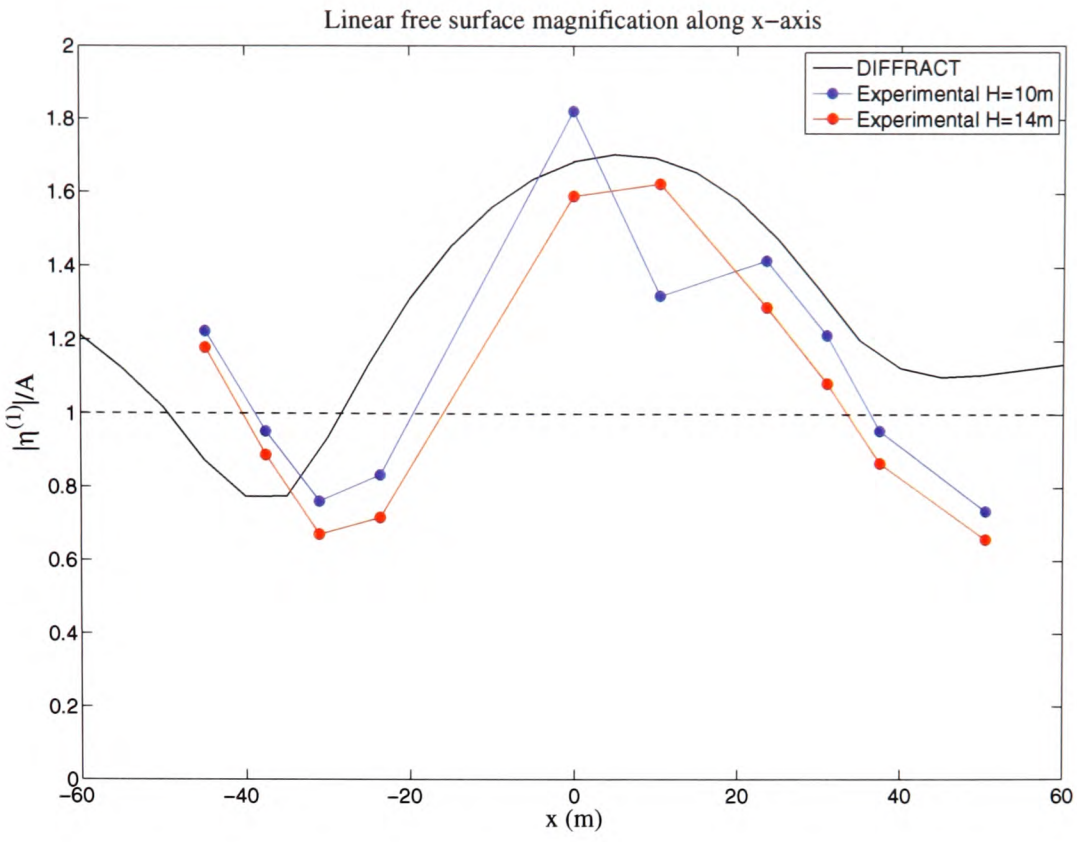

Figure 8.20: Comparison between the measured linear free surface magnification along the centreline of the LUNA structure (x-axis) and corresponding results computed by DIFFRACT. The horizontal dashed line corresponds to zero magnification.

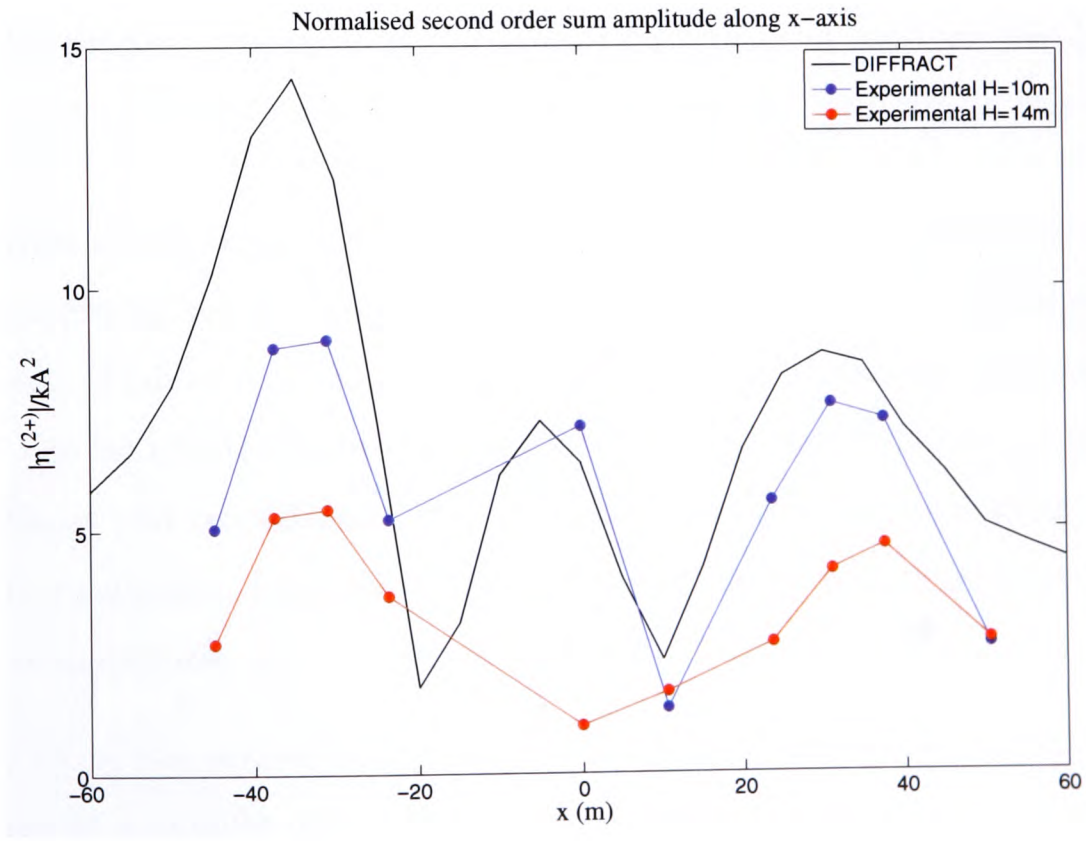

Figure 8.21: Comparison between the measured second order sum amplitude along the centreline of the LUNA structure (x-axis) and corresponding results computed by DIFFRACT.

It is clear from Figure 8.21 that significantly larger non-dimensional second order sum peaks are observed experimentally for the lower amplitude waves, H=10m, compared to the higher amplitude waves, H=14m. This was also noted by Ohl et al. (2001a) for an array of bottom-mounted circular columns. The recorded measurements are clearly marked in Figures 8.20 and 8.21 with circles and lines join these measurements to help illustrate the surface variation along the centre of the structure. Attention is drawn to the fact that the line joining the probes at locations x=-24m and x=0m in Figure 8.21 for the H=10m waves is perhaps misleading, as it is likely that if a measurement was recorded between these two probes then the deep trough predicted by second order diffraction theory would have been observed in the experiments. Ohl et al. used a more closely spaced array of measurement probes than was used in the LUNA model tests and so many of the trends identified by Ohl et al. are not as pronounced in the data studied here. However, some of the global trends in the second order profile identified by Ohl et al. are present in the LUNA data. These include:

1. The second order peaks coincide with peaks and troughs in the first order profile. Except for the absence of a second order peak near the centre of the structure for the H=14m waves, this observation is true for the LUNA results.

2. The second order troughs coincide with the maximum slopes of the first order profile. The measured troughs for the H=10m waves are located near the largest slopes in the first order profile. The measured second order trough at x=0 for the H=14m waves, which is not predicted by second order theory, does not conform to this trend.

The relative sizes of the linear and second order contributions along the centreline are now examined. Considering the H=10m waves, for which the most reliable green water measurements have been obtained, the magnitudes of the linear ($\eta^{(1)}$) and second order sum ($\eta^{(2+)}$) contributions can be inferred from Figures 8.20 and 8.21. Table 8.9 summarises the magnitudes of the linear and second order sum contributions for each probe along the centreline. For comparative purposes, both the linear and second order magnitudes are normalised by the linear wave amplitude, A.

The magnitudes of the second order contributions are considerable, exceeding the linear crest amplitude at a number of probes. For probes 7 and 8, which are located between the two front columns, the magnitudes of the second order sum contributions actually exceed the magnitudes of the linear contributions. However, as was discussed in Section 7.4.2 Chapter 7, it is clear from the linear surface elevation frequency response function between the two front columns (Figure 6.10 (a) Chapter 6) that the second order terms have excited a double

Probe	$\lvert\eta^{(1)}\rvert/A$	$\lvert\eta^{(2+)}\rvert/A$
4	1.22	0.70
7	0.95	1.22
8	0.76	1.24
9	0.83	0.73
11	1.82	0.99
12	1.32	0.18
13	1.42	0.78
14	1.22	1.05
15	0.96	1.01
16	0.74	0.36

Table 8.9: Linear and second order sum contributions along the centre of LUNA. H=10m probe measurements. Values are given to two decimal places.

frequency ($2 \times 0.079 = 0.158$Hz) resonance; the second largest peak in Figure 6.10 (a) occurs at 0.159Hz. Therefore it is not surprising that the second order contributions are so large between the two front columns and so long as the third and higher order terms are found to be comparatively small, it is still legitimate to use a second order diffraction solution based on perturbation analysis for predicting green water levels beneath multi-column structures. The second order sum contribution also exceeds the linear contribution at probe 15, which lies between the two back columns. This could also be the result of a resonant surface response although a linear elevation frequency response function has not been generated between the back columns to confirm this.

Waves over-topping the concrete columns and white water activity are thought to have a large effect on the green water levels measured between the columns and hence it would be difficult to draw any definite conclusions from these comparisons alone. Indeed, the incident wave amplitude magnified by diffraction effects (first and second order) exceeds the height of the concrete columns above mean sea level (7.07m) and hence the actual incident-scattered wave interaction will be different from that predicted by diffraction theory.

It follows that the difference in the measured results for H=10m and H=14m is likely to be due to differing degrees of white water activity around the structure and the extent to which waves over-top the concrete columns. Figure 8.22 shows a still image extracted from the video footage recorded during the H=14m tests. This image shows waves over-topping the columns together with significant white water, neither of which can be incorporated into a diffraction solution.

The measured second order sum elevation along the x-axis reaches peak values between the front and back columns. The locations of these peaks are predicted well by DIFFRACT although the magnitude of the responses are over predicted. The peak computed by DIFFRACT

Figure 8.22: Still image showing white water beneath the LUNA model. Incident waves are propagating towards the camera.

between the front columns ($|\eta^{(2+)}_{peak}|/kA^2 = 13.91$) exceeds the measured peaks by 55.8% for the $H = 10$m waves ($|\eta^{(2+)}_{peak}|/kA^2 = 8.93$) and 155.7% for the $H = 14$m waves ($|\eta^{(2+)}_{peak}|/kA^2 = 5.44$). The agreement is improved between the back columns where the DIFFRACT peak response ($|\eta^{(2+)}_{peak}|/kA^2 = 8.63$) is 13.9% and 85.2% larger than the $H = 10$m ($|\eta^{(2+)}_{peak}|/kA^2 = 7.58$) and $H = 14$m ($|\eta^{(2+)}_{peak}|/kA^2 = 4.66$) peaks respectively. The peak occurring at the centre of the structure for the $H = 10$m waves is reproduced very well by DIFFRACT; the DIFFRACT prediction ($|\eta^{(2+)}_{peak}|/kA^2 = 7.24$) exceeds the measured peak ($|\eta^{(2+)}_{peak}|/kA^2 = 7.13$) by only 1.5%.

The poor agreement found between the two upstream columns is not surprising considering the wave over-topping and white water observed in this region, which prevent the double frequency resonant surface mode from reaching the peak elevations predicted. The greatly improved agreement at the centre of the structure, where these highly nonlinear effects are likely to have a reduced effect, is very encouraging.

The comparatively good agreement found between the second order diffraction results and the H=10m wave measurements helps to demonstrate the validity of using second order diffraction theory for predicting green water levels beneath multicolumn structures. Conversely, the comparisons drawn between the second order diffraction results and the H=14m wave measurements could possibly serve to illustrate the limitations of second order diffraction theory at predicting extreme water levels beneath real offshore structures. However, as is

clear from the video footage, the errors found are likely to be the result of both white water activity and waves overtopping the concrete columns.

The significance of higher order nonlinear contributions, above second order, is not known. Upon inspection of the wave spectra at any one of the measurement probes around the structure, it is possible to identify harmonics up to $\sim$ 7th order, with those above second order obviously not being included in a second order diffraction code. Figure 8.23 shows estimates of both the undisturbed wave spectrum (recorded in the absence of the model) and the diffracted wave spectrum (recorded by probe 9 between the two front columns) for the H=14m waves. The large size of the wave tank and the ability to effectively absorb waves around the perimeter implies that the nonlinear harmonics identified are not likely to be caused by wave reflections from the sides. It would be interesting to investigate the significance of these higher order contributions using a fully nonlinear diffraction code, but this is not viable until a validated form of such a code becomes available.

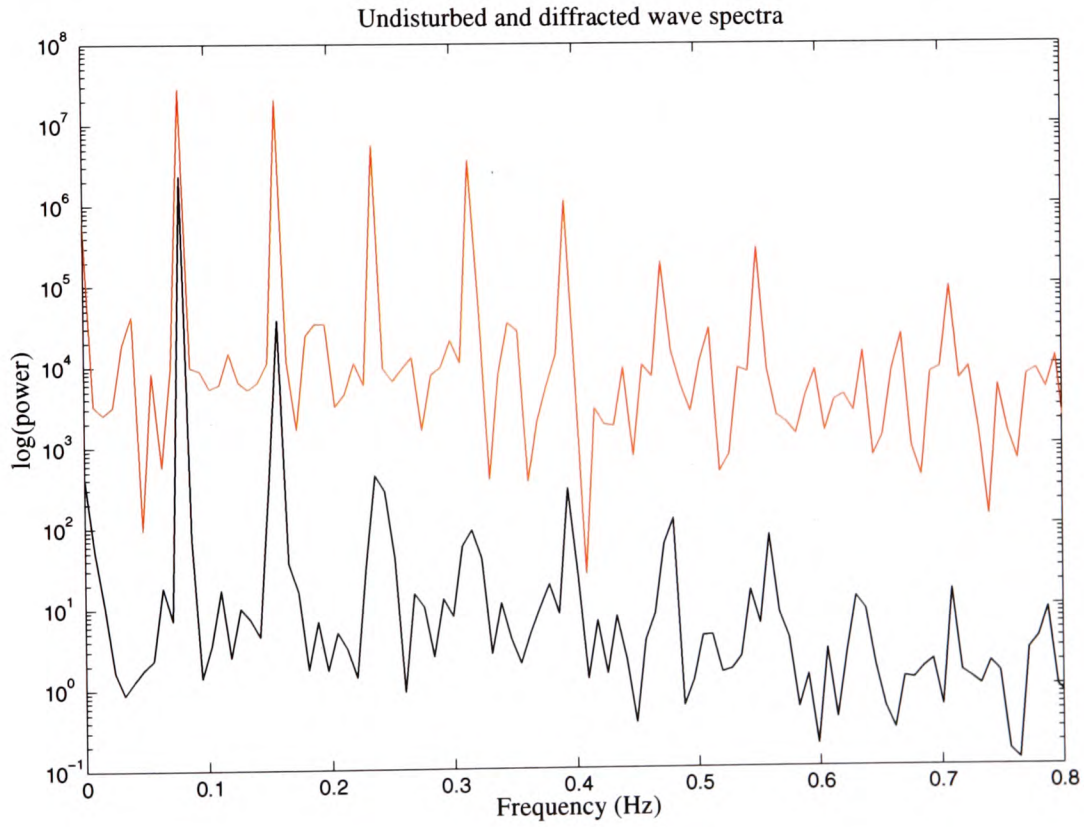

Figure 8.23: Undisturbed and diffracted wave spectra for H=14m waves. A logarithmic power scale has been used to help emphasise the nonlinear peaks present. The fundamental frequency is 0.079Hz (corresponding to a wave period of 12.7 seconds). Black line: undisturbed spectrum; red line: diffracted spectrum (probe 9).

The ability of diffraction theory to predict the total (linear + nonlinear components) green water level is now examined. The H=10m waves are considered. The largest total green

water elevation recorded along the centreline of the structure occurs at probe 11 and is equal to $2.27A$. Linear diffraction theory predicts the green water elevation at probe 11 to be $1.68A$, whereas second order diffraction theory (incorporating linear and second order terms) predicts the green water elevation at probe 11 to be $2.05A$, which is only 9.7% below the measured value. The maximum green water predicted by linear diffraction theory along the centreline is $1.69A$ and occurs at probe 12. Second order diffraction theory predicts the maximum green water level along the centreline to be $3.05A$, which occurs at probe 7. This suggests that either there is a problem with the numerical solution procedure at second order between the two closely spaced upstream columns, or that the considerable white water and wave over-topping observed in this region have mitigated the large surface responses associated with the resonant mode excited between the columns. Considering the extensive convergence testing undertaken and the white water and over-topping observed in the video footage, the latter scenario is certainly the more probable.

At the centre of the structure, where the largest measured elevation along the centreline was observed, incorporating second order terms into the diffraction solution provides an improved prediction of the total green water level. In fact, because the wave probes are sensitive to white water, the actual green water level will be lower than the level indicated by the probes and hence the additional measured elevation not predicted by diffraction theory ($2.27A$ - $2.05A$) is probably white water. It may be possible to determine whether the probes are measuring green or white water by looking carefully at the wave records; if the records appear wave-like then the record is likely to be showing green water. This has not been undertaken as part of this study. The location of the largest measured elevation at the centre of the structure, which itself is of great interest to platform designers, is well predicted by both linear and second order diffraction theories.

The accuracy of diffraction theory at predicting linear and second order runup values is now examined for the LUNA structure. Data from measurement probes 1, 5, 20 and 25 (Figure 4.3 Section 4.5 Chapter 4) are considered and comparisons are made with results generated using DIFFRACT in Chapter 7 (Figures 7.6 and 7.7). Linear ($\eta^{(1)}$) and second order sum ($\eta^{(2+)}$) contributions measured by these probes are given in Table 8.10 for both the H=10m and H=14m tests.

Probe	H=10m		H=14m	
	$\|\eta^{(1)}\|/A$	$\|\eta^{(2+)}\|/A$	$\|\eta^{(1)}\|/A$	$\|\eta^{(2+)}\|/A$
1	1.14	0.29	1.23	0.20
5	1.37	0.52	1.42	0.36
20	1.68	0.46	1.52	0.33
25	1.40	0.28	1.29	0.34

Table 8.10: Measured linear and second order sum contributions. Values are given to two decimal places.

For the four probes considered, the linear contribution exceeds the second order sum contribution on average by a factor of 3.8 for the H=10m waves and 4.6 for the H=14m waves. To aid a comparison between the values given in Table 8.10 and corresponding values from Figures 7.6, 7.7 and 7.8 (Chapter 7), the linear ($\eta^{(1)}$), second order sum ($\eta^{(2+)}$) and second order time-independent ($\eta_q^{(2-)}$) contributions computed using diffraction theory at the locations of probes 1, 5, 20 and 25 are given in Table 8.11.

Probe	$\|\eta^{(1)}\|/A$	$\|\eta^{(2+)}\|/A$	$\eta_q^{(2-)}/A$
1	0.96	0.35	-0.12
5	0.97	1.42	-0.12
20	1.60	0.86	+0.03
25	1.53	1.50	+0.03

Table 8.11: Linear, second order sum and second order time-independent (set-up/down) components computed using diffraction theory. Values are given to two decimal places.

The measured linear runup values are found to be in reasonable agreement with those predicted by linear diffraction theory, whereas the measured second order sum runup values are substantially lower than those predicted by second order diffraction theory. The poor agreement at second order is thought to be mainly caused by the truncation of the LUNA columns 7.07m above mean water level; the diffraction solutions assume that the columns extend above the maximum predicted runup values. Waves running up the smaller diameter steel columns (which support the deck structure) are also thought to have an appreciable effect on the measured runup results for probes 1, 5, 20 and 25, which all lie close to the steel columns. Indeed, the worth of all comparisons for the LUNA structure has been limited by such non-modelled factors.

Both the diffraction solutions and the model test data indicate that the magnitude of the second order contributions (sum and difference) to the overall diffracted wave field, both on and away from the columns, are considerable and hence should not be neglected in design. If linear terms are considered alone then the extreme green water magnifications beneath

LUNA will be under predicted by diffraction theory. It would be interesting to examine the significance of the second order contributions for steeper incident waves, say $\kappa A \approx 0.25$, which is a more typical value for a design storm wave; the regular waves considered in this paper have a steepness of $\kappa A \approx 0.14$. Steeper waves will have increased nonlinear contributions and so the error in the linear diffraction prediction is likely to be exacerbated further. However, increased steepness will almost certainly be accompanied by increased white water, which will further hinder the comparison between measured elevations and the diffraction solutions.

The wave probes used in the tests measure surface elevation at fixed locations around the model. Although the probes were deployed in regions where maximum water levels were expected to occur, it is unlikely that the probes recorded the highest water levels around the structure, which are obviously needed for airgap design. However, it is thought that the probes in the most energetic regions were sufficiently close together for a good estimate of the largest surface elevation to be made.

Using the model test data described by Ohl et al. (2001a), further comparisons have been made, in addition to those presented in this thesis, between diffraction solutions and measured surface elevations in the vicinity of an array of four bottom-mounted columns arranged at the vertices of a square. Comparatively little white water was observed during these tests, which were run for both regular waves and focused wave groups. For the regular wave tests the diffraction solutions were found to show closer agreement with the measured linear and second order components of the diffracted wave field. The focused wave tests have not been analysed. Although a thorough analysis of these data has not been undertaken as part of this study, the results produced thus far for incident regular waves suggest that second order diffraction theory (incorporating linear and second order terms) provides an improved prediction of the extreme water levels and their locations around the four columns. The comparisons made in this section for regular waves incident upon LUNA illustrate the difficulties encountered in predicting green water levels beneath real offshore structures.

8.5 Conclusions

The analysis tools developed in Chapter 5 for studying the Draupner field data were applied to the experimental irregular wave data. The advantage of applying these tools to the experimental data rather than the Draupner data is that there are many more instances of large waves, and hence there is considerably less sample variability on the mean properties of large waves.

The largest undisturbed crests were found to be higher and narrower than the largest troughs, which are less deep and more rounded. Predictably, this crest-trough asymmetry increases as the size of the crests and troughs increases. The linear contribution was found to dominate the average large crest profile for the undisturbed data. For the model test data, the higher order contributions - and in particular the second order contribution - were found to become more dominant as a consequence of the waves interacting with the model structure.

Stokes-type corrections were used to approximate the second and third order sum contributions to the undisturbed data. The sensitivity of this technique to the number of waves used was investigated, and it was concluded that at least 400-500 waves are needed to accurately compute the magnitude of the second order sum contribution. The undisturbed wave record was linearised by removing the second order contributions, producing a wave record in which the magnitudes of ordered crest height and trough depression are comparable over the full range of wave heights.

The second and third order sum contributions to the largest three waves in the undisturbed data were investigated. The significance of these contributions was found to increase with increasing crest height and it was concluded that, to fully capture the real magnitude and nature of these largest waves, a nonlinear wave theory must be used.

The ability of NewWave to model the largest waves in the undisturbed data was assessed. The agreement between the linear NewWave profile and the average linear profile was found to be better than that for the Draupner data. The fifth order NewWave profile closely matches the average large crest profile, although is slightly too narrow banded.

Spectra for the second order difference, second order sum and third order sum contributions to the undisturbed data were approximated, allowing suitable cut-off frequencies to be identified for the extraction of nonlinear contributions by filtering. Using this approach, the high frequency contributions (i.e. above third order) to the largest three waves in the undisturbed data were found to be considerable. A similar approach was applied to the model test data and the nonlinear contributions were found to extend over much broader ranges of frequencies, principally caused by a shift of energy to higher frequencies, and hence the extraction of the nonlinear contributions by filtering could not be performed.

In an effort to develop a technique for estimating the degree of directional spreading from a fixed Eulerian sensor, the effect of directional spreading on the size of the second order sum contribution was investigated. The analysis undertaken for the undisturbed data suggested that it was not possible to use the magnitude of the second order sum contribution to gauge

spreading.

The ability of linear diffraction theory to predict measured diffracted wave spectra at a number of locations in the vicinity of the LUNA structure was investigated for incident irregular waves. The spectral shapes were reproduced very well by linear diffraction although the predicted energy contents of the diffracted wave fields were lower than were measured. The discrepancy is likely to be due to phenomena not included in the modelling, predominantly wave interaction with the caisson and waves over-topping the concrete columns.

An approach to identify the linear frequency range of the model test data, based on the coherence function between the undisturbed and diffracted wave records, was proposed. Linear frequency ranges were estimated at a number of locations around the structure although these ranges were not verified.

Incorporating the diffraction analysis for LUNA into the surface response statistics method, produced accurate predictions for wave crest statistics around the structure; excellent agreement with experimental model test data was found.

The effect of directional spreading on the most extreme free surface magnifications beneath the LUNA structure was investigated and the data analysed showed that directional spreading increases the free surface magnifications around the downstream columns.

The ability of diffraction theory to predict wave measurements in the vicinity of the LUNA structure for incident regular waves was examined. The results presented showed that incorporating second order terms into the diffraction solution provides an improved prediction of the largest green water measurement beneath the deck. The location of the largest measured elevation was found to be well predicted by both linear and second order diffraction solutions. The principal causes of the observed discrepancies between the predicted and measured surface elevations are white water measurement (which cannot be distinguished from green water measurement by the wave probes) and waves overtopping the concrete columns.

Both the second order diffraction solutions and the experimental data presented in this chapter show that the magnitude of the second order contributions to the overall diffracted wave field are considerable, and hence should not be neglected in design.

Chapter 9

Conclusions and future work

This thesis is concerned with the modelling of extreme ocean waves and their diffraction by offshore structures, with the ultimate aim of proposing improved tools for guiding airgap design. A review of the most significant conclusions from this work and the implications for the offshore industry are discussed in this chapter, together with a suggested programme of future work.

9.1 Conclusions

For airgap design there are two objectives: (i) obtain a realistic model for large ocean waves and (ii) model how large ocean waves interact with a structure. Both of these objectives are addressed in this thesis and the principal conclusions drawn from this work are given in this section.

9.1.1 Extreme wave modelling

For airgap design one is interested in the largest waves occurring in a sea state, and so the accurate simulation of these waves is crucially important for obtaining realistic airgap predictions. This thesis uses field data from the North Sea and experimental model test data to explore the shapes of large free surface waves. A design wave, called NewWave, has been proposed as a good model for large ocean waves and has been validated against the measured wave data available, where excellent agreement has been found. Furthermore, unique features of a measured freak wave, namely the Draupner New Year wave, have been identified distinguishing it from a typical large wave, and the probability of occurrence of this event has been estimated.

NewWave has been used as the incident wave field in the wave-structure diffraction analysis because of its ability to accurately model the irregular shape and random background of large

ocean waves. Most previous research has considered only monochromatic wave fields. The ability to model the diffraction of real large ocean waves by structures obviously makes the use of diffraction theory as a tool for airgap design more appealing to the offshore industry.

9.1.2 Wave-structure interaction

Linear and second order water wave diffraction solutions have been implemented in this thesis to model wave-structure interaction. A number of tests have been performed to validate the diffraction solutions; first and second order comparisons have been made with published results, experimental data and results generated using alternative diffraction solutions for a number of structural configurations, and excellent agreement has been found for each comparison.

By studying the linear diffraction of monochromatic waves by linear arrays of columns and the LUNA configuration of columns, large magnifications in force and free surface elevation were found to exist for incident waves at critical frequencies, corresponding to a phenomenon known as near-trapping. Such extreme responses could have serious practical implications for column-supported structures, although the bandwidths of these magnification effects were found to be quite narrow, especially for large arrays of columns, and so one may suspect that the integrated effects over a continuous spectrum are not severe. Similar analysis at second order suggested that near-trapping of the second order wave occurs when its frequency coincides with the linear near-trapping frequency. The second order wave field at second order near-trapping was found to be remarkably similar to the linear wave field at linear near-trapping, suggesting that useful information on extreme second order responses can be obtained by studying linear diffraction alone.

The analysis presented for the diffraction of NewWaves by arrays of columns shows that, if an incident wave spectrum excites a linear or second order near-trapped mode, then the resulting diffraction magnifications of the free surface can be considerable. Therefore, although near-trapping is a phenomenon associated with monochromatic incident waves, which are obviously not an accurate representation of an ocean surface, it is still very important to avoid significant energy (e.g. close to the peak of the local sea spectrum) being concentrated around one of these critical frequencies. An offshore structure should thus be designed so that the local wave energy spectrum does not excite linear or second order near-trapped modes; the preliminary design of a multi-column offshore structure should include the selection of a suitable configuration of columns so that energy from the surrounding wave environment is small at both the linear and second order near-trapped frequencies. This would help to avoid large magnifications of the free surface in the vicinity of the structure and can be achieved

using linear diffraction theory alone.

The sizes of the linear and second order free surface magnifications resulting from wave interaction with the LUNA structure were found to be surprisingly large. If the incident wave spectrum excites a resonant mode, the diffraction solutions predict that an 11m incident crest can cause green water to be projected $\sim$ 30m above mean sea level beneath the deck.

Both the diffraction solutions and the experimental model test data indicate that the magnitudes of the second order sum and difference contributions to the overall surface response can be considerable. It follows, therefore, that they should be factored into the design process rather than ignored, as is common in current practice.

9.1.3 Diffraction theory as a tool for airgap design

This project addresses two of the key issues facing airgap design beneath multi-column gravity based structures: (i) whether diffraction solutions can accurately predict the magnitudes and locations of the most extreme green water levels; (ii) the difficulties associated with obtaining reliable green water measurements to validate diffraction solutions as possible design tools.

In order to assess the validity of using diffraction solutions for the purposes of airgap design, comparisons were made with measured wave data from a programme of wave tank experiments for the LUNA structure. For the test cases considered in this thesis, the use of linear diffraction theory for airgap prediction has been found to be inadequate, and incorporating second order terms into the diffraction solution provides an improved prediction of the largest green water measurements beneath the deck. The location of the largest measured elevation beneath LUNA was found to be predicted accurately by both linear and second order diffraction solutions.

The measurement of white water and waves overtopping the concrete columns have hindered comparisons between the model test data and the diffraction solutions. In addition, the inappropriate scaling of surface tension in the model tests (discussed in Section 4.4 Chapter 4) will have introduced further inaccuracies into the comparisons. However, the results presented for regular waves have helped to highlight the importance of second order contributions in the accurate prediction of extreme green water levels. It is hoped that further research in this area will be able to determine conclusively whether diffraction solutions alone can replace the need to carry out model tests during the preliminary design of multi-column gravity based structures. While model tests continue to be carried out, the wave analysis tools developed in this thesis can be used to interpret the measured data by approximating the magnitude of the linear and nonlinear contributions, and helping to identify solutions to mitigating extreme

green water responses.

By combining linear and second order diffraction analysis with the surface response statistics method of Tromans and Vanderschuren (1995), extreme crest statistics around the LUNA structure were accurately predicted; excellent agreement with experimental model test data was found. This approach to predicting wave statistics around a diffracting body could be a valuable tool for airgap design and, to the author's knowledge, this study is the first to implement such a methodology to produce realistic surface elevation statistics.

The emphasis of research in this field today is shifting to fully nonlinear diffraction solutions, which are computationally intensive. But this shift is perhaps premature, since research has not yet fully assessed what information second order theory can provide. From the viewpoint of a practicing engineer in the offshore industry, the focus should be on understanding what additional information second order theory can provide above linear theory and, only once this is understood, should the question be posed as to what additional information fully nonlinear solutions can provide.

The development of fully nonlinear diffraction codes is being pursued by a number of research groups and, to the author's knowledge, a validated code for an arbitrary three dimensional body is not available. Therefore, the application of fully nonlinear codes to assist in the design of offshore structures is some time away. If in the meantime second order diffraction theory can be shown to provide reliable guidance for the design of multi-column structures, then the offshore industry's reliance on inadequate linear theory can be avoided.

9.1.4 Final comment

With energy companies developing more offshore oil and gas infrastructure in what is perhaps becoming a more hostile ocean environment, there is an urgent need to improve current understanding of extreme ocean waves and their interaction with structures. Airgap design, which requires the accurate prediction of the maximum height above mean sea level to which green water is projected, is of particular interest to the offshore industry. In addressing this problem, this project has contributed to an improved understanding of extreme ocean waves and has implemented diffraction solutions for modelling the effects of these waves on offshore structures. Guidelines for the design of offshore structures have been outlined, enabling structural configurations to be selected that do not excite resonant surface responses. The comparisons made between the diffraction solutions and real wave data suggest that incorporating second order contributions into the diffraction solution provides an improved prediction of the green water levels beneath multi-column structures. However, further com-

parisons are needed for a number of structural configurations to instill sufficient confidence to replace expensive and time consuming model testing with the use of diffraction solutions.

It is hoped that the conclusions drawn from this work and the research initiated from these conclusions will ultimately allow the energy industry to develop offshore fields in hostile oceans more quickly and more safely. It is considered that the findings of this project are of use beyond the oil and gas industry. Indeed, the design wave and diffraction solutions implemented in this thesis can also be used to examine wave interaction effects with large arrays of columns, which potentially could be used for the supporting structure of a floating island.

9.2 Future work

Following on from the work undertaken in this DPhil project, some suggested areas of future work are as follows:

- Attempt to find further measured extreme/freak waves and study the second order difference contributions associated with these waves. Endeavour to identify further features that distinguish freak waves from 'typical' large waves and investigate possible physical mechanisms leading to the formation of such events. Both Statoil and Woodside Petroleum have offered field data, from the North Sea and Australia's North West Shelf respectively, for analysis.

- By studying the interaction of NewWaves with structures, investigate how sensitive the linear and second order diffracted wave fields are to the local wave parameters - e.g. how sensitive are the diffraction solutions to peak period, T_p, and significant wave height, H_s etc.? Conclusions on this would be useful to the offshore industry as the wave conditions at the location of a proposed platform are often not known very accurately - e.g. wave data may be available for a one year period only.

- Improve the convergence characteristics of the second order diffraction calculation by modifying the free surface mesh to include triangular and quadrilateral elements. Also increase the mesh sizes allowed by the DIFFRACT code. These changes will enable higher frequencies to be considered and so will allow: (i) a more thorough investigation of near-trapping at second order to be carried out; (ii) the second order diffraction of a NewWave based on a realistic sea spectrum (e.g. JONSWAP) to be considered.

- Carry out further comparisons between the diffraction solutions (linear and second or-

der) and measured wave data. Consider a number of structural configurations, preferably with large diameter columns extending up to the deck so that waves overtopping the columns will not hinder the comparisons. Use model test data and/or field data recorded around an offshore structure.

- Investigate the existence of near-trapped modes for non-cylindrical columns. According to Maniar and Newman (1997), the essential geometrical feature is not the column shape itself, but the periodicity of the array.

- Study the linear and second order diffraction of NewWaves based on a number of different wave spectra and spectral parameters. In particular, investigate the effects the peak frequency and broadness of the spectrum have on free surface magnifications. The purpose of this work is to help define clear guidelines, in addition to those given in this thesis, for the selection of structural configurations to avoid exciting resonant responses.

- Study linear and second order wave diffraction by different geometrical configurations of columns and identify a desirable configuration (in terms of minimising free surface magnifications) for a particular sea state. Clearly define a procedure for identifying this desirable configuration.

- Study the diffraction of a NewWave embedded into a random background and observe the effect of the random background on peak surface magnifications. This can be achieved using the so-called constrained NewWave, which embeds an extreme crest into a random sequence in such a way that the overall sequence is almost indistinguishable from a purely random occurrence of a large wave. Taylor, Jonathan, and Harland (1997) outline a procedure for achieving this.

- Study linear and second order wave diffraction by large arrays of columns (e.g. a 5 by 5 array of 25 columns) that could be used as the supporting structure for a floating island. Identify linear and second order near-trapped frequencies and investigate the resulting free surface magnifications when these resonant modes are excited by the local wave environment. Very efficient meshing schemes would need to be used to achieve converged second order results using the DIFFRACT code. The computation time for large arrays of columns would be very long using DIFFRACT and so an alternative approach for performing the free surface integral in the second order problem may be preferred - e.g. using an approach similar to that outlined by Malenica et al. (1999).

- Use diffraction theory to help develop an innovative design for a wave power device. Arrays of columns appear to attract wave energy, which is obviously undesirable for an offshore platform or a floating island, but perhaps desirable for a wave power device. One wave power device consisting of an array of columns is the Manchester Bobber (www.manchesterbobber.com), which is being developed by Manchester University and Royal Haskoning. Since large arrays of columns are again being considered, the approach outlined by Malenica et al. (1999) should probably be used for the second order calculation, in preference to using DIFFRACT.

- When a validated fully nonlinear diffraction code becomes available, investigate how the fully nonlinear diffracted wave field differs from the second order diffracted wave field for a four-column structure such as LUNA. It should be noted that even a fully nonlinear diffraction code will have difficulties modelling the details of breaking waves and broken waves, which are wave characteristics inevitably associated with extreme wave-structure interaction.

Bibliography

Abramowitz, M. and I. A. Stegun (1996). *Handbook of Mathematical Functions with Formulas, Graphs, and Mathematical Tables.* US Government Printing Office and Dover.

Baldock, T. E., C. Swan, and P. H. Taylor (1996). A laboratory study of nonlinear surface waves on water. *Phil. Trans. Roy. Soc. A354*, pp. 649–676.

Becker, A. A. (1992). *The Boundary Element Method in Engineering - A complete course.* McGraw-Hill.

Bendat, J. S. and A. G. Piersol (2000). *Random Data: Analysis and Measurement Procedures* (3 ed.). Wiley.

Bender, C. M. and S. A. Orszag (1978). *Advanced mathematical methods for scientists and engineers.* McGraw-Hill.

Boccotti, P. (1983). Some new results on statistical properties of wind waves. *Applied Ocean Research 5*(3), pp. 134–140.

Brebbia, C. (1980). *New developments in boundary element methods.* CML Publications.

Buldakov, E. V., R. Eatock Taylor, and P. H. Taylor (2004). Diffraction of a directionally spread wave group by a cylinder. *Applied Ocean Research 25*, pp. 301–320.

Chau, F. P. (1989). *The second order velocity potential for diffraction of waves by fixed offshore structures.* Ph. D. thesis, University College London.

Chau, F. P. and R. Eatock Taylor (1992). Second-order wave diffraction by a vertical cylinder. *Journal of Fluid Mech. 240*, pp. 571–599.

Cornett, A., V. Morin, and N. Durand (2002). Model tests to select deck elevations for the PA-B and LUN-A platforms. Technical report, Canadian Hydraulics Centre.

Dalzell, J. F. (1999). A note on finite depth second-order wave-wave interactions. *Applied Ocean Research 21*, pp. 105–111.

Dean, R. G. and R. A. Dalrymple (1991). *Water wave mechanics for engineers and scientists.* World Scientific.

Dean, R. G. and J. N. Sharma (1981). Simulation of wave systems due to nonlinear directional spectra. In *Int. Symp. on Hydrodynamics in Ocean Eng.*, Volume 453, Trondheim, Norway, pp. 1211–1222.

Duclos, G. and A. H. Clément (2004). Wave propagation through arrays of unevenly spaced vertical piles. *Ocean Engineering 31*, pp. 1655–1668.

Eatock Taylor, R. (1982). *Analysis of hydrodynamic loads by boundary element methods*, pp. 211–243. In Developments in Boundary Element Methods, Editors P.K. Banerjee and R.P. Shaw. Elsevier Applied Science Publishers.

Eatock Taylor, R., W. Bai, G. X. Wu, and Z. Z. Hu (2005). Numerical wave tanks based on finite element and boundary element modelling. In *Proc. OMAE 2005*, Volume 67508, Halkidiki, Greece.

Eatock Taylor, R. and F. P. Chau (1992). Wave diffraction theory - some developments in linear and nonlinear theory. *ASME Trans. Journal of Offshore Mech. and Arctic Eng. 114*, pp. 185–194.

Eatock Taylor, R. and G. Fonquernie (2001). *Second order diffraction in a focused wave group*, pp. 57–84. In Hydrodynamics in Ship and Ocean Engineering, Editor M. Kashiwagi. RIAM, Kyushu University.

Eatock Taylor, R. and J. B. Huang (1996). Application of second order diffraction analysis to TLP design. Internal report. Dept. of Eng. Science, University of Oxford.

Eatock Taylor, R. and J. B. Huang (1997). Second order wave diffraction by an axisymmetric body in monochromatic waves. *Proc. Roy. Soc. A453*, pp. 1515–1541.

Eatock Taylor, R. and P. Sincock (1989). Wave upwelling effects in TLP and semisubmersible structures. *Ocean Engineering 16*, pp. 281–306.

Eatock Taylor, R., J. Zang, W. Bai, and D. A. G. Walker (2006). Transients in wave diffraction by cylinders and cylinder arrays. In *Proc. 21st Intl. Workshop on Water Waves and Floating Bodies*, Loughborough University, UK.

Evans, D. V., M. Levitin, and D. Vassiliev (1994). Existence theorems for trapped modes. *Journal of Fluid Mech. 261*, pp. 21–31.

Evans, D. V. and R. Porter (1997). Near-trapping of waves by circular arrays of vertical cylinders. *Applied Ocean Research 19*, pp. 83–99.

Evans, D. V. and R. Porter (1998). Trapped modes embedded into the continuous spectrum. *Journal of Mech. and Appl. Math. 51*, pp. 263–274.

Faltinsen, O. M. (1990). *Sea loads on ships and offshore structures.* Cambridge University Press.

Faulkner, D. and W. H. Buckley (1997). Critical survival conditions for ship design. In *Proc. Intl. Conf. on Design and Operation for Abnormal Conditions*, Glasgow, UK, pp. 1–25.

Fenton, J. D. (1990). *Nonlinear wave theories*, pp. 3–25. In The Sea: Ocean Engineering Science Part A, Editors B. Le Méhauté and D.M. Hanes. John Wiley.

Forristall, G. Z. (1999). Wave crest distributions: Observations and second-order theory. *Journal of Phys. Oceanography 30*, pp. 1931–1943.

Ghalayini, S. A. and A. N. Williams (1991). Nonlinear wave forces on vertical cylinder arrays. *Journal of Fluids and Structures 5*, pp. 1–32.

Gibbs, R. (2004). *Walls of water on the open sea.* Ph. D. thesis, University of Oxford.

Greaves, D. M., A. G. L. Borthwick, G. X. Wu, and R. Eatock Taylor (1997). A moving boundary finite element method for fully non-linear wave simulations. *Journal of Ship Research 41*, pp. 181–194.

Hagen, O. (2002). Statistics for the Draupner January 1995 freak wave event. In *Proc. OMAE 2002*, Oslo, Norway.

Hasselmann, K., T. P. Barnett, E. Bouws, H. Carlson, D. E. Cartwright, K. Enke, J. A. Ewing, H. Gienapp, D. E. Hasselmann, P. Kruseman, A. Meerburgh, P. Muller, D. J. Olbers, K. Richter, W. Sell, and H. Walden (1973). Measurement of wind-wave growth and swell decay during the joint north sea wave project (JONSWAP). *Deutschen Hydrogr. A8*(12).

Havelock, T. H. (1940). The pressure of water waves upon a fixed obstacle. *Proc. Roy. Soc. 175*, pp. 409–421.

Haver, S. and O. J. Andersen (2000). Freak waves: Rare realizations of a typical population or typical realizations of a rare population? In *Proc. ISOPE 2000*, Seattle, USA, pp. 123–130.

Huang, J. B. and R. Eatock Taylor (1996). Second order interaction between waves and multiple bottom-mounted vertical circular cylinders. In *Proc. 11th Intl. Workshop on Water Waves and Floating Bodies*, Hamburg, Germany.

Huseby, M. and J. Grue (2000). An experimental investigation of higher-harmonic wave forces on a vertical cylinder. *Journal of Fluid Mech. 414*, pp. 75–103.

John, F. (1950). On the motion of floating bodies. *Comm. Pure Appl. Math. 3*, pp. 45–101.

Jonathan, P. and P. H. Taylor (1997). On irregular, non-linear waves in a spread sea. *ASME Trans. Journal of Offshore Mech. and Arctic Eng. 119*, pp. 37–41.

Joo, S. W., W. W. Schultz, and A. F. Messiter (1990). An analysis of the initial-value wavemaker problem. *Journal of Fluid Mech. 214*, pp. 161–183.

Kagemoto, H., M. Murai, M. Saito, B. Molin, and Š. Malenica (2002). Experimental and theoretical analysis of the wave decay along a long array of vertical cylinders. *Journal of Fluid Mech. 456*, pp. 113–135.

Kagemoto, H. and D. K. P. Yue (1986). Interactions among multiple three-dimensional bodies in water waves: an exact algebraic method. *Journal of Fluid Mech. 166*, pp. 189–209.

Kernot, M. P. (1995). *The second-order forcing and response of offshore structures in irregular seas.* Ph. D. thesis, University of Oxford.

Kharif, C. and E. Pelinovsky (2003). Physical mechanisms of the rogue wave phenomenon. *European Journal of Mechanics B/Fluids 22*, pp. 603–634.

Kim, M. H. and D. K. P. Yue (1989). The complete second order diffraction solution for an axisymmetric body Part 1. Monochromatic incident waves. *Journal of Fluid Mech. 200*, pp. 235–264.

Kim, M. H. and D. K. P. Yue (1990). The complete second order diffraction solution for an axisymmetric body Part 2. Bichromatic incident waves and body motions. *Journal of Fluid Mech. 211*, pp. 557–593.

Kjeldsen, S. P. (1997). Examples of heavy weather damage caused by giant waves. *Bulletin of the Soc. of Naval Architects of Japan 828*, pp. 744–748.

Kriebel, D. L. (1990). Nonlinear wave interaction with a vertical circular cylinder. Part 1. Monochromatic incident waves. *Ocean Engineering 17*, pp. 345–377.

Kriebel, D. L. (1992). Nonlinear wave interaction with a vertical circular cylinder. Part 2. Wave runup. *Ocean Engineering 19*, pp. 75–99.

Lee, C. H., H. D. Maniar, J. N. Newman, and X. Zhu (1996). Computations of wave loads using a B-spline panel method. In *Proc. 21st Symp. on Naval Hydrodynamics*, Trondheim, Norway.

Lee, C. H. and J. N. Newman (2004). *Computation of wave effects using the panel method.* In Numerical models in fluid-structure interaction, Editor S. Chakrabarti. WIT Press.

Lighthill, J. (1979). Waves and hydrodynamic loading. In *Proc. 2nd Intl. Conf. Behaviour of Offshore Structures*, Volume 1, pp. 1–40.

Lindgren, G. (1970). Some properties of a normal process near a local maximum. *Ann. Math. Statist. 41*, pp. 1870–1883.

Linton, C. M. and D. V. Evans (1990a). Corrigendum: The interaction of waves with arrays of vertical circular cylinders. *Journal of Fluid Mech. 218*, p. 663.

Linton, C. M. and D. V. Evans (1990b). The interaction of waves with arrays of vertical circular cylinders. *Journal of Fluid Mech. 215*, pp. 549–569.

Linton, C. M. and D. V. Evans (1992). Integral equations for a class of problems concerning obstacles in waveguides. *Journal of Fluid Mech. 245*, pp. 349–365.

Longuet-Higgins, M. S. (1962). Resonant interactions between two trains of gravity waves. *Journal of Fluid Mech. 12*, pp. 321–332.

Longuet-Higgins, M. S. (1967). On the trapping of wave energy round islands. *Journal of Fluid Mech. 29*, pp. 781–821.

Malenica, Š. (1997). Second order interaction of water waves with arrays of vertical circular cylinders. In *Proc. 2nd Congress of Croatian Soc. of Mech.*, pp. 599–606.

Malenica, Š., R. Eatock Taylor, and J. B. Huang (1999). Second-order wave diffraction by an array of vertical cylinders. *Journal of Fluid Mech. 390*, pp. 349–373.

Malenica, Š. and B. Molin (1995). Third harmonic wave diffraction by a vertical cylinder. *Journal of Fluid Mech. 302*, pp. 203–229.

Mallory, J. K. (1975). Abnormal waves on the south east coast of south africa. *Intl. Hydrographic Review 51*, pp. 99–129.

Maniar, H. D. and J. N. Newman (1997). Wave diffraction by a long array of cylinders. *Journal of Fluid Mech. 339*, pp. 309–330.

McCamy, R. S. and R. A. Fuchs (1954). Wave forces on piles: A diffraction theory. Technical Report 69, U.S. Army Corp. of Eng.

McIver, P. and D. V. Evans (1984). Approximation of wave forces on cylinder arrays. *Applied Ocean Research 6*, pp. 101–107.

Mei, C. C. (1978). Numerical methods in water-wave diffraction and radiation. *Annu. Rev. Fluid Mech. 10*, pp. 393–416.

Mei, C. C. (1989). *The applied dynamics of ocean surface waves.* World Scientific.

Moe, G. (1993). Vertical resonant motions of TLPs. Technical report, NTH.

Molin, B. (1979). Second order diffraction loads upon three-dimensional bodies. *Applied Ocean Research 1*, pp. 197–202.

Moubayed, W. I. and A. N. Williams (1995). Second-order hydrodynamic interactions in an array of vertical cylinders in bichromatic waves. *Journal of Fluids and Structures 9*, pp. 61–98.

Newman, J. N. (1990). Second-harmonic wave diffraction at large depths. *Journal of Fluid Mech. 213*, pp. 59–70.

Ochi, M. K. (1998). *Ocean Waves - The Stochastic Approach.* Cambridge University Press.

Ohl, C. O. G., P. H. Taylor, R. Eatock Taylor, and A. G. L. Borthwick (2001a). Water wave diffraction by a cylinder array. Part 1: Regular waves. *Journal of Fluid Mech. 442*, pp. 1–32.

Ohl, C. O. G., P. H. Taylor, R. Eatock Taylor, and A. G. L. Borthwick (2001b). Water wave diffraction by a cylinder array. Part 2: Irregular waves. *Journal of Fluid Mech. 442*, pp. 33–66.

Peregrine, D. H. (1983). Water waves, nonlinear schrodinger equations and their solutions. *Journal of the Austral. Math. Soc. B25*, pp. 16–43.

Pierson, W. J. and L. Moskowitz (1964). A proposed spectral model for fully developed wind seas based on the similarity theory of sa kitagorodskii. *Journal of Geophys. Research 69*, pp. 5181–5190.

Prevosto, M. and G. Z. Forristall (2002). Statistics of wave crests from models vs. measurements. In *Proc. OMAE 2002*, Volume 28443, Oslo, Norway.

Provosto, M. and B. Bouffandeau (2002). Probability of occurrence of a giant wave crest. In *Proc. OMAE 2002*, Volume 28446, Oslo, Norway.

Robin, A. and M. Olagnon (1991). Occurrence of extreme waves with respect to significant wave height. In *Proc. OMAE 1991*, Stavanger, Norway, pp. 1–9.

Sand, S. E., N. E. Ottesen-Hansen, P. Klinting, O. T. Gudmestad, and M. J. Sterndorff (1990). *Freak wave kinematics*, pp. 535–549. In Water Wave Kinematics, Editors A. Torum and O.T. Gudmestad. Kluwer Academic Publishers.

Simon, M, J. (1982). Multiple scattering in arrays of axisymmetric wave-energy devices. Part 1. A Matrix method using a plane wave approximation. *Journal of Fluid Mech. 120*, pp. 1–25.

Spring, B. H. and P. L. Monkmeyer (1974). Interaction of plane waves with vertical cylinders. In *Proc. 14th Intl. Conf. on Coastal Eng.*, pp. 1828–1845.

Stansberg, C. T. (2000). Nonlinear extreme wave evolution in random wave groups. In *Proc. ISOPE 2000*, Volume 3, Seattle, USA, pp. 1–8.

Stokes, G. G. (1847). On the theory of oscillatory waves. *Trans. Camb. Phil. Soc. 8*, pp. 441–455.

Taylor, P. H., P. Jonathan, and L. A. Harland (1997). Time domain simulation of jack-up dynamics with the extremes of a Gaussian process. *ASME Trans. Journal of Vibration and Acoustics 119*(4), pp. 624–628.

Taylor, P. H., D. A. G. Walker, R. Eatock Taylor, and A. C. Hunt (2005). On the estimation of directional spreading from a single wave staff. In *Proc. 5th Intl. Symp. on Ocean Wave Measurement and Analysis*, Madrid, Spain.

Taylor, P. H. and B. A. Williams (2004). Wave statistics for intermediate water depth - newwaves and symmetry. *ASME Trans. Journal of Offshore Mech. and Arctic Eng. 126*, pp. 54–59.

Teigen, P. and K. Trulsen (2001). Numerical investigation of nonlinear wave effects around multiple cylinders. In *Proc. ISOPE 2001*, Volume 3, Stavanger, Norway, pp. 369–378.

Theocaris, P. S. and N. I. Iokimidis (1977). Numerical integration methods for the solution of singular integral equations. *Q. Appl. Math. 35*, pp. 173–183.

Tromans, P. S., A. R. Anaturk, and P. Hagemeijer (1991). A new model for the kinematics of large ocean waves: Application as a design wave. In *Proc. ISOPE 1991*, Volume 3, Edinburgh, UK, pp. 64–71.

Tromans, P. S. and P. H. Taylor (1998). The shapes, histories, and statistics of non-linear wave crests in random seas. In *Proc. OMAE 1998*, Volume 1206, Lisbon, Portugal.

Tromans, P. S. and J. van Dam (1996). The probability distribution of extreme load on space frame structures. In *Proc. OMAE 1996*, Florence, Italy.

Tromans, P. S. and L. Vanderschuren (1995). Response based design conditions in the north sea. In *Proc. Offshore Tech. Conf.*, Volume 7382, Houston, USA, pp. 387–397.

Tucker, M. J. and E. G. Pitt (2001). *Waves in Ocean Engineering*. Elsevier.

Twersky, V. (1952). Multiple scattering of radiation by an arbitrary configuration of parallel cylinders. *Journal of the Acoust. Soc. of America 24*, pp. 42–46.

Ursell, F. (1951). Trapping modes in the theory of surface waves. *Proc. Camb. Phil. Soc. 47*, pp. 347–358.

van Unen, R. F., A. A. vand Beuzekom, G. Z. Forristall, J. P. Mathisen, and J. Starke (1998). Wacsis - wave crest sensor intercomparison study at the Meetpost Noordwijk measurement platform. In *Ocean '98 IEEE*, Nice, France, pp. 192–197.

Walker, D. A. G. and R. Eatock Taylor (2005). Wave diffraction from linear arrays of cylinders. *Ocean Engineering 32*, pp. 2053–2078.

Walker, D. A. G., P. H. Taylor, and R. Eatock Taylor (2005). The shape of large surface waves on the open sea and the Draupner New Year wave. *Applied Ocean Research 26*, pp. 73–83.

Walker, D. A. G., P. H. Taylor, R. Eatock Taylor, and J. Zang (2006). Diffraction theory as a tool for predicting airgap beneath a multicolumn gravity-based structure. *International Journal of Offshore and Polar Engineering 16*(3), pp. 175–182.

Wehausen, J. V. and E. Laitone (1960). Surface Waves. *Handbuch der Physik 9*, pp. 446–778.

Wu, G. X. and R. Eatock Taylor (1995). Time stepping solutions of the two dimensional non-linear wave radiation problem. *Ocean Engineering 22*, pp. 785–798.

Wu, G. X. and R. Eatock Taylor (2003). The coupled finite element and boundary element analysis of non-linear interactions between waves and bodies. *Ocean Engineering 30*, pp. 387–400.

Wu, G. X., Q. W. Ma, and R. Eatock Taylor (1998). Numerical simulation of sloshing waves in a 3D tank based on a finite element method. *Applied Ocean Research 20*, pp. 337–355.

Yuen, H. C. and B. M. Lake (1982). Nonlinear dynamics of deep water gravity waves. *Advances in Appl. Mech. 22*, pp. 153–180.

Zang, J., R. Gibson, P. H. Taylor, R. Eatock Taylor, and C. Swan (2006). Second order wave diffraction around a fixed ship-shaped body in unidirectional steep waves. *ASME Trans. Journal of Offshore Mech. and Arctic Eng. 128*, pp. 89–99.

Zang, J., P. H. Taylor, and R. Eatock Taylor (2003). Hydrodynamics of ship shaped floating bodies. Internal report. Dept. of Eng. Science, University of Oxford.

Appendix A

Boundary element method: Numerical implementation

The numerical evaluation of the boundary integral equation can be divided into five stages for convenience. These stages are outlined here for a two dimensional problem. An analogous procedure works for a three dimensional problem also.

STAGE 1: DIVISION OF THE BOUNDARY INTO ELEMENTS

The boundary of the studied domain is divided into a specified number of connected elements and the variation of the geometry, ϕ and $\frac{\partial \phi}{\partial n}$ must be described over each element. The variation can be constant, linear, quadratic, cubic or higher order. It should be noted that the geometry variation does not necessarily have to match that of the variables. Obviously, increasing the order of the variation over an element will produce more accurate solutions, but at the expense of extended computation time. It is generally accepted that for most applications the isoparametric quadratic element provides the best compromise between accuracy and efficiency. Isoparametric elements have the same order of variation for both geometry and the unknown variables. It is this type of element that is incorporated into the DIFFRACT code and hence is considered exclusively here.

The most convenient method for describing the behaviour of an element is to use shape functions. Shape functions use the nodal points on each element where the variable value is given and hence for a quadratic element in two dimensions, three nodes per element are needed; one at the midpoint and one at either end of the element. It is convenient to define a coordinate system, ξ, that is local to the element, having its origin at the midpoint and values of -1 and +1 at the end nodes. Therefore the geometry of an element can be described using the coordinates of its nodes and the shape functions as follows:

$$x(\xi) = \sum_{c=1}^{3} N_c(\xi) x_c = N_1(\xi)x_1 + N_2(\xi)x_2 + N_3(\xi)x_3 \tag{A.1}$$

$$y(\xi) = \sum_{c=1}^{3} N_c(\xi) y_c = N_1(\xi)y_1 + N_2(\xi)y_2 + N_3(\xi)y_3 \tag{A.2}$$

where the shape functions $N_c(\xi)$ are quadratic functions that must satisfy two conditions:

1. $N_c(\xi) = 1$ at node c
2. $N_c(\xi) = 0$ at the other two nodes

The shape functions can be readily derived as:

$$N_1(\xi) = \frac{-\xi}{2}(1-\xi) \tag{A.3}$$

$$N_2(\xi) = (1+\xi)(1-\xi) \tag{A.4}$$

$$N_3(\xi) = \frac{\xi}{2}(1+\xi). \tag{A.5}$$

It should be noted that the procedure outlined here is applicable to shape functions of any order.

As the elements considered are isoparametric, the same shape functions are used to describe the variation of the solution variables:

$$\phi(\xi) = \sum_{c=1}^{3} N_c(\xi) \phi_c = N_1(\xi)\phi_1 + N_2(\xi)\phi_2 + N_3(\xi)\phi_3 \tag{A.6}$$

$$\begin{aligned} \frac{\partial \phi(\xi)}{\partial n} &= \sum_{c=1}^{3} N_c(\xi) \left(\frac{\partial \phi}{\partial n}\right)_c \\ &= N_1(\xi) \left(\frac{\partial \phi}{\partial n}\right)_1 + N_2(\xi) \left(\frac{\partial \phi}{\partial n}\right)_2 + N_3(\xi) \left(\frac{\partial \phi}{\partial n}\right)_3 . \end{aligned} \tag{A.7}$$

STAGE 2: NUMERICAL INTEGRATION OF THE KERNELS

The local coordinate system, ξ, ranging from -1 to +1 was used because it shares the same limits with the Gaussian quadrature technique for numerical integration. The numerical integration is performed over each element making up the boundary using the local intrinsic coordinate, ξ, rather than using the boundary curve parameter, Γ.

To facilitate the transformation of variable from Γ to ξ it is necessary to calculate the Jacobian

of the transformation, $J(\xi)$:

$$J(\xi) = \frac{\mathrm{d}\Gamma}{\mathrm{d}\xi} = \sqrt{\left(\frac{\mathrm{d}x(\xi)}{\mathrm{d}\xi}\right)^2 + \left(\frac{\mathrm{d}y(\xi)}{\mathrm{d}\xi}\right)^2}. \tag{A.8}$$

To determine the components of the unit outward normal, n, in the x and y directions one must first define a unit tangential vector, $\widehat{\mathbf{m}}$:

$$\widehat{\mathbf{m}} = \frac{m_x}{|\mathbf{m}|}\,\mathbf{e_x} + \frac{m_y}{|\mathbf{m}|}\,\mathbf{e_y} \tag{A.9}$$

where $\mathbf{e_x}$ and $\mathbf{e_y}$ are unit vectors in the x and y directions and the magnitude of the vector $\mathbf{m}$ is given by:

$$|\mathbf{m}| = \sqrt{(m_x)^2 + (m_y)^2} = \sqrt{\left(\frac{\mathrm{d}x(\xi)}{\mathrm{d}\xi}\right)^2 + \left(\frac{\mathrm{d}y(\xi)}{\mathrm{d}\xi}\right)^2} \tag{A.10}$$

which is equal to the Jacobian, $J(\xi)$. Hence the components of the tangential vector $\mathbf{m}$ are:

$$m_x = \frac{1}{J(\xi)}\left[\frac{\mathrm{d}x(\xi)}{\mathrm{d}\xi}\right]; \tag{A.11}$$

$$m_y = \frac{1}{J(\xi)}\left[\frac{\mathrm{d}y(\xi)}{\mathrm{d}\xi}\right]. \tag{A.12}$$

The normal vector $\mathbf{n}$ is equal to the vector product of the vectors $\mathbf{m}$ and $\mathbf{e_z}$:

$$\begin{aligned}\mathbf{n} = \mathbf{m} \times \mathbf{e_z} &= \begin{vmatrix} \mathbf{e_x} & \mathbf{e_y} & \mathbf{e_z} \\ \frac{1}{J(\xi)}\left[\frac{\mathrm{d}x(\xi)}{\mathrm{d}\xi}\right] & \frac{1}{J(\xi)}\left[\frac{\mathrm{d}y(\xi)}{\mathrm{d}\xi}\right] & 0 \\ 0 & 0 & 1 \end{vmatrix} \\ &= \frac{1}{J(\xi)}\left[\frac{\mathrm{d}y(\xi)}{\mathrm{d}\xi}\right]\mathbf{e_x} - \frac{1}{J(\xi)}\left[\frac{\mathrm{d}x(\xi)}{\mathrm{d}\xi}\right]\mathbf{e_y}\end{aligned} \tag{A.13}$$

where $\mathbf{e_z}$ is the unit vector in the z direction, which is normal to the two-dimensional plane under consideration.

Therefore the components of the unit outward normal are:

$$n_x = \frac{1}{J(\xi)}\left[\frac{\mathrm{d}y(\xi)}{\mathrm{d}\xi}\right]; \tag{A.14}$$

$$n_y = \frac{-1}{J(\xi)}\left[\frac{\mathrm{d}x(\xi)}{\mathrm{d}\xi}\right]. \tag{A.15}$$

The differentials of the coordinates $x(\xi)$ and $y(\xi)$ with respect to ξ are given by:

$$\frac{\mathrm{d}x(\xi)}{\mathrm{d}\xi} = \frac{\mathrm{d}N_1(\xi)}{\mathrm{d}\xi}x_1 + \frac{\mathrm{d}N_2(\xi)}{\mathrm{d}\xi}x_2 + \frac{\mathrm{d}N_3(\xi)}{\mathrm{d}\xi}x_3 \tag{A.16}$$

$$\frac{\mathrm{d}y(\xi)}{\mathrm{d}\xi} = \frac{\mathrm{d}N_1(\xi)}{\mathrm{d}\xi}y_1 + \frac{\mathrm{d}N_2(\xi)}{\mathrm{d}\xi}y_2 + \frac{\mathrm{d}N_3(\xi)}{\mathrm{d}\xi}y_3 \tag{A.17}$$

and the differentials of the shape functions are:

$$\frac{\mathrm{d}N_1(\xi)}{\mathrm{d}\xi} = \xi - \frac{1}{2}; \tag{A.18}$$

$$\frac{\mathrm{d}N_1(\xi)}{\mathrm{d}\xi} = -2\xi; \tag{A.19}$$

$$\frac{\mathrm{d}N_3(\xi)}{\mathrm{d}\xi} = \xi + \frac{1}{2}. \tag{A.20}$$

The boundary integral equation 3.40 (Section 3.3 Chapter 3) can now be written in terms of the local coordinate, ξ, rather than the boundary curve parameter, Γ. The transformed boundary integral equation is:

$$C(\boldsymbol{P})\phi(\boldsymbol{P}) + \sum_{m=1}^{M}\sum_{c=1}^{3}\phi(\boldsymbol{Q})\int_{-1}^{1}K_1(\boldsymbol{P},\boldsymbol{Q})N_c(\xi)J(\xi)\,\mathrm{d}\xi = \sum_{m=1}^{M}\sum_{c=1}^{3}\frac{\partial\phi(\boldsymbol{Q})}{\partial n}\int_{-1}^{1}K_2(\boldsymbol{P},\boldsymbol{Q})N_c(\xi)J(\xi)\,\mathrm{d}\xi \tag{A.21}$$

where M is the total number of boundary elements. Referring to the integral functions containing K_1 and K_2 as $A_{m,c}$ and $B_{m,c}$ respectively, the boundary integral equation can be expressed more simply as:

$$C(\boldsymbol{P})\phi(\boldsymbol{P}) + \sum_{m=1}^{M}\sum_{c=1}^{3}\phi(\boldsymbol{Q})A_{m,c}(\boldsymbol{P},\boldsymbol{Q}) = \sum_{m=1}^{M}\sum_{c=1}^{3}\frac{\partial\phi(\boldsymbol{Q})}{\partial n}B_{m,c}(\boldsymbol{P},\boldsymbol{Q}). \tag{A.22}$$

A set of linear algebraic equations can now be formed by taking each node in turn as the source point $\boldsymbol{P}$ and evaluating the integrals in Equation A.21. The resulting equations can be written in matrix form as:

$$(C(\boldsymbol{P})[I] + [A])[\phi] = [B]\left[\frac{\partial\phi}{\partial n}\right] \tag{A.23}$$

where $[I]$ is the identity matrix and the matrices $[A]$ and $[B]$ contain the functions $A_{m,c}$ and

$B_{m,c}$ respectively. From here on the combined matrix ($[I] + [A]$) is referred to as $[A']$.

As discussed in Chapter 3, the fundamental solution is 'singular', which means that the kernels contain terms of the order $1/\nu$ or $\ln(1/\nu)$ as $\nu \rightarrow 0$. The kernels are dependent on the distance between $\boldsymbol{P}$ and $\boldsymbol{Q}$ and so it is now useful to examine three possibilities for the positions of $\boldsymbol{P}$ and $\boldsymbol{Q}$. The first two possibilities listed below describe the evaluation of the off-diagonal elements of the matrices $[A']$ and $[B]$ and the third possibility describes the evaluation of the diagonal elements.

1. **$\boldsymbol{P}$ and $\boldsymbol{Q}$ in different elements**

   In this case the kernels are not singular and so the standard Gaussian quadrature scheme can be applied:

$$\int_{-1}^{+1} f(\xi)\, d\xi = \sum_{g=1}^{G_i} f(\xi_g) w_g \tag{A.24}$$

   where G_i is the total number of Gaussian integration points and ξ_g is the Gaussian coordinate, which has an associated weight function w_g.

2. **$\boldsymbol{P}$ and $\boldsymbol{Q}$ in the same element but $\boldsymbol{P} \neq \boldsymbol{Q}$**

   The kernels are singular in this case although the shape function $N_c(\xi)$ in the vicinity of $\boldsymbol{P}$ is of the order $r(\boldsymbol{P}, \boldsymbol{Q})$, and so the product of the kernels and the shape function is not singular. Hence the integrals can again be evaluated using the standard Gaussian quadrature scheme.

3. **$\boldsymbol{P}$ and $\boldsymbol{Q}$ in the same element and $\boldsymbol{P} = \boldsymbol{Q}$**

   The standard Gaussian quadrature procedure can no longer be used because of the singularity of the kernels.

   For this case the evaluation of the integral involving the second kernel, K_2, is first discussed. From Equation 3.39 (Section 3.3 Chapter 3) it is clear that as $\boldsymbol{P}$ approaches $\boldsymbol{Q}$, the singularity is of the form $\ln(1/\nu)$ as $\nu \rightarrow 0$. This type of integral can be evaluated using the logarithmic Gaussian quadrature scheme:

$$\int_{0}^{+1} f(\nu) \ln\left(\frac{1}{\nu}\right) \mathrm{d}\nu = \sum_{gl=1}^{G_{li}} f(\nu_{gl}) w_{gl} \tag{A.25}$$

   where G_{li} is the total number of logarithmic Gaussian integration points used and ν_{gl} is the Gaussian coordinate, which has an associated weight function w_{gl}. Note that the

limits of integration here are different from those used in the BIE. To transform the integral variable from ξ to ν a simple linear transformation can be used (Becker 1992):

- If $\boldsymbol{P}$ is the first node of the element: $\nu = \frac{1}{2}(1+\xi)$.
- If $\boldsymbol{P}$ is the second node of the element then the element is divided into two sub-elements: $\nu = -\xi$ for $-1 < \xi < 0$ and $\nu = \xi$ for $0 < \xi < 1$.
- If $\boldsymbol{P}$ is the third node of the element: $\nu = \frac{1}{2}(1-\xi)$.

The first kernel, K_1, is now considered. It can be shown that K_1 contains terms of the order $1/\nu$ as $\nu \rightarrow 0$ and so it is no longer possible to use the Gaussian quadrature technique. Such singular kernels require specialist treatment (Theocaris and Iokimidis 1977). Furthermore, it is now necessary to calculate the parameter $C(\boldsymbol{P})$ since its contribution is added to the diagonal elements of $[A]$ to give the diagonal elements of $[A']$. Fortunately an alternative approach, based on the fact that the BIE matrices must apply to any physical problem with a unique solution, is available to evaluate the diagonal elements of $[A']$. Any physical problem can be chosen so long as the solution does not depend on the geometry. The simplest problem to consider is the case where the potential is constant, $\phi = \phi_c$ say, throughout the entire solution domain. This leads to zero potential gradients everywhere and so the right-hand side of Equation A.23 becomes zero:

$$[A'][\phi_c] = [B][0]. \tag{A.26}$$

Now, ϕ_c is the same for all nodes and so the sum of all the elements along any row of $[A']$ must be zero. The diagonal elements can therefore be determined from the summation of the non-diagonal elements using:

$$A'_{i,j} = -\sum_{j=1, j\neq i}^{N} A'_{i,j} \quad \text{for } i = 1, 2, 3, \ldots, N \tag{A.27}$$

where i and j are the row and column counters respectively, and N is the total number of nodes.

Stage 3: Application of the boundary conditions

Although all of the elements of the matrices $[A']$ and $[B]$ have now been calculated, the problem is not unique until a set of boundary conditions have been applied. A boundary condition can be a:

1. Prescribed potential.
2. Prescribed potential gradient.
3. Prescribed relationship between potential and potential gradient.

All nodes must have a prescribed value; if a node has no prescribed boundary condition then it is automatically assumed to have zero potential gradient.

To be able to solve the matrix equation numerically the matrices $[A']$ and $[B]$ of Equation A.23 must be rearranged into the form:

$$[A^*][x] = [B^*][y] \tag{A.28}$$

where $[x]$ contains all of the unknown variables and $[y]$ contains all of the known variables prescribed as boundary conditions. The matrices $[A^*]$ and $[B^*]$ are modified forms of $[A']$ and $[B]$ respectively. The final system of linear algebraic equations can be simplified further and written as:

$$[A^*][x] = [c] \tag{A.29}$$

where $[c]$ contains known coefficients. For an illustration of how this rearrangement is performed see Becker (1992) pages 52-56.

STAGE 4: SOLUTION OF THE ALGEBRAIC EQUATIONS

Upon application of the boundary conditions, the solution matrix $[A^*]$ is found to be non-symmetric and fully populated with non-zero coefficients. The most suitable solving technique to use in this case is Gaussian elimination (or any other direct technique) although iterative methods have also been used to good effect. It is important to note that if a problem has been properly defined then it should result in properly conditioned matrices; the matrices only become ill-conditioned or singular if there is a mistake in the formulated problem (e.g. two nodes having the same coordinates).

STAGE 5: CALCULATION OF THE INTERNAL VARIABLES

Solving the linear equations allows the values of potential and potential gradient at all nodes on the boundary to be calculated. It is then relatively straightforward to determine the potential at any interior point by substituting all of the boundary values into Equation A.21 and assuming the interior point to be the source point $\boldsymbol{p}$. The normal potential gradient